

VT-Forschungsbericht 2008-01

**Numerical Simulations of
Soot Formation in
Turbulent Flows**

Massimiliano Di Domenico

Deutsches Zentrum für Luft- und Raumfahrt e.V.
Institut für Verbrennungstechnik
Stuttgart



DLR

**Deutsches Zentrum
für Luft- und Raumfahrt e.V.**
in der Helmholtz-Gemeinschaft



Herausgeber

Deutsches Zentrum
für Luft- und Raumfahrt e.V.

Institut für
Verbrennungstechnik

Pfaffenwaldring 38-40
70569 Stuttgart

Telefon
Telefax

(0 7 11) 68 62 - 3 08
(0 7 11) 68 62 - 5 78

Als Manuskript gedruckt.
Abdruck oder sonstige Verwendung
nur nach Absprache mit dem Institut gestattet

D93, Stuttgart

Numerical Simulations of Soot Formation in Turbulent Flows

A thesis accepted by the Faculty of Aerospace Engineering and Geodesy of the
Universität Stuttgart in partial fulfillment of the requirements for the degree of
Doctor of Engineering Sciences (Dr.-Ing.)

by

Dipl.-Ing. Massimiliano Di Domenico

born in Rome

main referee: PD Dr.-Ing. P. Gerlinger

co-referee: Prof. Dr. rer. nat. habil. C.-D. Munz

Date of defence: 28th November 2007

Institute of Combustion Technology for Aerospace Engineering
Universität Stuttgart

Vorwort

Die vorliegende Arbeit entstand bei meiner mehrjährigen Tätigkeit am Institut für Verbrennungstechnik des Deutschen Zentrums für Luft- und Raumfahrt e.V. (DLR) in Stuttgart.

Ich möchte daher zuerst dem Institutsleiter Prof. Dr.-Ing. M. Aigner für die Möglichkeit zur Durchführung dieser Arbeit und die Unterstützung beim Aufbau der THETA-Gruppe danken. Ich bedanke mich außerdem bei Dr.-Ing. habil. B. Noll für die zahlreichen Diskussionen und die Einführung in die interessante Welt der numerischen Strömungssimulation.

Mein besonderer Dank gilt Herrn PD Dr.-Ing. P. Gerlinger für seine tägliche Betreuung, die wertvollen Ratschläge und zudem für die Übernahme des Hauptberichts. Ohne seine umfassende Erfahrung und den ständigen Zuspruch wäre ein erfolgreicher Abschluss dieser Doktorarbeit nicht möglich gewesen. Herrn Prof. Dr. rer. nat. C.-D. Munz danke ich für die Übernahme des Mitberichts und die nützlichen Korrekturen meines Manuskripts.

Eine komplette Auflistung aller ehemaligen und derzeitigen Kollegen, durch die meine wissenschaftlichen Kenntnisse verbessert wurden, ist kaum möglich. Daher möchte ich mich bei der gesamten THETA-Gruppe (T. Blacha, P. Ess, E. Ivanova und F. Rebosio) bedanken. Ihre Hilfe in der Erweiterung des CFD Codes THETA war unabkömmlich und hat erst die großen Fortschritte bei der Entwicklung dieses vielseitigen Werkzeuges ermöglicht.

Eine wissenschaftliche Arbeit kann ohne eine fundierte bibliographische Recherche nicht entstehen. Daher bedanke ich mich bei unserer Bibliothekarin J. Lotz für ihre Hilfe bei der Suche nach Literatur jeglicher Art.

Besondere Erwähnung haben K. Nold und P. Ess verdient, da diese Arbeit ohne ihre Korrekturen sicherlich weniger verständlich wäre. Ich danke auch den Mitarbeitern der Abteilung für Verbrennungsdiagnostik, insbesondere K.-P. Geigle, R. Giezendanner-Thoben, P. Kutne und O. Lammel, durch die ich ein besseres Verständnis der in dieser Arbeit angewandten experimentellen Daten und Methoden gewonnen habe. Ich möchte auch den Kollegen P. Le Clerq, M. Liu und D. Panara meinen Dank für die schöne Zeit, die wir zusammen am Institut verbracht haben, aussprechen.

Contents

List of Figures	7
List of Tables	13
List of Symbols	15
Zusammenfassung	21
Abstract	23
1 Introduction	25
1.1 Motivations	25
1.2 Goals of this work	26
2 Governing equations and numerical scheme	29
2.1 Transport equations in the finite-volume formulation	29
2.2 Chemical source term	31
2.3 Numerical methods	43
2.4 Modeling of transport phenomena	43
2.5 Laminar diffusion flames	46
3 Soot formation modeling in laminar flames	69
3.1 Introduction	69
3.2 A sectional approach for soot formation modeling	72
3.3 Soot particle equations	77
3.4 Model test and validation	82
3.5 Premixing effects on soot formation rate	94
4 Chemical kinetics in turbulent flows	111
4.1 Phenomenological description of turbulent flows	111
4.2 Averaged transport equations	112
4.3 PDF approach for the calculation of averaged source terms	114
4.4 Model validation	125

5	Soot formation in semi-technical scale burners	155
5.1	Introduction	155
5.2	The SiA semi-technical scale burner	156
6	Conclusions	175
A	Determination of the mixture transport properties	179
A.1	The calculation of pure species properties	179
A.2	Calculation of the mixture transport coefficients	183
B	Elements of numerical methods for Navier-Stokes equations	185
B.1	Gradient computation	185
B.2	Discretization of the convective terms	185
B.3	Discretization of the diffusive terms	186
B.4	Pressure-velocity coupling	187
B.5	Matrix-free linear solvers	188
C	A generalized fitting procedure for Arrhenius functions	191
C.1	Linearized algorithm	191
C.2	Levenberg-Marquardt iterative method	192
	Bibliography	195

List of Figures

2.2.1	Ignition of a H ₂ /air mixture, $\phi = 1$, $p = 10^5$ Pa, $T_0 = 1000$ K.	37
2.2.2	Source terms for ignition problem 2.2.1.	37
2.2.3	Eigenvalues of the Jacobian matrix for ignition problem 2.2.1.	38
2.2.4	Ignition of H ₂ /air mixtures at different equivalence ratios, $p = 10^5$ pa, $T_0 = 1000$ K.	39
2.2.5	Ignition of H ₂ /air mixtures at different pressures, $\phi = 1$, $T_0 = 1000$ K.	40
2.2.6	Ignition of H ₂ /air mixtures at different initial temperatures, $\phi=1$, $p = 1$ bar.	41
2.2.7	Ignition of H ₂ /air mixtures using different kinetic mechanisms, $T_0 = 1000$ K, $\phi=1$, $p = 1$ bar.	42
2.5.1	Mitchell's diffusion flame configuration.	47
2.5.2	Axial velocity field and temperature field for the Mitchell et al. flame [139].	49
2.5.3	Oxygen mass fraction field for the Mitchell et al. flame [139].	50
2.5.4	CH ₃ and CH mass fraction fields for the Mitchell et al. flame [139].	50
2.5.5	H and H ₂ mass fraction fields for the Mitchell et al. flame [139].	51
2.5.6	OH and H ₂ O mass fraction fields for the Mitchell et al. flame [139].	52
2.5.7	CO and CO ₂ mass fraction fields for the Mitchell et al. flame [139].	52
2.5.8	Effect of grid refinement: temperature and O ₂ fields.	53
2.5.9	Effect of grid refinement: OH field.	54
2.5.10	Effect of kinetic mechanism: temperature field.	55
2.5.11	Effect of kinetic mechanism: CH ₃ and H ₂ fields.	55
2.5.12	Effect of kinetic mechanism: CO ₂ and H ₂ O fields.	56
2.5.13	CH ₄ constant-pressure heat capacities for mechanisms [101] and [178].	57
2.5.14	Temperature and H ₂ O fields using constant and variable Lewis numbers.	58
2.5.15	CO and CO ₂ fields using constant and variable Lewis numbers.	58
2.5.16	Original and extended grids.	59
2.5.17	Effect of the outflow boundary on the results: temperature and H ₂ fields.	60
2.5.18	Effect of the inflow boundary condition: temperature field.	61
2.5.19	Inflow profiles for reference flame (subsection 2.5.1) and upstream-extended domain (subsection 2.5.5).	62
2.5.20	Effect of the inflow boundary condition: CO field.	62
2.5.21	Comparison between experimental and simulated temperature profiles at different heights above the burner: (a) 1.2 cm, (b) 2.4 cm, (c) 5.0 cm, respectively.	64

2.5.22	Comparison between experimental and simulated N ₂ mole fraction profiles at different heights above the burner: (a) 1.2 cm, (b) 2.4 cm, (c) 5.0 cm, respectively.	65
2.5.23	Comparison between experimental and simulated CO ₂ mole fraction profiles at different heights above the burner: (a) 1.2 cm, (b) 2.4 cm, (c) 5.0 cm, respectively.	66
2.5.24	Comparison between experimental and simulated axial velocity profiles at different heights above the burner: (a) 1.2 cm, (b) 2.4 cm, (c) 5.0 cm, respectively.	67
3.2.1	Sketch of a generic combustion process.	73
3.2.2	Schematic representation of the PAH sectional model and related processes. . .	74
3.3.1	Soot source term representation.	78
3.3.2	Graphical representation of the interaction between the PAH sectional method (four classes between 100 and 900 amu) and soot nucleation.	79
3.4.1	Temperature and soot-related species profiles versus time for the zero-dimensional reactor simulation. Symbols each 100 timesteps.	83
3.4.2	Ignition of a sooting mixture: influence of the number of PAH classes.	84
3.4.3	Ignition of a sooting mixture: influence of the pressure.	84
3.4.4	Acetylene and benzene molar fractions for the sooting methane/air flame of Smooke et al. [179].	86
3.4.5	Molar fractions of PAH (one to four) for the sooting methane/air flame of Smooke et al. [179]	86
3.4.6	Soot volume fraction and particle density number for the sooting methane/air flame of Smooke et al. [179]	87
3.4.7	Temperature profiles at several heights above burner of the sooting methane/air flame of Smooke et al. [179].	89
3.4.8	Methane profiles at several heights above burner of the sooting methane/air flame of Smooke et al. [179].	90
3.4.9	Acetylene profiles at several heights above the burner of the sooting methane/air flame [179].	91
3.4.10	Benzene profiles at several heights above the burner of the sooting methane/air flame of Smooke et al. [179].	92
3.4.11	Soot volume fraction profiles at several heights above the burner of the sooting methane/air flame of Smooke et al. [179].	93
3.5.1	Premixing effects on the temperature field of sooting ethylene/air flame [131]. .	96
3.5.2	Flame length as function of premixing for the sooting ethylene/air flame [131].	97
3.5.3	Premixing effects on the C ₂ H ₂ molar fraction of McEnally's ethylene/air sooting flame [131].	98
3.5.4	Premixing effects on the C ₆ H ₆ molar fraction of McEnally's ethylene/air sooting flame.	99
3.5.5	Premixing effects on the soot volume fraction of the McEnally's sooting ethylene/air flame [131].	100

3.5.6	Premixing effects on the soot particle density number of the McEnally's ethylene/air sooting flame.	101
3.5.7	Maximum soot volume fraction and maximum soot particle density number as function of premixing for the McEnally's sooting ethylene/air flame [131].	102
3.5.8	Influence of radiation on the temperature field of the sooting ethylene/air flame [131].	103
3.5.9	Influence of radiation on the soot volume fraction field of the sooting ethylene/air flame [131]. Maximum soot concentrations are given in brackets.	104
3.5.10	Axial temperature profiles comparison for the sooting ethylene/air flame [131].	105
3.5.11	Axial methane profiles for sooting ethylene/air flame [131].	107
3.5.12	Axial acetylene profiles for the sooting ethylene/air flame [131].	108
3.5.13	Axial benzene profiles for the sooting ethylene/air flame [131].	109
3.5.14	Axial soot volume fraction profiles for the sooting ethylene/air flame [131].	110
4.3.1	Unclipped and clipped temperature PDFs, $\langle T \rangle = 2000$ K.	117
4.3.2	Effects of the temperature fluctuations on α_T for the reaction $\text{H} + \text{O}_2 \rightarrow \text{OH} + \text{O}$. Arrhenius constants taken from [94].	119
4.3.3	Effects of the temperature fluctuations on α_T for the reaction $\text{H} + \text{H}_2\text{O}_2 \rightarrow \text{H}_2 + \text{HO}_2$. Arrhenius constants taken from [94].	119
4.3.4	Rate coefficients for the reactions used in Figs. 4.3.2 and 4.3.3.	119
4.3.5	Effects of the species fluctuations for a self-recombination reaction.	123
4.3.6	Effects of the species fluctuations for a heterogeneous recombination reaction.	124
4.4.1	Axial velocity and mixture fraction distributions for the H3 jet flame.	127
4.4.2	Temperature and OH distributions for the H3 jet flame.	128
4.4.3	Influence of the chemical kinetics on the temperature and H distributions of the H3 jet flame.	128
4.4.4	Influence of the C_1 model constant of the $k - \epsilon$ turbulence model on the axial velocity and temperature distributions of the H3 jet flame.	130
4.4.5	Influence of the Lewis number on the temperature and OH distributions of the H3 jet flame.	131
4.4.6	Temperature, temperature fluctuation intensity and turbulent scalar energy distributions of the H3 jet flame.	132
4.4.7	Effect of the temperature PDF on the temperature and OH distributions of the H3 jet flame.	133
4.4.8	Mixture fraction profiles for the H3 jet flame.	134
4.4.9	Temperature profiles for the H3 jet flame: influence of turbulence and thermochemistry modeling.	135
4.4.10	Temperature profiles for the H3 jet flame: influence of temperature and species turbulent fluctuations.	135

4.4.11	O ₂ mass fraction profiles for the H3 jet flame: influence of turbulence and thermo-chemistry modeling.	136
4.4.12	O ₂ mass fraction profiles for the H3 jet flame: influence of temperature and species turbulent fluctuations.	137
4.4.13	Temperature fluctuation intensity profiles for the H3 jet flame.	137
4.4.14	Turbulent scalar energy for the H3 jet flame.	138
4.4.15	Temperature and OH distributions of the lifted H ₂ /air flame [28].	140
4.4.16	HO ₂ and H ₂ O ₂ distributions of the lifted H ₂ /air flame [28].	140
4.4.17	Influence of the kinetic mechanism on the temperature distribution of the lifted H ₂ /air flame [28].	141
4.4.18	Influence of the kinetic mechanism on the OH distribution and lift-off distance of the lifted H ₂ /air flame [28].	142
4.4.19	Influence of the HO ₂ /H ₂ O ₂ submechanism on the temperature and OH distributions of the lifted H ₂ /air flame [28].	143
4.4.20	Influence of the coflow inlet temperature on the OH distribution of the lifted H ₂ /air flame [28].	144
4.4.21	Non-dimensional lift-off heights as functions of the inlet coflow temperatures with standard and modified C_1 constant of the $k - \epsilon$ turbulence model.	145
4.4.22	Influence of the constant C_1 of the $k - \epsilon$ turbulence model on the temperature field of the lifted H ₂ /air flame [28].	145
4.4.23	I_T and temperature fields of the lifted H ₂ /air flame [28].	146
4.4.24	OH predictions for the lifted H ₂ /air flame [28] with and without temperature PDF.	147
4.4.25	σ_Y and temperature predictions with the joint β -PDF for the lifted H ₂ /air flame [28].	148
4.4.26	OH predictions for the lifted H ₂ /air flame [28] with and without temperature and species PDFs.	148
4.4.27	N ₂ mass fraction profiles for the H ₂ /air lifted jet flame [28]: influence of turbulence and thermo-chemistry modeling.	149
4.4.28	N ₂ mass fractions profiles for the H ₂ /air lifted jet flame [28]: influence of temperature and species PDFs.	150
4.4.29	Temperature profiles for the H ₂ /air lifted jet flame [28]: influence of turbulence and thermo-chemistry modeling.	150
4.4.30	Temperature profiles for the H ₂ /air lifted jet flame [28]: influence of temperature and species PDFs.	151
4.4.31	H ₂ mass fractions profiles for the H ₂ /air lifted jet flame [28]: influence of turbulence and thermo-chemistry modeling.	152
4.4.32	H ₂ mass fractions profiles for the H ₂ /air lifted jet flame [28]: influence of temperature and species PDFs.	152
4.4.33	I_T profiles for the H ₂ /air lifted jet flame [28].	153

4.4.34	σ_Y profiles for the H ₂ /air lifted jet flame [28].	154
5.1.1	Schematic representation of a combustion chamber for propulsion applications [114].	156
5.2.1	Computational domain used to simulate the SiA semi-technical scale burner (a) and detail of the air swirling nozzle (b).	158
5.2.2	Three-dimensional representation of streamline in the SiA semi-technical scale combustor (C2H4-3-1.4-1 testcase).	160
5.2.3	Axial slices of temperature, axial velocity and O ₂ in the SiA semi-technical scale burner (C2H4-3-1.4-1 testcase).	161
5.2.4	Distributions for a 45-degrees cross section of the SiA semi-technical scale combustor (C2H4-3-1.4-1 testcase).	163
5.2.5	Soot volume fraction and soot particle density number on a 45-degrees cross section of the SiA semi-technical scale combustor (C2H4-3-1.4-1 testcase).	164
5.2.6	Comparison between laminar chemistry and the assumed-PDF calculations for the SiA semi-technical scale burner (C2H4-3-1.4-1 testcase): thermo- and fluid-dynamic variables.	165
5.2.7	Comparison between the laminar chemistry and the assumed-PDF calculations for the SiA semi-technical scale burner (C2H4-3-1.4-1 testcase): soot volume fraction and soot particle number distributions.	166
5.2.8	Comparison between simulations performed at 3 and 9 bar (C2H4-3-1.4-1 and C2H4-9-1.2-0.9 testcase): thermo- and fluid-dynamic quantities.	167
5.2.9	Comparison between simulations performed at 3 and 9 bars (C2H4-3-1.4-1 and C2H4-9-1.2-0.9 testcase): temperature and species fluctuations.	168
5.2.10	Comparison between simulations performed at 3 and 9 bars (C2H4-3-1.4-1 and C2H4-9-1.2-0.9 testcase): soot volume fraction.	169
5.2.11	Comparison between simulations performed with and without oxidation air (C2H4-3-1.4-1 and C2H4-3-1.4-0 testcases).	170
5.2.12	Temperature fluctuation distributions with and without oxidation air (C2H4-3-1.4-1 and C2H4-3-1.4-0 testcases).	171
5.2.13	Comparison of axial temperature profiles for the C2H4-3-1.4-1 testcase.	172
5.2.14	Comparison between numerical and experimental soot distributions in the SiA semi-technical scale combustor: 3 bar testcases.	173
5.2.15	Comparison between numerical and experimental soot distributions in SiA semi-technical scale combustor: 5 and 9 bar testcases.	174
5.2.16	Comparison between predicted and measured peak soot volume fractions at different pressures.	174
B.2.1	Generic cell-face configuration.	186

C.2.1 Comparison between fitting methods for backward Arrhenius function of reaction $\text{O}_2 + \text{H}_2 \rightleftharpoons 2\text{OH}$ in [101].	193
--	-----

List of Tables

2.1	Mechanisms used to simulate the ignition of a H ₂ /air mixture.	41
2.2	Boundary conditions for Mitchell's flame shown in Fig. 2.5.1.	47
3.1	Constants used in the soot formation model. Units are mol, m, s, K.	81
3.2	Initial condition for the ignition of a sooting mixture.	82
3.3	Boundary conditions for the methane/air flame of Smooke et al.	85
3.4	Adopted parameters for a sensitivity analysis study of the soot model. Units are mol, m, s, K.	88
3.5	Boundary conditions for the sooting ethylene/air flame [131].	94
3.6	Fuel inlet conditions for the sooting ethylene/air flame [131].	95
3.7	Comparison between predicted and measured flame length of sooting ethylene/air flame [131].	95
4.1	Boundary conditions for the H3 flame (Section 4.4.1).	126
4.2	Boundary conditions for the lifted H ₂ /air flame (Section 4.4.2).	139
5.1	Experimental conditions for the SiA semi-technical scale burner.	157

List of Symbols

Roman symbols

A	pre-exponential factor in the Arrhenius function
A_s	specific soot surface area
C	generic species name
C_p	specific heat capacity at constant pressure
D	diffusion coefficient
d	molecular diameter
d^m	dipole momentum
E_a	activation energy in the Arrhenius function
F_c	convective flux
F_d	diffusive flux
f_v	soot volume fraction
\mathbf{g}	gravitation vector
G	Gibbs free energy
H	molar enthalpy
h	specific enthalpy
h_f	specific heat of formation
\mathbf{I}	identity matrix
I_T	temperature fluctuation intensity
k	turbulent kinetic energy
k_b	Boltzmann constant

K_c	equilibrium constant
$k_{f/b}$	forward/backward rate constant
Le	Lewis number
m	atomic mass
M_i	species molecular mass
\mathbf{n}	surface normal
n_s	soot particle density number
N_{av}	Avogadro number ($6.022 \times 10^{23} \frac{1}{m^{-3}}$)
p	pressure
Pr	Prandtl number
Pr_ψ	turbulent Prandtl number of variable ψ
q_R	soot radiation source term
R	stiffness ratio
RR	reaction rate
Re	Reynolds number
S	molar entropy
s	cell surface
Sc	Schmidt number
S_n	swirl number
\mathbf{S}_s	cell boundary source term
\mathbf{S}_v	volumetric source term
T	temperature
t_b	third-body collision efficiency
TH	generic third body
\mathbf{v}	diffusion velocity
v	cell volume

v_{th} thermophoretic velocity

Y species mass fraction

Z mixture fraction

Greek symbols

α temperature exponent in the Arrhenius function

α_r primary to secondary air splitting ratio

α_T temperature PDF amplification factor

α_Y species PDF amplification factor

β collision frequency

ϵ dissipation of the turbulent kinetic energy

ϵ^k Lennard-Jones potential

ψ generic scalar

Γ gamma function

γ PAH collision efficiency

η soot oxidation efficiency

Λ eigenvalue of the chemical source term

λ heat conductivity

μ dynamic viscosity

μ_t turbulent dynamic viscosity

ν kinematic viscosity

ν' stoichiometric coefficient

Ω collision integral

Π viscous stress tensor

ρ density

σ^c collision diameter

σ_ψ variance of ψ PDF

σ_Y	turbulent scalar energy
τ_t	characteristic turbulent timescale
ω_i	chemical source term
ϕ	fuel equivalence ratio

Superscripts

q^0	reference value for q at T^0
\hat{q}	sample space for variable q
q'	fluctuating part of variable q
\mathbf{q}^T	transpose of vector \mathbf{q}
<i>add</i>	PAH-gas growth term
<i>coal</i>	PAH coalescence term
<i>form</i>	PAH formation term
<i>pgwth</i>	PAH-PAH growth term
<i>pox</i>	PAH oxidation term
<i>agg</i>	soot agglomeration term
<i>sgwth</i>	soot growth term
<i>nucl</i>	soot nucleation term
<i>sox</i>	soot oxidation term
$q t$	variable q calculated at time t

Subscripts

b	backward
f	forward
N_r	number of reactions
N_s	number of species

Miscellaneous

$[C]$	species concentration
-------	-----------------------

Δ difference operator

$\langle q \rangle$ mean value of variable q

$\|\mathbf{q}\|$ norm of vector \mathbf{q}

\mathfrak{R} universal gas constant

Zusammenfassung

Die vorliegende Arbeit beschäftigt sich mit der numerischen Simulation von Rußbildungsvorgängen unter gasturbinen-ähnlichen Bedingungen. Ziel der Arbeit ist die Entwicklung eines zuverlässigen Computerprogramms, mit dem der Trend von Rußverteilungen unter verschiedenen Betriebsbedingungen vorhergesagt werden kann. Hierzu müssen für die einzelnen chemischen und physikalischen Vorgänge eigenständige Modelle entwickelt werden.

Die derzeitig verfügbare Rechenleistung ermöglicht die Anwendung von Verbrennungsmodellen, die auf detaillierter chemischer Kinetik („Finite-Rate Chemistry“) basieren. Mit deren Hilfe lassen sich laminare Verbrennungsprozesse zuverlässig beschreiben. Die charakteristischen chemischen Zeitskalen solcher Verbrennungsprozesse erstrecken sich gewöhnlich über mehrere Größenordnungen. Die daraus hervorgehenden Gleichungssysteme bezeichnet man als „numerisch steif“. Um dennoch eine effiziente und stabile Lösung zu gewährleisten, sind spezielle numerische Verfahren nötig, die in Kapitel 2 vorgestellt werden. Der implementierte numerische Algorithmus wird anhand nulldimensionaler als auch axialsymmetrischer Simulationen validiert.

Ein Großteil der genutzten physikalischen Modelle wird an laminaren Diffusionsflammen getestet und die Ergebnisse werden diskutiert. Ein Schwerpunkt liegt hierbei auf der Untersuchung der Interaktion zwischen Flammenstruktur und Strömungsfeld. Die folgende Sensitivitätsanalyse zeigt, dass der verwendete kinetische Mechanismus einen starken Einfluss auf die Flammenstruktur ausübt. Insgesamt konnte eine gute Übereinstimmung von Temperatur- und Speziesprofilen mit experimentellen Daten erzielt werden.

Die Modellierung von Rußbildungsvorgängen in Flammen ist heutzutage aufgrund der immer strikteren Schadstoffemissionsgrenzen ein aktuelles Thema. Da die Rußbildung sehr komplexen Reaktionpfaden folgt und zahlreiche Spezies daran beteiligt sind, ist eine direkte Erweiterung des Gasphasenmodells auf die Rußvorläufer ausgeschlossen. Um den Rechenaufwand zu mindern, wird in dieser Arbeit ein sektionaler Ansatz für die Rußvorläufer verwendet. Die entsprechenden Transportgleichungen und Quellterme sind in Kapitel 3 aufgeführt. Das Rußmodell wird mit laminaren Methan/Luft Diffusionsflammen validiert. Der Vergleich von Rußvolumenbruchprofilen mit den experimentellen Daten verdeutlicht den starken Einfluss der verwendeten Arrhenius-Parameter auf die Genauigkeit der Ergebnisse. Anhand einer laminaren, teilvorge-mischten Acetylen/Luft Diffusionsflamme wird der Einfluss von Vormischungseffekten auf die Rußbildung untersucht. Beobachtete Abweichungen beim Rußvolumenbruch lassen sich in dem Falle direkt auf ungenügende Übereinstimmungen bei Benzol und Acetylen in fetten Flammenbereichen zurückführen.

Da die heutigen technischen Verbrennungssysteme höchste Wirkungsgrade erzielen sollen, sind hoch turbulente Strömungen, mit ihrem guten Mischverhalten, unumgänglich. Das nicht-lineare Verhalten der chemischen Reaktionsraten bezüglich Temperatur- und Spezieskonzentrationen macht die Berücksichtigung turbulenter Fluktuationen bei der Berechnung der chemischen Quellterme unvermeidbar. In dieser Arbeit wird eine vorgegebene Wahrscheinlichkeitsdichtefunktion („Assumed PDF - Probability Density Function“) für die Modellierung der oben erwähnten Fluktuationen hergeleitet und validiert. Transportgleichungen für die Varianz der Temperatur und die Varianz der sogenannten „turbulenten skalaren Energie“ (Summe der Varianzen aller Spezies) in Verbindung mit vorgegebenen Gauß- und β -Verteilung ermöglichen die Berechnung der chemischen Quellterme in den Favre-gemittelten Spezies-Transportgleichungen.

Der Einfluss des PDF-Ansatzes auf den Verbrennungsablauf wird für anliegende und abgehobene Flammen untersucht. Die numerischen Simulationen zeigen, dass die Temperatur-PDF die Form der Flamme und die Position des Zündpunktes von abgehobenen Flammen stark beeinflusst. In allen berechneten Fällen ist die Anwendung des PDF-Ansatzes für die Elementarreaktionen entscheidend und es wurden erhebliche Unterschiede in den Radikalkonzentrationen beobachtet.

Zur Demonstration der Anwendbarkeit des entwickelten Computerprogramms auf Fluggasturbinen wird eine halb-technische Brennkammer simuliert. Aufgrund der verwendeten Drallrzeugergeometrie und der zusätzlichen eingedüsten Sekundärluft bildet sich ein komplexes Strömungsfeld aus. Die Sekundärluft, die in der Mitte der Brennkammer einströmt, beeinflusst stark die Bildung der primären Rezirkulationzone. So entsteht in den Rechnungen ohne zusätzliche Oxidationsluft eine deutliche kleinere Rezirkulationzone am Düsenaustritt. Die Verwendung des PDF-Ansatzes wirkt sich entscheidend auf die Position des Zündpunktes und das Verhalten des Strömungsfeldes aus. Eine Verschiebung des Zündpunktes geht einher mit der Veränderung des Mischungsverhältnisses der Gase und damit mit einer starken Beeinflussung der Rußbildungsrate.

In Hinblick auf die Druckabhängigkeit des Rußbildungsprozesses wird eine Sensitivitätsanalyse durchgeführt. Die Temperatur- und Rußvolumenbruchfelder werden stark vom Druckniveau beeinflusst. Bei höherem Druck verändert sich das Temperaturfeld kaum, während die Wandwärmelast mit steigendem Druck weiter zunimmt. Die Höchstwerte des Rußvolumenbruches steigen mit dem Druck an und erreichen beim untersuchten 9-bar Fall den sub-ppm Bereich. Der Vergleich mit experimentellen Daten zeigt, dass die vorhergesagten Rußverteilungen teilweise deutlich von denen der Messungen abweichen. Mängel in der Turbulenzmodellierung und ihre Auswirkungen auf die Speziestransportgleichungen könnten diese Abweichungen erklären. Trotz der beschriebenen Unterschiede wird die Druckabhängigkeit des Rußvolumenbruches durch die numerischen Simulationen jedoch recht gut wiedergegeben.

Abstract

This work deals with the simulation of soot formation phenomena under gasturbine-like conditions. Main goal is the development of a reliable CFD simulation tool able to predict trends of soot formation under different operating conditions. In order to accomplish this task, the modeling of the significant physical phenomena involved in the process is needed.

The increasing computer power allows the use of detailed chemistry combustion models, which are able to give a reasonable description of chemical reactions taking place in reacting media. The characteristic timescales stemming from the changes in species concentrations range over several orders in magnitude. This disparity, known as *mathematical stiffness*, needs special methods in order to obtain an efficient and fast numerical solver. Such a procedure is presented in Chapter 2 together with validations for zero-dimensional and two-dimensional configurations.

The model benchmarking is done for axial-symmetric diffusion flames and an extended discussion of its physical features will be given. Of special interest is the interaction between the flame structure and the flowfield. Usually there is a strong sensitivity of the flame with respect to gas-phase reaction modeling which will be assessed by comparing simulations employing different kinetic mechanisms. An second source of uncertainties results from the chosen boundary conditions which are usually not know from experiments. Thus, the influence of outflow boundary conditions and preheating effects on the flame shape is investigated. The studied flames show a fairly good agreement with experimental temperature and species profiles, even if the uncertainties described above do not allow to draw unique conclusions concerning some of the observed discrepancies.

Because of the increasingly more stringent emission rules, soot formation in combustion is a topic of high priority. Since soot particles are the result of thousands of reactions involving hundreds of species, a direct extension of the finite-rate chemistry model is unfeasible. In order to retain the main features of the soot formation process and, at the same time, reduce the computational effort, a sectional approach for soot precursors and related reactions is chosen in this work (Chapter 3). The model validation is performed with a laminar methane/air diffusion flame, where a strong influence of Arrhenius parameters on the model accuracy has been observed. Moreover, an investigation of premixing effects on the soot formation will be given. It will be shown that the predictions of the soot volume fraction are directly related to the kinetic mechanism used and the degree of premixing. Observed discrepancies between experimental and numerical soot profiles are caused by a poor description of soot-related species (i.e. benzene and acetylene).

Because of the increasing demand of compact and efficient aeroengines, a high degree of turbulence is needed. This requires an appropriate modeling of the highly non-linear chemical source term with respect to temperature and species fluctuations. In this work an assumed Probability Density Function (hereafter PDF) approach for the description these fluctuations is presented and validated. Transport equations for the temperature variance and the so called “turbulent scalar energy” (sum of species variances) in conjunction with Gauss and β -PDF functions allow a closure of the chemical source term in the Favre-averaged species transport equations.

The influence of the assumed-PDF method on the combustion process will be investigated both for attached and lifted flames. These simulations will show that the temperature PDF plays an important role in the determination of the flame structure and ignition delay in lifted flame configurations. Moreover, the contribution of the assumed-PDF approach with respect to the prediction of radical species will be assessed.

Finally, the simulation of a semi-technical scale burner under gasturbine-like conditions will demonstrate the validity of the developed tools. Because of a swirler nozzle and secondary air inflows, a complex three dimensional flow develops. Momentum and location of the added oxidation air affect the extension and the shape of the primary recirculation zone. The use of the assumed-PDF approach was found to be critical for this testcase, since the ignition point, premixing degree of the burning medium and therefore soot formation are strongly affected.

A sensitivity analysis with respect to the influence of the operating pressure will be given. Temperature and soot volume fraction distributions show a different behavior at increasing pressures. The temperature remains nearly unchanged although a higher wall heat load is assessed. On the other hand, the soot formation is enhanced with increasing pressure and soot volume fractions reach sub ppm levels for the 9-bar testcase. The comparison with experimental data shows some contradicting results. If the predicted soot volume fraction distributions are compared with the experimental data, large differences are observed. On the other hand, numerical simulations are able to reproduce the experimentally observed pressure dependence of the peak soot volume fraction quite well.

1 Introduction

1.1 Motivations

Nowadays, combustion and its applications are fundamental in everyday's life. Propulsion, electrical power generation and heating systems are only few examples where bond energy stored in a fuel is released by chemical reactions. In spite of the wide range of applications where it takes place, a general definition of combustion can be formulated as follows: *“given two substances, called fuel and oxidant, combustion is a sequence of complex reactions between them associated with the release of thermal and (eventually) luminous energy”*. Both oxidant and fuel may be in a solid, liquid or gaseous state and reactions may take place among different ones. In most cases air represents the oxidant¹ and gaseous-gaseous reactions are the most important ones, at least in the applications considered in this work.

As in many other circumstances, practical applications of combustion took place long well before theoretical and experimental investigations started. Only in the last decades systematic studies of fundamental phenomena involved in combustion began to appear in the literature. At present days, more stringent environmental regulations impose the adoption of new combustion concepts in order to reduce pollutant formation and noise generation. The increasing oil demand requires a more economic and more efficient brand-new generation of combustors. Since these targets are not achievable with a simple use of engineering rules-of-thumb on which past systems relied, a synergy between experimental and numerical works is needed. That is the reason why combustion research now represents an unique tool in designing and improving combustion systems.

Experimental investigations of flame and combustion devices range from simple naked-eye observations to simultaneous, three-dimensional, laser-based quantitative measurements of local velocity, temperature and mixture composition. Such data are important to analyze flame phenomena and improve the combustion efficiency. At the same time, experiments can be used as benchmark for numerical simulations. One of most important drawbacks of most experiments is the limited amount of data which can be collected with a single measurement technique. As an example, temperature, main species concentrations and velocity measurements require at least two different measurement systems to be performed. Moreover, they have to run in parallel, in case that simultaneous data are needed. To complete the picture it should be added

¹In some non-conventional applications (i.d. space propulsion) more exotic components (i.d. HNO₃) may be employed.

that the lack of suitable experimental methods makes the investigation of many fundamental phenomena (i.e. trace-species chemistry) in complex geometries impossible.

For these reasons the numerical simulation of reacting systems is playing an increasing role in understanding combustion. In comparison with experimental methods, more information can be provided simultaneously. Flame structure and its interaction with the flowfield can be investigated and sensitivity studies can be performed at limited additional cost. However, the degree of complexity of a numerical simulation is often limited by the available computer power.

Of course, the benefits of combustion simulations are counterbalanced by difficulties embedded in the formulation of reliable models. An exact description of turbulence, combustion, pollutants formation and radiation is still far from being reached. Models with different degrees of complexity can be formulated and validated against simple testcases. The application of such models to real combustors is somewhat questionable since discarded phenomena and interactions may come into play. Thus, a correct evaluation of model limits and drawbacks is mandatory and represents one of the main tasks in combustion simulations.

1.2 Goals of this work

The present work is concerned with the development of a computer code able to give reliable predictions of soot formation rate in combustion chambers under gasturbine-like conditions. Despite the fact that a complete treatment of all important physical and chemical phenomena is impossible at present, the following aspects have to be considered:

- high-temperature gas chemistry which models chemical reactions which take place in the combustion process;
- soot² formation phenomena;
- turbulence-chemistry interaction which can not be neglected, since flows under consideration are usually fully turbulent.

The points mentioned above will be introduced and discussed in the next chapters. The theoretical basis and practical implementations will be described.

All physical models presented in Chapters 2-4 have been developed and validated within the scope of this Thesis. The in-house DLR THETA code has been employed as basis for the development. It should be noted that no detailed chemistry nor soot formation models was available in the starting version of the code. Similarly, turbulence-chemistry interaction (see Chapter 4) was taken in that version with a simple turbulent flamelet approach into account.

Each subject presents both modeling and numerical issues, which have to be considered in order to get a robust and accurate tool. As an example, the numerical stiffness associated with the chemical time scales is still an active field of research [37, 36]. The strong coupling between the species equations is another important issue, since it may destroy the good convergence properties of many iterative linear solvers. Chapter 2 will discuss these topics in detail.

²The definition of soot will be given in Chapter 3.

Soot formation represents one of the most active fields in fundamental [132] and applied chemistry [46]. Its complex nature does not allow a straightforward implementation by finite-rate chemistry models. Thus, some assumptions have to be made in order to make the problem tractable especially for complex, three-dimensional simulations. On one side the computational effort has to be reduced, on the other side the model should be kept as general as possible. A compromise is presented in Chapter 3.

Because of efficiency reasons, the energy density³ of gas turbine combustion chambers has to be as high as possible. This requirement can be fulfilled only if the flow is fully turbulent, since transport and mixing of reactants are faster. Simulations which would catch all details of a three-dimensional, unsteady turbulent flow are unfeasible, at least for real size combustors. Thus, FANS⁴ governing equations are considered since they provide the needed degree of accuracy. Issues and algorithms which are related to the averaging will be discussed in Chapter 4.

Simulations of a semi-technical scale burner will be presented in Chapter 5. A joint use of all models developed will be employed to investigate the soot formation in gasturbine-like conditions. Additionally, a sensitivity study with respect to several simulation parameters will be performed in order to assess the validity of the tools developed.

³The term “energy density” refers to the amount of energy released in the combustion chamber per unit of time, chamber volume and pressure.

⁴Favre-Averaged Navier-Stokes equations will be introduced in Chapter 4.

2 Governing equations and numerical scheme

2.1 Transport equations in the finite-volume formulation

The equations describing chemically reacting flows are directly derived from the mass conservation (for density and species mass fractions), momentum conservation, and energy conservation under the assumption that the fluid behaves like a perfect gas. These principles can be formulated for fluid particles moving through the domain (Lagrangian formulation) or for a continuum occupying a volume v having a boundary surface s (Eulerian formulation). If the Eulerian formulation is considered, a generic transport equation for each of the above physical quantities can be cast into the following expression

$$\frac{\partial}{\partial t} \int_v \rho \psi dv + \int_s \rho \psi \mathbf{V} \cdot \mathbf{n} ds = \int_v \mathbf{S}_v dV + \int_s \mathbf{S}_s \cdot \mathbf{n} ds. \quad (2.1.1)$$

The left hand side of Eq. (2.1.1) represents the change in time and spatial transport of ψ whereas the right hand side consists of source terms which act on the volume (S_v) and boundaries (S_s). In case a mixture of N_s species is considered, the solution vector has the following components

$$\Phi = \{\psi_i\} = \left\{ \rho, \mathbf{V}, h, Y_1, \dots, Y_{N_s-1} \right\}^T \quad (2.1.2)$$

Thus, $N_s + 4$ transport equations have to be solved.

Mass conservation law

The overall mass conservation is ensured by solving the continuity equation

$$\frac{\partial}{\partial t} \int_v \rho dv + \int_s \rho \mathbf{V} \cdot \mathbf{n} ds = 0 \quad (2.1.3)$$

where no source term appears. Thus, the rate of change of mass in the volume is equal to the mass flux through the volume's surface.

Momentum conservation equation

In the momentum equation contributions to the right hand side of Eq. (2.1.1) result from pressure, viscous, and gravitational forces. The corresponding transport equation is given by

$$\frac{\partial}{\partial t} \int_v \rho \mathbf{V} dv + \int_s \rho \mathbf{V} \mathbf{V} \cdot \mathbf{n} ds = \int_v \rho \mathbf{g} dv + \int_s \mathbf{\Pi} \cdot \mathbf{n} ds. \quad (2.1.4)$$

Assuming a Newtonian fluid (viscous forces are directly proportional to shear stresses) the second-order tensor

$$\mathbf{\Pi} = -p\mathbf{I} + \mu \left[\nabla \mathbf{V} + (\nabla \mathbf{V})^T + \frac{2}{3} \mathbf{I} \nabla \cdot \mathbf{V} \right] \quad (2.1.5)$$

represents the actions of pressure and surface forces in normal and tangential directions [7].

Energy conservation equation

The energy equation can be derived directly from the second principle of thermodynamics. However there is a certain degree of freedom in choosing the appropriate thermodynamic variable. Since only low-Mach number flows will be calculated in this work (thermodynamic pressure is nearly constant¹) the static enthalpy h

$$h(T, Y_i) = \sum_{i=1}^{N_s} Y_i \left(\Delta h_{f_i}^0 + \int_{T^0}^T C_p(T') dT' \right) \quad (2.1.6)$$

is chosen. Since its definition includes the heat of formation Δh_f^0 , no source term due to chemical reactions appears in the corresponding transport equation

$$\frac{\partial}{\partial t} \int_v \rho h dv + \int_s \rho h \mathbf{V} \cdot \mathbf{n} ds = \int_v \rho \mathbf{g} \cdot \mathbf{V} dv - \int_s \mathbf{S}_S^h \cdot \mathbf{n} ds \quad (2.1.7)$$

where \mathbf{S}_S^h represents heat fluxes through the volume's surface (Fourier's law). The only radiation losses included in Eq. (2.1.7) are related to the soot particles (Chapter 3) and are described later.

Species transport equations

Balance equations for each species Y_i are given by

$$\frac{\partial}{\partial t} \int_v \rho Y_i dv + \int_s \rho Y_i \mathbf{V}_i \cdot \mathbf{n} ds = \int_v \omega_i dv \quad (2.1.8)$$

where the convective velocity \mathbf{V}_i

$$\mathbf{V}_i = \mathbf{V} + \mathbf{v}_i \quad (2.1.9)$$

¹The low-Mach number hypothesis implies also that the work of dissipation forces in Eq. (2.1.7) can be neglected.

includes both flow (\mathbf{V}) and diffusion (\mathbf{v}_i) velocities. The latter represents the velocity of the species i around particle mass center [110] and is due to species diffusion properties. Several formulations of \mathbf{v}_i can be found in literature which offer different degrees of accuracy. In this work a gradient-like form based on the *Fick's law* is used:

$$\mathbf{v}_i = -\frac{D_i}{\rho}\nabla Y_i. \quad (2.1.10)$$

neglecting some other types of diffusion effects (i.d. Dufour, Soret). Since this work is focused on the computation of turbulent reacting flows, this approximation should have no influence on the numerical results. Nevertheless, the relative importance of the neglected effects has to be kept in mind if laminar testcases are treated, where the differential diffusion of light species (e.g. hydrogen) becomes important.

Eqs. (2.1.3), (2.1.4), (2.1.7) and (2.1.8) form a stiff, non-linear set of $N_s + 4$ strongly coupled partial differential equations with $N_s + 6$ unknowns. Additional relations are

- the gas law for a mixture of perfect gases

$$p = \rho \mathcal{R}T \sum_{i=1}^{N_s} \frac{Y_i}{M_i}, \quad (2.1.11)$$

- the enthalpy definition (2.1.6),
- the heat flux term \mathbf{S}_S^h

$$\mathbf{S}_S^h = -\lambda \nabla T + \rho \sum_{i=1}^{N_s} h_i Y_i \mathbf{v}_i, \quad (2.1.12)$$

- diffusion coefficients² μ , λ , D_i ,
- and in particular by the chemical source term ω_i , which will be described in the following section.

2.2 Chemical source term

In order to give a mathematical formulation of the chemical source term appearing in Eq. (2.1.8) a generic, reversible chemical reaction is introduced by



²Even if the term “diffusion coefficient” should only refer to D_i , here it has been extended to all coefficients related to molecular transport phenomena (i.e. viscosity, thermal conductivity).

The forward (RR_f) and the backward (RR_b) reaction rates are expressed according to the “Law of Mass Action” [198]

$$RR_f = k_f \prod_{j=1}^{N_s} [C_j]^{\nu'_j}, \quad (2.2.2)$$

$$RR_b = k_b \prod_{j=1}^{N_s} [C_j]^{\nu''_j}, \quad (2.2.3)$$

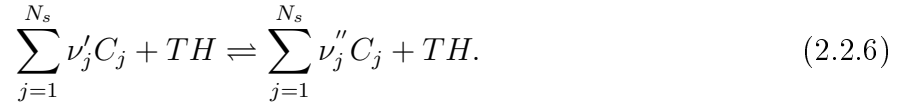
by a function of species concentrations [198]. The overall reaction rate is calculated as

$$\Delta RR = RR_f - RR_b. \quad (2.2.4)$$

The rate coefficients k_f and k_b (Eqs. (2.2.2) and (2.2.3)) are calculated by the so-called “Arrhenius function”

$$k = AT^\alpha \exp\left(-\frac{E_a}{\Re T}\right) \quad (2.2.5)$$

which is strongly non linear for most reactions. In case of recombination/dissociation reactions often the interaction with so called “third bodies” is required. There are species which do not take part in the reaction [110] but add/remove vibrational energy from the compound, thus promoting the dissociation or the recombination process. These effects are introduced in Eq. (2.2.1) by a virtual reactant which appears on both sides of the reaction equation



In most cases all species present in the mixture may act as a third body and its concentration is given by a linear combination of the physical species

$$[TH] = \sum_{j=1}^{N_s} t_{b_j} [C_j] \quad (2.2.7)$$

where $t_{b_j} \geq 0$ is the third body efficiency of the j -th species.

The forward and backward reaction rates k_f and k_b are related by the thermodynamic equilibrium constant

$$K_c = \frac{k_f}{k_b} \quad (2.2.8)$$

which can be calculated from the Gibbs free energy [110]

$$\Delta G^0 = \sum_{j=1}^{N_s} (\nu''_j - \nu'_j) (H_j^0 - TS_j^0). \quad (2.2.9)$$

Thus

$$K_c = \left(\frac{p}{\Re T}\right)^{\Delta\nu} \exp\left(-\frac{\Delta G^0}{\Re T}\right) \quad (2.2.10)$$

where $\Delta\nu$ is the difference between forward and backward reaction orders

$$\Delta\nu = \sum_{j=1}^{N_s} \nu_j'' - \sum_{j=1}^{N_s} \nu_j'$$

From Eqs. (2.2.8), (2.2.9) and (2.2.10) it follows that only k_f has to be calculated from Arrhenius parameters, whereas k_b can be derived from the equilibrium condition.

In a reacting mixture of N_s species a *kinetic mechanism* is a set of N_r elementary reactions³ defined by Eq. (2.2.1) consisting out of reactants, products, and Arrhenius coefficients. Once a single mechanism has been selected, the source term in Eq. (2.1.8) is calculated as the sum over all reactions

$$\omega_i = M_i \sum_{r=1}^{N_r} (\nu_{i_r}'' - \nu_{i_r}') k_{f_r} \left(\prod_{j=1}^{N_s} [A_j]^{\nu_{j_r}'} - \frac{1}{K_c} \prod_{j=1}^{N_s} [A_j]^{\nu_{j_r}''} \right). \quad (2.2.11)$$

In order to avoid the calculation of equilibrium constants K_c during the simulation and to treat both forward and backward reactions in the same way, an alternative approach has been developed and is described in Appendix C. This algorithm casts the backward reaction rate k_b into the Arrhenius form (2.2.5) for a large temperature interval. In this case we can consider any kinetic mechanism as a set of $2N_r$ irreversible reactions

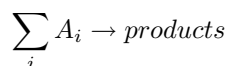
$$\omega_i = M_i \sum_{r=1}^{2N_r} \omega_{i_r} = M_i \sum_{r=1}^{2N_r} (\nu_{i_r}'' - \nu_{i_r}') k_r \prod_{j=1}^{N_s} [A_j]^{\nu_{j_r}'}. \quad (2.2.12)$$

It should be pointed out that there is no physically unique reaction mechanism which is able to describe a combustion process (i.e. ignition delay, heat release) under all conditions.⁴ Therefore, part of this work is also concerned with the investigation of several kinetic schemes and their influence on results.

2.2.1 Source term linearization

As will be pointed out in subsection 2.2.2, the characteristic chemical timescales may differ by several orders of magnitude. Thus, without any special mathematical treatment stability requirements would allow to solve the species equations (2.1.8) only by adopting extremely small timesteps [83]. This would make most calculations unfeasible because of the enormous computational time required to reach a steady state solution. In order to overcome this problem, an implicit treatment of the source term in the discretized transport Eq. (2.3.1) is applied. Equation (2.2.12) outlines clearly that source term ω_i may be highly non-linear with respect to the

³Global reactions like



are included in a similar manner but their treatment is not repeated here for sake of brevity.

⁴In fact, a large part of combustion research community is devoted to the creation of reaction mechanisms which should be as comprehensive as possible.

species mass fractions and temperature. Since a linear solver is employed, (see Appendix B.5), all transport equations have to be linearized with respect to the solution variables. Concerning the subvector of thermo-chemical variables

$$\Psi = \begin{Bmatrix} h \\ \mathbf{Y} \end{Bmatrix} \quad (2.2.13)$$

this linearization yields

$$\omega_i(\Psi^{t+\Delta t}) = \omega_i(\Psi^t) + \left. \frac{\partial \omega_i}{\partial \Psi} \right|^t \Delta \Psi + \mathcal{O}(\|\Delta \Psi\|^2) \quad (2.2.14)$$

where $\left. \frac{\partial \omega_i}{\partial \Psi} \right|^t$ is the i -th line of the Jacobian matrix, calculated at time t . The linearized source term is then included in the transport equation (Eq. (2.1.8)).

The calculation of the Jacobian matrix in Eq. (2.2.14) may be performed both analytically or numerically, using a finite-difference approach. In this work the analytical approach is preferred since it yields a more robust algorithm and avoids round-off errors. The first column of the Jacobian comes from derivatives of the source term with respect to enthalpy. Due to the Arrhenius form of the reaction rates (2.2.5), ω_i explicitly depends on the temperature only. Thus, derivatives with respect to h are calculated using the chain rule

$$\left. \frac{\partial \omega_i}{\partial h} \right|_{\mathbf{Y}} = \left. \frac{\partial \omega_i}{\partial T} \right|_{\mathbf{Y}} \left. \frac{\partial T}{\partial h} \right|_{\mathbf{Y}} \quad (2.2.15)$$

where the first term can be calculated directly from (2.2.5)

$$\left. \frac{\partial \omega_i}{\partial T} \right|_{\mathbf{Y}} = \frac{M_i}{T} \sum_{r=1}^{2N_r} \omega_{i_r} \left(\alpha_r + \frac{E_{a_r}}{\mathfrak{R}T} - \sum_{j=1}^{N_s} \nu'_{j_r} \right) \quad (2.2.16)$$

whereas the second term

$$\left. \frac{\partial T}{\partial h} \right|_{\mathbf{Y}} = \frac{1}{C_p} \quad (2.2.17)$$

comes from Eq. (2.1.6). The species derivatives come from two contributions

$$\left. \frac{\partial \omega_i}{\partial Y_k} \right|_{h, Y_j, j \neq k} = \left. \frac{\partial \omega_i}{\partial T} \right|_{h, Y_j, j \neq k} \left. \frac{\partial T}{\partial Y_k} \right|_{h, Y_j, j \neq k} + \left. \frac{\partial \omega_i}{\partial Y_k} \right|_{T, h, Y_j, j \neq k}. \quad (2.2.18)$$

The second term of the right hand side of Eq. (2.2.18) can be derived from definition (2.1.6) using the constant enthalpy condition (valid in adiabatic, low Mach number flows), resulting in

$$\left. \frac{\partial h}{\partial Y_k} \right|_{h, Y_j, j \neq k} = 0 = h_k - h_{N_s} + C_p \left. \frac{\partial T}{\partial Y_k} \right|_{h, Y_j, j \neq k} \quad (2.2.19)$$

which yields

$$\left. \frac{\partial T}{\partial Y_k} \right|_{h, Y_{j,j \neq k}} = \frac{h_{N_s} - h_k}{C_p} \quad (2.2.20)$$

considering that only $N_s - 1$ species are independent and the last species mass fraction is obtained from the normalization condition

$$Y_{N_s} = 1 - \sum_{j=1}^{N_s-1} Y_j. \quad (2.2.21)$$

From the definition of concentration

$$[A_j] = \rho \frac{Y_j}{M_j} \quad (2.2.22)$$

and Eq. (2.2.7) it follows for the density derivatives

$$\left. \frac{\partial \rho}{\partial Y_k} \right|_{T, h, Y_{j,j \neq k}} = - \frac{\rho}{\sum_{\ell=1}^{N_s} \frac{Y_\ell}{M_\ell}} \left(\frac{1}{M_k} - \frac{1}{M_{N_s}} \right). \quad (2.2.23)$$

species and third body concentrations. Thus, the second term in Eq. (2.2.18) can be written as

$$\left. \frac{\partial \omega_i}{\partial Y_k} \right|_{h, T, Y_{j,j \neq k}} = M_i \sum_{r=1}^{2N_r} \omega_{i_r} \left[\left(\sum_{j=1}^{N_s} \nu'_{jr} \frac{1}{\rho} \frac{\partial \rho}{\partial Y_k} \right) + \frac{\nu'_k}{Y_k} - \frac{\nu'_{N_s}}{Y_{N_s}} + \frac{\rho}{[TH]} \left(\frac{t_{b_k}}{M_k} - \frac{t_{b_{N_s}}}{M_{N_s}} \right) \right]. \quad (2.2.24)$$

2.2.2 Stiffness and chemistry

A definition of *stiffness* is introduced here in order to justify the use of implicit methods in handling the chemical source term. As mentioned above, timescales associated with chemical reactions span several orders of magnitude, since in a complex reacting system both fast and slow dynamics exist. From the mathematical point of view, these timescales are related to the linearized source term and obtained from the eigenvalues of the Jacobian matrix $\frac{\partial \omega_i}{\partial \Psi}$

$$\tau_{c_i} = [|\operatorname{Re}(\Lambda_i)|]^{-1}. \quad (2.2.25)$$

A possible quantification of the stiffness is the so-called *stiffness ratio* [27]

$$R = \frac{\max_{i=1 \dots N_s} [|\operatorname{Re}(\Lambda_i)|]}{\min_{i=1 \dots N_s} [|\operatorname{Re}(\Lambda_i)|]} \quad (2.2.26)$$

provided that

$$\operatorname{Re}(\Lambda_i) < 0 \quad (2.2.27)$$

$\forall i = 1 \dots N_s$. That is, the stiffness is the ratio between the fastest and the slowest timescales. Another possible definition, due to Curtiss and Hirshfelder [82], is more pragmatic: “*stiff equations are equations where certain implicit methods, [...] , perform better, usually tremendously*

better, than explicit ones". That means that a faster and more efficient solution method can be formulated if an implicit treatment of stiff equations is employed. Even if they add some computational cost, implicit methods have to be preferred to explicit schemes since the latter can fail even if the timestep requirements are fulfilled [83].

2.2.3 Constant-pressure adiabatic reactor

In this section testcases concerning the source term (2.2.11) are presented in order to demonstrate some important features of the chemistry equations. The main underlying hypothesis are:

1. the velocity is zero everywhere;
2. neither spatial gradients of temperature nor of concentration are present;
3. the system is closed and isolated, no mass or energy exchanges are allowed;
4. the volume changes to keep the pressure constant.

Applying hypothesis (2) and (3) to the second law of the thermodynamics, a constant enthalpy condition is obtained. Thus, a system of $N_s - 1$ coupled Ordinary Differential Equations (ODEs) in the following form

$$\frac{dY_i}{dt} = \frac{\omega_i}{\rho} \quad (2.2.28)$$

is integrated.

Hydrogen-air ignition

The system studied is a stoichiometric, atmospheric, H_2 /air mixture with initial temperature $T_0 = 1000 K$. The chosen conditions are in the explosion region, where the high-temperature equilibrium condition can be reached in a finite time [110]. The kinetic scheme used to describe the reacting mixture contains 9 species and 21 reversible reactions [149] and has been validated against different configuration, ranging from flow-reactors to premixed flames.

In Fig. 2.2.1 the change of temperature and species mass fractions in time are shown. The temperature increases strongly and reactions bring the system to the equilibrium condition after an initial ignition delay. Because no unique definition of this parameter exists [110, 198], in this work it is defined as the time at which the H_2O concentration slope reaches a maximum [149]

$$\tau_{ign} = t \left(\frac{d[H_2O]}{dt} \Big|_{max} \right). \quad (2.2.29)$$

From this simulation a value of $\tau_{ign} \approx 200 \mu s$ is found, which is in good agreement with the value given in Ref. [149]. Regarding the species behavior, water vapor increases monotonically whereas radicals like H, O and OH reach significant values at high temperatures only. A further distinction between OH, on one side, and O and H on the other side can be made. The first has a monotone increase up to its equilibrium value whereas O and H concentrations first reach

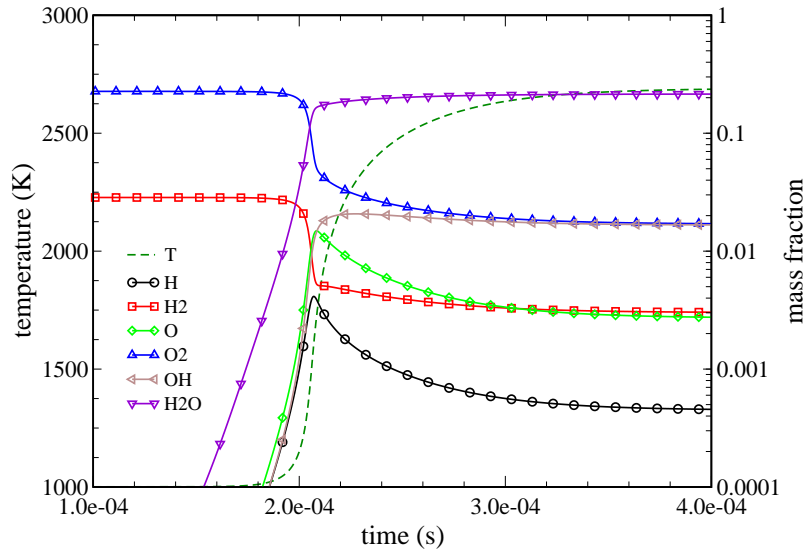


Figure 2.2.1: Ignition of a H_2/air mixture, $\phi = 1$, $p = 10^5 \text{Pa}$, $T_0 = 1000 \text{K}$.

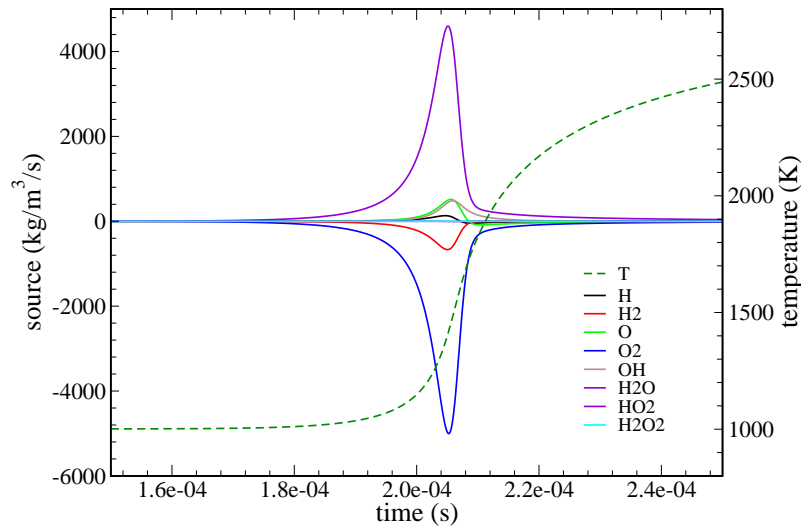


Figure 2.2.2: Source terms for ignition problem 2.2.1.

super-equilibrium levels and afterward drop due to recombination reactions. These differences are quite important for turbulent flames, where turbulent transport of highly reactive radicals may ignite pockets of fresh mixture [194]. In Fig. 2.2.2 species source terms are shown. Both O_2 and H_2O reach similar peaks with opposite signs whereas H and O present both positive and negative values. As expected, the reaction zone is limited to a small region of the simulated period and in multi-dimensional flow this means that the flame front⁵ occupies a region significantly smaller than the whole domain. This represents one of the most challenging aspects in combustion simulations: a good resolution of these zones should be achieved keeping the computational cost low.

As pointed out in subsection 2.2.2, a rough estimation of the system stiffness can be given by an eigenvalue evaluation. In Fig. 2.2.3 the non-zero real eigenvalues of the Jacobian (2.2.14) are plotted. A large difference between fast and slow scales is observed at the beginning. At later

⁵In a multi-dimensional problem the “flame front” can be defined as the region of the simulated domain where heat release and reactions take place.

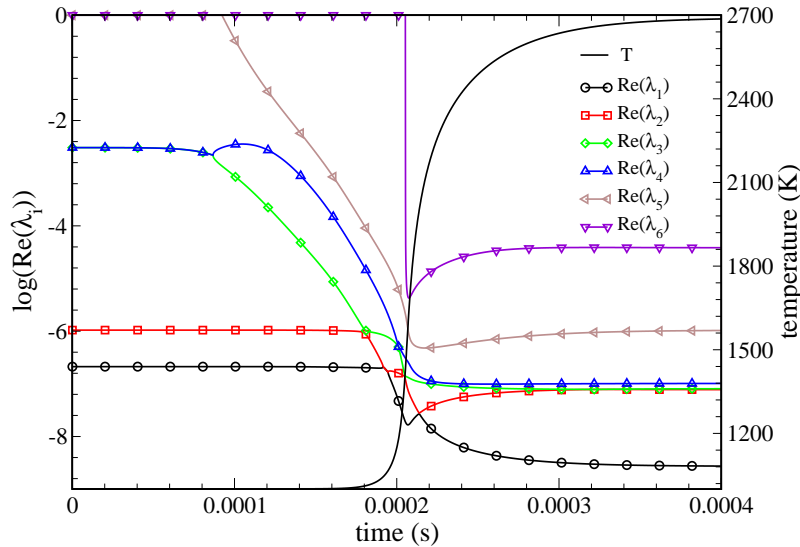


Figure 2.2.3: Eigenvalues of the Jacobian matrix for ignition problem 2.2.1.

times the spectrum of the Jacobian matrix is reduced but is still large enough to classify the system as stiff. Another important aspect are the signs of these eigenvalues: being all negative yields to the absolute stability condition if a first/second order A-stable integration scheme is used [83]. The imaginary part of the eigenvalues (not plotted here) are all zero and therefore no oscillatory behavior arises.

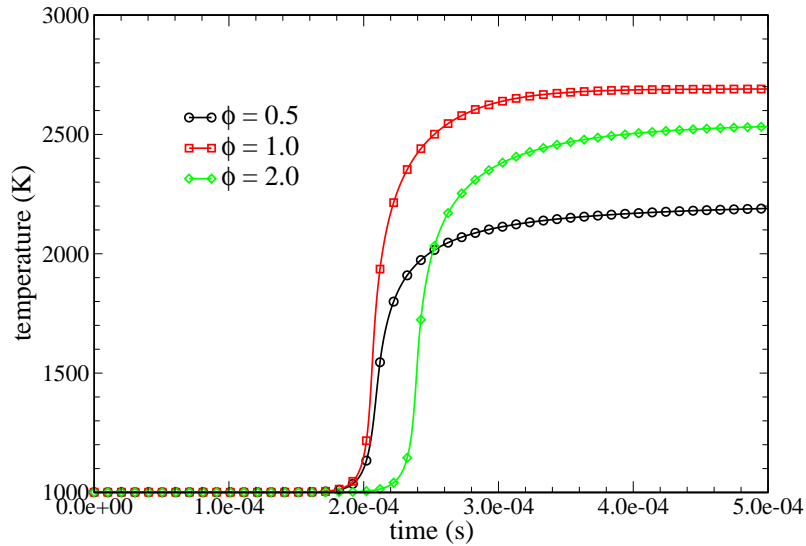
Influence of the simulation parameters on the ignition delay

In order to assess the correctness of the source term implementation several tests have been carried out. The first parameter being investigated is the fuel/air ratio normalized by its stoichiometric value, the so-called *fuel equivalence ratio*

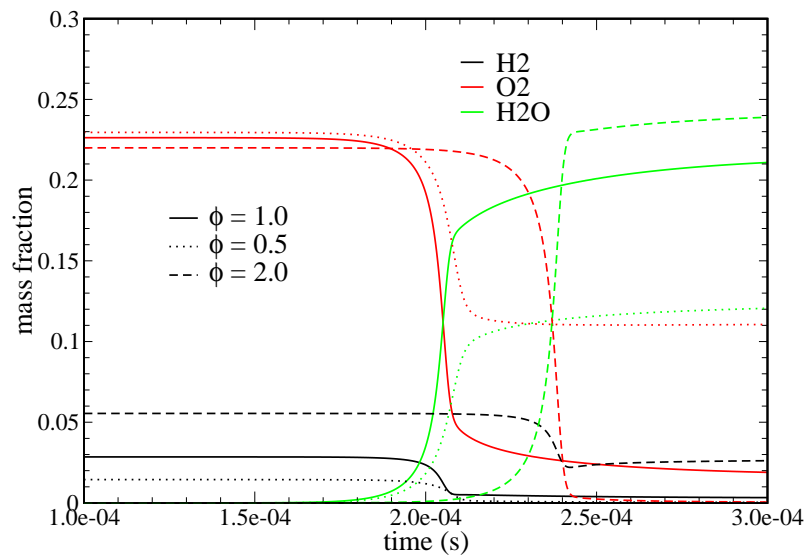
$$\phi = \frac{\left(\frac{f}{o}\right)}{\left(\frac{f}{o}\right)_{st}}. \quad (2.2.30)$$

The mixture is called *lean* if $\phi < 1$ and *rich* if $\phi > 1$. Results of simulations using different ϕ are plotted in Fig. 2.2.4. First, it can be noticed that the equilibrium temperature reached at the end of the simulation has a maximum for stoichiometric mixtures. As can be seen later, a similar behavior is observed in diffusion flames where the maximum temperature is located in a small sheet lying around the stoichiometric surface. The second aspect is the variation of the ignition delay with the equivalence ratio ϕ . A lean mixture does not show an appreciable change in the ignition delay, even if a slightly smaller overall reaction rate is predicted. For the rich mixture the ignition delay is increased by a factor of about 10% because the OH radical production is delayed, as shown in Fig. 2.2.4(c). Moreover, it can be observed that the ratio between H and O curves (i.e. slope and maximum) are unchanged in all cases but the rich one.

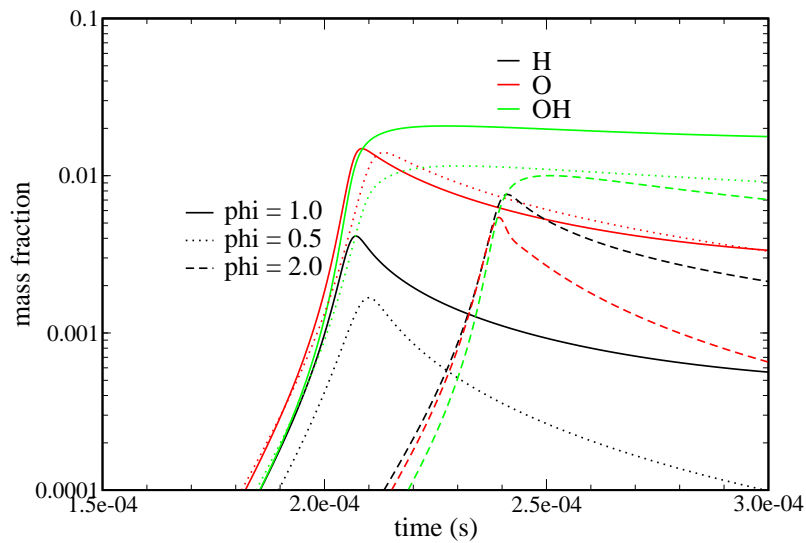
The second set of simulations is concerned with the influence of the pressure on the ignition delay. Because the mass law (2.2.2) holds, higher pressure yields to higher reactant concentrations and higher reaction rates. In Fig. 2.2.5 such an expectation is confirmed for pressures ranging from 0.1 to 1 bar. It is observed that the ignition delay is directly proportional to the



(a) temperature



(b) stable species



(c) radicals

Figure 2.2.4: Ignition of H₂/air mixtures at different equivalence ratios, $p = 10^5$ pa, $T_0 = 1000$ K.

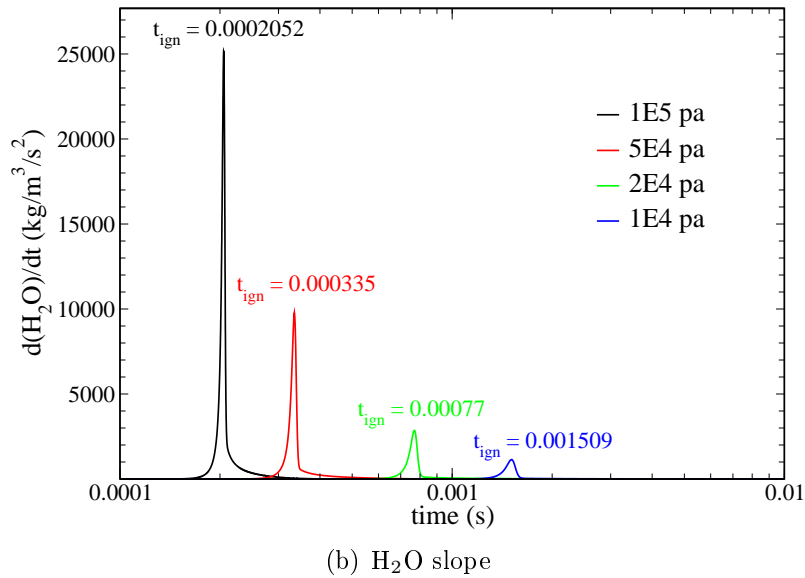
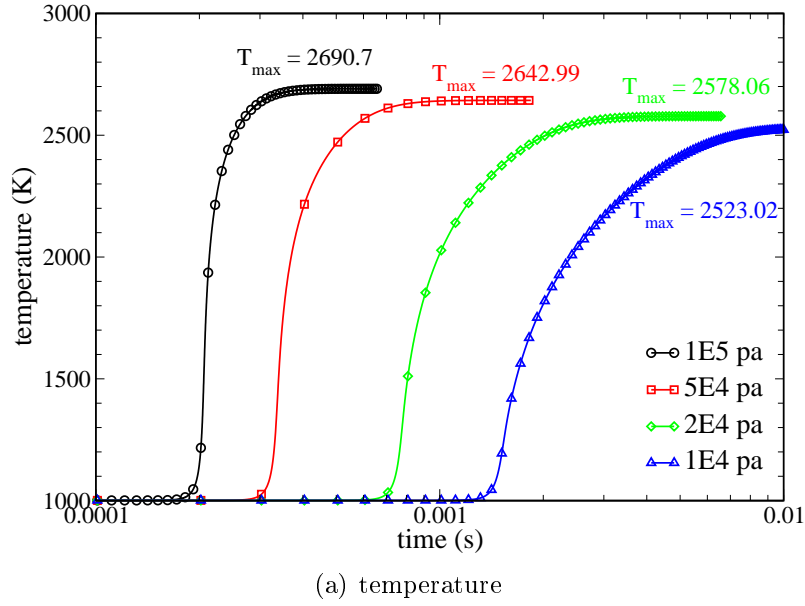


Figure 2.2.5: Ignition of H₂/air mixtures at different pressures, $\phi = 1$, $T_0 = 1000$ K.

pressure change varying by about one order of magnitude. On the other hand, the equilibrium temperature is only slightly influenced, indicating that the dominating reactions reach similar equilibria at different pressures. According to Eq. (2.2.10) this means that for such reactions the number of reactants and products is the same ($\Delta\nu = 0$) and there is no pressure dependence of K_c .

The Arrhenius parameter E_a gives an indication of the energy barrier that molecules have to overcome during the collision to allow the formation of the product [110]. In case the term (2.2.5) has a positive activation energy, the exponential factor is proportional to the number of molecules which have kinetic energies higher than E_a at temperature T and it goes to 1 at very high temperatures⁶. It becomes obvious that higher initial temperatures yield to more energetic collisions and thus faster reaction rates. In Fig. 2.2.6 results are shown for simulations which

⁶This results from the Boltzmann distribution of a perfect gas in thermal equilibrium [195].

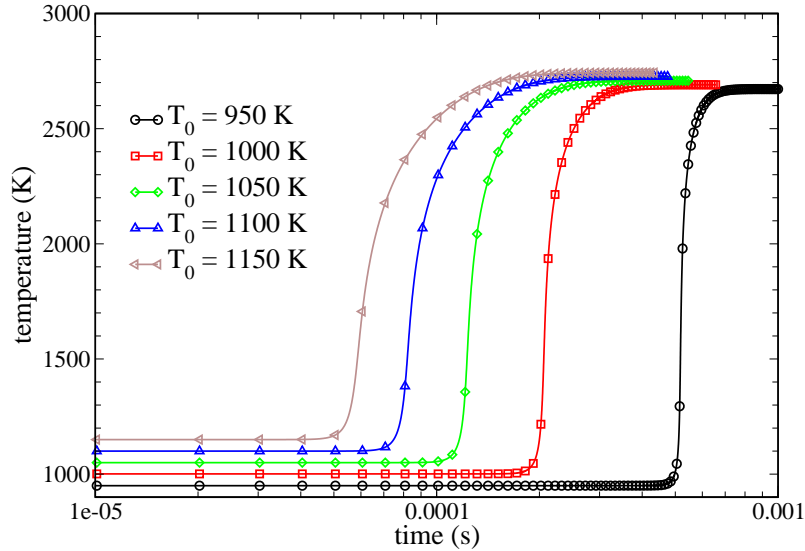


Figure 2.2.6: Ignition of H_2/air mixtures at different initial temperatures, $\phi=1$, $p = 1$ bar.

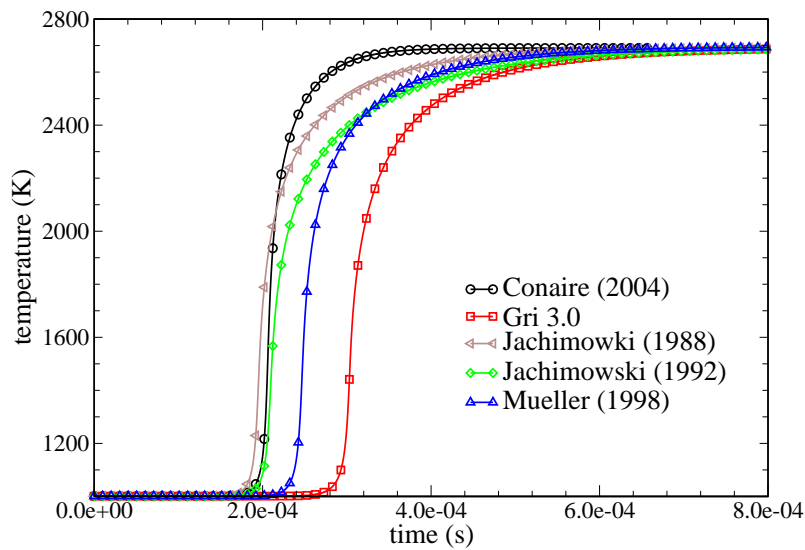
Table 2.1: Mechanisms used to simulate the ignition of a H_2/air mixture.

Mechanism	N_s	N_r	T_{max} (K)	τ_{ign} (μs)
Ó Connaire et al.	9	21	2691	205
GRI 3.0	9	28	2692	303
Jachimowski	9	19	2692	209
Müller et al.	9	21	2695	246

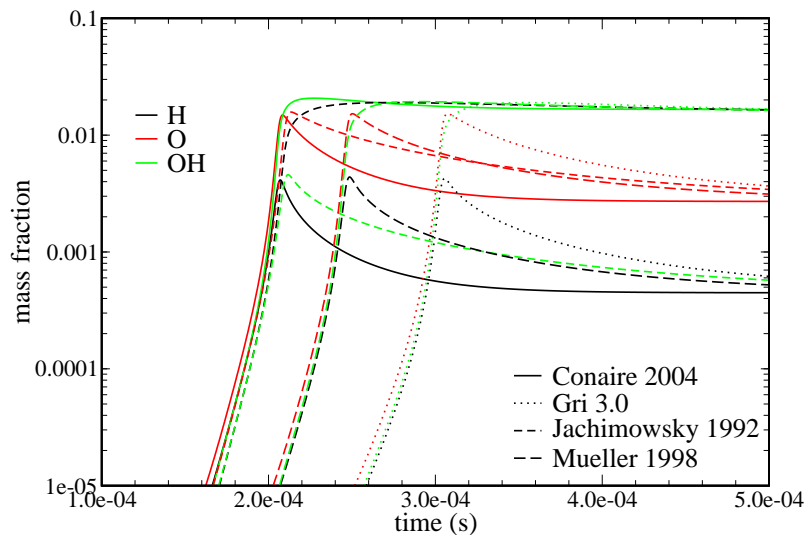
adopt different initial temperatures T_0 . The ignition delays and equilibrium temperatures are affected by T_0 as expected. However, the influence of T_0 is higher at the low temperatures due to the exponential behavior of Eq. (2.2.5). Moreover, near the ignition point the influence of single reactions (i.e. branching ones) is more pronounced. For the same reasons the temperature gradients are steeper for low ignition temperatures whereas a smoother increase is obtained at higher T_0 .

The last parameter investigated is the kinetic mechanism used to describe the combustion process. Several simulations have been carried out using the kinetic schemes summarized in Table 2.1. In Fig. 2.2.7 the resulting temperature plots are shown. The first mechanism has already been employed in the previous simulations and was proposed by Ó Connaire [149]. The second scheme is from Ref. [144] and in some extent it was also used to issue the kinetic mechanism in Ref. [149]. The GRI mechanism [178] was developed mainly for natural gas combustion, even if the subset involving H_2/air species has been extensively used to simulate hydrogen flames [178]. The Jachimowski mechanism [94, 95] was originally used in supersonic combustion and it may be interesting to compare it with other mechanisms validated against reactor experiments or low-Mach number flows. All mechanisms use the same set of species (H_2 , O_2 , OH , O , H , HO_2 , H_2O_2 and H_2O) but contain different reaction paths.

Examining the third column of Table 2.1, all tested mechanisms reach the same temperature at the end of the simulation. For the above-mentioned consideration and according to Eq. (2.2.10) it can be concluded that there is a general agreement between the different thermodynamic databases adopted by the different mechanisms. On the other hand (see fourth column), a large sensitivity of the ignition delay to the kinetic mechanisms is observed. In particular, the GRI3.0 mechanism predicts an ignition delay which is about 30% longer than that of ÓConnaire et al. The Jachimowski's mechanism predicts a similar τ_{ign} , but a slower heat release, which approaches the performance of the Mueller et al. scheme.



(a) temperature



(b) radicals

Figure 2.2.7: Ignition of H_2 /air mixtures using different kinetic mechanisms, $T_0 = 1000$ K, $\phi=1$, $p = 1$ bar.

2.3 Numerical methods

2.3.1 Low-Mach number formulation

As may be shown analytically [187], compressible flow solvers become numerically stiff as the zero-Mach limit is approached. That is because the ratio between the convective timescales (given by the velocity field) and acoustic wave timescales (given by the pressure field) decreases for Ma approaching zero. The convergence of the system may be compromised and different solution methods usually have to be used when dealing with high and low Mach number flows. Since steady-state problems at low Mach number are considered in this work, the continuity equation (Eq. (2.1.3)) is replaced by an equation for pressure and the equation set $(\mathbf{V}, p, h, \mathbf{Y})$ is solved in a sequential fashion until a converged solution is obtained. Details of the solution algorithm are given in Appendix B and are shortly summarized here:

1. momentum and pressure equations are solved iteratively until the mass conservation law is fulfilled;
2. additional model equations (i.e. turbulence, radiation, species) are solved in a sequential manner;
3. energy and species equations are solved in a coupled fashion in order to retain the strong coupling between them and increase robustness;
4. steps 1-3 are repeated until the steady-state condition is reached.

The domain is subdivided into small control volumes Δv , delimited by planar faces Δs and Eq. (2.1.1) is applied to each of them in the following form

$$\rho \frac{\Delta \psi}{\Delta t} \Delta v = \sum_{\Delta s} [F_{\psi}^c(\psi^t, \psi^{t+1}) + F_{\psi}^d(\psi^t, \psi^{t+1})] + \rho S_v(\psi^t, \psi^{t+1}) \Delta v. \quad (2.3.1)$$

The fluxes through the cell interfaces F_{ψ}^c and F_{ψ}^d consists of convective and diffusive parts. In general they are non-linear functions of solution vector ψ and therefore a linearization is needed. Moreover, fluxes and source terms can be calculated using variable ψ at different times. Methods using only known values from time t belong to the class of *explicit methods* whereas methods which use $\psi^{t+\Delta t}$ as well are called *implicit methods*. Because in this work only steady flowfields are investigated, implicit methods are preferred due to the larger timestep allowed.

2.4 Modeling of transport phenomena

2.4.1 Dimensionless parameters

Diffusive fluxes appearing in Eqs. (2.1.4), (2.1.7) and (2.1.8) are here modeled with a term proportional to the gradient of the transported variable [198, 110]. It has been demonstrated

that this approach is able to give a reasonable description of momentum, energy and species transport for low-speed, Newtonian flows.⁷

Based on the transport coefficients μ , λ and D_i , dimensionless parameters can be formed. They represent ratios between the characteristic times of different physical phenomena. In particular

- the Prandtl number represents the ratio between momentum and energy transport

$$Pr = \frac{C_p \mu}{\lambda}; \quad (2.4.1)$$

- the Lewis number is the ratio between energy and mass transport (here for the species pair i, j)

$$Le_{ij} = \frac{\lambda}{\rho C_p D_{ij}}; \quad (2.4.2)$$

- the Schmidt number is the ratio between momentum and mass transport

$$Sc_{ij} = \frac{\mu}{\rho D_{ij}}. \quad (2.4.3)$$

From Sc and Pr definitions follows

$$Le_{ij} = \frac{Sc_{ij}}{Pr}. \quad (2.4.4)$$

The calculation of transport coefficients (in particular D_{ij}) may be expensive and in convection-dominated problems (i.e. turbulent flows) their influence may be marginal. In such cases simplifications ($Le = 1$) may be used where D_{ij} coefficients are not independent any more. In subsection 2.5.4 the influence of such a hypothesis on laminar flame configurations will be discussed.

If the temperature dependence of the non-dimensional parameters is neglected,

$$Pr = .7 \quad (2.4.5)$$

$$Le_{ij} = 1 \quad (2.4.6)$$

$$Sc_{ij} = Le_{ij} Pr \quad (2.4.7)$$

can be assumed. Thus, species and energy transport have proportional timescales, regardless of the species considered or the temperature range.

⁷It should be pointed out that in multi-component mixtures the transport of the single species by collision has to take into account the interaction among all other species [110]. Even if more exact, such an approach would yield very high computational costs, unfeasible in complex simulations. Therefore, it will not be considered here.

From the enthalpy definition (2.1.6) temperature gradients can be calculated as a sum of enthalpy and species gradients

$$\nabla T = \frac{1}{C_p} \left(\nabla h - \sum_{i=1}^{N_s} h_i \nabla Y_i \right) \quad (2.4.8)$$

and the heat flux (2.1.12) becomes

$$\mathbf{q} = -\frac{\lambda}{C_p} \nabla h + \sum_{i=1}^{N_s} \left(\frac{\lambda}{C_p} - \rho D_i \right) h_i \nabla Y_i. \quad (2.4.9)$$

In case that Eq. (2.4.6) holds, the second term in Eq. (2.4.9) is identically zero, leaving an homogeneous, second-order term in the enthalpy equation (2.1.7).

Similarly, if Fick's law (2.1.10) holds, all diffusive fluxes (Eqs. (2.1.4), (2.1.7) and (2.1.8)) have the following form

$$F_\psi^d = \int_s D_\psi \nabla \psi \cdot \mathbf{n} ds, \quad (2.4.10)$$

where D_ψ is a generic diffusion coefficient (different for each transport equation). The calculation of transport coefficients can be further simplified by relations (2.4.5) and (2.4.7): in this case only the viscosity is calculated as a function of the temperature (see Appendix A), whereas λ and D_i are derived from simple algebraic expressions. The temperature dependence of D_ψ has to be considered in laminar, reacting flows. On the other hand, in this work the pressure dependence is not very critical because of the narrow Mach number range considered. Details about the calculation of the transport properties are given in Appendix A.

Even if the hypotheses (2.4.5), (2.4.6) and (2.4.7) may save computational time, it should be noted that they may cause misleading results. Since light, small species (like atomic hydrogen) diffuse faster than bigger molecules, simplifications like (2.4.6) are wrong in cases where such species play an important role. Moreover, some additional effects (i.e. Soret, Dufour) may contribute to mass and energy transport. In particular they can play an important role in ignition and stabilization of non-premixed configurations [34]. Even in turbulent regimes flow laminarization often occurs in regions where the flame stabilizes, thus increasing the importance of molecular transport models.

Concerning the numerical behavior of the discretized system (2.3.1), diffusive fluxes like (2.4.10) smooth the ψ gradients and yield a more stable numerical scheme [153]. Moreover, such terms increase the diagonal dominance of the algebraic system and therefore the stability of any iterative linear solver [168]. On the other hand, the species gradients in (2.4.9) introduce a non-diagonal term which does not depend directly from enthalpy. As explained in Appendix B, solvers for linear system employed in this work use a diagonal preconditioning and therefore such a term may decrease the convergence rate.

2.5 Laminar diffusion flames

Laminar diffusion flame represent the most simple yet real configuration where all terms from Eq. (2.1.1) are required for the mathematical description. In this case both chemistry and transport phenomena are important and the influence of the different modeling assumptions has to be assessed. As the diffusion flame regime is present in technical applications, correct predictions of simple laminar flames are a prerequisite for simulating more complex systems.

Because of their simplicity, laminar diffusion flames have been studied extensively, and both experimental and numerical data are available. Unfortunately, in most experiments only simple fuels are adopted, namely hydrogen and methane. Concerning the geometry, mainly axisymmetric configurations [140, 61] or slot burners [148, 6] are used. From the view of combustion modeling, first approaches were based on flame-sheet models [139], which did not solve detailed transport equation sets for all species but needed a careful calibration of the model constants. Moreover, the pressure-velocity coupling was still an active field of research and a unique set of equations for this problem was not established yet (see Refs. [180, 182] for examples of the stream-vorticity approach and Ref. [205] for a possible primitive-variable approach). Later, solutions of the fully-coupled species and energy transport equations became feasible with asymptotic analyses [172, 173] and detailed kinetic schemes [205, 148]. Massive code parallelization finally allowed to break the barrier of the single-computer power [55]. Some studies were also devoted for understanding the influence of different parameters (Lewis number [34], fuel massflow [6]) on the flame. A current field in the laminar flow regime configuration are triple flames obtained by a partial premixing between fuel and oxidizer at the fuel inlet [17, 8]. Such a configuration gives also indications about lifted-flame stabilization mechanisms in turbulent flows [161] which are fundamental in technical applications.

Mitchell's diffusion flame

The confined, attached, methane/air laminar diffusion flame presented in Ref. [139] by Mitchell et al. is taken here as a reference flame. The configuration shown in Fig. 2.5.1 is quite simple: there are two coaxial inflows (air and fuel) and an external chimney to avoid ambient disturbances. Actually the upper part of the experimental facility is more complex than shown in the sketch with screens and air passages to avoid buoyancy-driven instabilities. In the original work [139] no information about these devices is given, thus a simple zero-gradient outflow has been assumed. The chimney is modeled as a constant-temperature wall and the radiation term in the energy equation is neglected. This assumption should not affect the results, as experimental works showed that in sooting-free flames radiation losses are small. Concerning the inlet conditions a fully-developed, laminar, pipe flow is assumed for the fuel. A bulk profile has been adopted for the air inflow because the use of a perforated plate was reported. The geometrical and thermochemical boundary conditions are summarized in Table 2.2.

In subsection 2.5.1 a baseline simulation is presented. Insights concerning the finite-rate chemistry model as well as the main flame's characteristics are discussed in this section. The

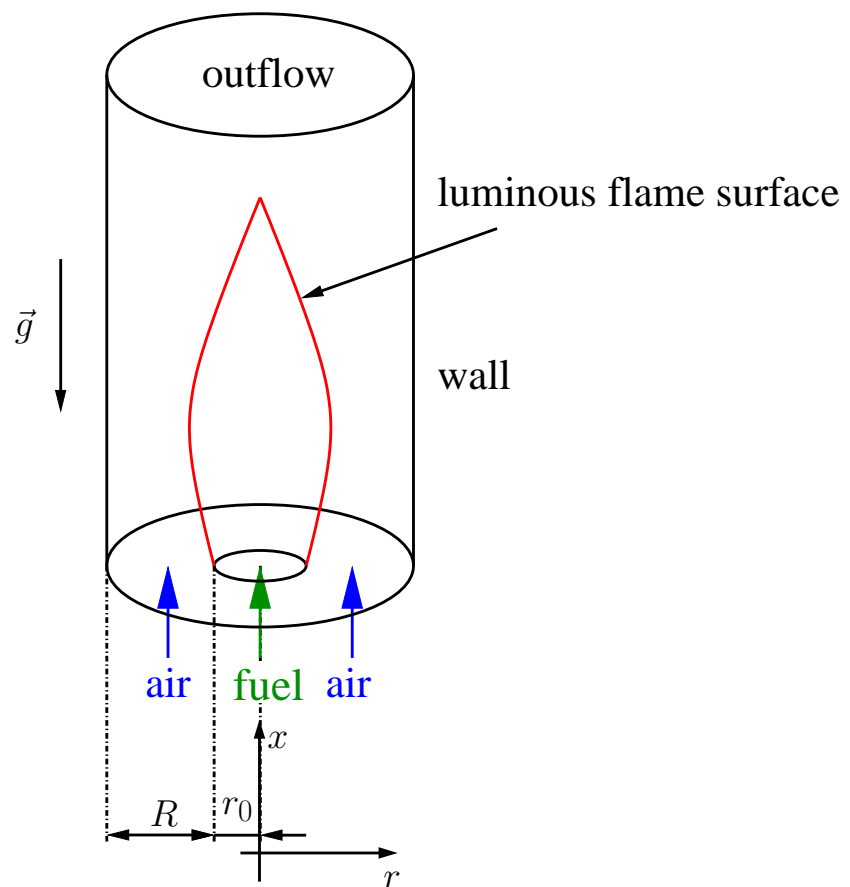


Figure 2.5.1: Mitchell's diffusion flame configuration.

Table 2.2: Boundary conditions for Mitchell's flame shown in Fig. 2.5.1.

	radius(mm)	composition ¹	temperature(K)	velocity($\frac{m}{s}$) ²
fuel inlet	6.35	CH ₄ :1	300	.045
air inlet	25.4	O ₂ :.23 N ₂ :.77	300	0.0988
wall	-	zero gradient	300	0
outflow	-	zero gradient	zero gradient	zero gradient
axis	-	zero gradient	zero gradient	zero gradient

¹ Species mass fractions.² For the fuel inlet the bulk velocity is given.

influences of the adopted chemical mechanism and of transport models will be shown in subsections 2.5.3 and 2.5.4, respectively. A further aspect which is worth investigating is the influence of boundary condition on the flame's geometry (subsection 2.5.5). To conclude the section, results will be compared with experimental data available in the same work [139].

2.5.1 Reference simulation

The baseline simulation has been carried out using the unity Lewis number hypothesis, and only viscosity and heat conduction coefficients have to be calculated using molecular data (see Appendix A). The mechanism which describes the methane/air chemistry is taken from Ref. [101] and consists of 17 species and 58 reversible reactions. The simulated domain is a cylinder slice (5 degrees, 10 cm height) starting from the fuel tube exit. Concerning the computational grid, 70x40 elements are used in axial and radial direction, respectively. The grid spacing is adjusted in order to get a more dense grid resolution in zones where mixing and reactions take place.

In this section some features of the diffusion flame will be presented. The velocity field given in Fig. 2.5.2(a) shows two important aspects. The low inflow velocity in conjunction with high flame temperatures result in a buoyancy-driven flame with its typical conical shape. At the flame tip several meters per second are attained since volume forces dominate the flow field. Combined effects of buoyancy and walls produce the recirculation zone visible in the left part of the plot. This recirculation zone has already been observed in the original work [139] and is due to the flame confinement. As will be discussed in subsection 2.5.5, such a boundary condition (negative velocities at the outflow boundary) can result in an unstable and/or unsteady solution.

In Fig. 2.5.2(b) the temperature field and (super-imposed) the stoichiometric line are plotted. The flame height⁸ is about 8 centimeter. The following observations hold:

- the stoichiometric line lies on a constant-temperature contour which is slightly lower (2186 K) than the adiabatic flame temperature at stoichiometric conditions (about 2200 K).
- because of suction effects some streamlines cross the stoichiometric line first at the bottom of the flame (when going from the lean to the rich fuel side) and a second time (in the opposite direction) at the flame's tip. The length (time) between these two instants is important for the production and oxidation of radical and intermediate species. As will be explained in subsection 2.5.4, different flame lengths yield different residence times for the fluid particles in the fuel rich region.

The penetration of the streamlines becomes more clear when looking at the oxygen field shown in Fig. 2.5.3. The oxygen entering the fuel rich region at lower flame sections causes in a slightly premixed regime. Such an effect is due to the finite-rate chemistry which includes characteristic

⁸The flame height is the distance (along the axis) from the burner to the point where the maximum temperature is reached.

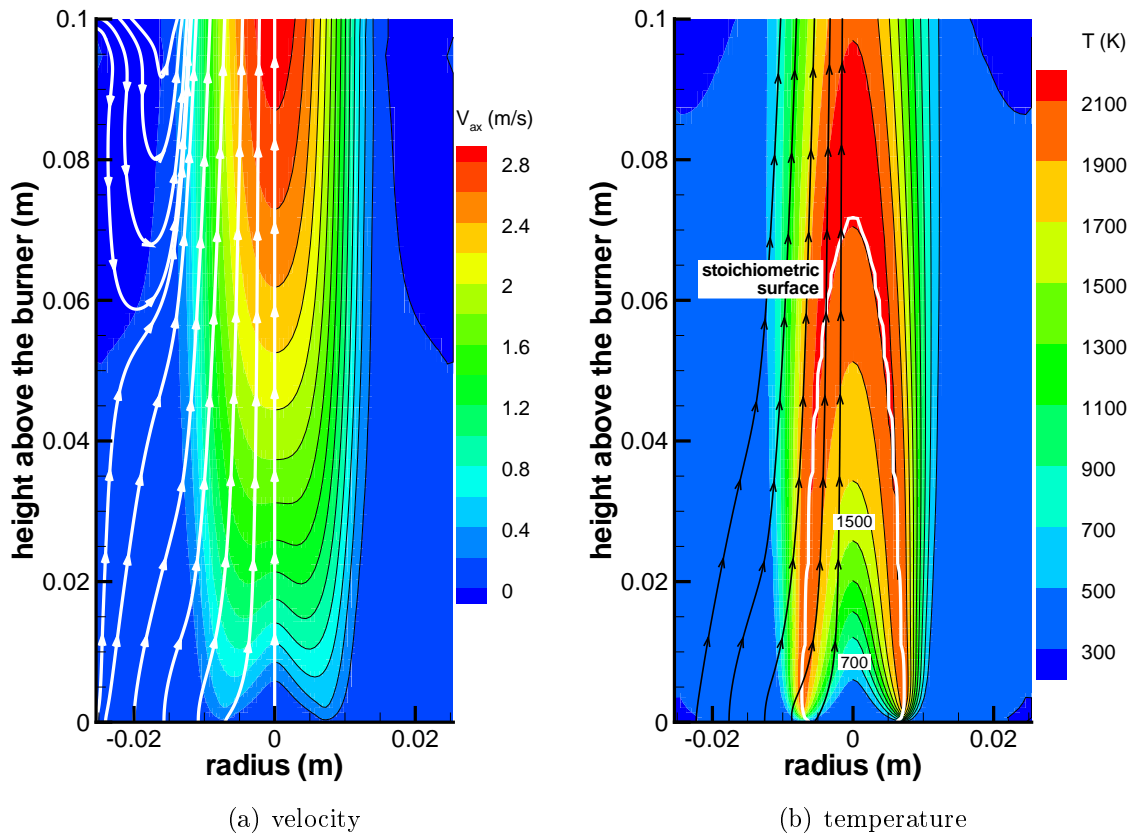


Figure 2.5.2: Axial velocity field and temperature field for the Mitchell et al. flame [139].

chemical times and allows oxygen and fuel to coexist. If such timescales would not be taken into account (i.e. fast-chemistry or flame-sheet approaches [139]), such situation could not be predicted and premixing effects would be neglected.

Some intermediate molecules resulting from the methane decomposition and oxidation are shown in Figs. 2.5.4-2.5.5. Carbon-containing species are formed on the rich side of the flame. CH_3 radicals are present mainly in the lower flame sections as a result of the CH_4 decomposition by



A further step in the fuel break-up phase is the production of CH radicals. This is a mandatory step in the carbon conversion process and, as we can see in Fig. 2.5.4, it is produced in a small thin layer lying near the stoichiometric line, where heat release takes place. Because of this property, CH chemiluminescence is used to determine the position of the flame front in laminar and turbulent flames [53].

One of last steps involved in the methane decomposition is the H production. As shown in Fig. 2.5.5(b), this process also takes place near the stoichiometric line but in the fuel lean region. Thus, the H radical can also be employed as reaction marker. In Fig. 2.5.5(a) it is noted that H_2 is formed in the rich region and reaches its maximum at a height of about 5.5 cm. Downstream of this location most of the produced H_2 is converted into water vapor before

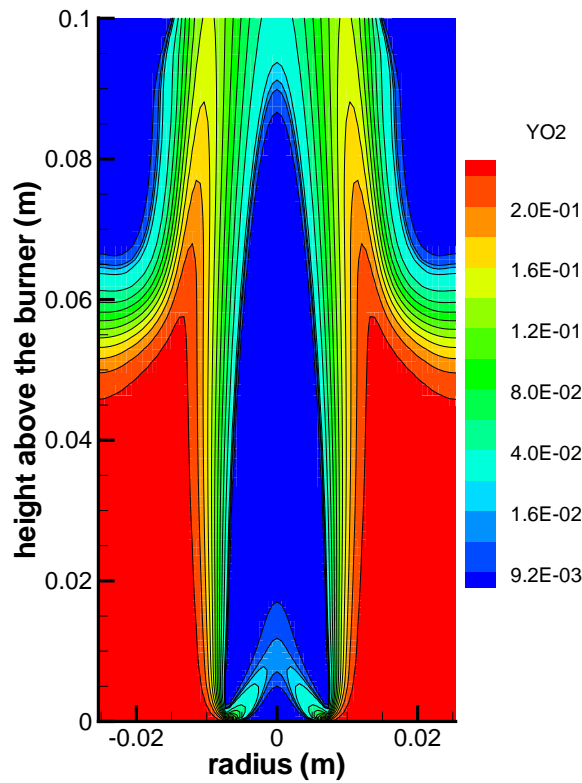


Figure 2.5.3: Oxygen mass fraction field for the Mitchell et al. flame [139].

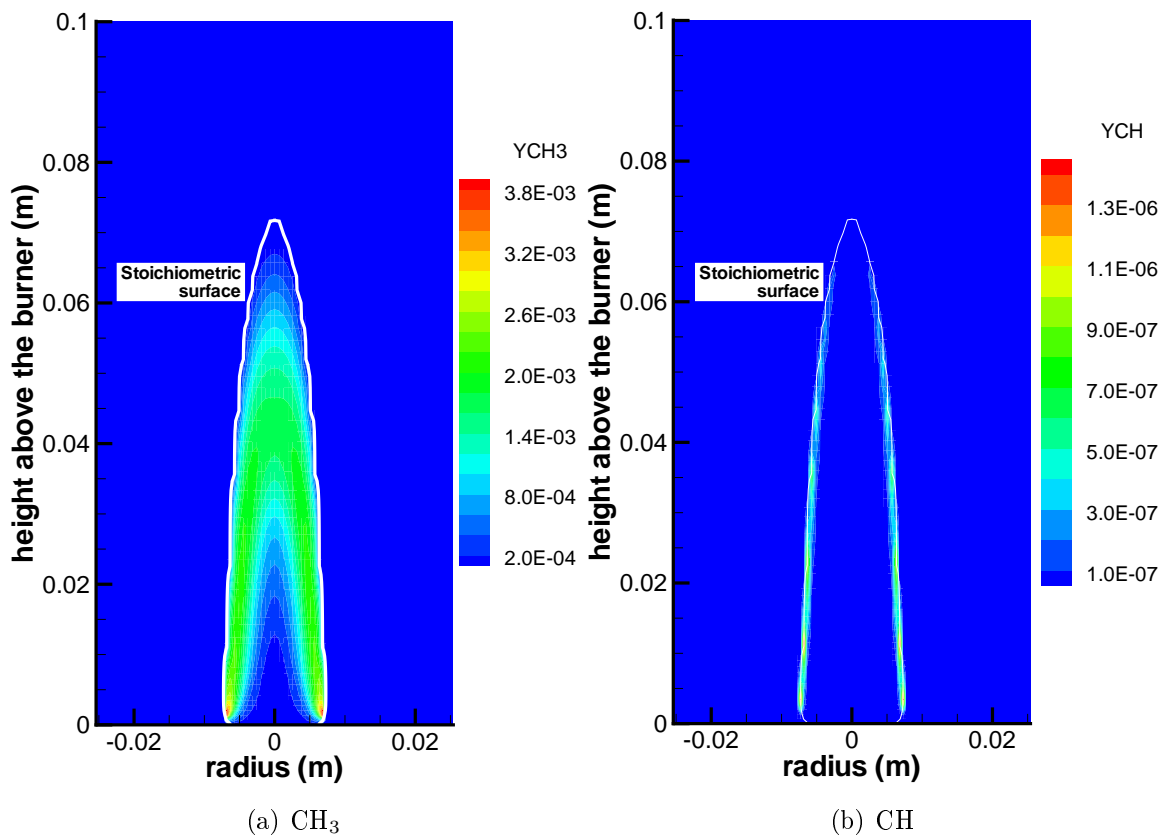


Figure 2.5.4: CH₃ and CH mass fraction fields for the Mitchell et al. flame [139].

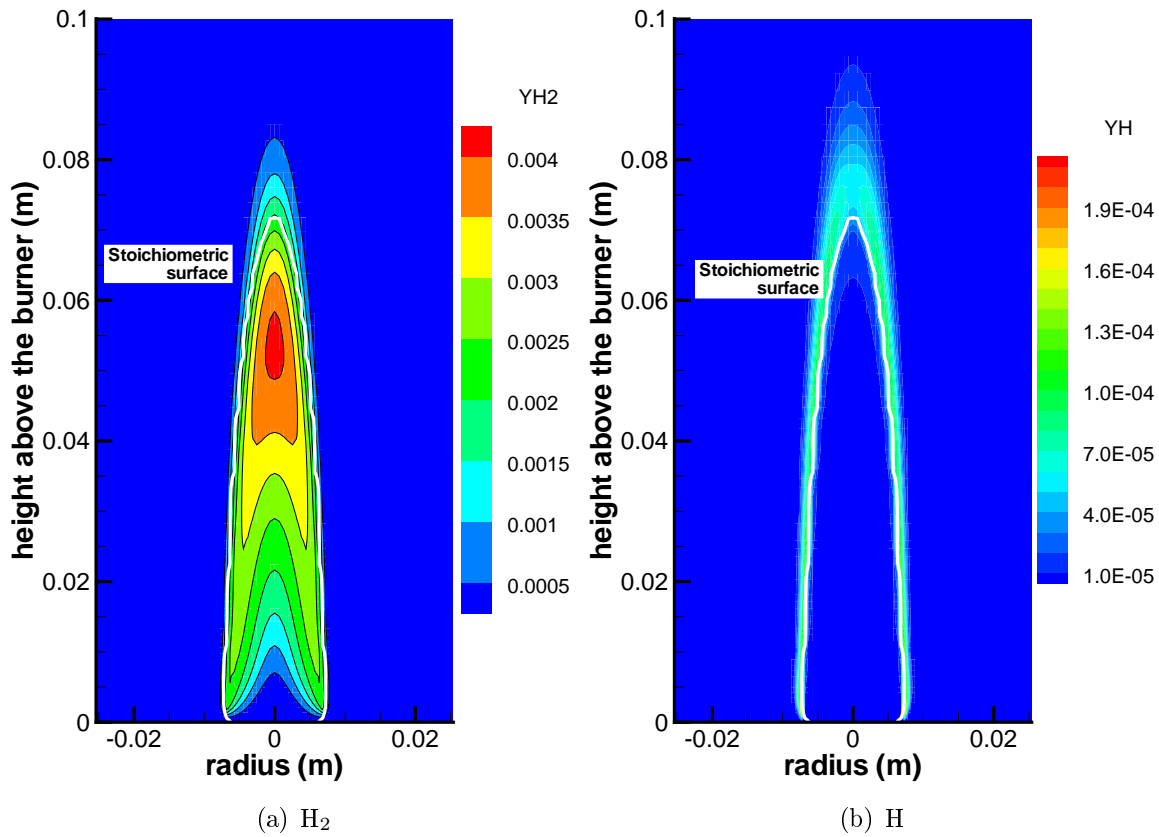


Figure 2.5.5: H and H_2 mass fraction fields for the Mitchell et al. flame [139].

reaching the flame tip and only a small amount crosses the stoichiometric line. In case of a global fuel-rich combustion, this phenomenon can be exploited to produce hydrogen and (as will be seen shortly) carbon monoxide.

Once methane is completely decomposed into smaller molecules, recombination and heat release take place in the fuel lean region. A large amount of water is produced by means of OH recombination with H. According to the OH plot in Fig. 2.5.6, the formation of this radical is related to high temperatures and thus to the heat release in the flame. The highest OH concentrations can be found in the flame's wings, where highest species gradients occur and reaction-diffusion phenomena are predominant.

On the right plot of Fig. 2.5.6 water mass fractions are shown. Comparing this plot with the temperature distribution in Fig. 2.5.2, a correlation between water production and heat release is observed. Water is produced by the recombination of molecules containing hydrogen (like H, H_2), coming from the fuel rich side, and molecules containing oxygen (O, OH) coming from the fuel lean one.

CO and CO_2 distributions are given in Fig. 2.5.7. Since the combustion takes place in excess of air, CO can be burned and converted into CO_2 . Comparing the two plots it becomes clear that the CO_2 formation follows the CO, once that fluid particles reach the oxygen-rich zone. In case of overall rich combustion it is even possible that this conversion remains incomplete yielding high CO emissions.

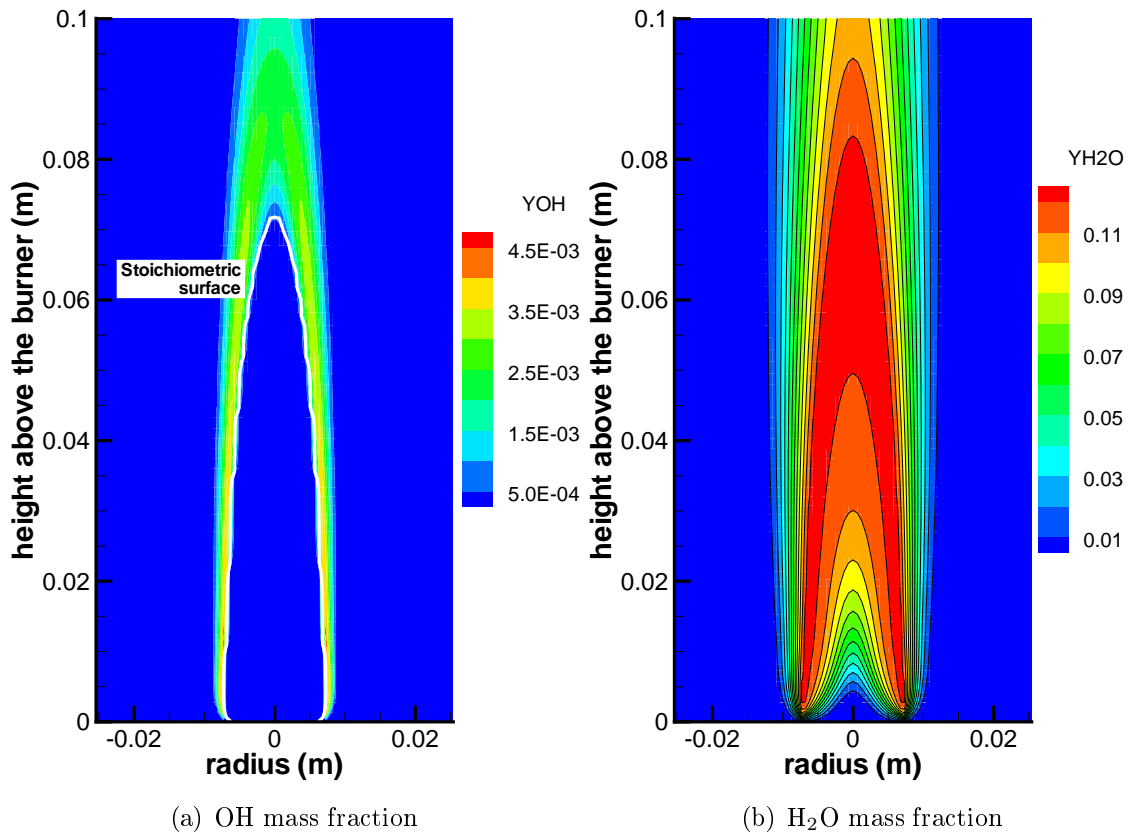


Figure 2.5.6: OH and H_2O mass fraction fields for the Mitchell et al. flame [139].

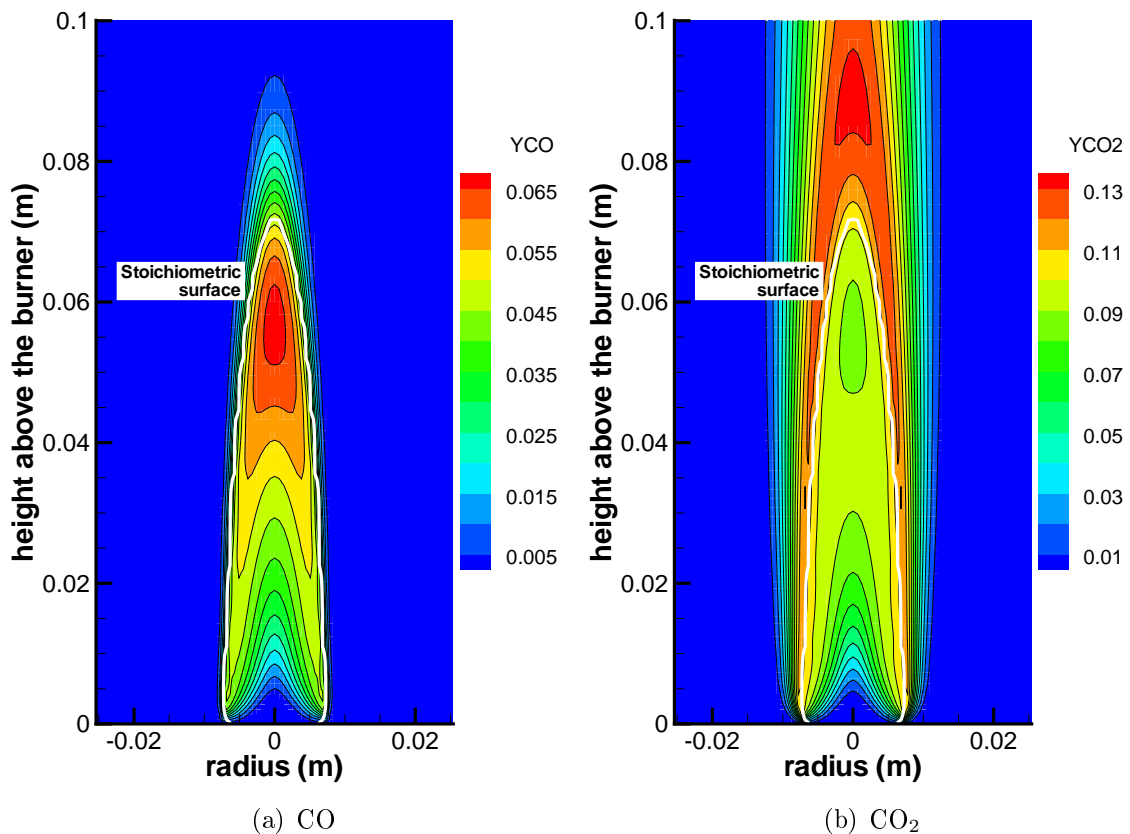


Figure 2.5.7: CO and CO_2 mass fraction fields for the Mitchell et al. flame [139].

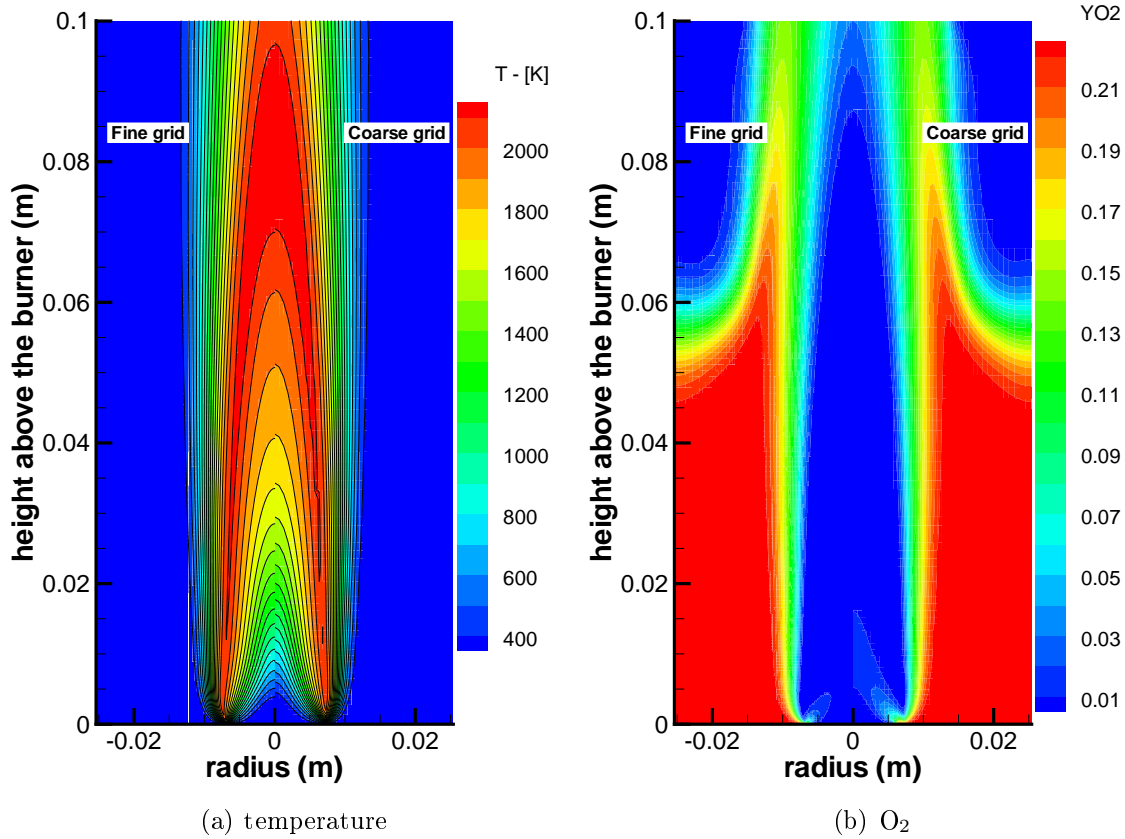


Figure 2.5.8: Effect of grid refinement: temperature and O₂ fields.

2.5.2 Effects of grid refinement

Computational Fluid Dynamics (CFD) relies on a discretized form of Eqs. (2.1.3), (2.1.4), (2.1.7) and (2.1.8) (see Appendix (B)). This means that an important source of error is the so-called *truncation error*, which depends on the adopted discretization methods and the used computational grid [58]. In order to assess the influence of the grid resolution, an additional simulation has been performed on a refined grid, which is obtained by doubling the number of points in both coordinate directions and adjusting the stretching rate accordingly.

In Fig. 2.5.8(a) temperature fields for both grids are compared. Since second order discretization methods are used for convection and diffusion, the differences are not very large and mainly appear along the axis near the inlet. These discrepancies may come from the amount of air penetrating into the fuel rich side (as shown in Fig. 2.5.3) which depends on the flame resolution. Since the flame thickness is defined by a balance of terms (i.e. convection, diffusion) depending on spatial gradients, it becomes obvious that grid resolution has a strong influence in this region.

Figures 2.5.8(b) and 2.5.9 confirm this hypothesis. In both plots only the lower part of the flame is affected by grid resolution. Since OH concentration is directly related to heat release, higher values are reached on the refined grid (Fig. 2.5.9), where gradients are stronger. For the same reasons, the amount of penetrating oxygen is lower and its burn-out is faster. On the

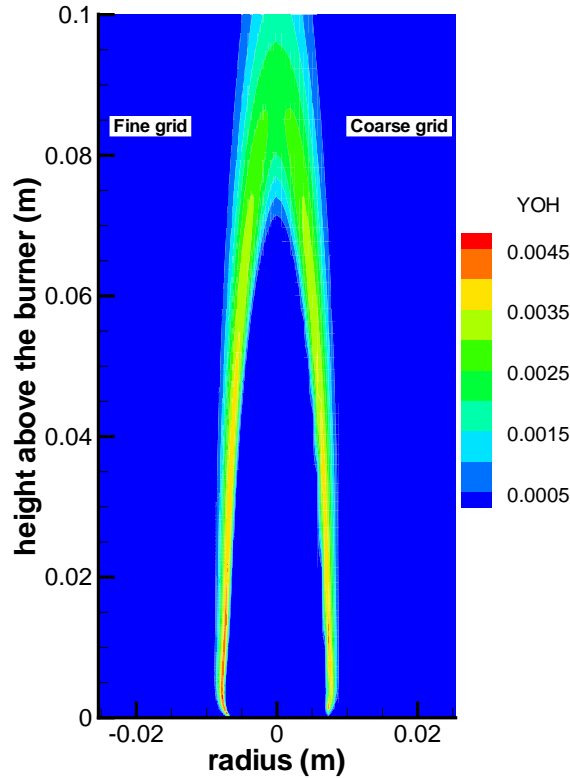


Figure 2.5.9: Effect of grid refinement: OH field.

other hand, the flame length does not depend on the grid refinement, as left and right wings join the axis at the same height.

2.5.3 Effect of the kinetic mechanism

The kinetic scheme adopted to describe the gas-phase chemistry may have a strong influence, even for diffusion flames where the diffusion between fuel and air is known to be the leading stabilization mechanism. Beside the Kee mechanism [101] used in the above simulation, the widely used GRI3.0 mechanism [178] has been tested. It consists of 36 species, 219 reversible reactions and has been extensively used and validated for natural gas combustion, where methane is one of the most abundant components [178]. In Fig. 2.5.10 the temperature fields predicted by the two different mechanisms are shown. From the position of the stoichiometric surface we can assess that the flame length is slightly sensitive to the adopted kinetics. However, the behaviors of the temperature fields are quite different for the two simulations. In particular, the GRI mechanism predicts a slower heat release rate in the fuel rich regions while comparable performance is achieved in fuel lean ones, thus yielding the same flame length.

Further details concerning the differences between the two mechanisms can be found in Figs. 2.5.11 and 2.5.12. In Fig. 2.5.11(a) methyl radical mass fractions are shown and large differences between the two mechanisms are found. In particular, the amount of CH_3 predicted by the GRI mechanism is much lower and this is mainly due to the higher number of included reaction channels for the fuel decomposition. On the other hand, the GRI mechanism predicts higher

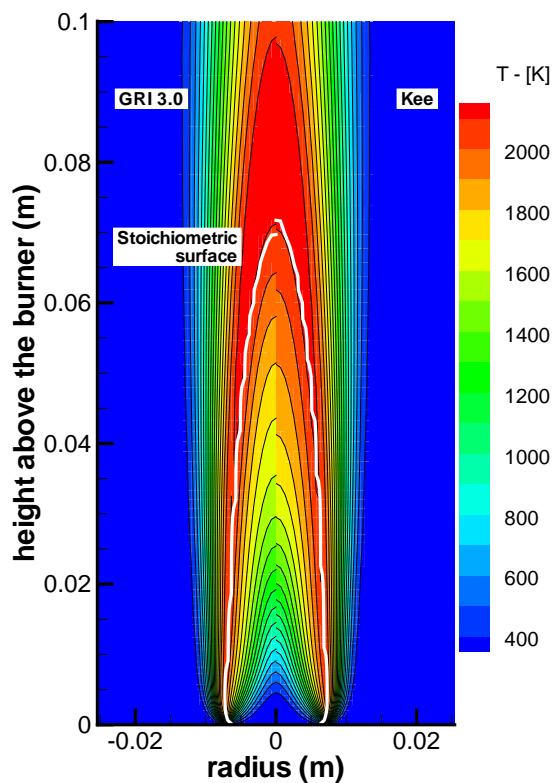
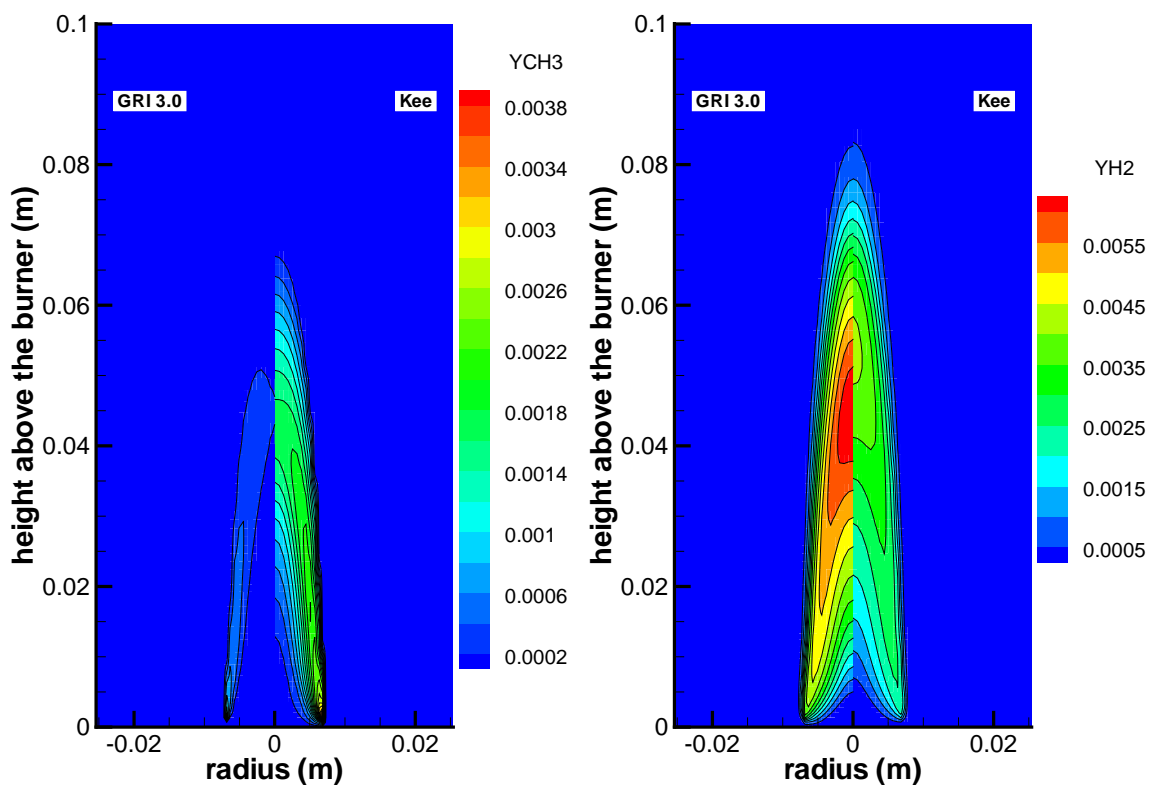


Figure 2.5.10: Effect of kinetic mechanism: temperature field.



(a) CH_3

(b) H_2

Figure 2.5.11: Effect of kinetic mechanism: CH_3 and H_2 fields.

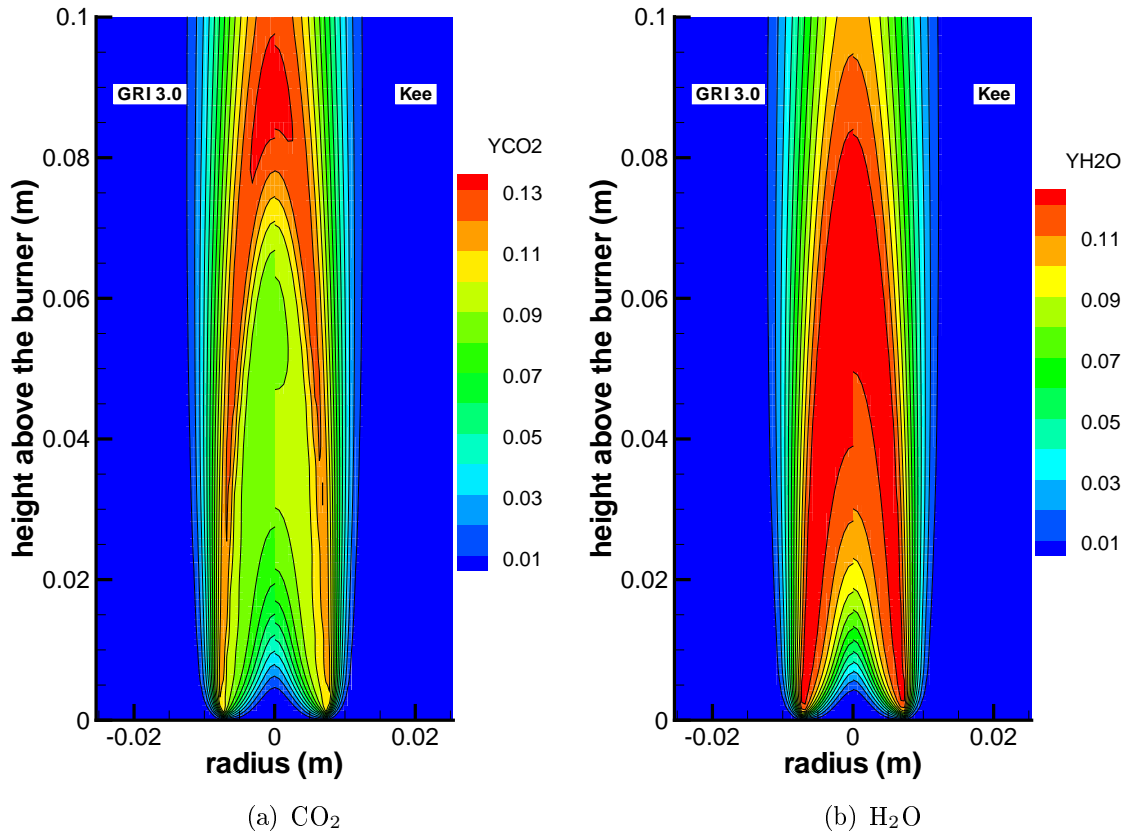


Figure 2.5.12: Effect of kinetic mechanism: CO₂ and H₂O fields.

H₂ (Fig. 2.5.11(b)) concentrations even in the low section of the flame. Downstream, the burn-out is also faster than for Kee's mechanism, resulting in approximately the same amount of hydrogen at the flame tip. This means that in the GRI mechanism reactions involving H₂ are faster at low temperatures, both the formation and oxidation directions.

Concerning the production of CO₂ (Fig. 2.5.12(a)), the GRI predictions show a monotone increase along the axis and a higher peak value near the flame tip. Moreover, the predicted water concentration (Fig. 2.5.12(b)) is consistent with the predictions above since peak values are reached at lower sections.

It results from Fig. 2.5.10 that temperature increase predicted by the GRI mechanism is lower, meaning that a slower heat release is predicted. This behavior can not be explained by the inclusion of the C₂ and C₃ species in the GRI mechanism, since plots of these species (not shown here) show their low concentrations and a complete burn out before the flame tip. Similarly (Figs. 2.5.11 and 2.5.12), a steeper increase of the intermediate and final combustion products is observed for the GRI mechanism. On the other hand, different thermodynamic databases are adopted in the two simulations. Normalized constant-pressure heat capacities for methane are plotted for both mechanisms in Fig. 2.5.13. The distance between the two curves is bigger at higher temperatures and similar differences have been found for other species. Since temperature is calculated according to Eq. (2.1.6), these differences may explain the observed discrepancies in the temperature predictions.

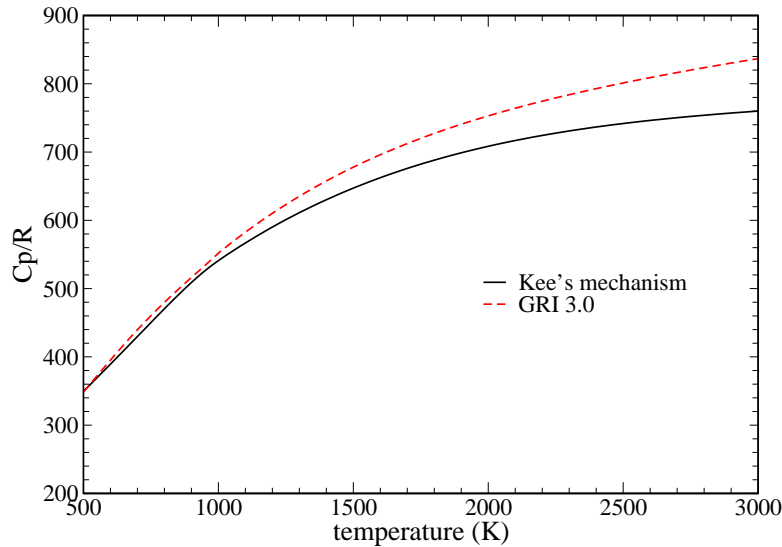


Figure 2.5.13: CH_4 constant-pressure heat capacities for mechanisms [101] and [178].

2.5.4 Influence of transport phenomena modeling

In this subsection the hypothesis $Le = 1$ is relaxed and binary diffusion coefficients for each species pair are calculated from molecular data; details are given in Appendix A. The assumption of a constant Lewis number should be more critical for radical species, which in turn are important in the determination of the flame length and the overall reaction rate. Moreover, an additional term appears in the energy equation (2.1.7) due to the transport of species with different enthalpies (2.1.12) and this has an influence on the temperature field.

In Fig. 2.5.14(a) temperature contours are shown for constant and variable Lewis numbers. Adopting the stoichiometric line as an indicator of the flame length, the variable-Lewis number simulation predicts a flame which is about 25% shorter. As explained above, such a big difference is due to an enhanced transport of radical and intermediate species within the flame sheet. This is particularly important for highly reactive atomic species like O and H, which have a higher mobility than the constant Lewis number hypothesis predicts. Since they are the rate-limiting species in the conversion process, the use of $Le = 1$ limits their mobility and therefore the overall heat release rate.

Concerning the water mass fraction (Fig. 2.5.14(b)), the most important difference between the two simulations is the location of the maximum: using a multi-diffusion model it is located in the flame's wings and it is about 10% lower than the corresponding value for $Le = 1$. This is partially due to the reduced residence time (the flame is shorter) but also to a different distribution of water precursors, like O, H and OH.

CO and CO_2 mass fractions are plotted in Fig. 2.5.15. The CO distribution shows that the reduced residence time and steeper temperature gradients along the axis reduce its maximum and promote its conversion into CO_2 . On the other hand, CO_2 is affected in an opposite manner. The peak value is higher (+20%) and it is reached at lower sections since the conversion $\text{CO} \rightarrow \text{CO}_2$ is faster. Moreover, the CO_2 distribution along the axis is monotone in comparison with the unity-Lewis number calculation (Fig. 2.5.7).

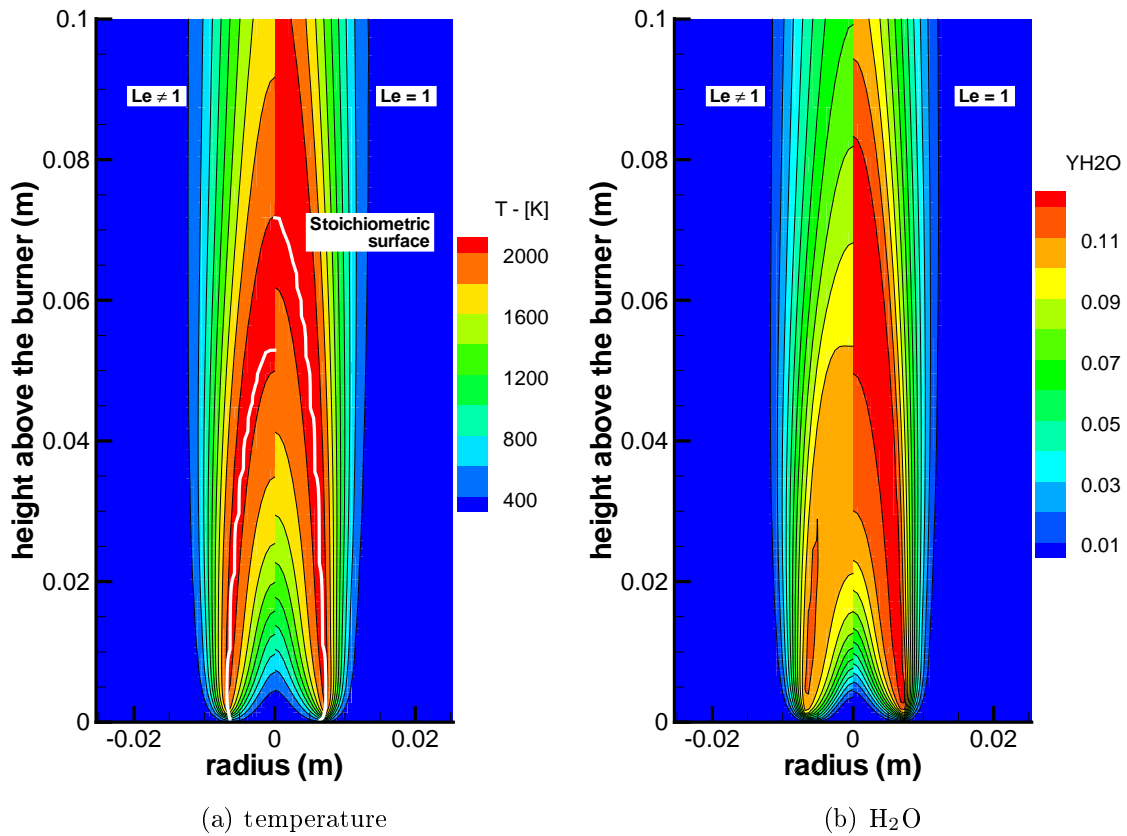


Figure 2.5.14: Temperature and H₂O fields using constant and variable Lewis numbers.

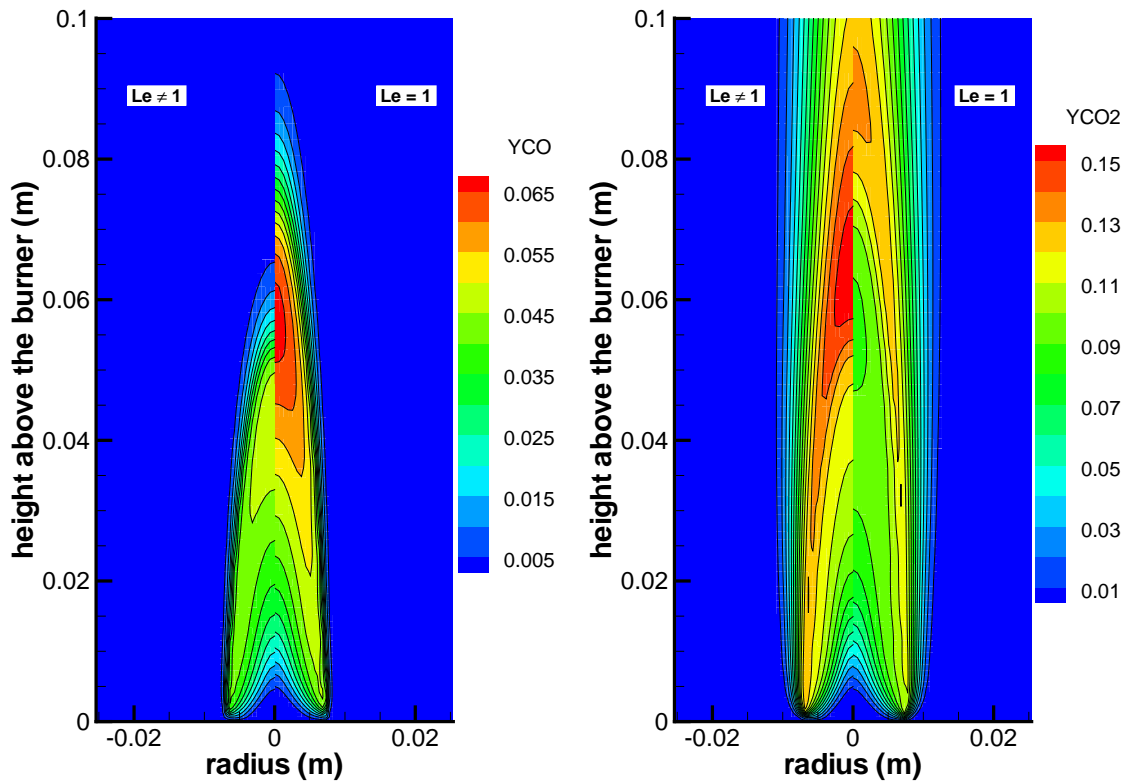


Figure 2.5.15: CO and CO₂ fields using constant and variable Lewis numbers.

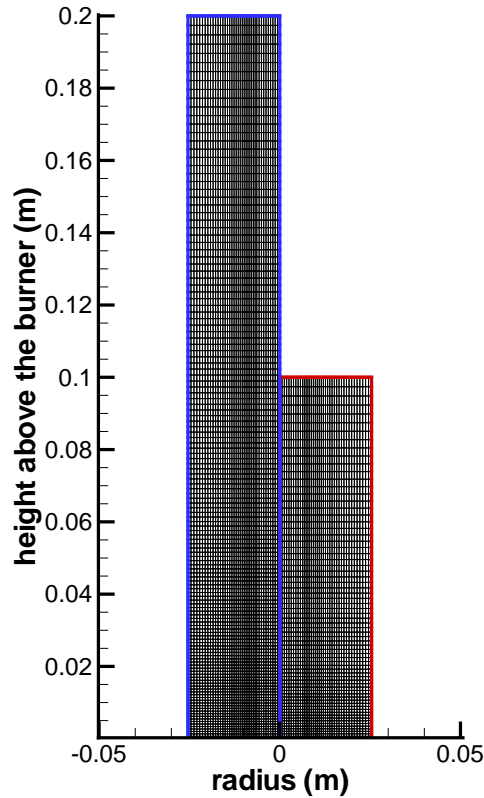


Figure 2.5.16: Original and extended grids.

2.5.5 Influence of boundary conditions

Even if the studied geometry is rather simple, the set up of the boundary conditions (both for the inflow and the outflow) is not trivial. In a subsonic flow the characteristic theory says that for an outflow three of the four physical quantities have to be extrapolated from interior points whereas the fourth one has to be fixed according to the operating conditions. The most common choice in steady-state calculations is to fix the static pressure and to extrapolate the velocity vector within a chosen accuracy. At the inlet the three velocity components are given and the pressure is extrapolated. When treating problems where recirculation zones occur (as in the present case), negative velocities appear at the outflow and a mixed inlet/outlet boundary conditions is required. Since the implementation of such a boundary conditions is out of the scope of this work, only a study on the influence of the recirculation zone on the flame shape is performed. For this purpose, a downstream-extended grid is used. The reference and extended grids are shown in Fig. 2.5.16. In case of the extended grid the number of axial grid points is doubled but the stretching rate is adjusted accordingly to preserve the same numerical accuracy in the lower region.

Results of both grids are compared in Fig. 2.5.17 concerning the temperature and H_2 mass fraction. In the first plot it can be observed that the stoichiometric line does not change when using the modified grid, therefore the independence of flame length from the outer recirculation can be assessed. Both temperature and H_2 contours show no visible variations between both simulations and the same is valid for velocity and other species plots (not shown here).

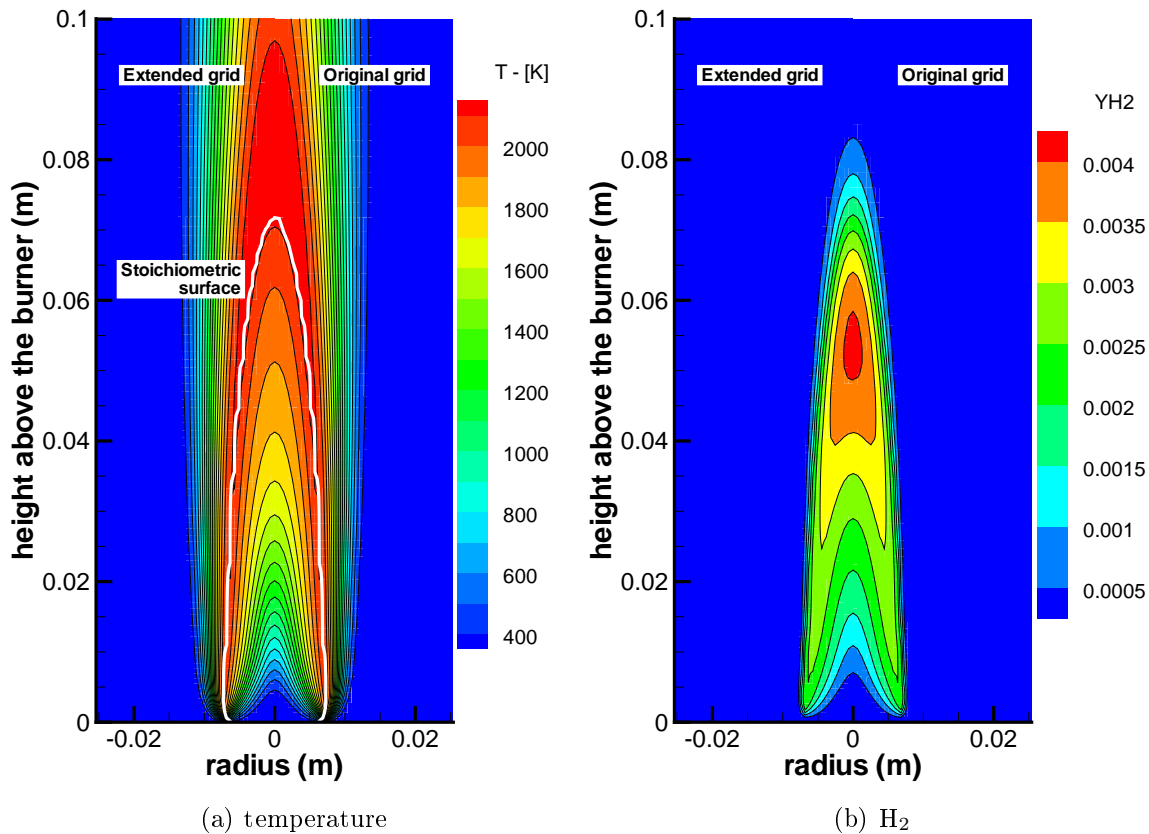


Figure 2.5.17: Effect of the outflow boundary on the results: temperature and H_2 fields.

Next, a mathematically-correct formulation for the inflow boundary values have to be determined. Since the flame is attached to the burner, a strong heat exchange takes place between the hot gases and the fuel pipe. This heat transfer will yield a non-uniform inlet temperature distribution which affects the fuel and air inflow velocity profiles. A well-posed problem would have to include the conjugate heat transfer between the fuel tube and the gas in order to resolve this interaction. Since such a treatment is beyond the scope of this work, a different approach is used here. Similarly to the investigation of the outflow recirculation vortex, the influence of the inflow boundary condition is studied by using an upstream-extended simulation domain. In this case small portions (about 1 cm) of fuel pipe and air coflow have been meshed and included in the simulation. Moreover, a linear distribution for the pipe temperature is assumed [79]. The asymptotic value is 300 K whereas 400 K is the pipe temperature at the burner exit. Now the inlet flow velocity and temperature profiles are imposed away from the burner exit and the development of the thermal and momentum boundary layer is resolved.

In Fig. 2.5.18 temperature fields for reference and extended domains are compared. Examining the stoichiometric line it can be assessed that the flame length is strongly affected by the inflow conditions. Even if the inlet mass flows are identical, the non-constant boundary conditions at the burner exit ($x = 0$) enhance the mixing for the simulation which adopts the extended domain.

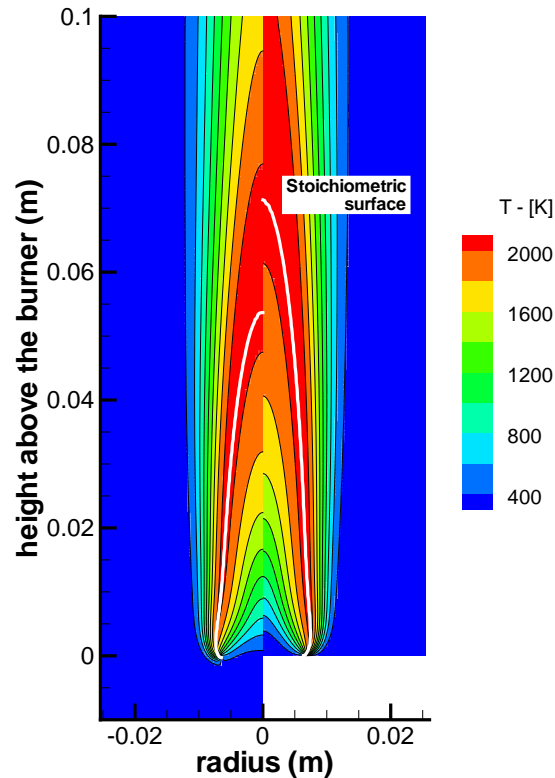


Figure 2.5.18: Effect of the inflow boundary condition: temperature field.

A comparison of the inflow profiles of both simulations is shown in Fig. 2.5.19. Both velocity and temperature show big differences near the burner lip. In particular there is a strong acceleration of the coflow and the stronger gradients increase momentum and mass transport, the driving phenomena in determining the overall reaction rate and the flame length. The species production rate is also affected by the variation of the inflow conditions, as shown for CO in Fig. 2.5.20.

2.5.6 Comparison with the experimental data

In this section a comparison between simulations and experimental data available in Ref. [140] is presented. Radial temperature distributions at different heights above the burner are shown in Fig. 2.5.21. There is a good overall agreement between simulations and experiments. The best results are achieved using the multi-diffusion transport model in conjunction with GRI-3.0 mechanism. The peak temperature is well predicted, meaning that radiation effects do not influence the energy balance too much. Nevertheless, a systematic shift between the experiment and the simulations is observed concerning the maximum temperature location and flame position. Moreover, large discrepancies occur at the inner (fuel rich) part of the flame, where the adopted kinetics may not be able to correctly describe low-temperature fuel-rich reaction paths. In particular at a height of 2.4 cm the simulations predict too high temperatures, leading to an higher expansion of the gases and a lateral shift of the flame front. Despite the differences observed among the different simulations, it can be noticed that all profiles attain similar slopes

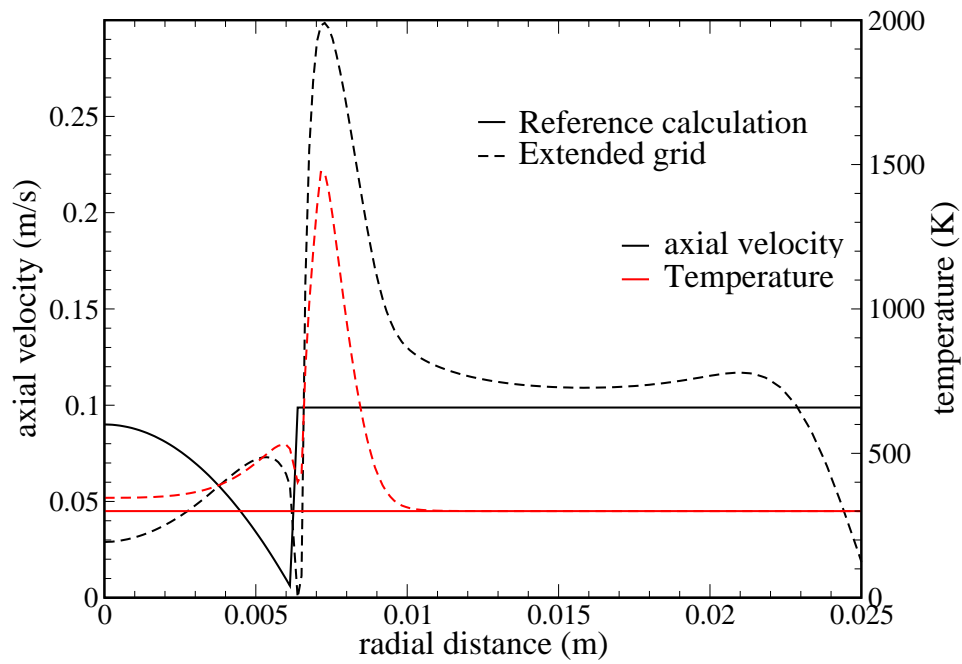


Figure 2.5.19: Inflow profiles for reference flame (subsection 2.5.1) and upstream-extended domain (subsection 2.5.5).

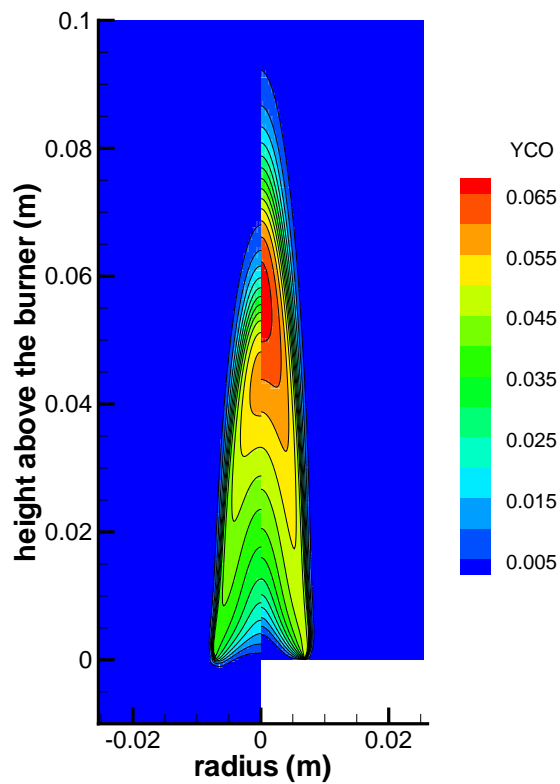
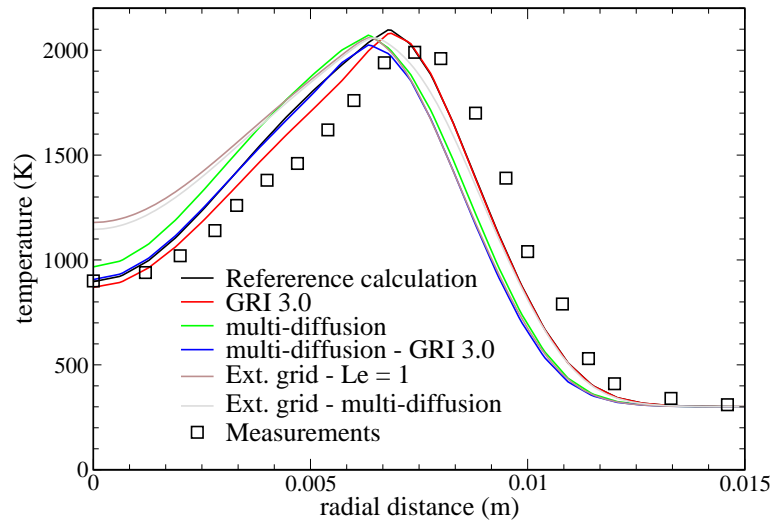


Figure 2.5.20: Effect of the inflow boundary condition: CO field.

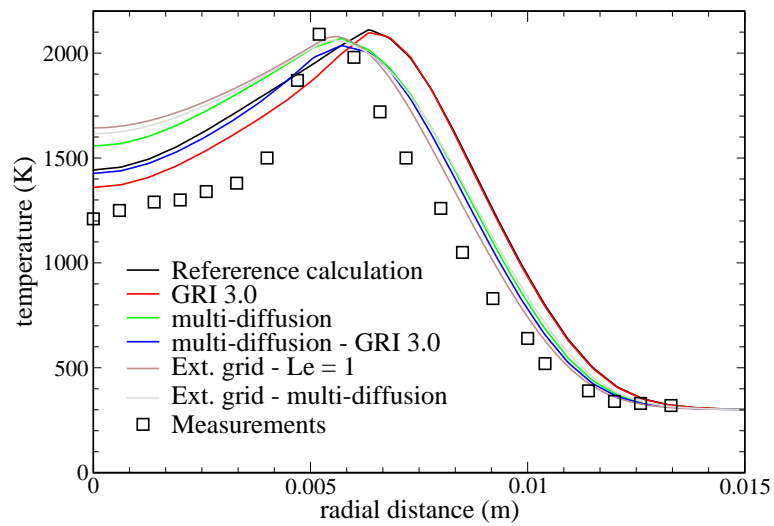
in the lean part where the agreement with the experimental data is quite good if the systematic shift is removed.

The N_2 profiles shown in Fig. 2.5.22 can be used to track the mixing process between the two streams since under the given conditions only a few ppm of NO_x are produced. There are large differences not only between the different transport models, but also between simulations adopting different boundary conditions. The best agreement with the experiment is obtained for the upstream-extended grid and the multi-diffusion model. Comparing Fig. 2.5.21 with Fig. 2.5.22, a good correlation between temperature and N_2 profiles is observed. This means that the simulation predicting the highest mixing rates also shows the highest temperature along the axis. This, however, is not the case for the measurements. It seems that, even if the mixing rate is high, slow reactions keep the temperatures low. As pointed out in subsection 2.5.5, heat exchange with the fuel pipe has an influence on the temperature field and could be responsible for such a behavior. The temperature profiles in Fig. 2.5.21 and the CO_2 profiles in Fig. 2.5.23 give an indication about the flame shape. In particular, the predicted flame is too long, even for the case with the fastest mixing rate.

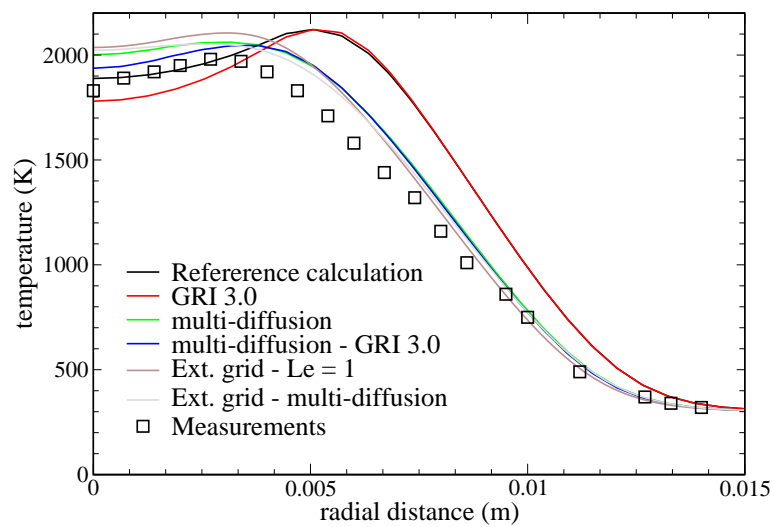
More indications concerning differences between simulations and experiment can be obtained from the axial velocity profiles (Fig. 2.5.24). A strong correlation between mixing, temperature and velocity is observed caused by the buoyancy-driven nature of this flame. Moreover, at higher sections all predicted axial velocity profiles lie above the experimental points, meaning that the acceleration predicted is too strong. Center-line deviations can be due to the lower predicted temperatures and therefore higher densities. Such a reason can not be claimed for points away from the axis, where a better agreement for the temperature is achieved. In this case the stabilizing screens and flow controllers may play a role in determining the global shape. Additionally, nozzle thickness (not reported in the original work) can affect the near field and the subsequent mixing.



(a)

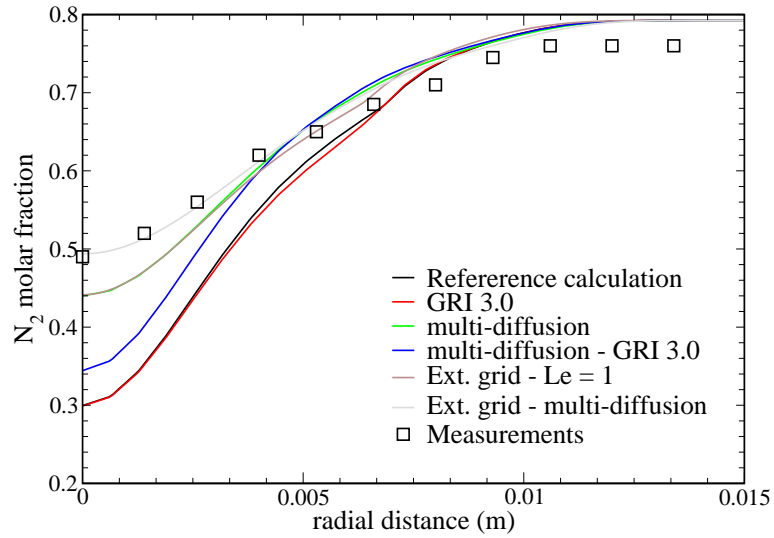


(b)

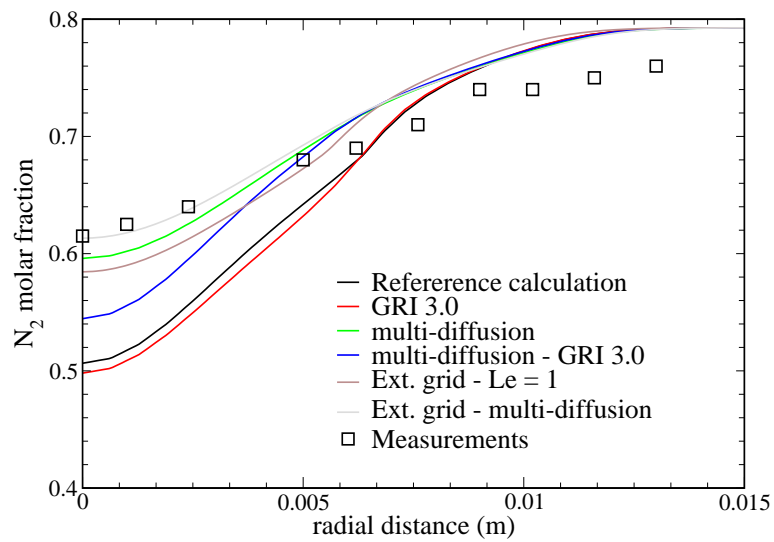


(c)

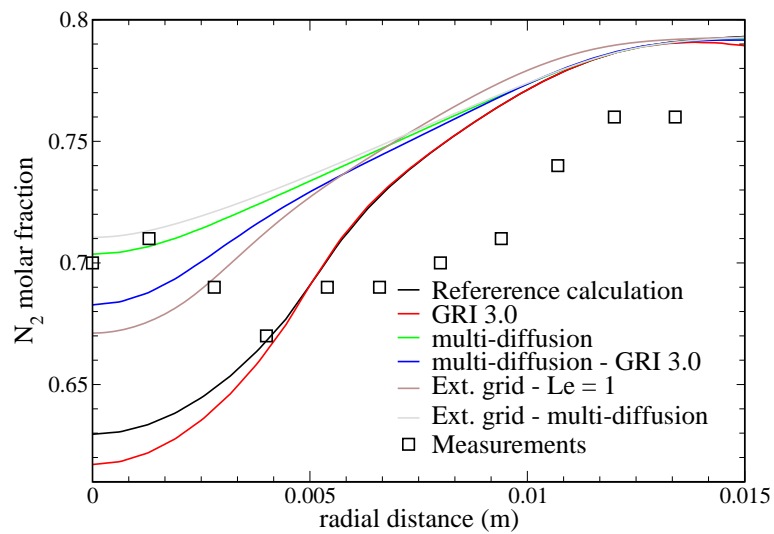
Figure 2.5.21: Comparison between experimental and simulated temperature profiles at different heights above the burner: (a) 1.2 cm, (b) 2.4 cm, (c) 5.0 cm, respectively.



(a)

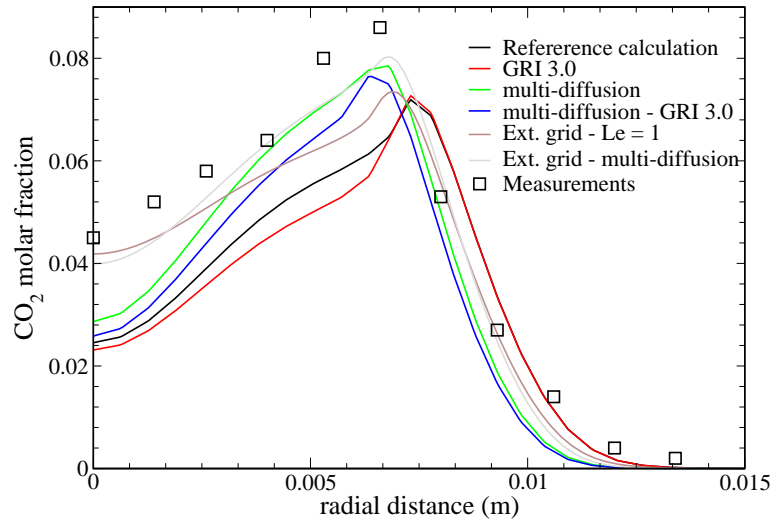


(b)

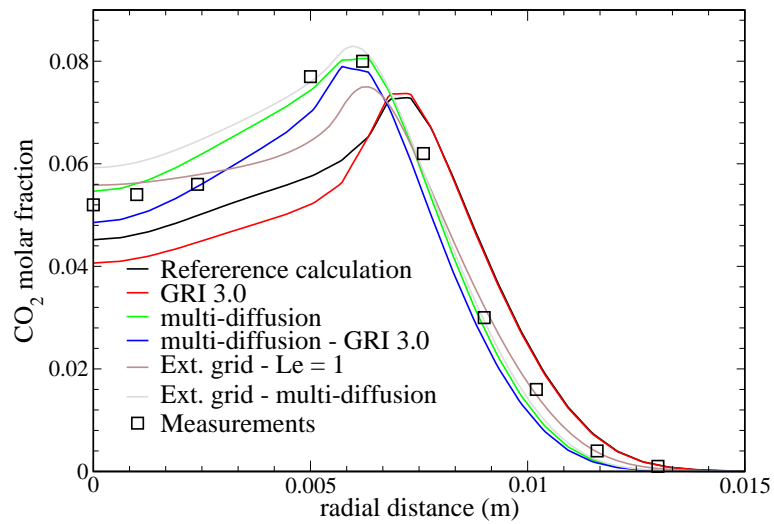


(c)

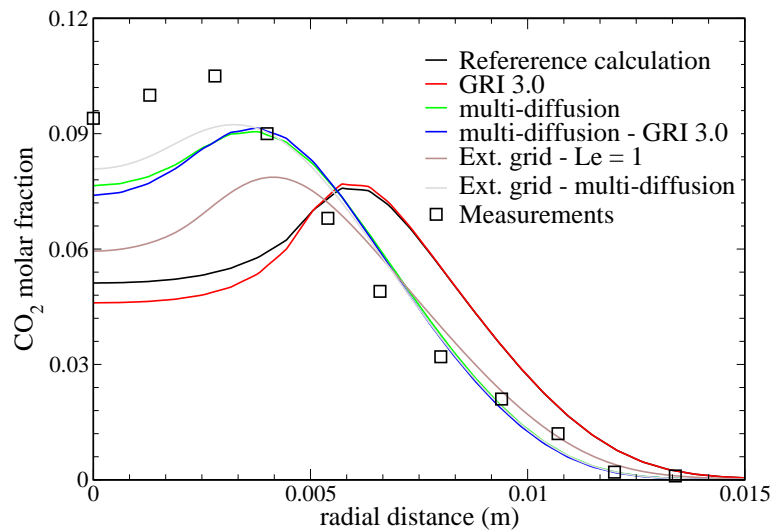
Figure 2.5.22: Comparison between experimental and simulated N_2 mole fraction profiles at different heights above the burner: (a) 1.2 cm, (b) 2.4 cm, (c) 5.0 cm, respectively.



(a)

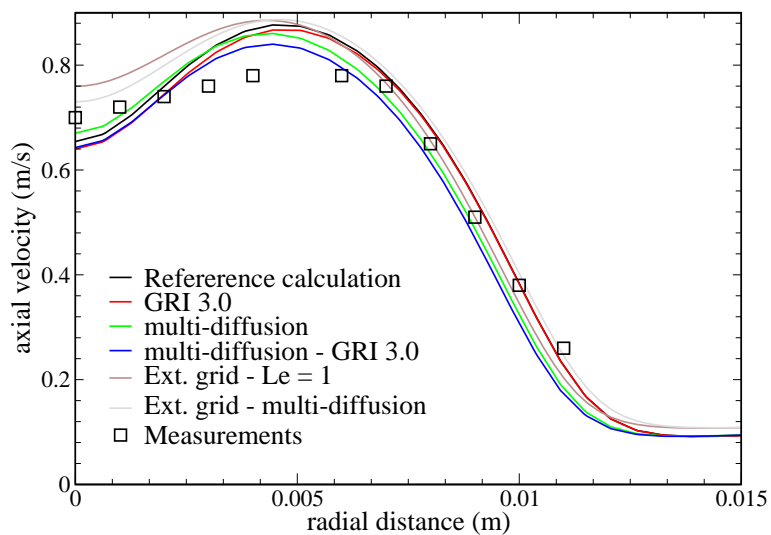


(b)

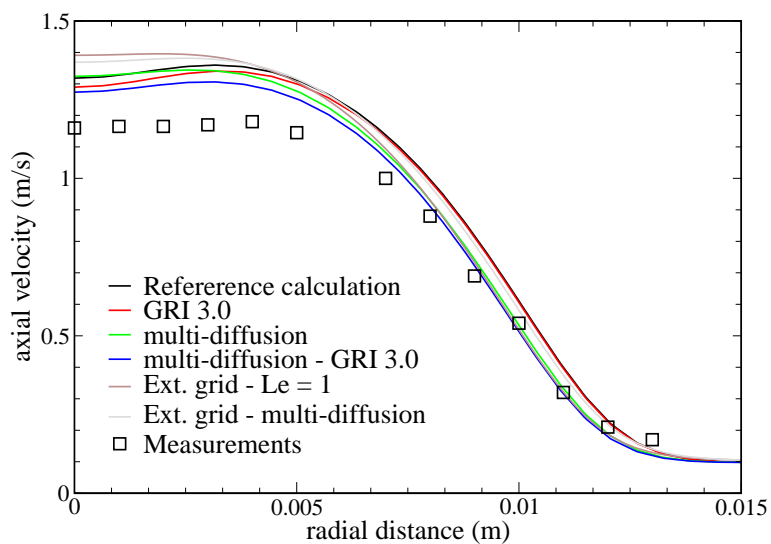


(c)

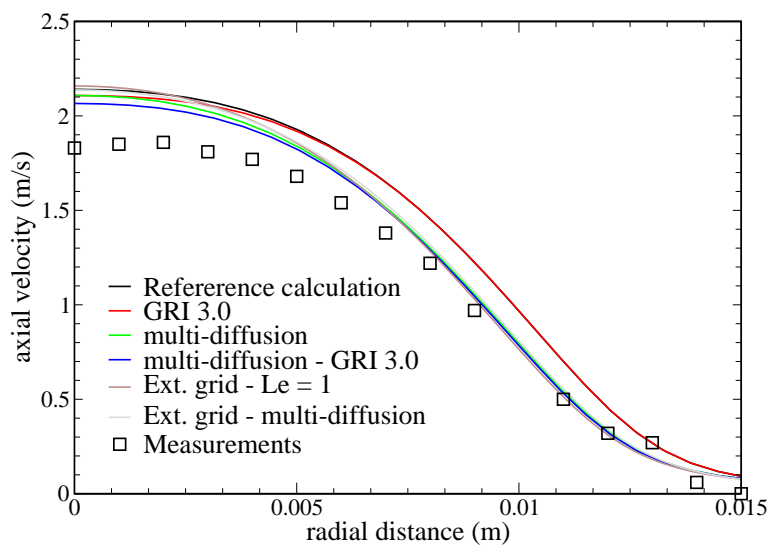
Figure 2.5.23: Comparison between experimental and simulated CO₂ mole fraction profiles at different heights above the burner: (a) 1.2 cm, (b) 2.4 cm, (c) 5.0 cm, respectively.



(a)



(b)



(c)

Figure 2.5.24: Comparison between experimental and simulated axial velocity profiles at different heights above the burner: (a) 1.2 cm, (b) 2.4 cm, (c) 5.0 cm, respectively.

3 Soot formation modeling in laminar flames

3.1 Introduction

The term “soot” refers to tiny solid particles composed mainly of carbon atoms, produced by incomplete combustion of hydrocarbons. Despite the fact that researchers have already been concerned with soot for several decades, there are still many open questions in soot-related formation processes. It has been demonstrated that soot and its precursors are a human carcinogen [11] and contribute to global warming, so its production in engines should be avoided [202]. Numerical simulations of sooting flames may help to minimize the soot production already in the design phase of propulsion devices [134]. On the other hand, soot particles enhance radiation, thus yielding a higher energy exchange in radiation-dominated systems (i.e. boilers). Therefore, the knowledge and control of soot formation processes are fundamental in many applications.

Soot particles are formed in the fuel-rich regions of the flame because of the lack of the necessary oxygen to complete the combustion. In classical diffusion flame configurations [97] the particles formed are transported into leaner zones where they are eventually converted into smaller ones by oxidation. If a large amount of soot is produced and the residence time in oxygen-rich regions is insufficient, particles can escape from the high-temperature regions and be present in the exhaust gases producing the so-called “smoking flames”.

Due to agglomeration, soot masses may range from several hundred of thousands of atomic mass units¹ (amu) up to millions of amu. Main constituent is carbon, although young particles still contain a large amount of hydrogen [164], which therefore can be used as an index of the particle’s age and its surface reactivity [4, 51]. Smaller particles have a spherical shape and their growth takes place at the surface by the addition of gaseous molecules. If soot particles reach a critical size, further growth mainly takes place by the coagulation among soot particles themselves. Since these latter can not re-arrange their shape into spheres (in order to minimize the surface tension), chain-like structures are obtained [150].

Since first studies, experimental works provided an invaluable tool in understanding the main phenomena involved in soot formation [40, 48]. In order to isolate different soot formation phenomena as far as possible, simple configurations were studied [167]. The laminar, premixed flame represents one of the most studied configuration [32, 91, 124, 134, 136, 151, 171, 193,

¹One atomic mass unit corresponds to $\frac{1}{12}$ of the mass of the carbon-12.

203, 204] since there is only one main direction along which the flame and soot develop. The flame structure is mainly determined by an equilibrium between reaction and diffusion [110] and both kinetics and soot formation models can be easily validated against these data. Since the sooting characteristics of a flame depends on the operating conditions, those works were concerned with pressures ranging from several millibar [52, 166] up to several bar [18, 191]. Even if the experiments at lower pressures have no counterpart in technical applications, they give insight into the coupling between soot and chemistry since the flame front is thicker and thus more suitable for experimental investigations. On the other hand, measurements performed at high pressure are required since most industrial and propulsion applications work under those conditions and the models developed need corresponding validation datasets.

Another branch of experimental works is devoted to diffusion flames [189, 169, 51, 54]. This combustion regime is present, at least in some regions, in most propulsion devices. Studies of such configurations provide additional information about the interaction between soot formation and flowfield. For example, the amount of soot depends on the ratio between the fuel and oxidation mass inflow, since the extent of the fuel-rich region and the soot particle's residence time depend on it [97]. For the same reasons, a different sooting behavior in normal and inverse diffusion flames has been observed² [97].

The type of fuel is another important parameter which influences the amount of soot produced. Experimental works showed that the molecular structure of the fuel (linear vs aromatic) determines the sooting tendency [132] with few exceptions (i.e. methane). Most of the experimental research was focused on simple fuels (containing one or two carbon atoms) since for such fuels an adequate description of the chemical kinetics is available and models could be tested. On the other hand, real fuels are a blend of hundreds of different hydrocarbons in liquid phase and the intrinsic complexity in reaction and vaporization issues makes such experiments less attractive. Nevertheless, some workers tried to overcome those problems, at least for laminar flames [185].

Additional measuring uncertainties are added when turbulence comes into play. Single-shot measurements are able to give insights into the soot formation in turbulent flows but they are still expensive and difficult to perform. Although several works exists [25, 90], the interaction between soot formation and turbulent fluctuations is still an open field of research [39, 107].

From the modeling point of view, the way how soot is formed and interacts with gaseous species is still under development. Because of the intrinsic complexity of the phenomena involved, it is difficult for a model to satisfactorily describe soot formation under all conditions. Experimental data indicate that soot particles are the result of a long sequence of reactions involving many molecules. Some of them act like bottlenecks in the formation processes but their experimental detection and quantification is still an issue. These factors have to be taken into account when soot models are developed, since experimental datasets still lack in some key data. Additionally, instationary behavior typical of most real devices yield variations of the local gas composition which, in turn, can enhance or lower the sooting characteristic of the

²In the inverse diffusion flame configuration the central jet contains the oxidizer, in most cases air.

mixture. In conclusion, the formulation of a soot formation model is still a formidable task and all numerical results still have to be considered from the qualitative point of view. Nevertheless, such simulations perform quite well in sensitivity analyses, to predict trends and give insights into the coupling among the different phenomena [80].

Concerning the numerical modeling of soot formation, two different trends can be outlined according to their theoretical basis and degree of complexity. Models which have the goal to describe soot physics in a most complete way belong to a first group. In order to achieve such a completeness, both experimental data, basic chemistry research, ab-initio and quantum simulations [196] and group additivity methods [184, 197] are used in order to accurately describe kinetics and thermodynamic properties of soot and related species. A satisfactory description of the soot formation paths and phenomena (within a high degree of accuracy) can be obtained at expense of the model's complexity [100]. The resulting models are able to give good predictions for a large range of operating conditions without changes in the model parameters. Nevertheless, since there are limits in the experimental database and in the computational resources, these models are validated and used only against simple fuels and low-dimensional, laminar configurations [181]. Even if the use of such models in real geometries is prohibitive, some attempts for turbulent, full-scale technical applications start to appear in literature [98].

In order to overcome that extreme numerical effort, simpler semi-empirical soot formation models have been proposed. The most simple ones link the soot formation rate to a single scalar like the fuel mass fraction [89, 97] or an intermediate species concentration [26] in conjunction with simple one- or two-reaction combustion models. Even the fuel smoking point (maximum height for a flame which does not soot) has been used to estimate the amount of soot formed in a flame [113]. In such approaches unknown model parameters have to be fitted according to experimental data [189, 190]. Such an approach yields a simple system of PDEs which is suited for carry out engineering calculations. On the other hand, the performances of such models are highly testcase-dependent. A higher degree of generality is achieved by conserved-scalar approaches [57, 102], where complex chemistry (hundreds of reactions) is included in an implicit, decoupled manner by the definition of the mixture fraction. However, the applicability of these hypotheses is restricted concerning the soot chemistry since its timescales are usually different from the flame's ones. Additional improvements are obtained if additional transport equations for soot mass fraction and particle density number are solved [9]. Nowadays, new approaches like artificial neural network methods [91] or lumping techniques [164] are available and may overcome some issues related to the determination of the soot's properties. If real-scale devices have to be modeled and turbulence comes into play, only the use of additional hypotheses (i.e. partially stirred plug flow reactor [105]) sooting combustion becomes tractable.

The formulation presented in this work wants to bridge the described approaches. In order to handle soot formation under different conditions and keep the degree of simplification low, a general model is required. On the other hand, complex three-dimensional computations (see Chapter 5) do not allow a straightforward application of a fully-detailed soot model. Thus, the model developed here represents a compromise between these needs, since it based on

a simplified yet complete treatment of all significant phenomena involved in soot formation. Beside the description of the combustion chemistry (already presented in Chapter 2), the soot model consists out of two parts: the formation of the gaseous soot precursors as described in Section 3.2 and the solid soot particles, which are treated in Section 3.3. The soot model is validated in subsection 3.4.2 against a laminar, diffusion methane/air flame. Afterwards, the model is employed to investigate premixing effects on the soot formation rate in laminar flames (Section 3.5).

3.2 A sectional approach for soot formation modeling

Phenomenological description of the soot formation process

Even if the combustion of most hydrocarbons involves thousands of reactions and hundreds of species, some steps can be outlined as fundamental [192]:

- break-up of the fuel molecules which are attacked by the oxidizer, radicals or generic third bodies (pyrolysis). The rate at which this process takes place depends on the inter-molecular forces and therefore is highly fuel dependent. Reactions involved in this step depend on the local temperature and stoichiometry. Even the kind and the amount of small hydrocarbon fragments produced at the end of this step are fuel dependent. Therefore each fuel class has to be considered by a separate reaction mechanism.
- recombination of small molecules into unsaturated fragments with few carbon atoms. These species can be either oxidized by radicals (like O, OH) or form bigger molecules, namely aromatics. The dominating paths depend on the local thermodynamic conditions (stoichiometric ratio, temperature, composition) but similarities in the combustion of different hydrocarbons have been outlined.
- polymerization which produces bigger aromatics, so-called Polycyclic Aromatic Hydrocarbons (PAHs). These species have been recognized to be the main soot precursors [49].

The described processes are graphically summarized in Fig. 3.2.1, where emphasis is given to the fact that the soot formation can be seen as a side path of the combustion process. Thus, the main steps presented in the previous chapter should not be modified whether the soot model is included or not. Thus, it is assumed that soot may affect the heat release and the amount of combustion products but not the reaction paths.

3.2.1 Outline of the PAH sectional model

In this work the entry point of the soot formation model is the definition of the soot precursors. Many studies have been performed to understand which molecules lie between the gas-phase radicals and the first soot particles. There is a general agreement that the gas phase reactions represent the rate-limiting steps for soot [130]. Different models have been proposed, but the

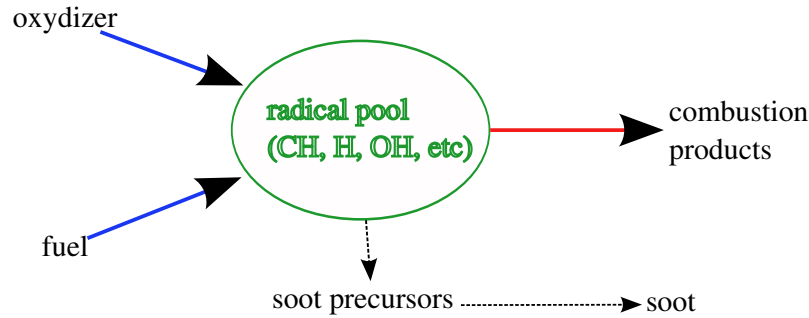


Figure 3.2.1: Sketch of a generic combustion process.

most accepted ones use Polycyclic Aromatic Hydrocarbons (PAHs) as fundamental species [74, 136, 165]. Only in few publications non-PAH soot precursors have been proposed [174].

In this work the introduction of the PAHs as soot precursors is preferred since the model has to perform well with different fuel classes. Since the products of the fuel break-up depend on the type of fuel, their influence on the soot formation may vary. In case that simple C_1 and C_2 fuels are considered, the pyrolysis must not directly affect soot formation. On the other hand, complex fuels which contain large cyclic hydrocarbons may decompose directly into aromatics, which form PAHs. That is the reason why soot models which are based only on to the concentration of small species (i.e. acetylene [119]) may perform well for simple fuels but not for more complex ones.

PAHs have masses which range from that of small hydrocarbons produced by the fuel break-up up to the mass of incipient soot particles [32, 171].³ They mainly consist out of several aromatic rings and have a planar structure. Because of the broad mass interval covered, a large number of species can be formed by addition or subtraction of small hydrocarbons (i.e. acetylene). The inclusion of these species and the solution of corresponding transport equations would make the model unfeasible for multi-dimensional applications. Moreover, the experimental detection of species with masses higher than 400-500 amu suffers from high uncertainties [132] and validation datasets are scarce. Because of these considerations, a sectional method (or chemical lumping approach) seems to be a good compromise between completeness (fundamentals of PAH physics are retained) and computational effort (only a few transport equations are added).

The main idea of the sectional method is to divide the mass interval covered by the PAHs into N_p equally-spaced classes. Each class has its own transport equations written in terms of balance between convection, diffusion and source

$$\frac{\partial \rho Y_{\text{PAH}_i}}{\partial t} + \nabla \cdot (\rho \mathbf{V} Y_{\text{PAH}_i}) = \nabla \cdot (\rho D_{\text{PAH}_i} \nabla Y_{\text{PAH}_i}) + S_v^{\text{PAH}_i}. \quad (3.2.1)$$

The PAH formation mechanism is still under investigation, however some fundamental steps have been identified. In particular, it seems that benzene formation is a preliminary step in the mass growing process [133]. After that, PAHs can collide, absorb smaller molecules and,

³In this work our attention is focused on neutral PAHs, although in some experimental and theoretical work ionic species has also been stated and discussed [84, 124].

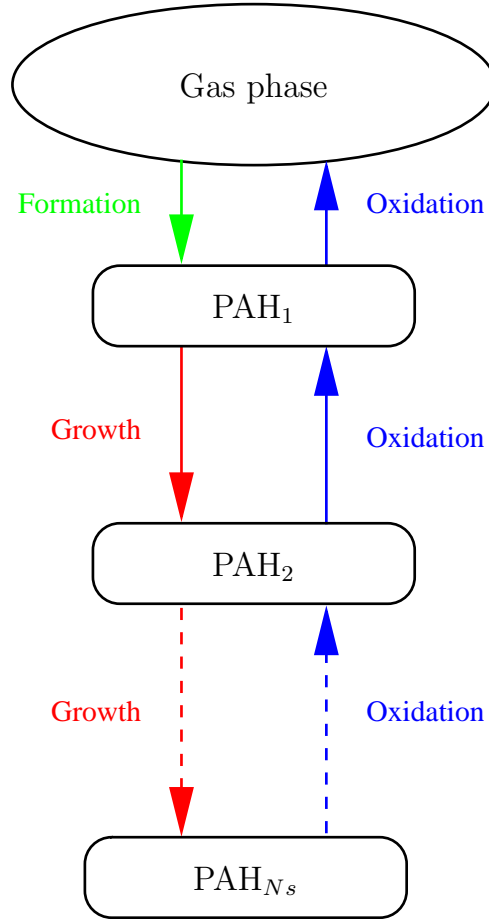
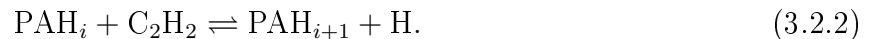


Figure 3.2.2: Schematic representation of the PAH sectional model and related processes.

when they are big enough, form incipient soot particles. As demonstrated in experiments and simulations, an important role in the PAHs growth is played by acetylene, which is involved in the widely accepted **H**ydrogen **A**bstraction by **C**₂**H**₂ **A**ddition (HACA) mechanism [4]



The process links the PAH growth rate to the acetylene concentration. As a side effect, hydrogen radicals are produced. Oxidation reactions, responsible for the PAH size reduction, work in the opposite direction.

An overview of the sectional PAH model and the related chemical processes is given in Fig. 3.2.2 while the mathematical formulation for the PAH source is given in Eq. (3.2.3). The source terms may have different forms and rate constants for each class and it reflects the physical phenomena (formation, growth, oxidation) in which the particular class is involved

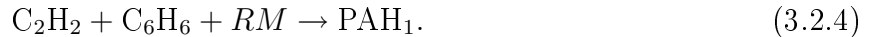
$$S_v^{PAH_i} = M_{form} S_v^{form} + M_{add} S_v^{add} + M_{coal} S_v^{coal} + M_{growth} S_v^{pgwth} - M_{ox} S_v^{por}. \quad (3.2.3)$$

The molecular masses M_k are chosen to enforce mass conservation. A similar approach has been proposed by Zamuner and Dupoirieux [206], but in their work the PAH interval was divided in two classes only and a linear distribution was assumed. The present approach has

also been used by Wen et al. [199], where its superior performance with respect to a simpler acetylene-based inception model [118, 119] in kerosene flames has been demonstrated.

3.2.2 Formation of the first PAH class

In this work benzene is considered to be the species from which the PAH formation starts by the one-step irreversible reaction



The introduction of the “reaction marker” RM is required since Eq. (3.2.4) represents a simplification of the real steps involved. As will be shown later, acetylene and benzene are formed in fuel-rich regions even at relatively low temperatures. On the other hand, high PAH concentrations are found at high temperatures in the most reactive, yet fuel-rich flame zones [151]. Thus, the reaction marker is used to limit the PAH formation step in these zones and avoid the production of PAHs in other regions. Which species is best suited as reaction marker is an open question. As shown by the laminar flame calculations of Section 2.5, several molecules can be used to track the flame front and the reactive zones. In this work CH and H are investigated and results are presented in Section 3.4.

The rate constant of Eq. (3.2.4) is modeled by an Arrhenius function. The choice of the corresponding parameters (activation energy and pre-exponential factor) is a fundamental task. As pointed out above, this step is a purely mathematical abstraction which can not be investigated experimentally. Thus, a trial and error method is used. In this work two different sets of parameters are tested and discussed. The first one is taken from the work of Zamuner and Dupoirieux [206], where they are fitted against experimental and numerical data obtained from more advanced models. The second ones come from the work of Skj ot-Rasmussen et al. [177], where transport equations for real PAH species have been solved but all PAH growth reactions have the same Arrhenius parameters. Further details will be given in subsection 3.4.

3.2.3 PAH growth by small molecule addition

Since all PAHs have a similar structure, the growth process can be described by a step which is similar to the PAH formation. Experimental and numerical works identified acetylene to be the main growth species and the HACA mechanism is formulated on this basis. In this work a simplified version of Eq. (3.2.2) is adopted



Species lumping has the consequence that the growth process affects only the heaviest part of the PAH class. Thus, only the last subinterval of mass ΔM will move from the k -th class to

the $(k + 1)$ -th one, and a scaling factor is introduced in the reaction rate

$$S_v^{add} = k_{f(3.2.5)} [\text{C}_2\text{H}_2] [\text{PAH}_i] \left(\frac{\Delta M}{M_{w_{k+1}} - M_{w_k}} \right). \quad (3.2.6)$$

Concerning the Arrhenius parameters of the rate constant $k_{f(3.2.5)}$, a similarity between formation and growth is assumed, and the same constants are used for both source terms. Moreover, no attempt to formulate class-dependent parameters is done in this work.

3.2.4 PAH coalescence

The present approach allows the introduction of phenomena like the collision among PAHs, which provides an important contribution to the PAH growth, in particular if complex fuels (i.e. blends which contain aromatic molecules) are considered [199]. Presently only collisions between PAHs belonging to the same class are considered. This assumption may reduce the total growth rate, but if the PAH mass interval is kept constant and N_p is increased (the size of the single interval decreases) the growth rate has to converge to a finite value. In subsection 3.4.1 a simple zero-dimensional calculation is performed to demonstrate this. The PAH coalescence is expressed as



where PAH_k^m is the fraction of k -th class leading by coalescence to the m -th PAH. Since the number of PAH classes and PAH mass intervals are given, the PAH_k^m can be found by simple algebraic relations if an equi-spaced distribution is assumed. The reaction rate of Eq. (3.2.7)

$$S_v^{coal} = -2\gamma_{kk}\beta_{kk}N_{av} [\text{PAH}_k^m]^2$$

is based on the kinetic theory of perfect gases. The collision frequency β_{kk} is based on an averaged PAH collision diameter [23]

$$d_k = d_A \sqrt{\bar{n}_c} \quad (3.2.8)$$

where $d_A = 1.395\sqrt{3} \text{ \AA}$ is the approximate size of a single aromatic ring. The reduced mass is defined as the harmonic mean of colliding masses

$$\mu_{ij} = \frac{m_i \cdot m_j}{m_i + m_j} \quad (3.2.9)$$

and the collision frequency is calculated from

$$\beta_{ij} = 2.2 \sqrt{\frac{\pi k_b T}{2 \mu_{ij}}} (d_i + d_j)^2 \quad (3.2.10)$$

where k_b is the Boltzmann constant. In this work a constant value for the collision efficiency γ_{kk} is assumed, even if a size-dependent formulations has been proposed in the past [138].

3.2.5 PAH oxidation

The PAH oxidation is performed by oxidizers like O_2 and OH . The generic oxidation step is given by



where OX and OXP are the oxidizer and the oxidation product, respectively. Again, the oxidation reaction rate

$$S_v^{pox} = k_{f(2.2.2)} [PAH_i] [OX] \left(\frac{\Delta M}{M_{w_k} - M_{w_{k-1}}} \right)$$

has to be corrected by a factor which takes into account that only the lightest portion of the k -th PAH class moves to the next lower class.

3.3 Soot particle equations

Since sizes and masses of the soot particles cover a large range, global parameters are needed to describe the soot particle distribution. One of the most accepted approaches, called method of moments, assumes a particle size distribution and solves equations of some low-order moments (mean, variance). Because of short residence times of soot in real combustion devices, a mono-disperse distribution (all particles have the same size) can be assumed without a loss in accuracy⁴ [54, 203]. In this case only two additional transport equations for the soot mass fraction Y_s and the soot particle density number n_s have to be solved

$$\frac{\partial \rho Y_s}{\partial t} + \nabla \cdot (\rho \mathbf{V}_s Y_s) = S_v^{Y_s} \quad (3.3.1)$$

$$\frac{\partial \rho n_s}{\partial t} + \nabla \cdot (\rho \mathbf{V}_s n_s) = S_v^{n_s} \quad (3.3.2)$$

where

$$S_v^{Y_s} = M_{nucl} S_v^{nucl} + M_{gwth} S_v^{sgwth_{1+2}} - M_{ox} S_v^{sox} \quad (3.3.3)$$

$$S_v^{n_s} = N_A (S_v^{nucl} - S_v^{agg}) \quad (3.3.4)$$

and N_A is the Avogadro number. In Eqs. (3.3.1) and (3.3.2) there is no diffusion, since soot particles are solid and do not interact by collisions. On the other hand, the actual soot velocity \mathbf{V}_s is the sum of the flow velocity and a thermophoretic contribution (see subsection 3.3.5)

$$\mathbf{V}_s = \mathbf{V} + v_{th} \cdot \quad (3.3.5)$$

Since the soot distribution is mono-disperse, the average soot particle diameter is calculated by an algebraic relation

$$d_s = \sqrt[3]{\frac{6 f_v}{\pi n_s}} \quad (3.3.6)$$

⁴It should be kept in mind that more complicated soot size distributions (i.e bimodal functions [207]) are possible under particular conditions, as experimental and numerical data show.

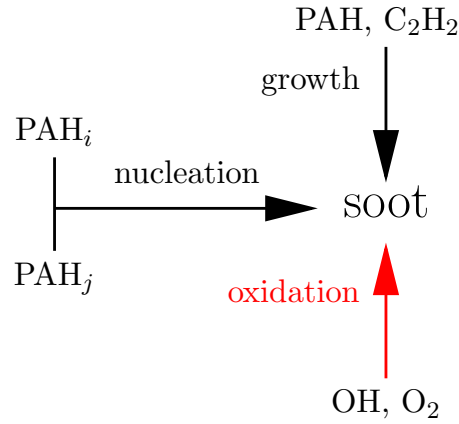


Figure 3.3.1: Soot source term representation.

where

$$f_v = \frac{\rho Y_s}{\rho_s}$$

is the so-called soot volume fraction ($\rho_s \sim 1800 \text{ kg m}^{-3}$ [119]). If details about the soot distribution are needed, additional transport equations or different methods (i.e. advanced method of moments [5, 10], population balance equations [209], bin-models [163], see also [175]) have to be used.

Concerning the interaction between the soot particles and the flow field, it should be remembered that soot particles are small ($d_s \sim 10^{-8} \text{ m}$), and the ratio between the inertia and viscous forces [176] on the soot particles

$$\tau_s = \frac{\rho_s d_s^2}{\mu} \quad (3.3.7)$$

is negligible. Thus, drag effects on the flowfield can be neglected and no additional source terms in momentum equations are needed.

A simplified representation of the processes included in the soot transport equations is given in Fig. 3.3.1. Soot particles are supposed to be formed by the collision between PAHs with a total mass exceeding a given minimum soot mass. The growth processes are responsible for adding mass to the particles: main contributions are the condensation of small species on the soot surface and collision between soot and PAHs. Similarly to the PAH submodel, soot oxidation is included.

3.3.1 Soot nucleation

Soot nucleation takes place in a mass interval where no experimental data are available. Nevertheless it is commonly accepted that soot is formed by collisions between PAHs. In agreement with other works [206], a minimum soot mass of 1200 amu is assumed, which corresponds to a soot particle size of about 1 nm. The formation of the incipient soot particles involving the i -th and j -th PAH classes is



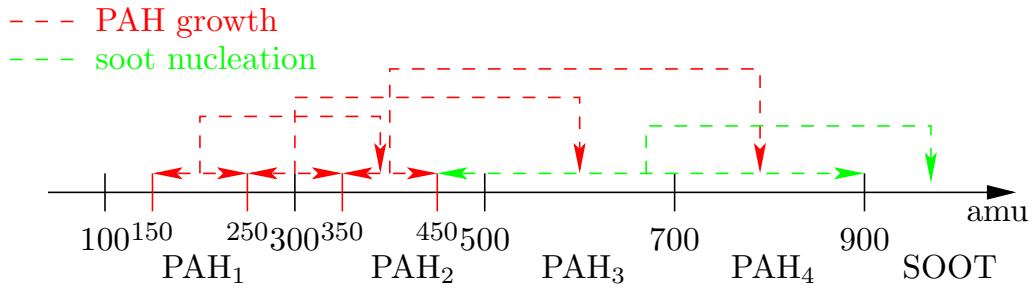


Figure 3.3.2: Graphical representation of the interaction between the PAH sectional method (four classes between 100 and 900 amu) and soot nucleation.

under the condition

$$M_{\text{PAH}_i}^{nc_j} + M_{\text{PAH}_j}^{nc_i} \geq M_{C_s}^m \quad (3.3.9)$$

where $M_{\text{PAH}_i}^{nc_j}$ and $M_{\text{PAH}_j}^{nc_i}$ are the masses within the i -th and j -th classes which satisfy Eq. (3.3.9). An example of the interaction between the PAH sectional method and soot nucleation is given in Fig. (3.3.2). The total nucleation rate is obtained by summing these contributions over all possible (i, j) combinations

$$S_v^{nucl} = \sum_{(i,j)} \gamma_{ij} \beta_{ij} N_{av} [\text{PAH}_i^{nuc_j}] [\text{PAH}_j^{nuc_i}], \quad (3.3.10)$$

where collision frequency β_{ij} is calculated according to Eq. (3.2.10).

3.3.2 Soot growth

The condensation of both small molecules and PAHs on soot contributes to the growth of the soot mass and diameter [54, 104]. In this work both contributions are included, even if some works [108] point out that the growth process takes place only through condensation of PAHs (Eq. (3.3.14)) on soot, while acetylene is only indirectly added by the PAH growth process (Eq. (3.2.5)).

Concerning the first part, experimental [204] and numerical investigations [103] indicate acetylene to be the most important growth species



Since the definition of a “soot concentration” does not make sense⁵, Eq. (2.2.2) can not directly be applied to calculate the corresponding soot source term. Because reaction (3.3.11) takes place on the soot surface, the soot surface area per unit of volume A_s is used. For a monodisperse distribution the latter quantity is obtained from the soot volume fraction and density number by

$$A_s = [36\pi n_s (f_v)^2]^{\frac{1}{3}}. \quad (3.3.12)$$

⁵As explained above, soot particle sizes range over a broad interval and a single molecular mass can not be defined.

The reaction rate is then calculated as

$$S_v^{sgwt1} = k_{(3.3.11)} [C_2H_2] A_s. \quad (3.3.13)$$

The condensation of large PAH molecules on the soot surface is modeled by



and the reaction rate is calculated according to the kinetic theory of gases by

$$S_v^{sgwth2} = \gamma_{is} \beta_{is} [PAH_k] n_s. \quad (3.3.15)$$

The soot-PAH collision frequency β_{is} is calculated similarly to Eq. (3.2.10), where the soot diameter (3.3.6) is used.

3.3.3 Soot oxidation

Soot oxidation is responsible for the reduction of soot mass and diameter [147]. The generic oxidation reaction has the form



Even if the role of different species in the soot oxidation is still under research, O_2 and OH have been identified as the most important ones [54, 143]. Experimental results indicate that the oxidation efficiency is species-dependent. Thus, a parameter η_i is introduced in the reaction rate

$$S_v^{soxi} = \eta_i k_{(3.3.16)} [OX_i] A_s. \quad (3.3.17)$$

In this work $\eta_{OH} = .13$ and $\eta_{O_2} = 1$ are used. In some works a temperature-dependent efficiency was proposed in order to achieve better predictions (i.e. smoking point and soot volume fractions) of smoking flames [121].

3.3.4 Soot agglomeration

Agglomeration reduces the number of particles while increasing the diameters. According to Transmission Electron Microscopy (TEM) pictures, two different kinds of agglomeration steps can be recognized, depending on the age of soot:

- at early stages the soot particles can rearrange themselves to attain a spherical shape;
- at later stages they form long, chain-like structures.

It is obvious that these two processes have a different influence on the specific surface area and therefore on the growth and oxidation terms (Eqs. (3.3.11) and (3.3.17)). The agglomeration at

Table 3.1: Constants used in the soot formation model. Units are mol, m, s, K.

PAH constants					
$N_p = 4^*$	$M_{min}^{PAH} = .1 \frac{\text{kg}}{\text{mole}}$	$M_{max}^{PAH} = .9 \frac{\text{kg}}{\text{mole}}$	$\Delta M = \frac{1}{10N_p} (M_{max}^{PAH} - M_{min}^{PAH})$		
Formation	C ₂ H ₂ addition	PAH addition	Oxidation		
RM	H			O ₂	OH
A_p^{for}	1.5e8	A_{pi}^{add} 1.5e8	$\gamma = 0.3$	A_{pi}^{ox}	2e6 2.1e7
T_p^{for}	11300	T_{pi}^{add} 11300		T_{ai}^{ox}	3800 2300
Soot constants					
Nucleation	C ₂ H ₂ condensation	PAH addition	Oxidation		
				O ₂	OH
$\gamma = 0.3$	A^{con} 350	$\gamma = 0.3$	A_{pi}^{ox}	742	8.82
	T_a^{con} 12100		T_{ai}^{ox}	19800	0
			γ	1	.13

* If not stated otherwise.

early stages does not have an influence on the total amount of soot but introduces an additional sink term in the n_s equation

$$S_v^{agg} = -k_{agg} n_s^{\frac{11}{6}} A_s \quad (3.3.18)$$

where $k_{agg} = 3$. Since the residence times in technical combustors are quite short and due to the lack of experimental data, no attempt is made in this work to model the second stage of agglomeration (see for example [99]).

An overview of the soot model constants is given in Table 3.1. If not stated otherwise, they are used for all simulations of soot formation presented in the following sections and chapters.

3.3.5 Thermophoresis

According to the kinetic theory of gases [195], the amount of energy exchanged by collisions between gaseous molecules and solid soot particles is a function of the gas temperature. In case of spatial temperature gradients, these interactions result in a net force for the soot in the opposite direction of the temperature gradient. This phenomenon is called *thermophoresis* and can be modeled as

$$\mathbf{v}_{th} = -C_{th} \nu \frac{\nabla T}{T}. \quad (3.3.19)$$

According to [170], $C_{th} = 0.55$ fits well with experimental data. A rough estimation of this term in laminar flames results in thermophoretic velocities of about several centimeters per second [170]. Even if this contribution is small compared to turbulent fluctuations, these values are comparable with the flow velocities of many laminar testcases. Since any soot formation model has to be validated against laminar experiments (Section 3.4), thermophoresis has to

Table 3.2: Initial condition for the ignition of a sooting mixture.

Gas composition (mass fractions)	ϕ	T_0 (K)	p (pa)
C ₂ H ₄ .15	5	1700	1e5
O ₂ .1			
N ₂ .75			

be included. Concerning its implementation, \mathbf{v}_{th} is a convective term and has to be handled accordingly (see Appendix B).

3.4 Model test and validation

In a first step a validation of the soot formation model is performed against simple testcases: zero-dimensional simulations in order to study the influence of the model parameters (in particular those concerned with the PAH modeling), and laminar diffusion flames in order to get a comprehensive assessment of the model performance.

3.4.1 Adiabatic, constant pressure reactor

A zero-dimensional simulation of a homogeneous, adiabatic, constant-pressure reactor is investigated under the hypothesis asserted in Section 2.2.3. The initial conditions are given in Table 3.2 and they are chosen in order to produce a significant amount of soot. The chemical kinetics description consists of 63 species and 338 reactions and is derived from the work of Appel et al. [4] by deleting species heavier than benzene. Four PAH classes are used for the mass interval of the soot precursors.

In Fig. 3.4.1 temperature, PAH and soot concentrations are shown. Because of the high fuel/oxidizer ratio, the temperature rise is slow and equilibrium conditions are not reached within the simulation time.⁶ Some qualitative observations can be made:

- the production of the PAHs has a well defined delay in comparison to the temperature rise;
- PAH classes are formed consecutively, with the lightest PAH first and the heavier ones later; their peak values reach the same order. It should be noted that from the first to the second PAH class these maxima increase. Later on, the soot concentration becomes significant and heavier classes experience a competition between PAH growth and condensation on the soot surface. Therefore, lower PAH maxima are obtained.

Concerning the soot, the prompt rise at the beginning is due to the nucleation process which is related to the availability of PAHs. On the other hand, because of low PAH concentrations soot growth due to acetylene addition plays the most important role. Indeed, the asymptotic constant soot growth rate is due to the almost constant acetylene concentration since the latter is only marginally affected by the soot formation.

⁶For the same reason the oxidation process does not affect the results.

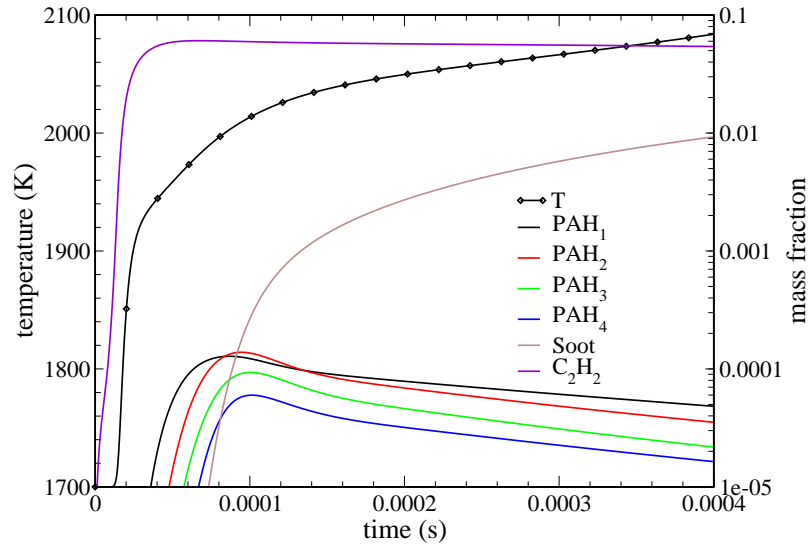


Figure 3.4.1: Temperature and soot-related species profiles versus time for the zero-dimensional reactor simulation. Symbols each 100 timesteps.

Model sensitivity to the number of PAH classes and pressure

Since the chosen number of PAH classes may have an influence on the soot formation rate, a sensitivity study is performed. In Fig. 3.4.2 soot mass fraction and soot density number are shown for different numbers of PAH classes. From this plot it becomes evident that soot nucleation and growth are characterized by different timescales. Two different regimes in the soot density number are outlined, namely before and after reaching the peak value. In the first region the nucleation is responsible for a fast increase in n_s where many small particles are formed. After the maximum is reached, the soot density number decreases because of agglomeration. The soot mass grows monotonically but with a certain delay in comparison to the soot density number. A higher number of PAHs delays the onset of soot since both nucleation and growth phases are shifted to later times. On the other hand, the peak concentrations are higher and bigger particles are produced. Nevertheless, the differences between these calculations are limited. About 20% difference between the highest and the lowest concentration are obtained at the end of the simulation time. Since soot measurements in flames usually suffer from higher experimental errors (at least 30% [133]) and a similar, constant slope is attained at the end of all simulations, it can be concluded that the number of PAH classes plays a minor role for the determination of the soot formation rate. Additional considerations are postponed to the discussion of laminar sooting flames (subsection 3.4.2).

The influence of the pressure on chemical kinetics has already been shown in section 2.2.3. Here some additional considerations are given concerning the soot formation rate. In Fig. 3.4.3 a comparison between 1 bar and 10 bar calculations is shown. Since all processes are accelerated at higher pressure⁷, the x -axis uses a normalized time ($t_{end}^{1\text{ bar}} = 4 \cdot 10^{-4}$, $t_{end}^{10\text{ bar}} = 4 \cdot 10^{-5}$). Beside the differences at the end of the simulations which are due to different equilibrium conditions, similar trends are observed for both pressures. Formation of the lightest PAH takes place at

⁷PAH and soot source terms are at least first-order reactions, as Eqs. (3.2.4)-(3.3.14) show.

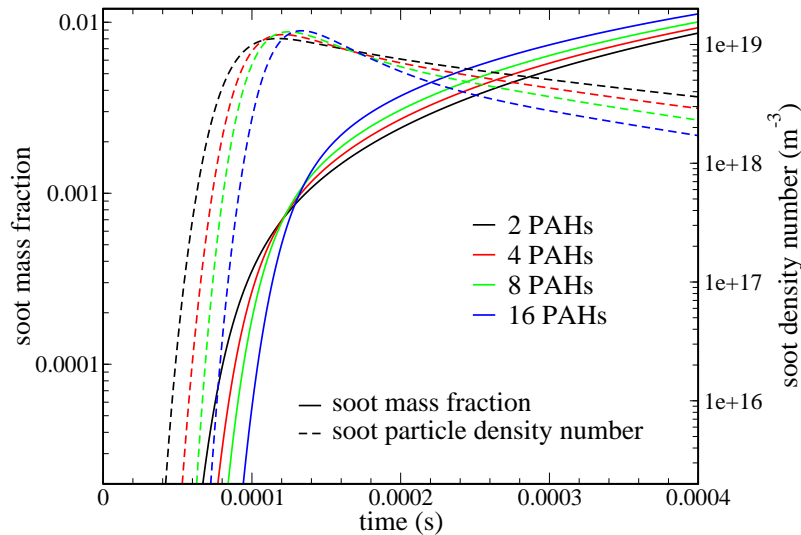


Figure 3.4.2: Ignition of a sooting mixture: influence of the number of PAH classes.

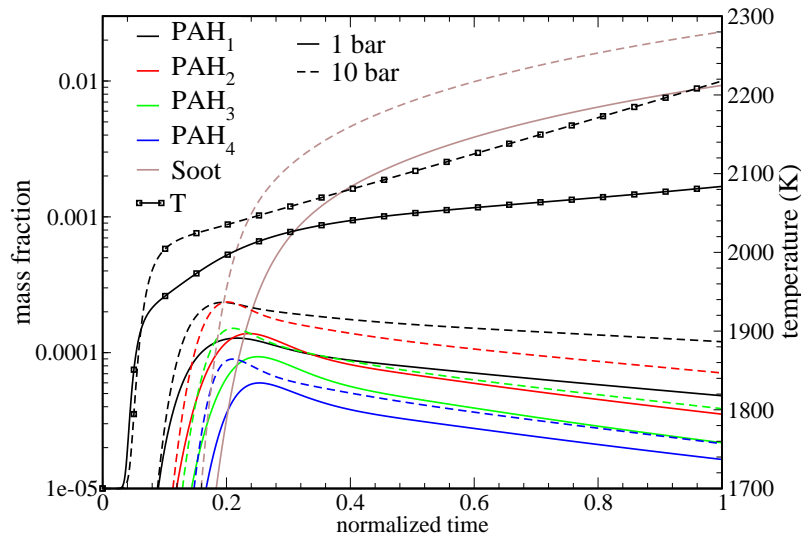


Figure 3.4.3: Ignition of a sooting mixture: influence of the pressure.

similar normalized times. On the other hand, heavier classes are more affected by the increased pressure since growth processes play a more important role.

3.4.2 Sooting methane/air diffusion flame

In order to validate the soot model, an atmospheric, confined, laminar, methane/air diffusion flame is simulated and results are compared with the experimental data provided by Smooke et al. [179]. The experimental set-up is similar to the one shown in Fig. 2.5.1. Geometric data and boundary conditions are given in Table 3.3. The fuel inflow is assumed to be fully developed. A flat profile is adopted for the coflow, since the use of a honeycomb filter is reported. Preheating effects [79, 189] and the nozzle material [77] may play a fundamental role in the sooting characteristics of this flame [179]. In Ref. [179] an increased inflow temperature is used to take these effects into account. Due to a lack of experimental data concerning the boundary conditions, the same approach is adopted here.

Table 3.3: Boundary conditions for the methane/air flame of Smooke et al.

	radius (mm)	composition	temperature (K)	velocity ($\frac{m}{s}$) ¹
fuel inlet	5.56	CH ₄ : 1.0	420	0.0552
air inlet	47.625	O ₂ : .23 N ₂ : .77	420	.1254
wall	-	zero gradient	300	0
outflow	-	zero gradient	zero gradient	zero gradient
axis	-	zero gradient	zero gradient	zero gradient

¹ For the fuel inlet the bulk velocity is given.

The kinetic scheme used to model the gas-phase chemistry is responsible for a correct description of the heat release and the temperature field. Moreover, the soot model depends on a correct prediction of the so-called “key species”, acetylene and benzene. The reference simulation adopts the mechanism of Bittker [20] because of the relative small number of reactions included. Since this mechanism was originally derived to describe benzene depletion, propargyl self-combination and acetylene addition to C₄-species are added according to the work of D’Anna and Kent [45] and Dias et al. [50]. If not stated otherwise, the soot model parameters used in this simulations are those summarized in Table 3.1. No radiation model is included since the flame produces only sub-ppm soot concentrations [143].

3.4.2.1 Reference simulation

Since the configuration is similar to the one studied in the previous chapter, temperature and main species plots are not shown again. Moreover, only small amounts of soot are formed and the soot model should not affect main species concentrations. Thus, the considerations made in subsection 2.5.1 are still valid. Thus, attention is focused on species related to soot, namely acetylene and benzene. In Fig. 3.4.4 their plots are shown together with the line of stoichiometric ratio. Both species are confined to fuel-rich regions and are burned as they approach the stoichiometric line. Along a streamline highest benzene concentrations occur before acetylene reaches its maximum. The reason is that at low temperature methane pyrolysis privileges the benzene formation and only at increased temperatures it shifts to paths resulting in acetylene.

Mass fractions of the four PAH classes, soot volume fraction and soot particle density number are plotted in Figs. 3.4.5 and 3.4.6, respectively. High PAH concentrations are found in the flame wings, where high temperatures and fuel-rich conditions promote the formation of soot precursors and their conversion into soot. The PAH cascade is well visible and for higher PAH classes the peak values are obtained further downstream. The interaction between the PAHs and soot become clearer if Fig. 3.4.5 and Fig. 3.4.6 are compared. The first two PAH classes are characterized by distributions which are complementary to the one of soot. This means that

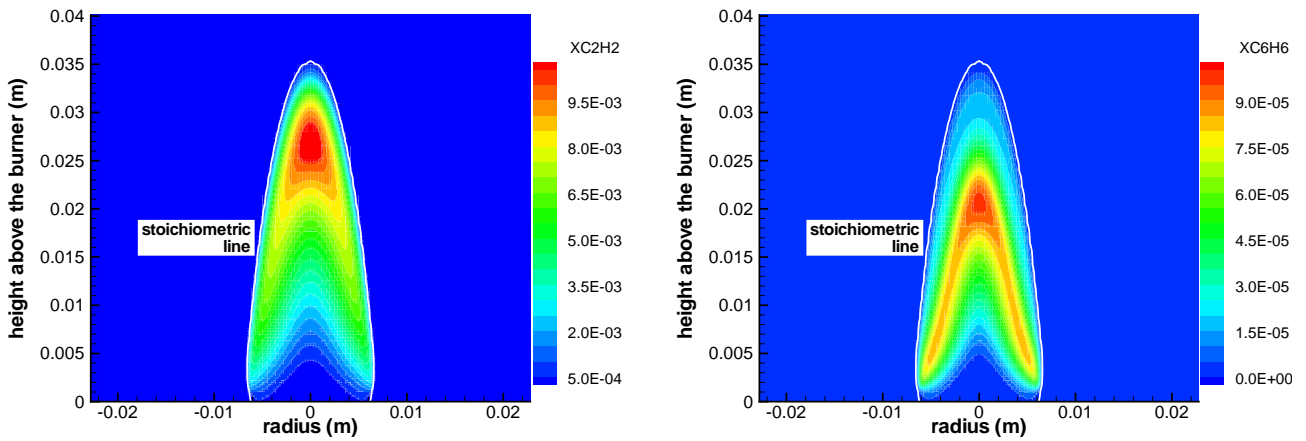


Figure 3.4.4: Acetylene and benzene molar fractions for the sooting methane/air flame of Smooke et al. [179].

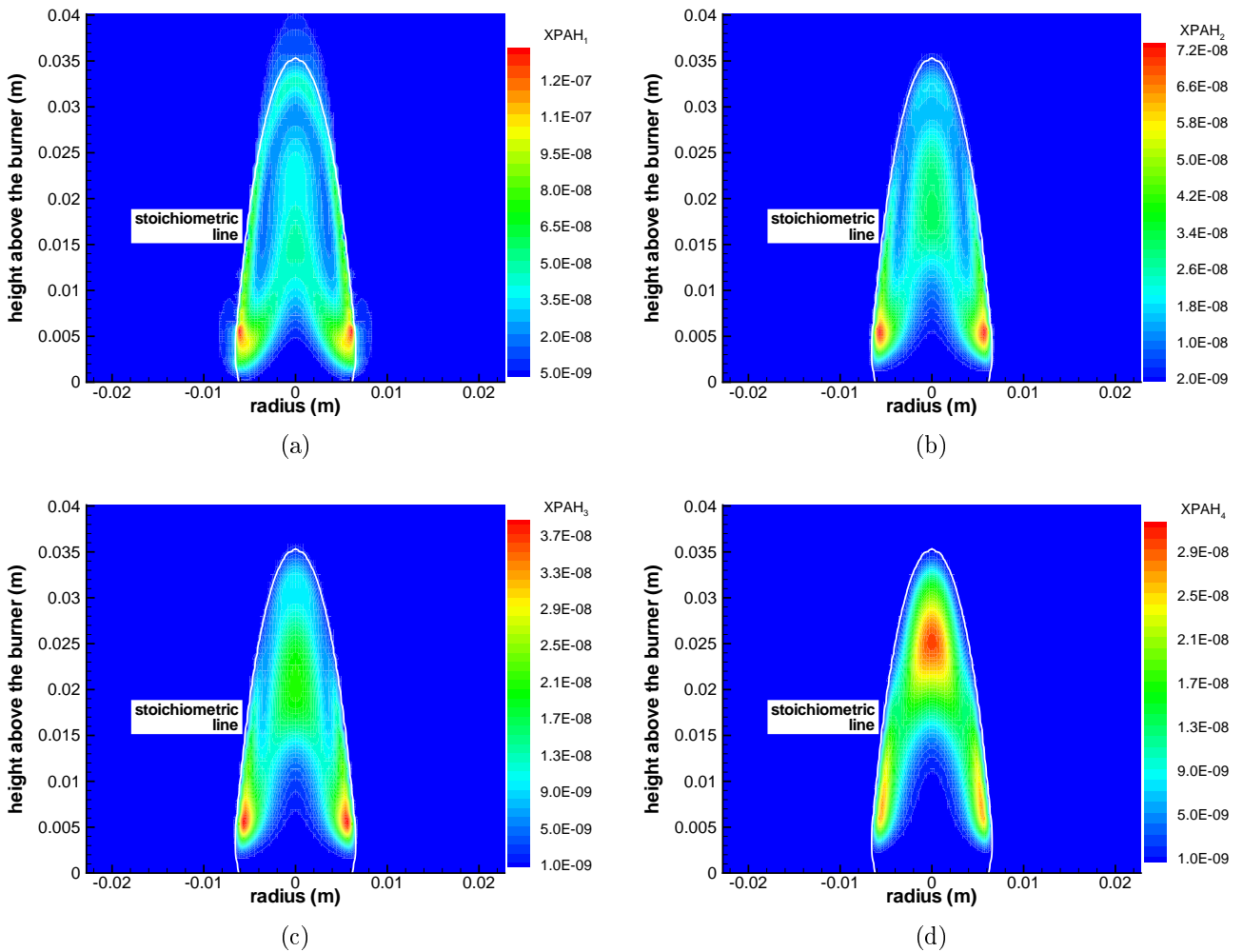


Figure 3.4.5: Molar fractions of PAH (one to four) for the sooting methane/air flame of Smooke et al. [179]

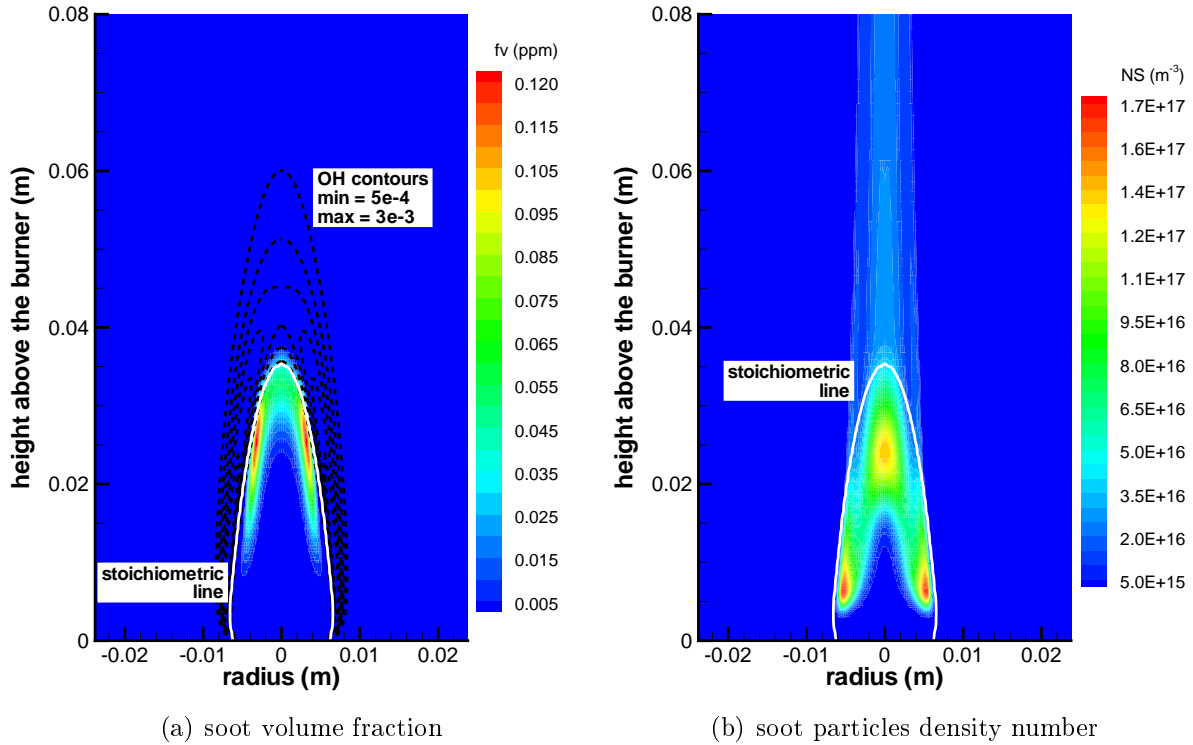


Figure 3.4.6: Soot volume fraction and particle density number for the sooting methane/air flame of Smooke et al. [179]

these classes are completely consumed by the soot nucleation and growth process. On the other hand, the fourth class (and partially the third one) shows maxima at locations where high soot concentrations are attained and this indicates that bigger PAHs are not entirely converted into soot. In any case all PAH classes are absorbed or oxidized before they reach the stoichiometric line.

Figure 3.4.6(a) shows that soot formation is a process limited to fuel-rich regions and that soot particles are oxidized before they reach the flame tip. Most of the soot is concentrated in the flame's wings, as pointed out in many experimental works [142]. The use of the reaction marker RM in the PAH formation step (Eq. (3.2.4)) is motivated by the comparison of the Fig. 3.4.6(a) with benzene and acetylene distributions plotted in Fig. 3.4.4. The omission of a reaction marker would yield a soot production spread over the whole fuel-rich region, which is in contrast with the cited experimental data.

The differences among the nucleation and growth timescales found in zero-dimensional simulations are now correlated to the flowfield. A comparison of the two plots in Fig. 3.4.6 shows that the maximum of the soot mass fraction is located more than two centimeters downstream the peak of the soot particle density number N_s . Moreover, a second peak of N_s along the flame's axis is caused by the high concentrations of soot precursors near the flame tip. However, a local maximum in soot mass does not appear, since the soot particles are close to the stoichiometric line and little time is left before they are oxidized by OH radicals [86] (the OH contours are plotted in the same image).

Table 3.4: Adopted parameters for a sensitivity analysis study of the soot model. Units are mol, m, s, K.

Simulation	Number of PAH classes	$A_{p_i}^{for}$	$T_{a_i}^{for}$	[RM]
1	4	1.5e8	11300	H
2	4	3.98e7	5100	H
3	4	3.98e7	5100	CH
4	8	3.98e7	5100	H

3.4.2.2 Validation of the soot model

The validation of the soot model is related to the determination of the model constants introduced in Sections 3.2 and 3.3, with the aim to get a good agreement with experimental data. It should be kept in mind that the soot model has to be as general as possible as to allow different operating conditions. Therefore, only few parameters should be tuned and as far as possible generally accepted values from literature should be used. That is especially true for the soot particle sub-model, for which large experimental datasets exist. On the other hand, the adoption of a sectional approach for PAH chemistry in the present form is new and does not have many counterparts in the literature.

A closer look at the PAH sub-model reveals that there are only few parameters which have a large influence on the overall performance. In particular, exponential factors in the PAH formation and growth steps (by acetylene addition) are of great importance. Additionally, the reaction marker and the number of PAH classes as free parameters. Both values are investigated in a sensitivity study and the corresponding parameters are summarized in Table 3.4.

Concerning the Arrhenius coefficients, the reference simulation adopts parameters taken directly from the work of Zamuner and Dupoirieux [206]. The Arrhenius coefficients used in the remaining simulations are taken from the reaction mechanism of Skyøt-Rasmussen et al. [177], where formation and growth of the most abundant PAH molecules are described by elementary reactions. Since the HACA mechanism adopted in that work prescribes similar rates (regardless of the PAH size), the same Arrhenius parameters are used here to describe the formation and growth of the lumped species.

The influence of the reaction marker is also taken into account by testing two species, namely H and CH. Both radicals are associated with the most reactive zones of the flame and reach their maximum in the fuel rich region (see Figs. 2.5.4 and 2.5.5 in Chapter 2). Moreover, their concentrations differ by several orders in magnitude and a significant influence on the soot model performance may be expected.

Simple zero-dimensional simulations have already shown that the number of PAH classes used has an influence on the soot growth rate. Thus, an additional simulation with eight PAH classes is performed to investigate effects on the diffusion flame.

In a first step a comparison with experimental data in terms of temperature, acetylene and benzene is performed. Smooke et al. [179] measured temperature and species distributions at

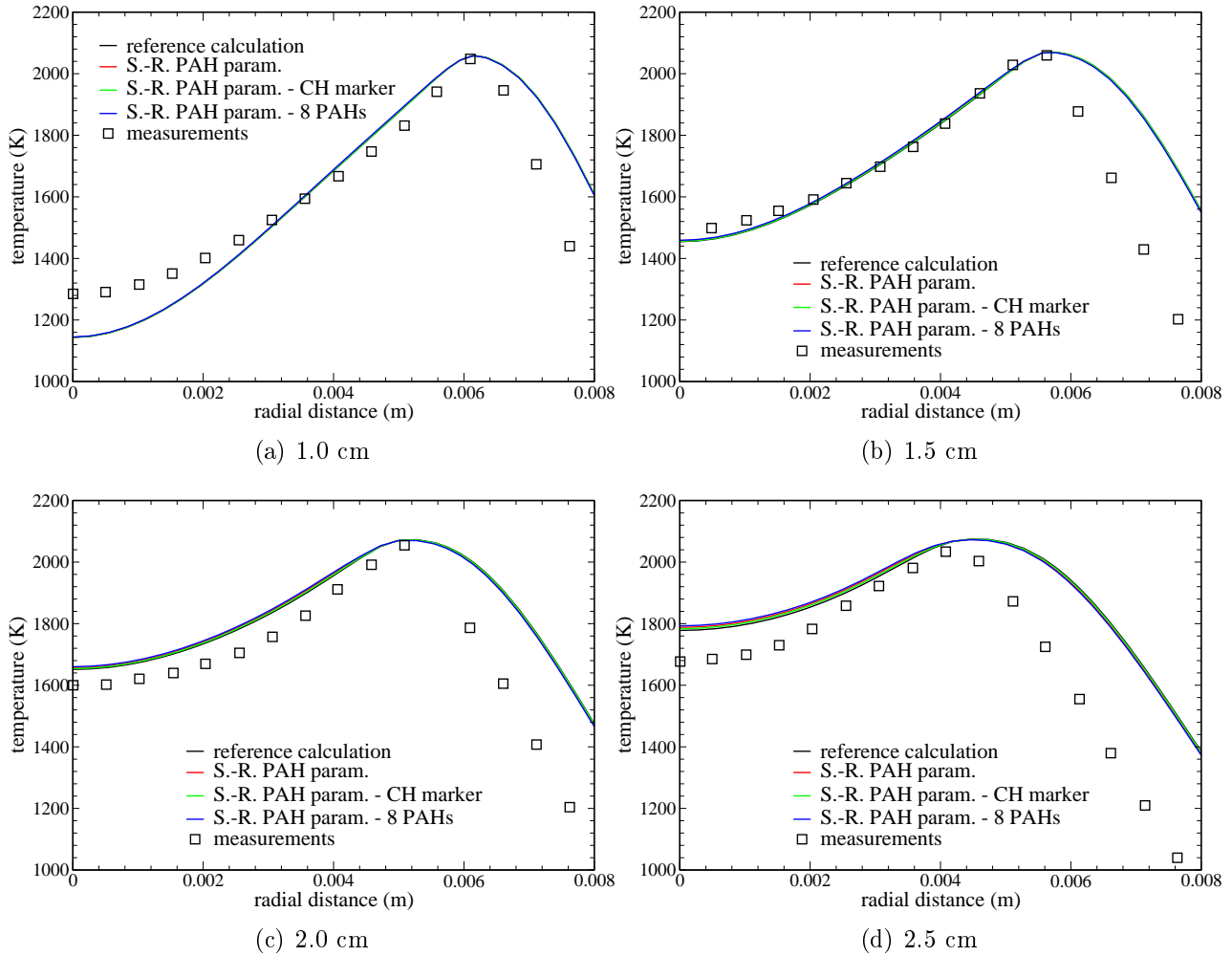


Figure 3.4.7: Temperature profiles at several heights above burner of the sooting methane/air flame of Smooke et al. [179].

distances of 1.0, 1.5, 2.0, and 2.5 cm above the burner. In Fig. 3.4.7 temperature profiles are given for simulations using the parameters summarized in Table 3.4. Since the amount of soot is small, changes in the soot model parameters have no significant impact on these profiles, and CH_4 plots (Fig. 3.4.8) show a similar trend.

The temperature profiles of Fig. 3.4.7 show a fairly good agreement with the experimental results. The differences in the peak temperatures are less than 40 K at all heights and show (as expected) that radiation effects are not important. However, the calculated peak locations do not shift towards the axis as in the experiments. As before in case of a non-sooting flame (see Section 2.5) the greatest discrepancies are found along the axis where the temperature is underpredicted near the burner (at 1.0 and 1.5 cm) and overpredicted further downstream (at 2.0 and 2.5 cm). Since the simulated stoichiometric line reaches the axis at a height of 3.5 cm, all measuring stations lie in the fuel-rich region, where the temperature increases with increasing height. Thus, these discrepancies may be due to a poor description of the fuel-rich chemistry. On the fuel-lean side the temperature slope, which results from the equilibrium between reactions and molecular transport, is well reproduced. Nevertheless, the flame thickness is significantly overpredicted. Since a grid convergence study has been performed for a similar

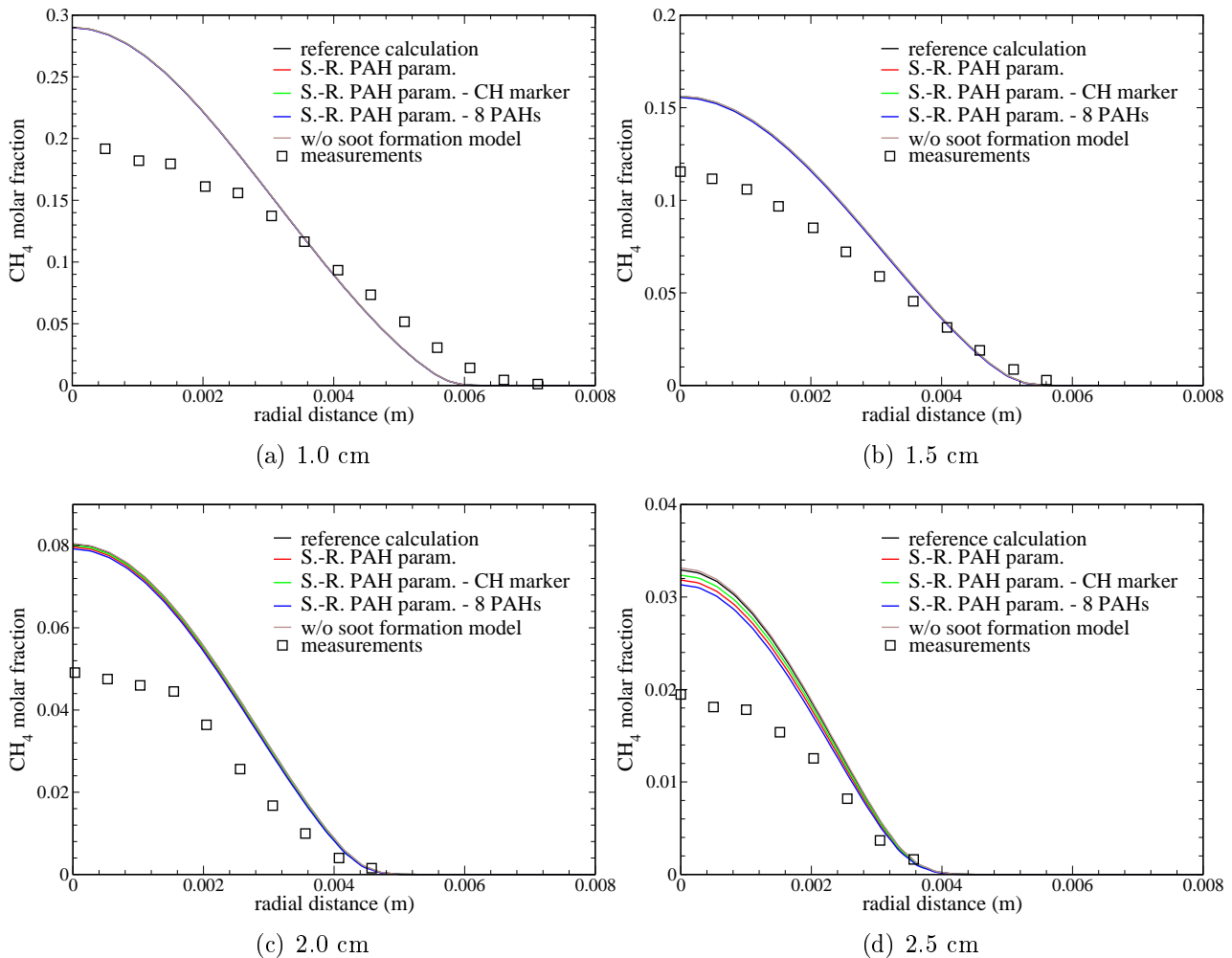


Figure 3.4.8: Methane profiles at several heights above burner of the sooting methane/air flame of Smooke et al. [179].

flame (see subsection 2.5.2), discretization errors are unlikely to be the cause of this discrepancy. Instead, confinement effects (see Section 2.5) may play a role. The external recirculation zone may push the flame towards the burner and therefore it may also be responsible for the shift of the peaks.

Figure 3.4.8 shows that the predicted rate of fuel depletion is too low. The differences between simulations are relatively small and only appear at the highest measurement station. Therefore, these discrepancies can not be attributed to the soot model but they may be related to bad temperature predictions, and even if overpredicted temperature profiles should yield a faster methane pyrolysis.

The profiles for the key species of the soot formation model (acetylene and benzene) are plotted in Figs. 3.4.9 and 3.4.10. The parameter variation now shows a significant impact on the plots, since these species are directly involved in soot production. The agreement with the experimental data is very good at locations where a good agreement for the temperature is observed. This highlights the high sensitivity of the C_2H_2 and C_6H_6 formation paths to the temperature. Moreover, even if the benzene formation paths of D'Anna and Kent [45] are included, benzene concentrations are underpredicted at most locations, regardless of the local

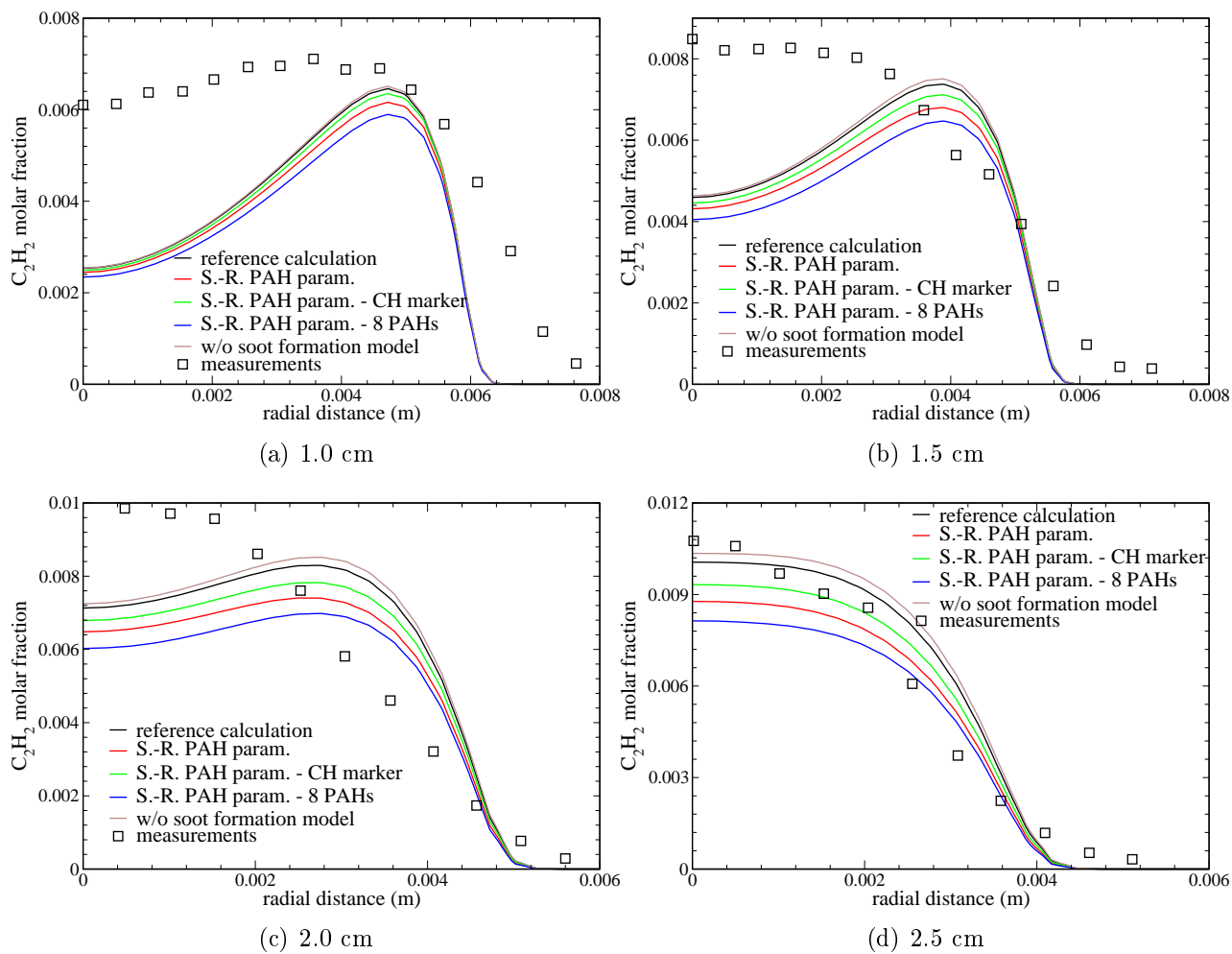


Figure 3.4.9: Acetylene profiles at several heights above the burner of the sooting methane/air flame [179].

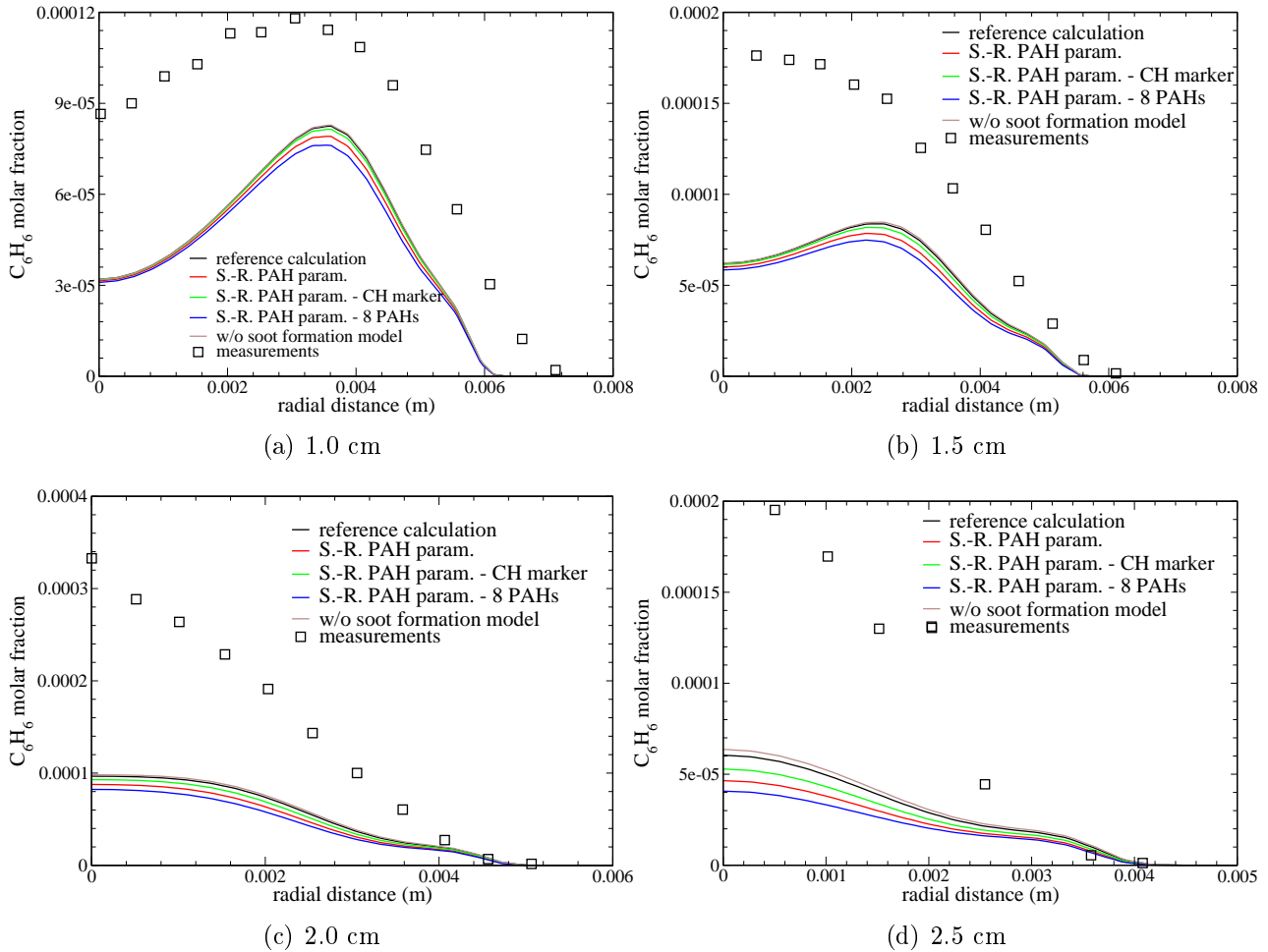


Figure 3.4.10: Benzene profiles at several heights above the burner of the sooting methane/air flame of Smooke et al. [179].

thermodynamic conditions. Probably the skeleton mechanism adopted is not able to describe reaction paths of C_4 - C_6 hydrocarbons correctly. Nevertheless, it should be observed that soot particles are formed in a thin layer near the stoichiometric line (see Fig. 3.4.6), where both temperature and main species profiles are in good agreement with the experiment. This means that the finite-rate combustion model provides a good basis for the soot model validation.

Soot volume fraction profiles are shown in Fig. 3.4.11. In comparison with the experimental data the model is able to reproduce the main features of the soot formation. Concerning the influence of the model parameters, the greatest impact comes from the Arrhenius coefficients used. The maximum soot concentration is changed by a factor of five if the Skjøt-Rasmussen [177] parameters are used. On the other hand, the reaction marker plays only a marginal role, despite the fact that H and CH concentrations differ by more than three orders in magnitude ($[H]^{max} \simeq .02 \frac{\text{moles}}{\text{m}^3}$, $[CH]^{max} \simeq 10^{-5} \frac{\text{moles}}{\text{m}^3}$). Concerning the number of PAH classes, the results are consistent with the simulations of the zero-dimensional reactor. The soot formation rate increases with an increasing number of classes even if the soot concentration peaks occur at similar locations.

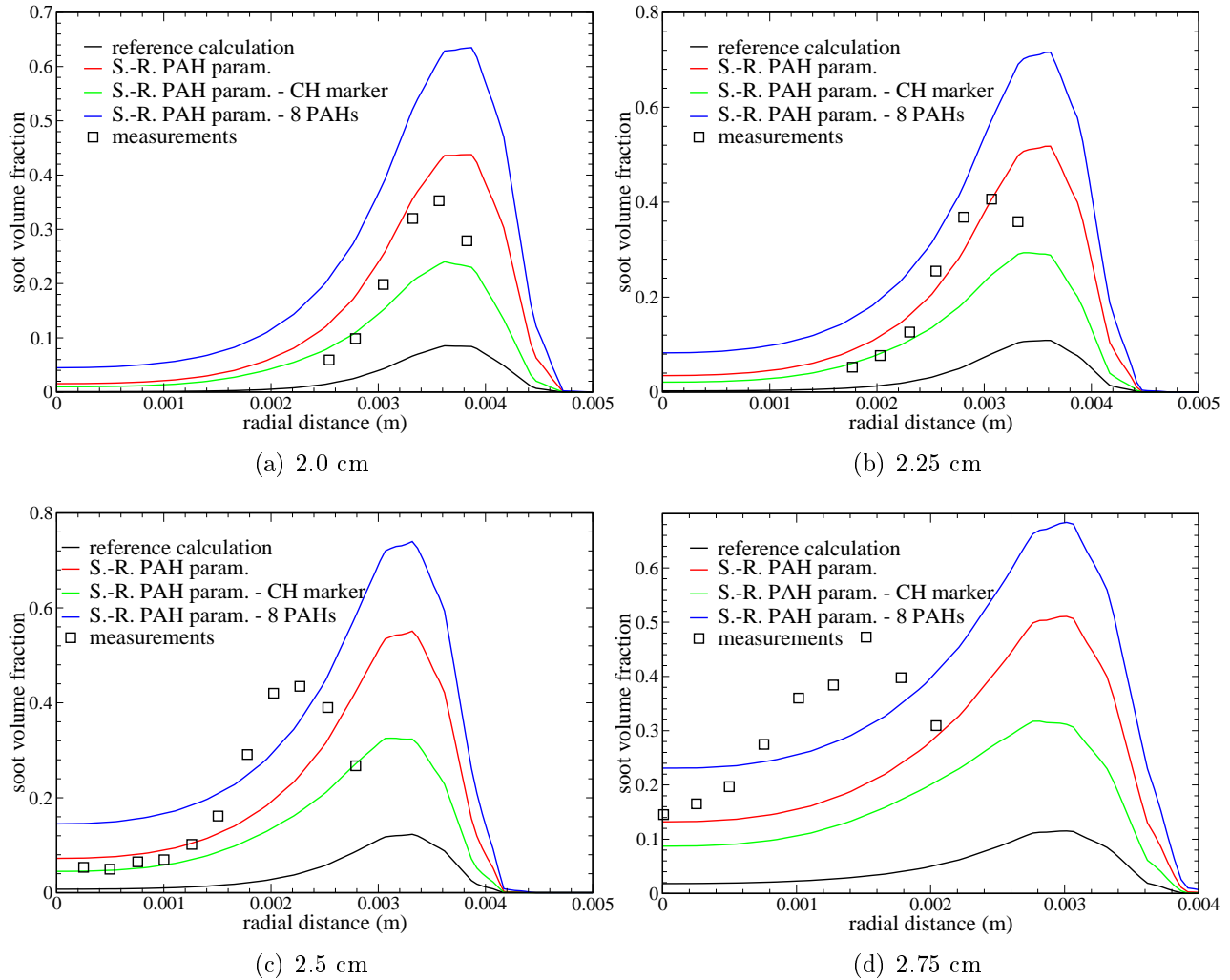


Figure 3.4.11: Soot volume fraction profiles at several heights above the burner of the sooting methane/air flame of Smooke et al. [179].

The radial shift of the peak values already observed before are confirmed by the discrepancies in soot quantities. With increasing distance from the burner the numerically predicted peaks are shifted more and more outwards in radial direction. This trend is not observed in the experiment and may be related to the boundary condition. Moreover, the underpredicted acetylene and benzene concentration may limit the PAH formation and the subsequent soot nucleation rates along the centerline. Similar discrepancies were also found by Smooke [179] and in the work of Kennedy et al. [103] whereas D'Anna and Kent propose a model which does not suffer from this problem [46].

In summary it has been shown that the soot model is able to give a reasonable description of the physical phenomena involved. The model parameters used in simulation 2 (see Table 3.4) provide the best agreement with experimental data and thus are adopted in the next sections.

Table 3.5: Boundary conditions for the sooting ethylene/air flame [131].

	radius(mm)	composition	temperature(K)	velocity($\frac{m}{s}$)
air inlet	54.0	O ₂ : 0.23 N ₂ : 0.77	300.	.338
fuel inlet	6.0	see Table 3.6	300.	see Table 3.6
wall	-	zero gradient	300	0
outflow	-	zero gradient	zero gradient	zero gradient
axis	-	zero gradient	zero gradient	zero gradient

3.5 Premixing effects on soot formation rate for a coflow, ethylene/air diffusion flame

A laminar, partially-premixed, ethylene/air diffusion flame is simulated in order to study the premixing effects on the soot formation. The chosen testcase has been investigated experimentally by McEnally and coworkers [131]. The flame is confined and the geometry is similar to the one presented in Fig. 2.5.1. Main difference is a metallic plate which partially covers the coflow in order to increase the flame stability [131]. In the experiments the premixing rate ranges from ∞ (pure fuel) to 3 (the lower limit at which flashback issues occur). The boundary conditions are given in Table 3.5. Fuel velocity and compositions change with the stoichiometric ratio as listed in Table 3.6. For both inlets (fuel and coflow) the N₂ and C₂H₄ volumetric flows are kept constant. With an increasing degree of premixing the additional oxygen increases the bulk velocity. The used kinetic scheme consists of 63 species and 338 reversible reactions, derived from the work of Appel et al. [4] by dropping all reactions involving species with molecular weights higher than benzene. Concerning the soot model, four PAH classes are used and the model parameters given in Table 3.1. PAH formation and growth are calculated with the parameter of Table 3.4.

3.5.1 Premixing effects on the flame structure

Temperature fields for different values of ϕ are plotted in Fig. 3.5.1. The flame length, defined as the location along the axis where the temperature reaches its maximum, is clearly affected by the premixing. Table 3.7 and Fig. 3.5.2 give a comparison between the corresponding experimental and numerical values. The general trend is well reproduced even if some discrepancies are evident. For nearly pure fuel conditions the flame length is underpredicted whereas at lower ϕ it is overpredicted. Concerning the $\phi = \infty$ case, the predicted flame length is in good agreement with the simulations performed for a methane flame in the previous subsections (2.5 for a non-sooting and 3.4.2 for a sooting flame). The similar variation of the flame length with the degree of premixing shows that overall interaction between chemistry, convection and transport

Table 3.6: Fuel inlet conditions for the sooting ethylene/air flame [131].

ϕ	composition	velocity ($\frac{m}{s}$) ¹	ϕ	composition	velocity ($\frac{m}{s}$) ¹
∞	C ₂ H ₄ : 0.306 O ₂ : 0.0 N ₂ : 0.694	.108	6	C ₂ H ₄ : 0.174 O ₂ : 0.100 N ₂ : 0.726	.189
24	C ₂ H ₄ : 0.258 O ₂ : 0.037 N ₂ : 0.705	.128	4	C ₂ H ₄ : 0.144 O ₂ : 0.124 N ₂ : 0.732	.228
12	C ₂ H ₄ : 0.223 O ₂ : 0.063 N ₂ : 0.714	.148	3	C ₂ H ₄ : 0.122 O ₂ : 0.140 N ₂ : 0.738	.268

¹ The bulk velocity is given and a fully-developed laminar flow is assumed.

Table 3.7: Comparison between predicted and measured flame length of sooting ethylene/air flame [131].

ϕ	∞	24	12	6	4	3
H_{sim} (mm)	70.58	69.02	69.02	64.50	60.25	54.96
H_{exp} (mm)	71.5	69.8	67.3	61.8	56.9	52.5

phenomena is well described. The systematic shift may be caused by preheating effects, which become more important if the flame becomes shorter.

In the non-premixed or slightly premixed cases the smooth temperature increase along the axis is caused by the fuel pyrolysis which is a slow endothermic process. On the other hand, an increased amount of oxygen in the fuel yields a second flame front near the burner and the temperature increase takes place in a thin layer. For the same reasons the fuel burning rate is higher and the maximum temperature along the flame's wings is reached sooner. Such a behavior has already been observed by other researchers [8, 161] and similar results are reported by Bennet et al. [17].

Acetylene and benzene plots are shown in Figs. 3.5.3 and 3.5.4, respectively. The two species have a different behavior with respect to premixing. The acetylene concentrations decrease as the premixing degree increases, since most of the species concurring in the C₂H₂ formation are oxidized faster into stable products. On the other hand, the benzene production is enhanced by an increase in premixing, even in case of shorter residence times due to an enhanced combustion rate. A similar trend has been found in measurements [131] although the highest concentrations are shifted towards less premixed cases.

The soot volume fraction and the soot particle density number are plotted in Figs. 3.5.5 and 3.5.6, respectively. Both quantities are strongly affected by the degree of premixing. The

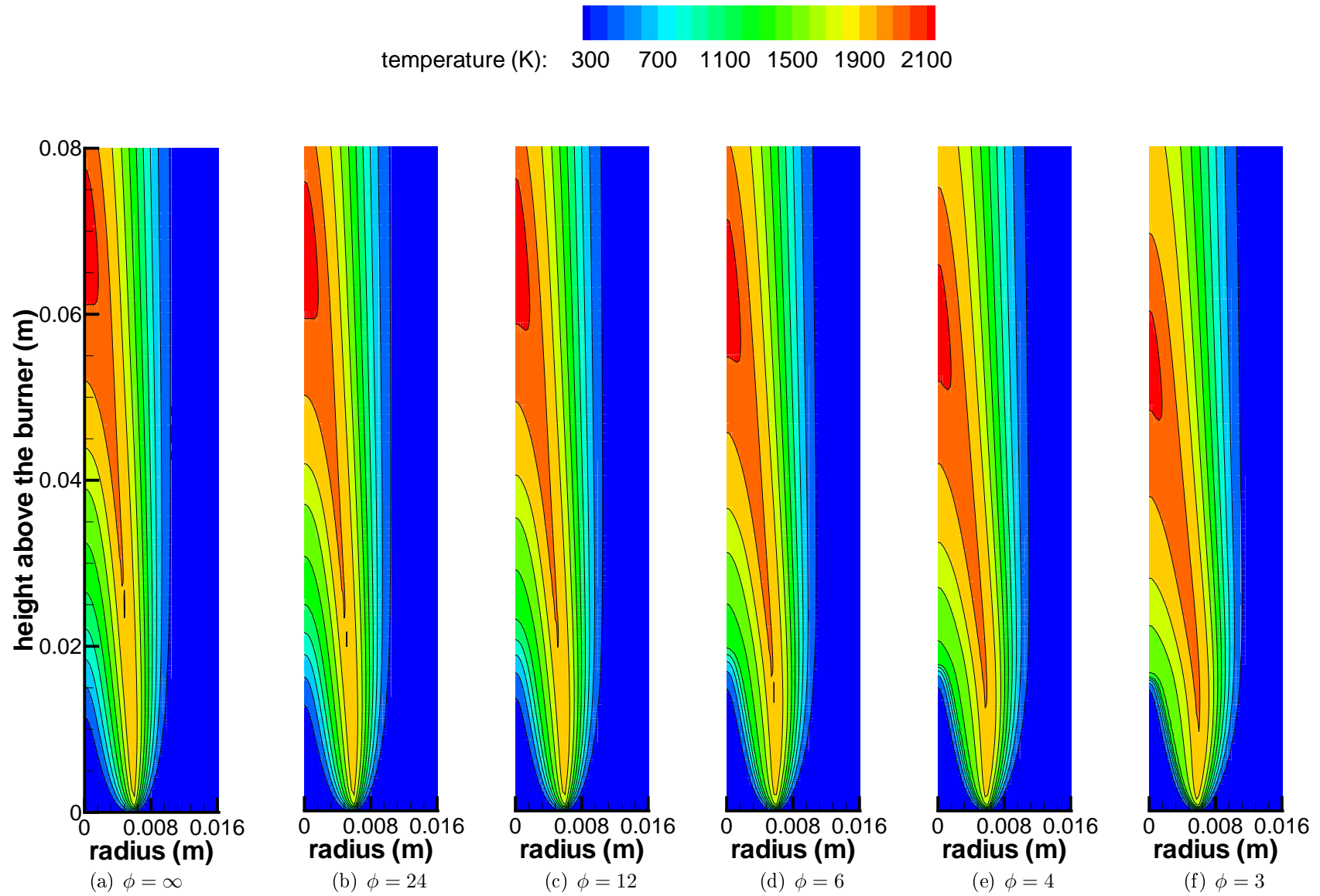


Figure 3.5.1: Premixing effects on the temperature field of sooting ethylene/air flame [131].

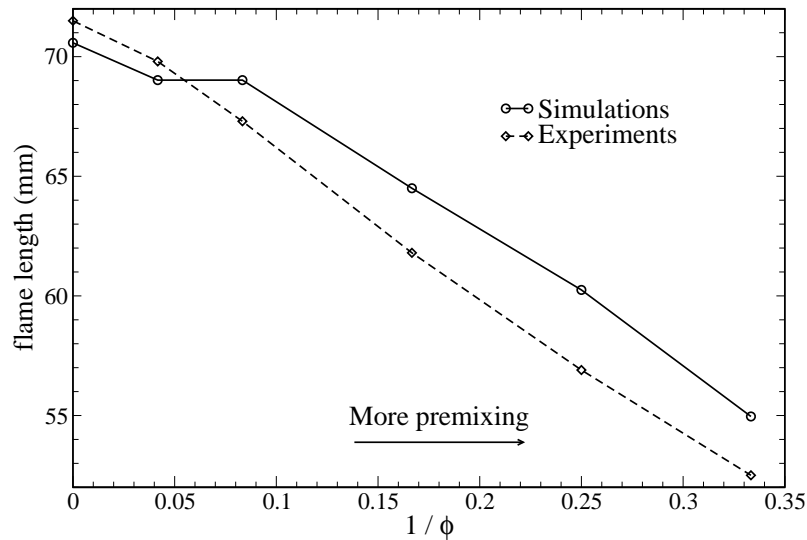


Figure 3.5.2: Flame length as function of premixing for the sooting ethylene/air flame [131].

comparison of Fig. 3.5.5 with Figs. 3.5.3 and 3.5.7 shows that the acetylene concentrations correlate well with the soot volume fractions. This is a further proof that the major contribution to soot mass is given by the acetylene addition. The soot particle density number does neither have a monotone behavior with respect to premixing nor have a strong correlation with the benzene concentration.

Figure 3.5.6 shows that there are several regions where soot formation takes place and that their extension is affected by the degree of premixing. Under pure-fuel conditions or with small amounts of oxygen, favorable conditions for soot formation and growth are found only in the wings of the flame. The second region, located around the axis, is too close to the stoichiometric line and the soot oxidation takes place well before the soot particles have reached a considerable mass [47]. At lower stoichiometric ratios both zones merge into a single layer.

3.5.2 Effects of soot radiation

If the soot volume fraction rises above the ppm-threshold, radiation effects may become important and affect the flame structure. Since, the amount of soot predicted in most non-premixed testcases is significantly above this empirical limit, a sensitivity study with respect to the influence of radiation is performed. A simple radiation model for gases which are considered optically thin [113] is used in order to take soot radiation losses into account. Self-absorption effects are neglected and soot radiation is modeled by a volumetric source term

$$q_R = C_R f_v T^5 \quad (3.5.1)$$

in the enthalpy equation (2.1.7). The exponent in Eq. (3.5.1) takes the black-body theory ($\propto T^4$) and the variation of the soot radiation spectrum with the temperature ($\propto T$) into account. The choice of the constant C_R is not unambiguous and different values are used in the literature [44, 76, 78]. Additionally, optically-thin radiation models are known to overpredict the radiation losses near the centerline, where self-absorption effects may become important.

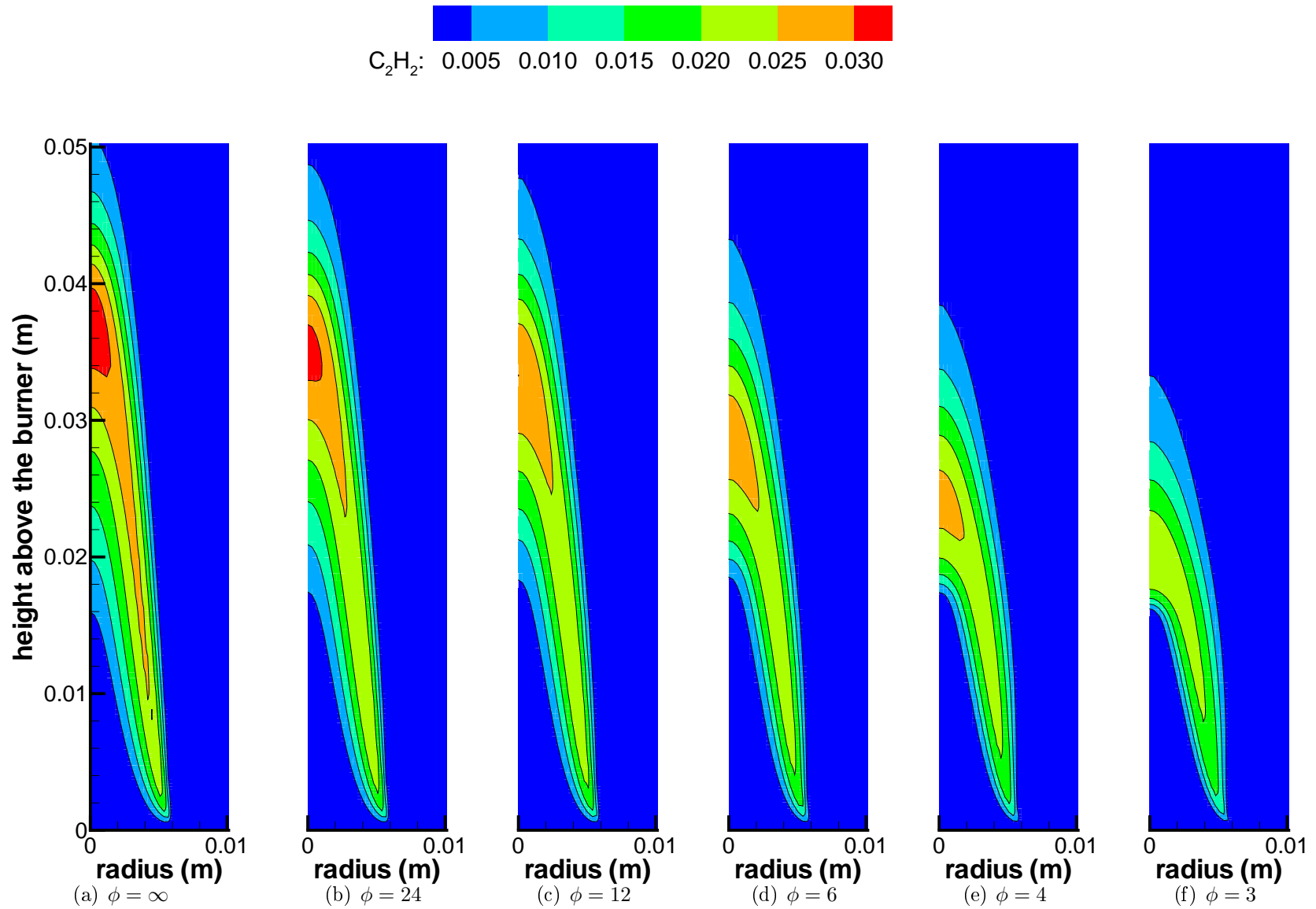


Figure 3.5.3: Premixing effects on the C₂H₂ molar fraction of McEnally's ethylene/air sooting flame [131].

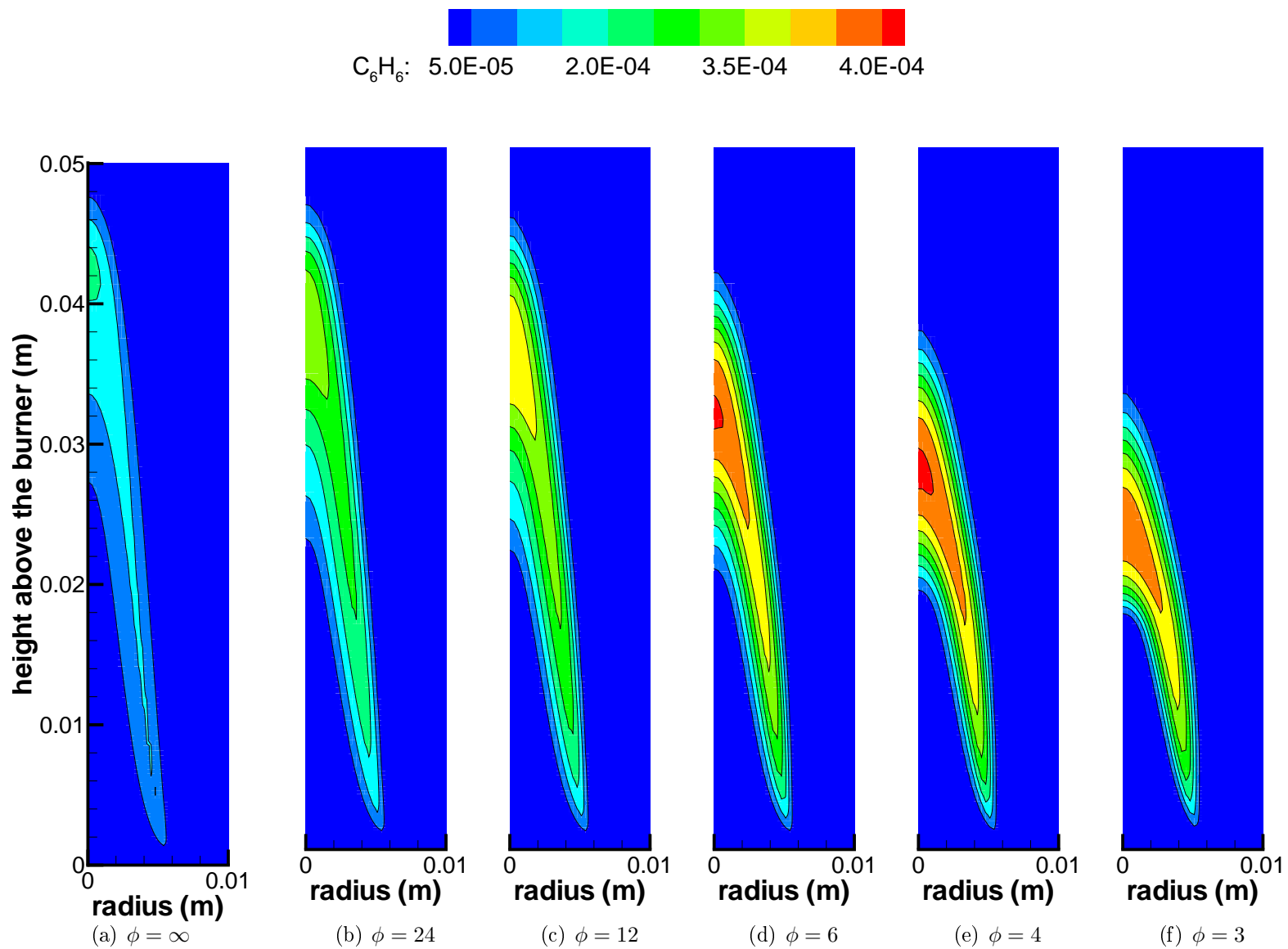


Figure 3.5.4: Premixing effects on the C_6H_6 molar fraction of McEnally's ethylene/air sooting flame.

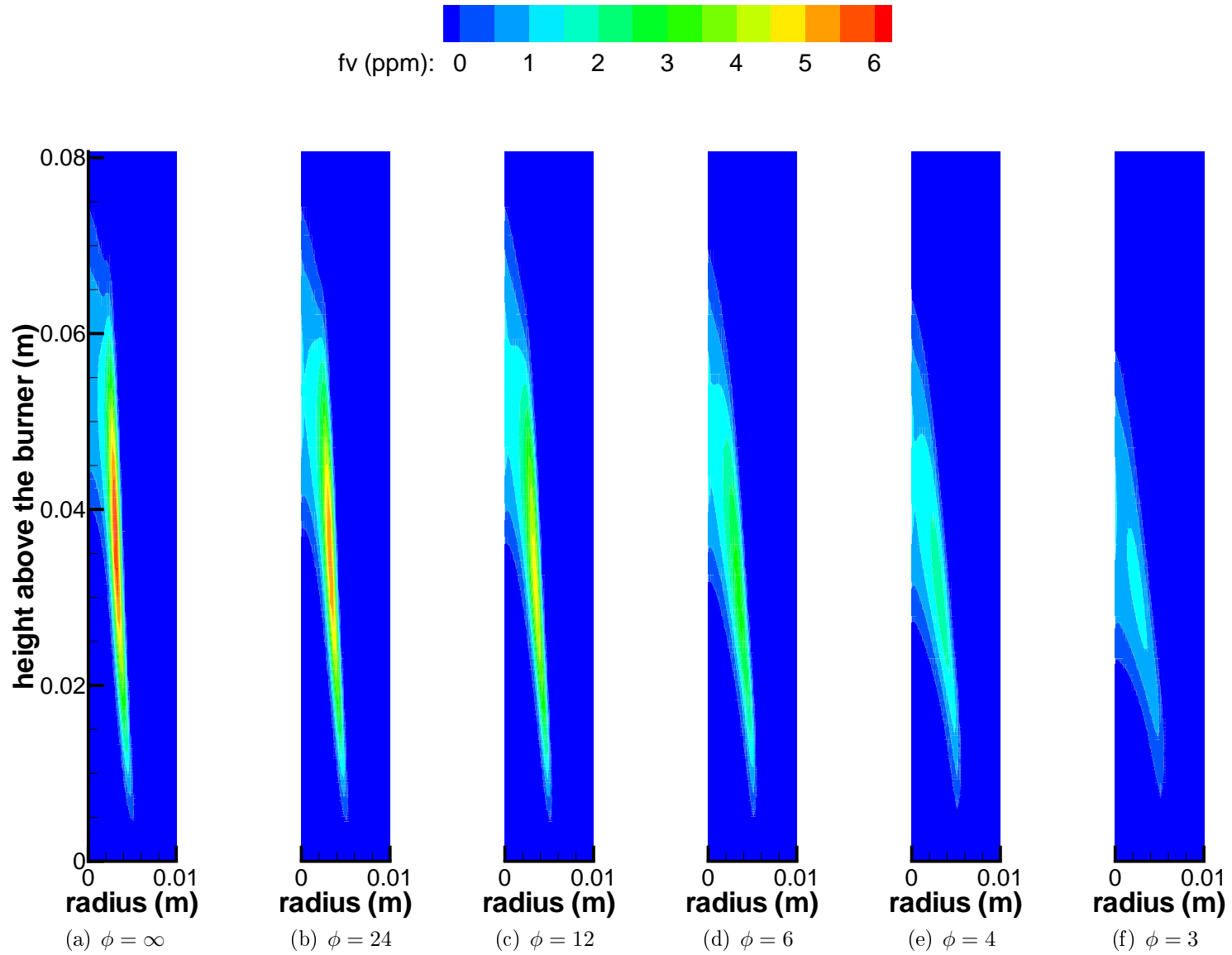


Figure 3.5.5: Premixing effects on the soot volume fraction of the McEnally's sooting ethylene/air flame [131].

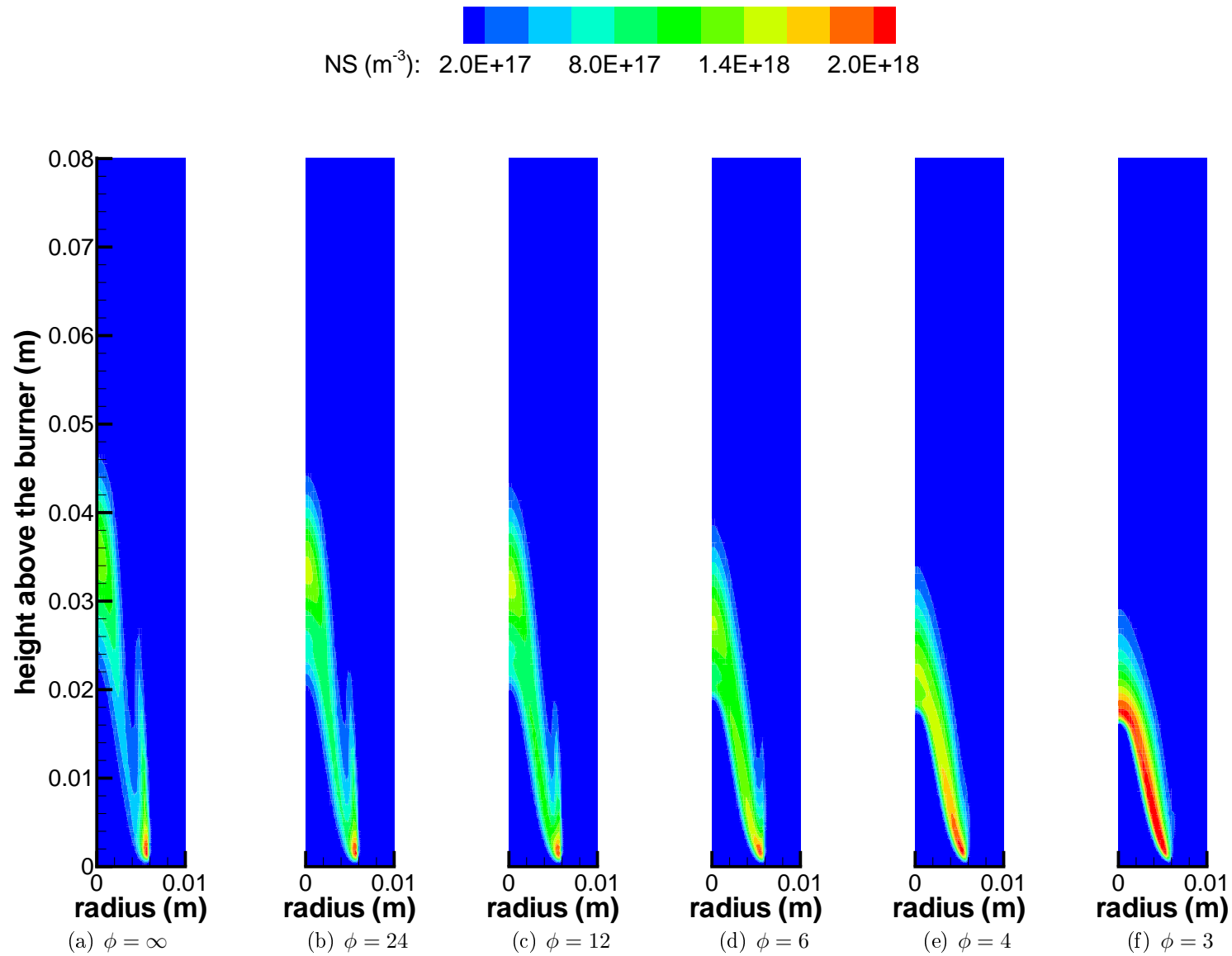


Figure 3.5.6: Premixing effects on the soot particle density number of the McEnally's ethylene/air sooting flame.

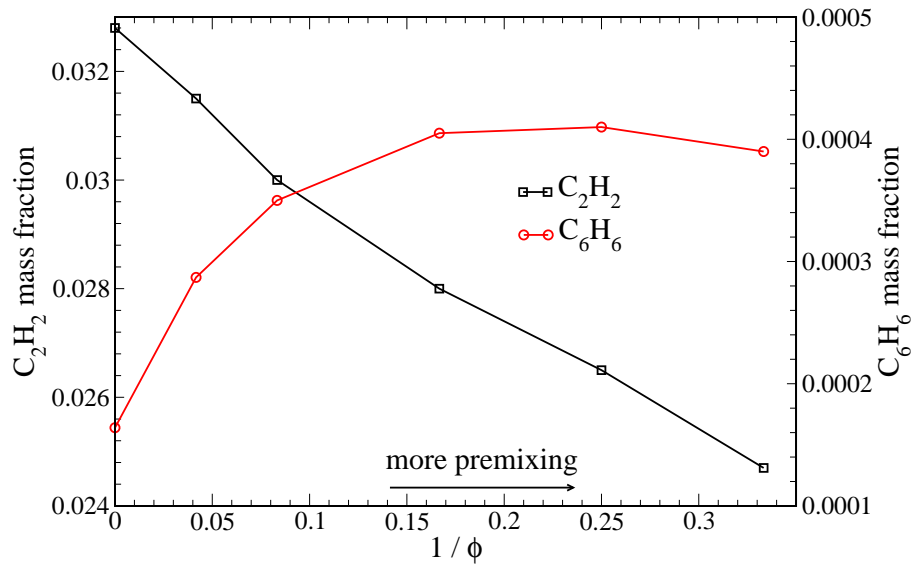
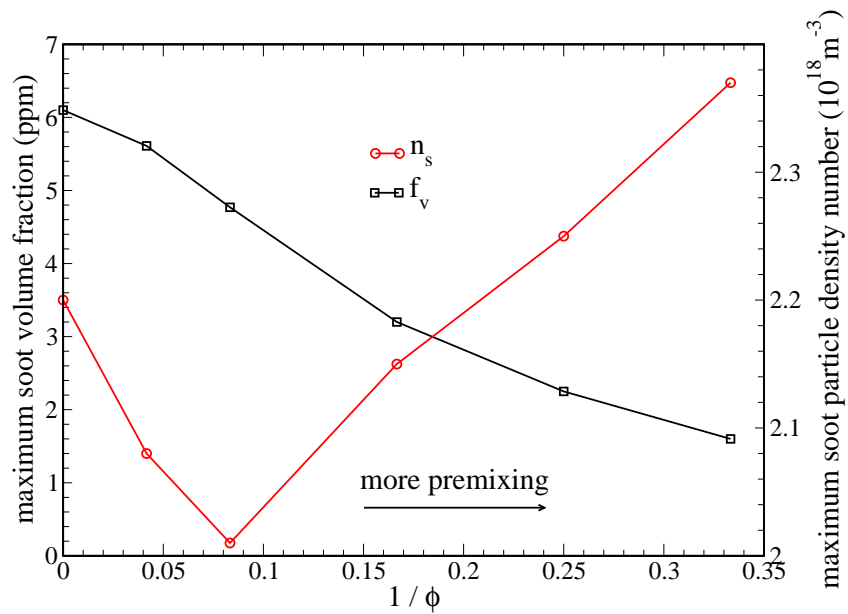
(a) C_2H_2 and C_6H_6 (b) f_v and n_s

Figure 3.5.7: Maximum soot volume fraction and maximum soot particle density number as function of premixing for the McEnally's sooting ethylene/air flame [131].

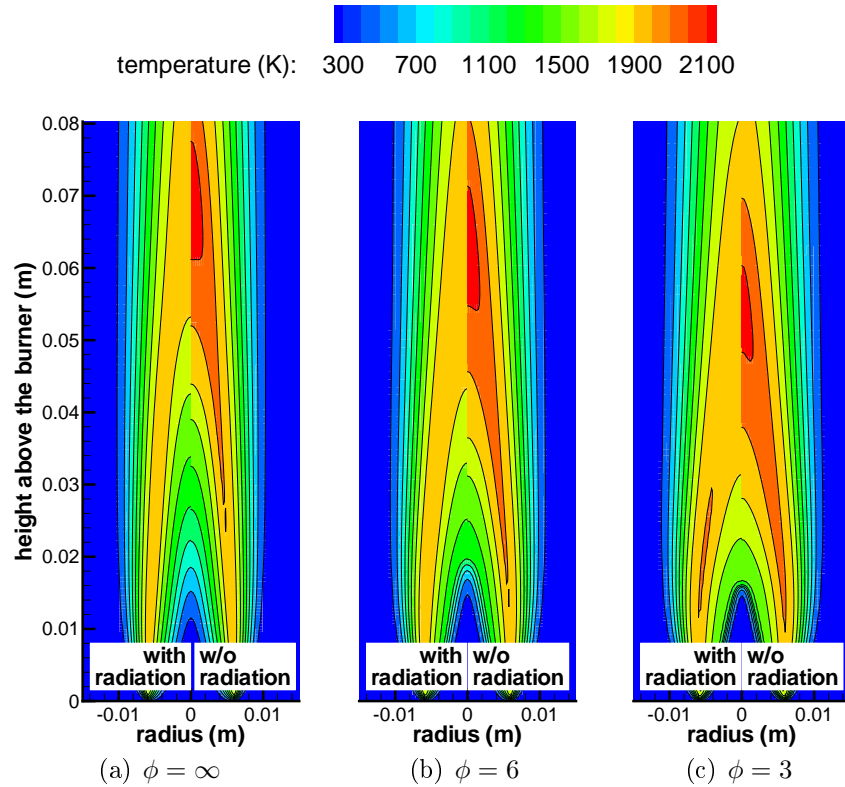


Figure 3.5.8: Influence of radiation on the temperature field of the sooting ethylene/air flame [131].

Since the comparison with experimental data will be performed in terms of axial profiles,

$$C_R = 10^{-4} \frac{\text{kJ}}{\text{s m}^3 \text{K}^5} \quad (3.5.2)$$

is chosen to reproduce roughly the same peak temperature at $\phi = \infty$, which represents the most sooting case (see Fig. 3.5.5).

In Fig. 3.5.8 temperature fields calculated with and without radiation are compared for several stoichiometric ratios. Temperature does not peak at the axis when radiation is included. Moreover, the temperature drop is more pronounced for the most sooting cases (i.e. $\phi = \infty$) and the temperature rise along the axis is slowed down.

The comparison in terms of soot volume fraction is given in Fig. 3.5.9 for the same stoichiometric ratios. The soot formation pattern is not affected by the radiation whereas the maxima (in the insets between brackets) are. This behavior is consistent with the sensitivity of the soot model to temperature shown in the previous section. Since the radiation losses decrease the mixture temperature in the soot-rich regions, the growth process is inhibited and lower soot concentrations are achieved. On the other hand, the radiation term does not seem to affect the soot concentration along the axis because of the short residence times of the soot particles in this region.

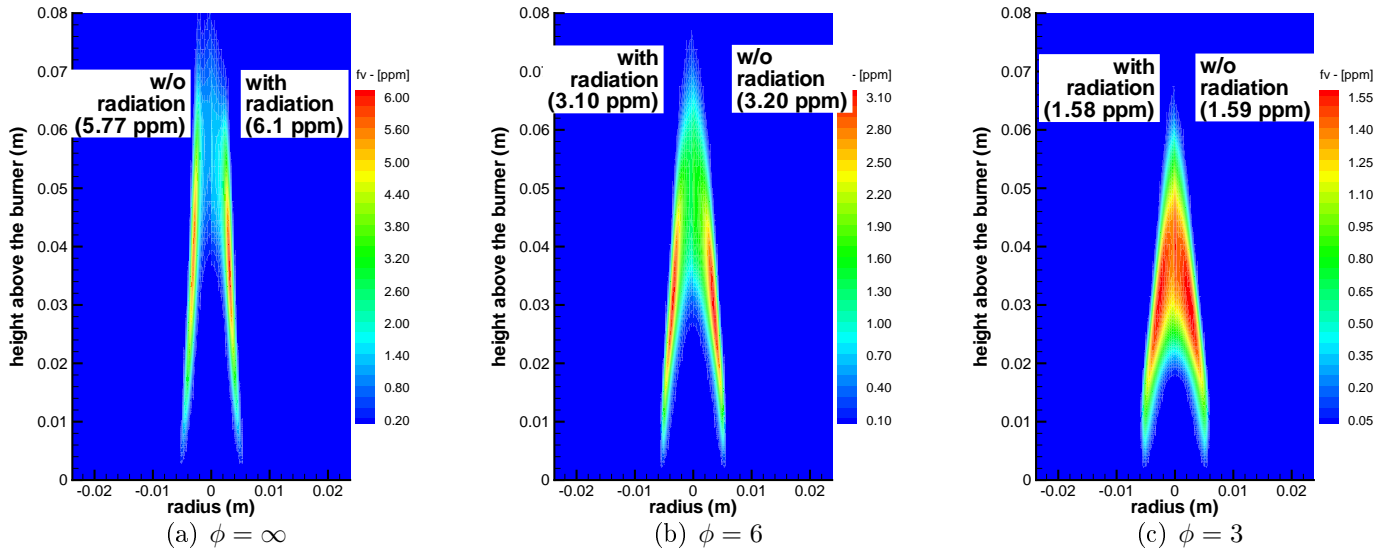


Figure 3.5.9: Influence of radiation on the soot volume fraction field of the sooting ethylene/air flame [131]. Maximum soot concentrations are given in brackets.

3.5.3 Comparison with experimental data

Temperature and species profiles are shown in Figs. 3.5.10-3.5.13. The case $\phi = \infty$ includes an additional simulation where the fuel inlet temperature is set to 450 K, in order to have a rough estimation of the preheating effects.

Concerning the temperature profiles, the overall behavior is well reproduced in the whole stoichiometric range and the predicted flame lengths are in good agreement with the experiments. When soot radiation is included, the profiles become flatter and the definition of the flame length is more ambiguous. The temperature drop due to radiation varies between 210 K (non-premixed) and 120 K (the most premixed flame). In most of cases the consideration of radiation losses improves the predictions, although such a simple model is not able to take the interaction between the flame wings (where most of the soot is formed) and the flame axis (where measurements are available and self-absorption effects are important) into account. For this reason at ϕ three and four best results are obtained if soot formation and radiation losses are not included.

According to similar simulations (see subsections 2.5 and 3.4.2), the chemical kinetics [4] seems to have some problems to accurately describe the heat release in fuel-rich regions. The temperature gradients are underpredicted in the non-premixed cases and overpredicted in the others. As may be seen from Fig. 3.5.10(a), an increased fuel inlet temperature improves the results near the burner only. Since the same temperature behavior is obtained downstream, it can be concluded that the inlet enthalpy is not important for the observed discrepancies. The temperature drop which takes place at about two-thirds of the flame height is not reproduced by any calculation. It can be noticed that this is more pronounced at lower premixing rates and thus may be due to soot radiation losses.

Axial methane and acetylene profiles are given in Figs. 3.5.11 and 3.5.12. All simulations without the non-premixed case predict the region where these species are produced very well.

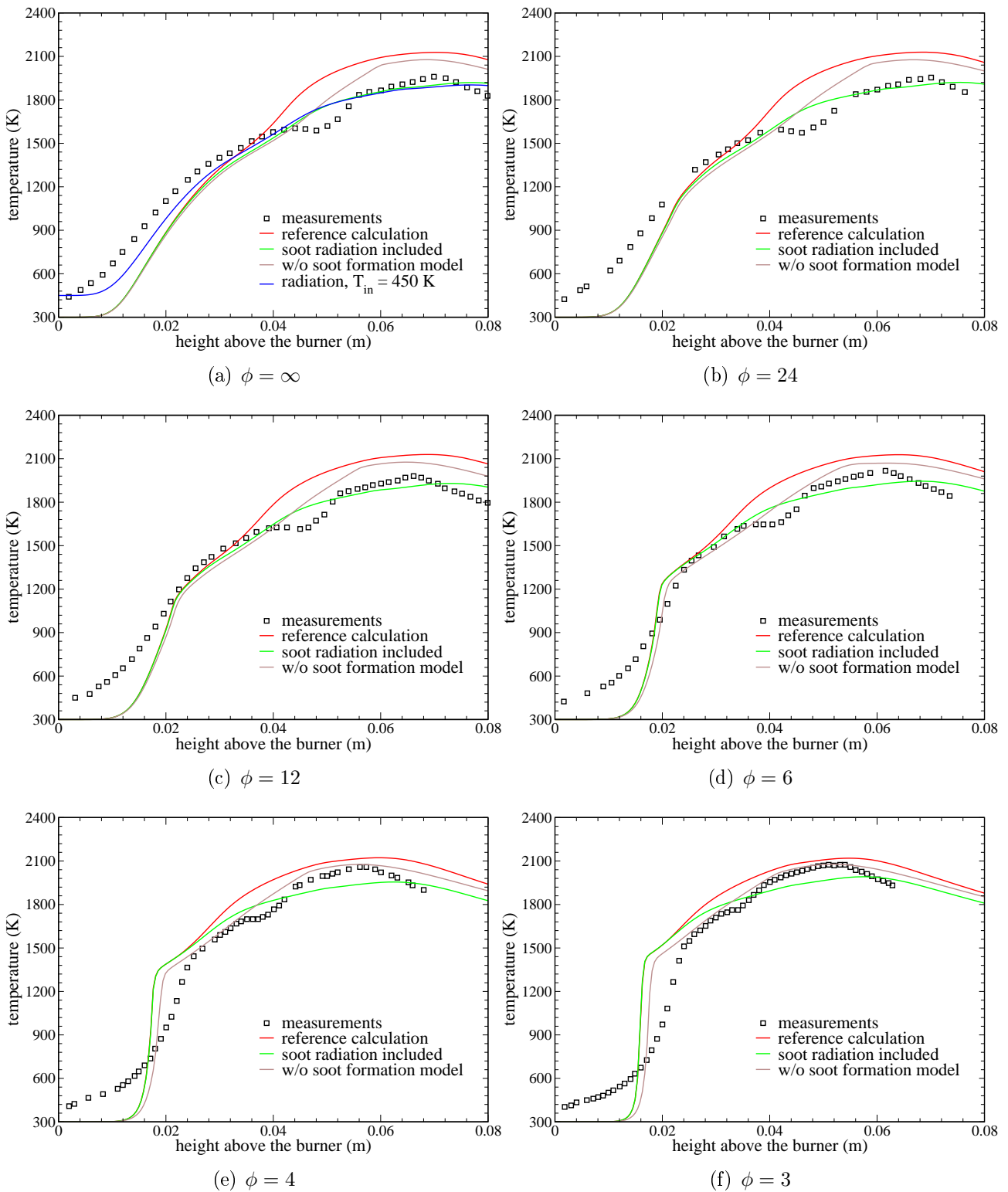


Figure 3.5.10: Axial temperature profiles comparison for the sooting ethylene/air flame [131].

The differences observed near the burner are consistent with the temperature profiles of Fig. 3.5.10 and support the hypothesis of a poor description of the fuel-rich chemistry. Concerning the overall behavior, the soot formation model plays a significant role and a better agreement is achieved if it is included. The only exception is for small values of ϕ , where the soot concentration is strongly overpredicted (see Fig. 3.5.14). The methane concentration reaches lower peak values if soot formation is considered, due to the acetylene consumption mechanism. Soot radiation losses have a minor influence on these plots. The non-premixed testcase shows a somewhat different behavior and deserves additional considerations. The methane concentration does not seem to be affected by the soot formation and the profiles are significantly wider than in the experiments. Acetylene formation is delayed whereas its peak and the successive oxidation are well predicted.

Benzene axial profiles are plotted in Fig. 3.5.13. There is a systematic underprediction for the fuel-rich cases and an overprediction in the lean ones. In all simulations but the pure-fuel one the discrepancies in the maximum benzene concentrations between numerical and experimental profiles range from 30% to 75%. Since the chemical kinetics has been initially validated against premixed flames [4], it may lack some formation and/or destruction paths which come into play in diffusion flames. The $\phi = \infty$ testcase represents the upper bound of such a deficiency, since benzene is largely underpredicted and the soot formation rate consequently underestimated.

The comparison between the measured and simulated axial profiles of soot volume fractions are given in Fig. 3.5.14. The agreement achieved here is strictly correlated to predictions of the benzene concentration. In the most sooting testcases radiation changes the soot maximum values up to 25%, whereas only minor changes are observed for a higher inlet temperature. The peak location is very well predicted which means that the phenomena behind the soot formation are captured at all stoichiometric ratios. These peaks are quite insensitive to changes in the inlet composition, as they remain constant for the whole stoichiometric range. At lower premixing rates the underpredictions are partially mitigated by the good agreement of the acetylene concentrations, as it represents the main contribution to the soot growth.

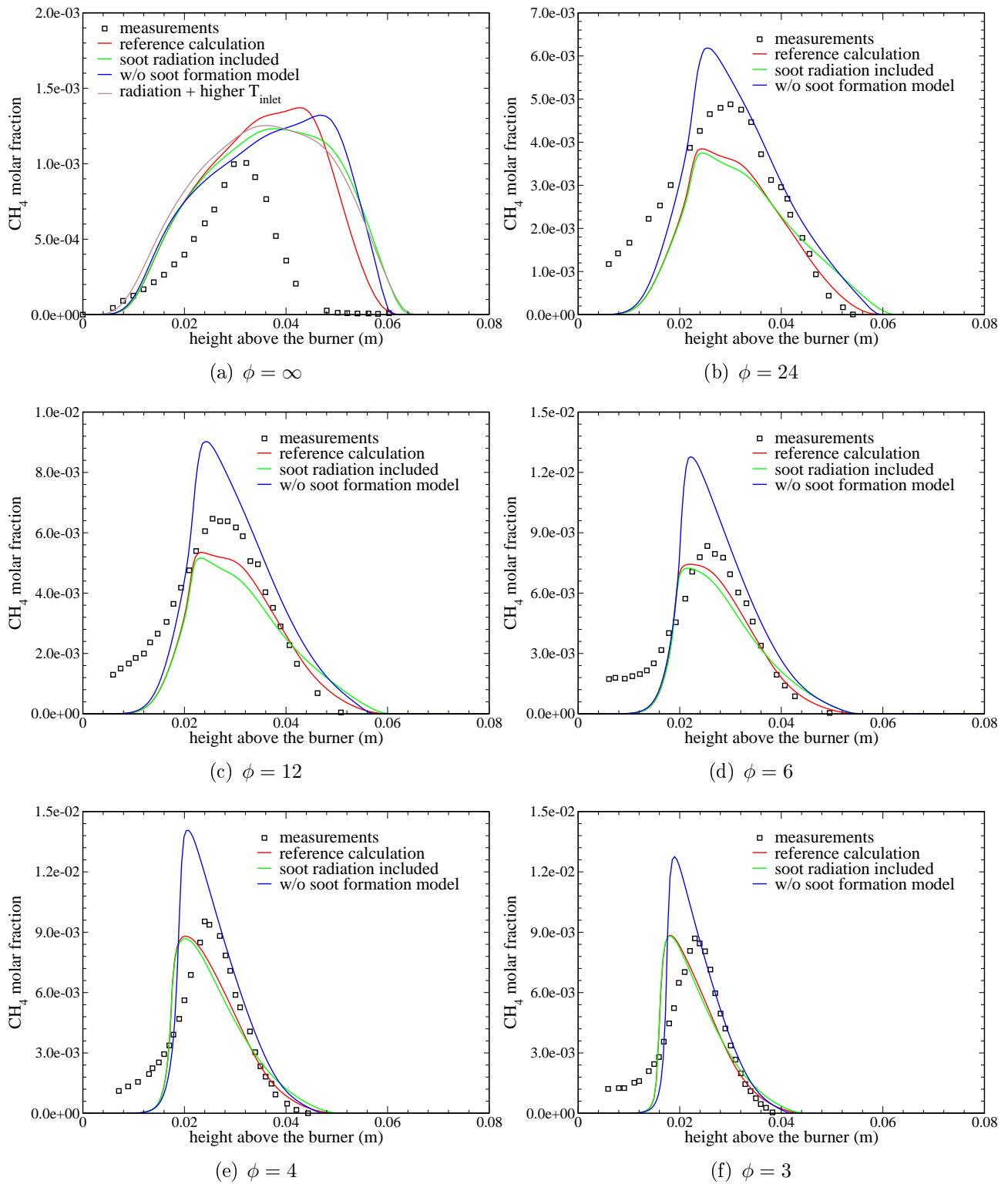


Figure 3.5.11: Axial methane profiles for sooting ethylene/air flame [131].

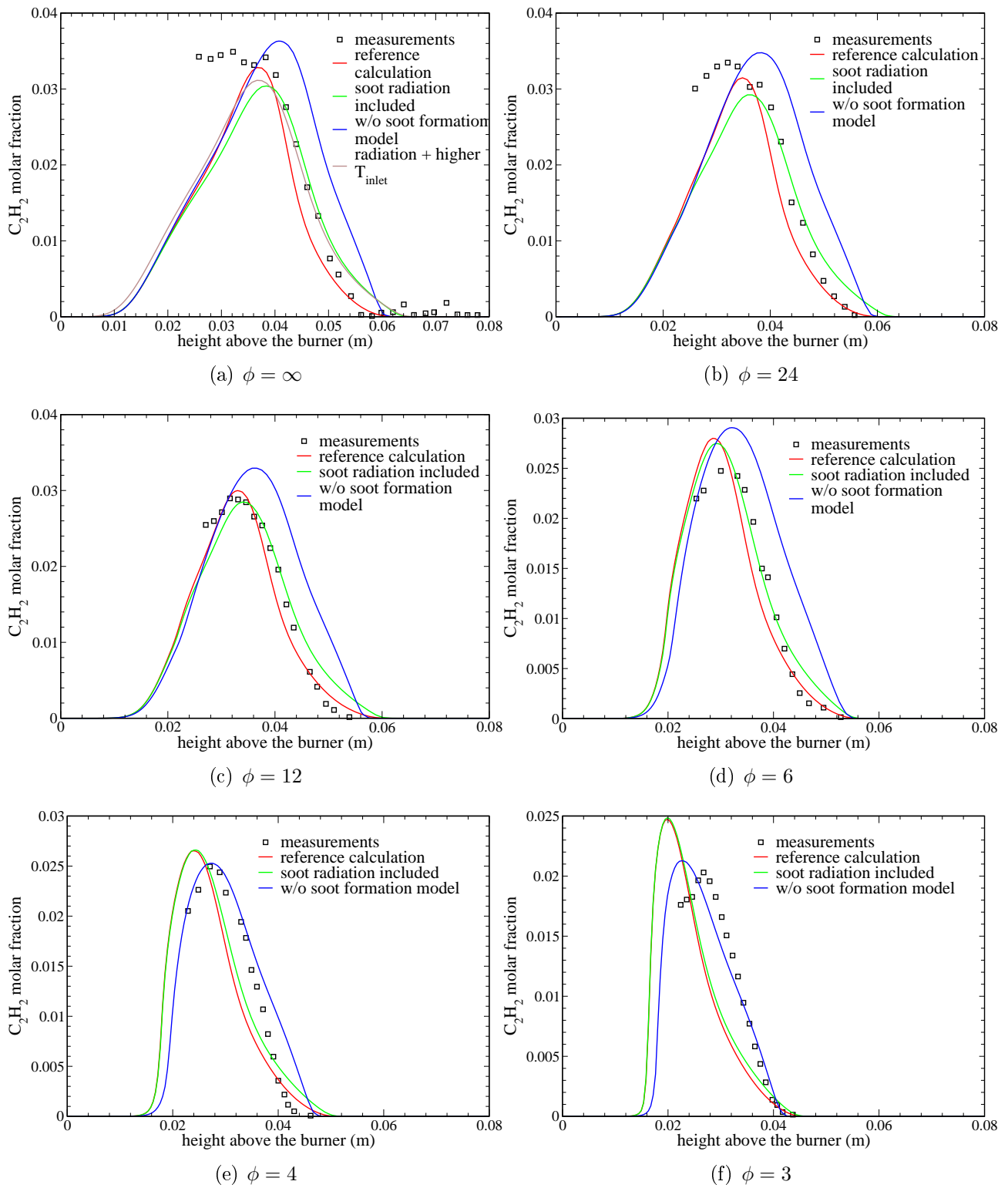


Figure 3.5.12: Axial acetylene profiles for the sooting ethylene/air flame [131].

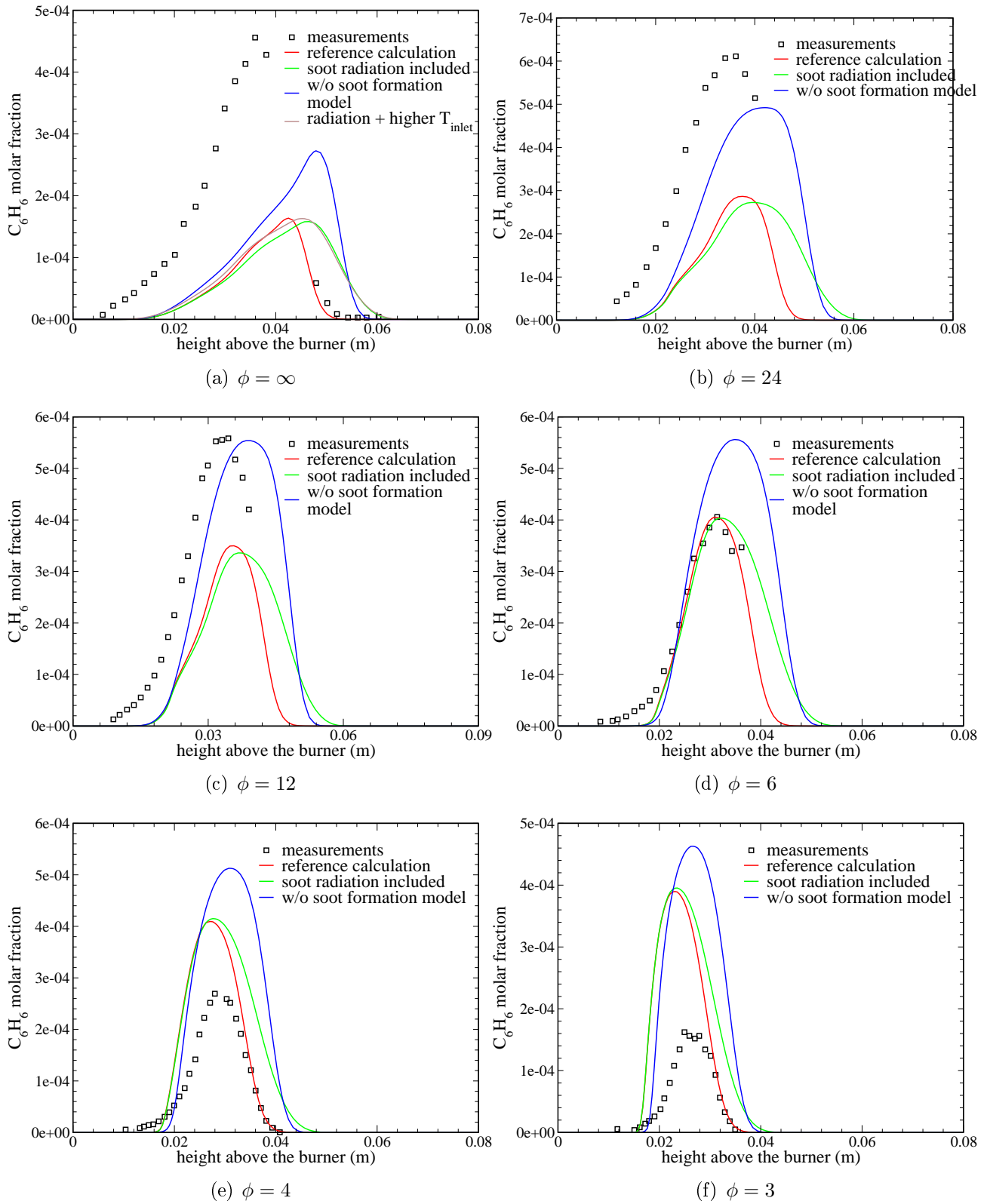


Figure 3.5.13: Axial benzene profiles for the sooting ethylene/air flame [131].

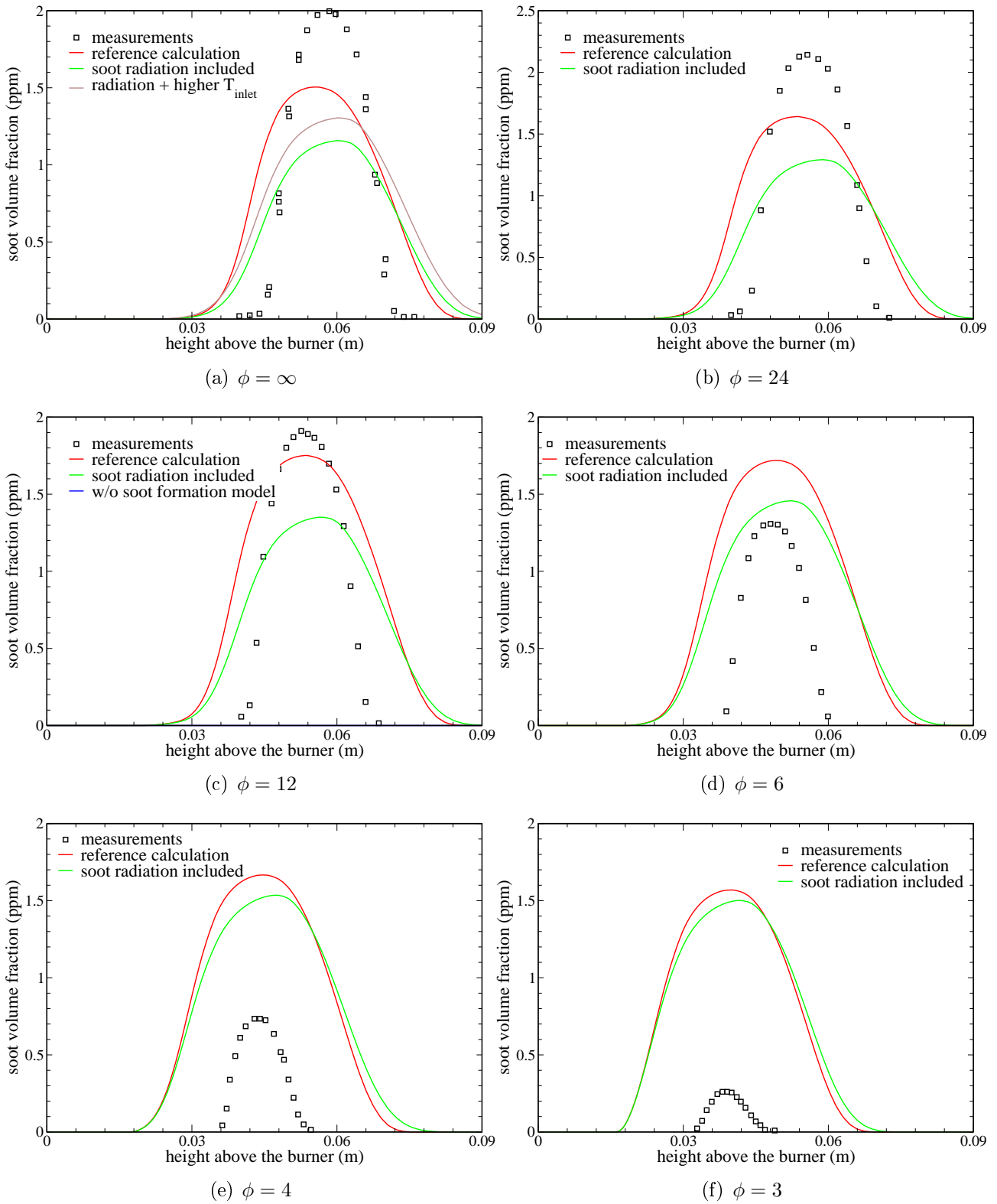


Figure 3.5.14: Axial soot volume fraction profiles for the sooting ethylene/air flame [131].

4 Chemical kinetics in turbulent flows

4.1 Phenomenological description of turbulent flows

The non-dimensional number which gives an indication about the flow regime is the so called Reynolds number

$$Re = \frac{\rho V_{in} D}{\mu}. \quad (4.1.1)$$

In the simulations presented in the previous chapters the Re number (based on the fuel pipe diameter) was below the critical limit (3000 in case of a round pipe), thus the flow can be considered *laminar*. The fluid particles flow in parallel layers and the spacial scales of the flow are in the range of the characteristic dimensions of the problem (i.d. flame length). Under these conditions, the fluid dynamic structures which need to be resolved are in a small interval around the characteristic lengths. This means that volumes into which the domain has to be discretized should not be smaller than the smallest scales. A completely different situation is found in real combustion devices, where much higher Reynolds numbers are achieved ($> 10^5$) and inertia forces prevail over viscous ones. Under such conditions the non-linear behavior of the convective terms creates smaller structures and the flow regime is called *turbulent*. The resolution of all turbulent structures in space and time for practical applications is beyond the actual computational capabilities.

A well-known behavior of turbulent flows is its inherent randomness. Any flow variable which is measured in two different realizations of the same experiment may differ because of small disturbances which are out of the researcher's control (i.e. roughness, vibrations). In order to give a practical characterization of turbulent flows, statistical treatments and averaged quantities have to be introduced. In the most general case, an averaging over a large number of realizations has to be performed. In the particular case where the boundary conditions are statistically stationary, averages can be performed over time [160]. By such a statistical treatment of the flow, small-scale details and parts of the complexity of an unsteady flow description are discarded¹.

One of the most significant effects of the turbulent structures on the averaged flowfield is the enhanced transport of momentum, energy and species in comparison to laminar flows. Macroscopic² effects may be modeled by the so-called *Boussinesq hypothesis* which introduces

¹It should be also pointed out that in most cases numerical simulations should be able to provide only such averaged flow features which are affected by these small structures but do not show them.

²The word is quoted since here it is not related to the mean molecular free path but to the problem's geometry. Even for the smallest turbulent structures the continuum hypothesis still remains valid.

an fictitious “eddy” viscosity. Under this simplification, averaged transport equations can be solved and useful information about the mean flow extracted.

In the next section the Boussinesq hypothesis will be introduced briefly in order to understand how and in which cases it can be applied. Even if this is a powerful approach, it shows significant limits in case complex non linear terms (i.e. a chemical source term) are included in the transport equations. Thus, the rest of this chapter will be devoted to the development of a strategy to close the chemical source term and achieve a coupling between chemistry and turbulent fluctuations.

4.2 Averaged transport equations

A widely accepted approach decomposes the flow variables into averages and fluctuations (also called *unresolved components* [96])

$$\psi(\mathbf{x}, t) = \langle \psi \rangle(\mathbf{x}, t) + \psi'(\mathbf{x}, t) \quad (4.2.1)$$

where the fluctuating term has zero mean

$$\langle \psi' \rangle = 0. \quad (4.2.2)$$

Since only statistically-stationary flows are considered in this work, the mean can be calculated as a time averaged quantity. In reacting flows large density variations occur and density-weighted (or Favre) averaged quantities

$$\langle \psi \rangle = \frac{1}{\langle \rho \rangle \Delta t} \int_t^{t+\Delta t} \rho \psi dt \quad (4.2.3)$$

offer advantages. The integration time Δt has to be significantly larger than the characteristic turbulent timescale. This is required in order to obtain a value for $\langle \psi \rangle$ which is independent from the chosen averaging interval.

The presented decompositions are substituted in the momentum, energy and species equations (Eqs. (2.1.4), (2.1.7) and (2.1.8)) and a time-averaging Eq. (4.2.3) is performed. The resulting transport equations contain some non-linear terms which can be divided into two groups:

- convective terms, which can be splitted into two parts

$$\langle \mathbf{V} \psi \rangle = \langle \mathbf{V} \rangle \langle \psi \rangle + \langle \mathbf{v}' \psi' \rangle \quad (4.2.4)$$

where the first one is a function of averaged variables³ only, whereas the second one requires modeling;

³The turbulence terminology refers to these terms as closed, since no additional hypothesis or models are required to calculate them.

- species source terms which are highly non-linear (see Eq. (2.2.4)) and a decomposition according to Eq. (4.2.1) would yield to a high number of high order correlations. In some works [145] some attempts to overcome this problem by using a Taylor expansion of the Arrhenius function have been made. Even if such an approach is appealing, the highly non-linear behavior of this function slows down the series's convergence [62]. Thus, it did not reach a wide use within the scientific community. It may be concluded that the Reynolds decomposition does not represent a feasible method to calculate the averaged chemistry source terms.

The closure problem plays a central role in turbulent flow since no ultimate solution exists. The closure of the convective terms is not related to combustion (even if it is affected by it) and several models have been proposed. In this work the Boussinesq hypothesis is used to link unclosed terms to the gradients of mean quantities

$$\langle \mathbf{V}'\psi \rangle = -\frac{\mu_t}{Pr_\psi} \nabla \langle \psi \rangle \quad (4.2.5)$$

where the coefficient μ_t is called “turbulent viscosity” and represents the effects of turbulent fluctuations on the mean flow field. The constant Pr_ψ takes into account that the transport of the scalar quantity ψ by turbulence depends on the scalar's nature. Assuming Eq. (4.2.5) the closure problem is not solved but shifted to the determination of μ_t . A dimensional analysis suggests that it should be calculated from characteristic turbulent length and time scales. In order to determine these quantities, many approaches exist with different degrees of complexity. Zero-equation methods (no additional equations are added to the system) have been used with success for cold, external flows [200] but a geometry-independent formulation does not exist. Two-equation turbulence models show more general properties. They are *complete*, since characteristic turbulent space and time scales can be derived without additional problem-related assumptions. In this work the extensively used standard $k - \epsilon$ turbulence model [200, 160] is employed [112]. This model should perform equally well for simple testcases and complex geometries. Transport equations are solved for the turbulent kinetic energy

$$k = \frac{1}{2} \langle \mathbf{v} \cdot \mathbf{v} \rangle \quad (4.2.6)$$

and the turbulent dissipation rate

$$\epsilon = \frac{\mu}{\rho} \langle \nabla \mathbf{v} \cdot \nabla \mathbf{v} \rangle. \quad (4.2.7)$$

The required turbulent viscosity is related to these quantities by

$$\mu_t = C_\mu \rho \frac{k^2}{\epsilon} \quad (4.2.8)$$

where C_μ is a modeling constant.

4.3 PDF approach for the calculation of averaged source terms

In any turbulent flow local statistics may be described by the Probability Density Function [59] (hereafter PDF) $f(\xi)$ for any arbitrary random variable ξ . The PDF delivers the probability $P\{\}$ that in any realization the value ψ lies between ξ and $\xi + d\xi$

$$P\{\xi \leq \psi \leq \xi + d\xi\} = f(\xi) d\xi \quad (4.3.1)$$

where ξ represents the *sample space*, the interval of possible values which ψ can assume. In the same manner, the *joint* PDF of n random variables $\Xi = \{\xi_1, \dots, \xi_n\}^T$ is the probability that any realization $\Psi = \{\psi_1, \dots, \psi_n\}$ lies between Ξ and $\Xi + d\Xi$

$$P\{\xi_1 \leq \psi_1 \leq \xi_1 + d\xi_1; \dots; \xi_n \leq \psi_n \leq \xi_n + d\xi_n\} = f(\Xi) d\Xi. \quad (4.3.2)$$

In this case the *marginal* PDF of a single variable is obtained by integration of the joint PDF in the remaining sample space

$$f(\xi_i) = \int_{\xi_j, j \neq i} f(\Xi) d\xi_1 \dots d\xi_{i-1} d\xi_{i+1} d\xi_n. \quad (4.3.3)$$

The normalization property of any PDF claims

$$\int_{\xi} f(\xi) d\xi = 1. \quad (4.3.4)$$

Since the PDF gives a complete statistical description of ξ (or Ξ) at one point, one time, local mean

$$\langle \psi \rangle = \int_{\xi} \xi f(\xi) d\xi \quad (4.3.5)$$

and variance

$$\langle \psi'^2 \rangle = \int_{\xi} (\xi - \langle \psi \rangle)^2 f(\xi) d\xi \quad (4.3.6)$$

can be calculated once the distribution is known. More important, any function which depends on the random variable ξ can be averaged in the same manner

$$\langle S(\psi) \rangle = \int_{\xi} S(\xi) f(\xi) d\xi. \quad (4.3.7)$$

Thus, if the joint PDF of temperature and composition is given, the averaged chemical source terms can be calculated exactly.

Concerning the methods for calculating a PDF, different approaches are found in the literature:

- a PDF transport equation may be solved. This method is called *transported PDF approach* [141, 158] and has revealed to be quite general yet computational expensive, in particular in reacting flows. In principle, the joint PDF may contain an arbitrary number of random variables [159], but usually only species and energy are considered [109, 120], since numerical experiments showed that in most of cases the velocity field may not affect the PDF evolution [69].
- the PDF's shape is assumed. The method is called *assumed PDF approach* which exists mainly in two different versions:
 - only a few low-order moments (i.e. mean, variance) are solved globally to obtain the PDF. The averaging process can then be performed during runtime or, more efficiently, by the use of precomputed look-up tables [64].
 - a varying number of moments is used to define “local” assumed PDF distributions, which may be based on the maximization of the entropy [157] or on the turbulence decay properties [71, 72]. This approach is likely to give a better match with the experimental results in comparison to the “global” presumed PDF method, since an arbitrary number of moments can be included [156] and non canonical PDFs represented. However, this approach is impractical and has never been used in real applications.

Since the source term is a function of $N_s + 1$ variables, the multidimensionality of the PDF prevents the use of conventional, finite volume methods for solving a transported PDF equation. Thus, different solution strategies (i.e. Monte Carlo solution methods) have to be used. Their complexity and the need to develop new algorithms are still issues and delay their use on a larger scale. The use of locally presumed PDF methods would require that expensive source term integrations are performed during runtime. Thus, in this work a globally-assumed PDF approach is chosen.

Even if there are many unresolved issues, PDF methods represent a general framework that is independent from the combustion regime under consideration. Other approaches, like strained laminar flamelets [87, 88, 154], fast chemistry, progress variable [73], or CMC [106] methods (see [24, 70] for old yet complete reviews), are based on hypothesis which are seldom satisfied in the whole domain of complex technical combustors (i.e. swirl-stabilized combustion chambers) where local extinction as well as thin and broadened reacting regions may occur at the same time [43, 128].

4.3.1 Assumed PDF formulation for reacting flows

Since a turbulence model is used to close the convective terms in the transport equations, the assumed PDF approach is employed here to average the species source terms only. In this case the joint PDF should include the temperature T and species mass fraction vector \mathbf{Y} . Due to the intrinsic difficulties in the formulation of cross-correlation terms, up to now the assumed

joint temperature-species PDF have only been used in low-dimensional spaces, with few species [22, 33, 81] or additional hypotheses [15, 117].

In this work statistical independence of T and \mathbf{Y} [66] is adopted. Thus, a splitted form of the PDF is obtained

$$f(\hat{T}, \hat{\mathbf{Y}}) = f_T(\hat{T}) f_{\mathbf{Y}}(\hat{\mathbf{Y}}). \quad (4.3.8)$$

From Eq. (2.2.12) temperature and species mass fraction dependencies are clearly separated. It follows that the averaged source term is obtained as the product of several averaged terms

$$\langle \omega_i^f \rangle = M_i \sum_r (\nu_i'' - \nu_i') \left\langle \frac{k_{f_r}(\hat{T})}{\hat{T}^{\sum_j \nu_{jr}'}} \right\rangle \left\langle \left(\frac{p}{\Re \sum_{\ell} \frac{\hat{Y}_{\ell}}{M_{\ell}}} \right)^{\sum_j \nu_{jr}'} \prod_j \left(\frac{\hat{Y}_j}{M_j} \right)^{\nu_{jr}'} \right\rangle. \quad (4.3.9)$$

A similar expression holds for the backward reaction. Such an approach has already been adopted in the past and it has been shown that it is able to predict many turbulence-chemistry interaction effects [64]. In the following sections both f_T and $f_{\mathbf{Y}}$ will be presented along with the additional transport equations required to determine their second-order moments.

4.3.2 Assumed temperature PDF

Because of the strong non-linear dependence of the Arrhenius function from temperature, the averaged rate constant in Eq. (4.3.9) is expected to differ strongly from values calculated with averaged temperatures.⁴ Therefore, the influence of the temperature fluctuations has to be included. The PDFs observed experimentally depend largely on the configuration and the combustion regime (premixed/diffusion flame) and they range from Gaussian to bimodal distributions [126]. From the modeling point of view, in previous works both β and Gaussian PDF have been adopted successfully in numerical simulations of turbulent flames [60]. The Gaussian PDF offers some advantages in comparison with the β PDF, since the latter is defined in the interval $[0, 1]$ and the determination of a suitable normalization factor can be an issue [21, 63].

In this work a clipped Gaussian PDF has been chosen to statistically describe the temperature field. The clipping is carried out and Dirac's δ functions are added. This is needed since the canonical Gaussian function is defined in the interval $(-\infty, \infty)$ and thus outside any physical temperature range. The resulting distribution

$$f(\hat{T}; \langle T \rangle, \sigma_T) = C_m \delta(T_m) + \underbrace{\frac{1}{\sqrt{2\pi\sigma_g}} \exp\left[-\frac{(\hat{T} - T_g)^2}{2\sigma_g}\right]}_{f_g(\hat{T}; T_g, \sigma_g)} + C_M \delta(T_M) \quad (4.3.10)$$

is limited to the interval $[T_m, T_M]$ and contains two additional coefficients, C_m and C_M , which are related to the clipped tails [122]. The choice of the interval $[T_m, T_M]$ should be set according

⁴In this statement it is implicitly assumed that Arrhenius functions are not linear with temperature, i.e. both α and E_a in Eq. (2.2.5) are not zero.

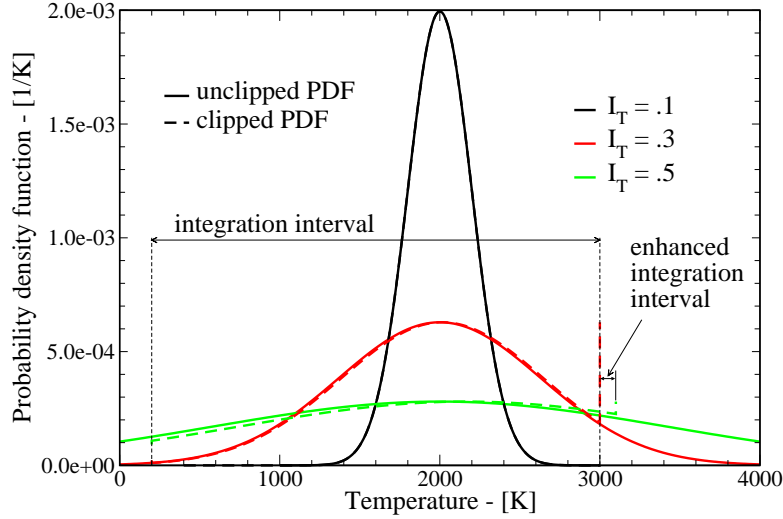


Figure 4.3.1: Unclipped and clipped temperature PDFs, $\langle T \rangle = 2000$ K.

to the testcase and the kinetic data⁵, but an interval $[300, 3000]$ covers most of the practical cases. It should also be noted that the distribution (4.3.10) is not longer symmetric, since the clipping is not. Therefore, moments of the unclipped distribution (T_g, σ_g) are in general different from the given moments $(\langle T \rangle, \sigma_T)$. Figure 4.3.1 compares several PDFs based on the same mean temperature but different temperature variances σ_T and subsequently different values of the temperature fluctuation intensity

$$I_T = \frac{\sqrt{\sigma_T}}{\langle T \rangle}. \quad (4.3.11)$$

In order to calculate the unknown moments of the unclipped distribution (T_g, σ_g) , an iterative algorithm has to be adopted. Since the moments of the clipped PDF are given $(\langle T \rangle, \sigma_T)$ and the Dirac δ peaks depend on the clipped portions, Eqs. (4.3.5) and (4.3.6) provide the necessary conditions to find the unknowns T_g and σ_g

$$f_1 = \int_{\hat{T}} \hat{T} f(\hat{T}; \langle T \rangle, \sigma_T) d\hat{T} - \langle T \rangle = 0, \quad (4.3.12)$$

$$f_2 = \int_{\hat{T}} (\hat{T} - \langle T \rangle)^2 f(\hat{T}; \langle T \rangle, \sigma_T) d\hat{T} - \sigma_T = 0. \quad (4.3.13)$$

Equations (4.3.12) and (4.3.13) are non-linear with respect to $\langle T \rangle$ and σ_T and a Newton algorithm is used. Starting from a guessed vector $\{T_g^{(0)}, \sigma_g^{(0)}\}^T$ the i -th iteration

$$\begin{Bmatrix} T_g \\ \sigma_g \end{Bmatrix}^{(i+1)} = \begin{Bmatrix} T_g \\ \sigma_g \end{Bmatrix}^{(i)} + \begin{bmatrix} \frac{\partial f_1^{(i)}}{\partial T_g} & \frac{\partial f_1^{(i)}}{\partial \sigma_g} \\ \frac{\partial f_2^{(i)}}{\partial T_g} & \frac{\partial f_2^{(i)}}{\partial \sigma_g} \end{bmatrix}^{-1} \begin{Bmatrix} f_1 \\ f_2 \end{Bmatrix}^{(i)} \quad (4.3.14)$$

⁵In particular, the range of validity of the Arrhenius function and thermodynamic coefficients should be taken into account.

provides the $(i + 1)$ -th approximate solution. The algorithm stops if the Eqs. (4.3.12) and (4.3.13) are satisfied up to a small tolerance. Particular care has to be taken in case that large portions of the PDF are clipped: in such cases the integration interval is slightly enlarged (see Fig. 4.3.1) in order to allow convergence of the Newton method.

Averaged reaction rate calculation

If the temperature PDF is given, the averaged reaction rates are obtained by integration with the classical Simpson's quadrature formula [3]. In order to evaluate the influence of the temperature fluctuations, an *amplification factor*, being the ratio between the averaged and the "laminar chemistry"⁶ temperature dependent source term contributions,

$$\alpha_T = \log \left(\left\langle \frac{k_f(\hat{T})}{\hat{T}^{\sum_j \nu'_j}} \right\rangle \cdot \frac{\langle T \rangle^{\sum_j \nu'_j}}{k_f(\langle T \rangle)} \right) \quad (4.3.15)$$

is defined. Positive values are obtained if the temperature fluctuations enhance the reaction rate and negative values otherwise. Figures 4.3.2 and 4.3.3 show α_T for two reactions taken from the Jachimowski mechanism [94]. In the first plot there is a significant enhancement of the reaction rate at low temperatures and high temperature fluctuations. Such a behavior is especially important for a correct prediction of the ignition delay in turbulent flows, since these are the typical conditions at which it takes place. A different situation is given in Fig. 4.3.3, where the reaction is either enhanced or suppressed depending on T and I_T . Figure 4.3.4 explains these differences by showing the temperature dependence of the rate constants. For the first reaction there is a super-linear trend in the whole temperature range, while for the second one two different ranges are observed depending on the sign of the second derivatives. Due to the strongly varying behavior of different reactions, no general conclusions about the influence of the temperature fluctuations on the combustion process can be drawn and each case has to be examined separately.

4.3.2.1 Interpolation procedure

The Newton-like algorithm (4.3.14) and the averaging procedure are computationally expensive and should not be executed at every timestep (or under-relaxation step). Therefore, two-dimensional lookup tables are used where averaged Arrhenius coefficients are stored as function of the mean temperature and temperature variance [64]. The main drawback of such an approach is its high memory requirement, which increases with the number of (T, σ_T) points and the size of the kinetic scheme.

⁶The term "laminar chemistry" indicates that the source term is calculated with the mean variables, without considering the influence of the turbulent fluctuations. From the mathematical point of view, it is equivalent to set

$$f_T(\hat{T}) = \delta(\hat{T} - \langle T \rangle)$$

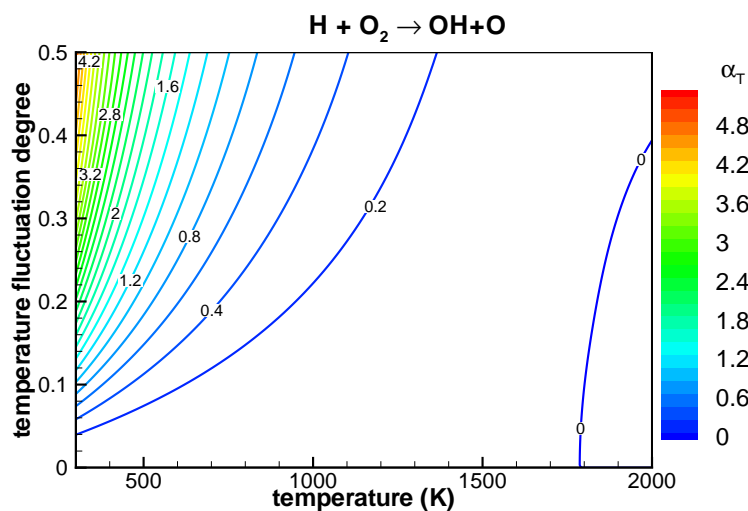


Figure 4.3.2: Effects of the temperature fluctuations on α_T for the reaction $\text{H} + \text{O}_2 \rightarrow \text{OH} + \text{O}$. Arrhenius constants taken from [94].

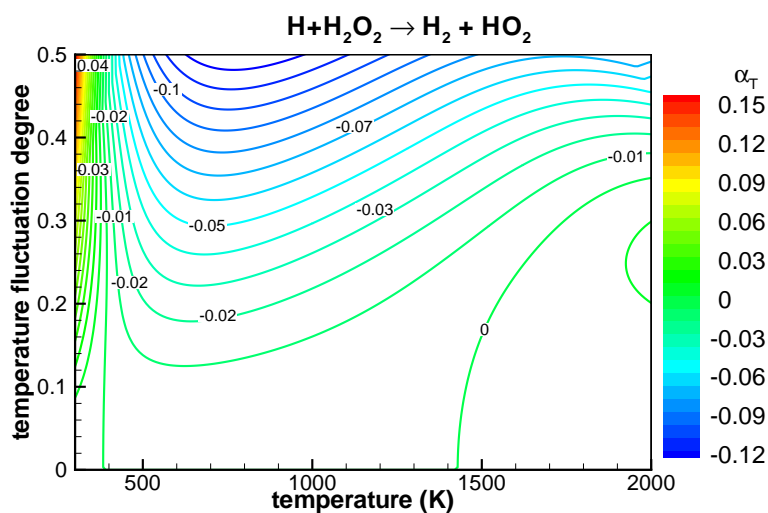


Figure 4.3.3: Effects of the temperature fluctuations on α_T for the reaction $\text{H} + \text{H}_2\text{O}_2 \rightarrow \text{H}_2 + \text{HO}_2$. Arrhenius constants taken from [94].

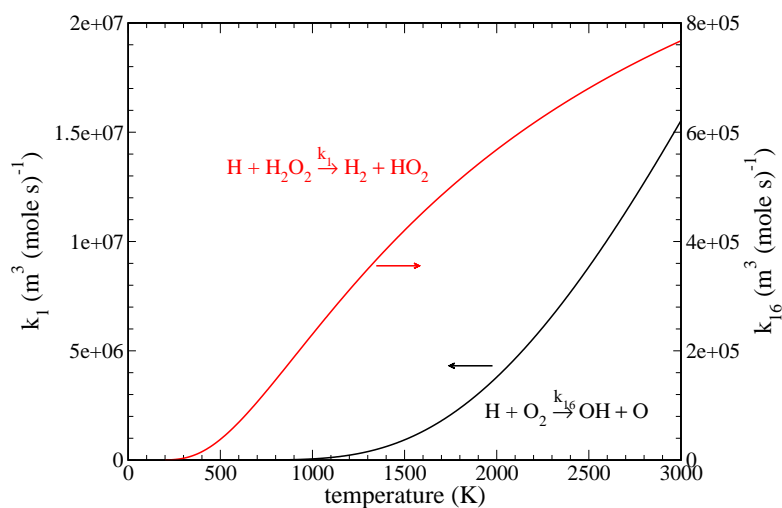


Figure 4.3.4: Rate coefficients for the reactions used in Figs. 4.3.2 and 4.3.3.

In this work a different low-storage method is implemented. Here the $\langle k_{f_r}(\hat{T}) \rangle$ is fitted at each I_T point by an Arrhenius function

$$\langle k_{f_r}(\hat{T}) \rangle \simeq A_{f_r}(I_T) \langle T \rangle^{\alpha_r(I_T)} \exp\left(-\frac{E_{a_r}(I_T)}{\Re \langle T \rangle}\right) \quad (4.3.16)$$

according to the fitting procedure described in the Appendix C. After that, the Arrhenius coefficients in Eq. (4.3.16) are interpolated over the I_T space by means polynomial functions of p -th order. In this way only $3 \times (p+1) \times N_r$ floats have to be stored, independently from the number of grid points used in $\langle T \rangle$ and I_T directions. Additionally, since the interpolation casts $\langle k_f \rangle$ into the canonical Arrhenius form, the implicit treatment of the Eq. (4.3.16) does not require neither a complete reformulation nor additional terms in the Jacobian matrix (Eq. (2.2.14)).

4.3.2.2 Temperature variance equation

In order to have a complete description of the temperature PDF, an additional transport equation is needed from which the variance of a temperature-related variable may be obtained. In past works, the variance of energy, enthalpy or temperature has been adopted [64]. The implementation of a transport equation for the variance of the enthalpy is straightforward but the relation between σ_h and σ_T has to be formulated by adopting additional modeling assumptions. On the other hand, the derivation of a σ_T equation also requires some additional hypotheses⁷ but the calculation of I_T is computationally inexpensive. Moreover, most of the experimental data of turbulent flames provide σ_T and therefore the comparison is easier.

Provided that the Boussinesq hypothesis holds and neglecting the turbulent fluctuation effects on the transport coefficients, a modeled and simplified temperature variance transport equation in differential form is given by [65]

$$\frac{\partial(\langle \rho \rangle \sigma_T)}{\partial t} + \nabla \cdot (\langle \rho \rangle \sigma_T \langle \mathbf{V} \rangle) = \nabla \cdot \left(\frac{\mu_t}{Pr_{\sigma_T}} \nabla \sigma_T \right) + 2 \frac{\mu_t}{Pr_{\sigma_T}} \nabla \langle T \rangle \cdot \nabla \langle T \rangle - C_{\sigma_T} \langle \rho \rangle \frac{\sigma_T}{\tau_t}. \quad (4.3.17)$$

The source term in Eq. (4.3.17) is represented by the gradients of the averaged temperature. This is in analogy with the k equation where the velocity gradients are responsible for producing turbulent kinetic energy. Following the turbulence cascade, the temperature fluctuations are dissipated at the Kolmogorov scale by the molecular diffusion. In this work a linear dependence of the dissipation term on the turbulent timescale (τ_t) is assumed. The comparison between simulations and experimental results (already performed in the literature [64]) achieved the best agreement for $C_{\sigma_T} = 2.0$. The transport equation for σ_T is added to the solution vector (2.1.2) but is solved uncoupled. Therefore, derivatives of the chemical source term with respect to σ_T are not included in the Jacobian matrix given in Eq. (2.2.14).

⁷In particular, it is assumed that temperature and species fluctuations have a minor influence on the enthalpy-temperature relation, Eq. (2.1.6).

In the derivation of the Eq. (4.3.17) some terms (i.e. temperature-source term correlations) are neglected even if they may have a strong influence on predictions. However, previous works already demonstrated that simple modeling approaches for these terms in a framework of uncorrelated temperature and species PDFs (see Eq. (4.3.8)) are responsible for a strong dissipation of temperature fluctuations [16] not observed in experiments. Since only few attempts to model these terms are known [15] and not a widely accepted method exists, it has been decided to neglect them.

4.3.3 Assumed species PDF

In a similar way as for temperature, the definition of a species PDF requires second-order moments for its definition. Equations for the variances of species may be written in a similar form as Eq. (4.3.17). However, for an increasing number of species the solution of the related transport equations would make three-dimensional simulations unfeasible.

For this reason a multi-variate β PDF is used to describe the influence of the species fluctuations on the reaction rates [68]. This approach has several major advantages:

- it gives a reasonable description of the scalar mixing during all stages (from initial δ -peaks up to the final Gaussian distributions [67]), as shown by DNS [56].
- the averaged species production rate has an analytical form and neither look-up tables nor interpolation algorithms are necessary.
- only one additional transport equation for the sum of the species variances⁸

$$\sigma_Y = \sum_{i=1}^{N_s} \langle Y_i'^2 \rangle \quad (4.3.18)$$

has to be solved.

As counterpart, bimodal distributions W peaks away from the boundary can not be predicted [66] with this PDF.

The β PDF for a single variable $x \in [0, 1]$ is defined as

$$f(\hat{x}; \langle x \rangle, \sigma_x) = \frac{\Gamma(\alpha + \beta)}{\Gamma(\alpha)\Gamma(\beta)} \hat{x}^{\alpha-1} (1 - \hat{x})^{\beta-1} \quad (4.3.19)$$

where α and β are functions of the first two moments of the distribution

$$\langle x \rangle = \frac{\alpha}{\alpha + \beta}, \quad (4.3.20)$$

$$\sigma_x = \frac{\alpha\beta}{(1 + \beta)^2 (\alpha + \beta + 1)}, \quad (4.3.21)$$

⁸Hereafter σ_T will be called *turbulent scalar energy* [67] since its definition is analogous to the turbulent kinetic energy k (4.2.6).

and the Γ function is [75]

$$\Gamma(\beta) = \int_0^{\infty} t^{\beta-1} \exp(-t) dt. \quad (4.3.22)$$

In case of a multivariate joint β -PDF of species mass fractions, N_s functions $\Gamma(\beta_i)$ have to be defined. Each β_i depends on the averaged species mass fractions and the turbulent scalar energy

$$\beta_i = \langle Y_i \rangle \left[\frac{\sum_{j=1}^{N_s} \langle Y_j \rangle (1 - \langle Y_j \rangle)}{\sigma_Y} - 1 \right]. \quad (4.3.23)$$

Thus, the joint β -PDF is defined as

$$P(\hat{\mathbf{Y}}; \langle \mathbf{Y} \rangle, \sigma_Y) = \frac{\Gamma(\sum_{j=1}^{N_s} \beta_j)}{\prod_{j=1}^{N_s} \Gamma(\beta_j)} \prod_{j=1}^{N_s} (\hat{Y}_j)^{\beta_j-1} \delta\left(1 - \sum_{j=1}^{N_s} \hat{Y}_j\right) \quad (4.3.24)$$

where the Dirac's δ function is introduced to limit the PDF to the subspace where the vector $\hat{\mathbf{Y}}$ sums up to one. The variance of a single species can be calculated as

$$\langle Y_j'^2 \rangle = \frac{\langle Y_j \rangle - \langle Y_j \rangle^2}{\sum_j \beta_j + 1}. \quad (4.3.25)$$

The analytical expression for the product of species mass fractions (Eq. (2.2.2)) can be found by exploiting some properties of the β and Γ functions. Here only final expressions are given; for an exhaustive demonstration see [13] or [68]. For a generic reaction which does not involve third bodies it becomes

$$\left\langle \prod_{j=1}^{N_s} (Y_j)^{\nu_j} \right\rangle = \frac{\prod_{j=1}^{N_s} \prod_{i=1}^{\nu_j} (\beta_j + \nu_j - i)}{\prod_{i=1}^N (B + N - i)}, \quad (4.3.26)$$

where

$$B = \sum_{j=1}^{N_s} \beta_j \quad (4.3.27)$$

and

$$N = \sum_{j=1}^{N_s} \nu_j. \quad (4.3.28)$$

In the case that third-body reactions are considered, an additional factor

$$\left\langle \prod_{j=1}^{N_s} (Y_j)^{\nu_j} \left(\sum_{j=1}^{N_s} t_{b_j} Y_j \right) \right\rangle = \underbrace{\left\langle \prod_{j=1}^{N_s} (Y_j)^{\nu_j} \right\rangle}_{\text{Eq.(4.3.26)}} \left[\sum_{j=1}^{N_s} t_{b_j} (\beta_j + \nu_j) \right] \quad (4.3.29)$$

which includes third-body efficiencies is added.

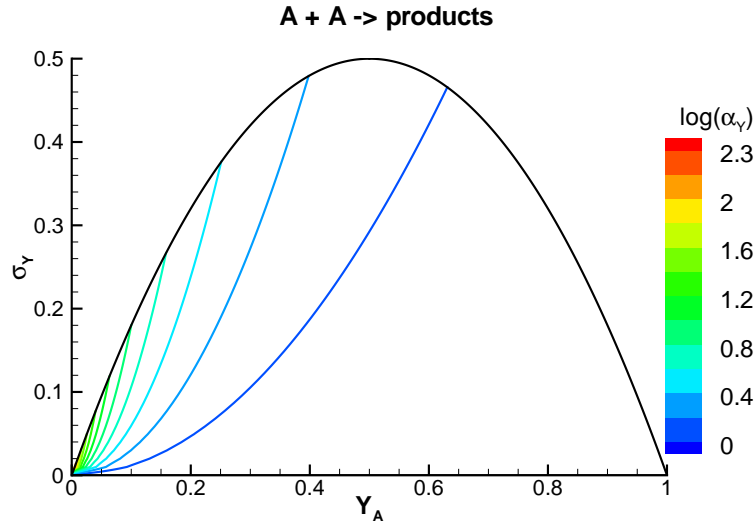


Figure 4.3.5: Effects of the species fluctuations for a self-recombination reaction.

Influence of the species fluctuation

The influence of the β -PDF on the species source term can be assessed by examining the amplification factor

$$\alpha_Y = \frac{\left\langle \prod_{j=1}^{N_s} (Y_j)^{\nu_j} \right\rangle}{\prod_{j=1}^{N_s} (\langle Y_j \rangle)^{\nu_j}} \quad (4.3.30)$$

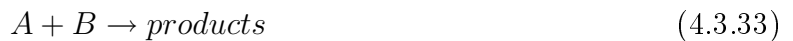
for simple two body reactions [13] in a two-components mixture. In case of self-recombination



the species fluctuations enhance the averaged reaction rate. The corresponding amplification factor can be derived from Eq. (4.3.26)

$$\alpha_Y^{AA} = 1 + \frac{\sigma_Y (1 - \langle Y_A \rangle)}{\langle Y_A \rangle \left(1 - \sum_j \langle Y_j \rangle^2 \right)} \quad (4.3.32)$$

and is shown in Fig. 4.3.5 in a logarithmic scale. The highest amplification factors are achieved near the origin for small concentrations of A . On the other hand, heterogeneous reactions as



are suppressed by the species fluctuation since the amplification factor

$$\alpha_Y^{AB} = 1 - \frac{\sigma_Y}{1 - \sum_j \langle Y_j \rangle^2} \quad (4.3.34)$$

is always less than one. Figure 4.3.6 shows the corresponding symmetric behavior.

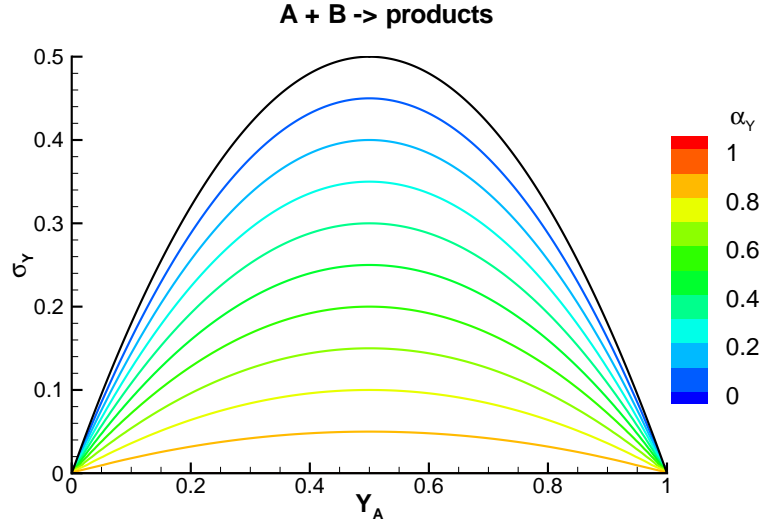


Figure 4.3.6: Effects of the species fluctuations for a heterogeneous recombination reaction.

4.3.3.1 Implicit treatment of the averaged reaction rate

Since the formulation of the averaged source term is affected by species fluctuations, the Jacobian matrix depends on the assumed PDF approach. Derivatives with respect to mass fractions are calculated using the chain rule

$$\frac{\partial}{\partial Y_k} \left\langle \prod_j (Y_j)^{\nu_j} \right\rangle \Big|_{h, Y_{j,j \neq k}} = \sum_{\ell=1}^{N_s} \frac{\partial}{\partial \beta_\ell} \left\langle \prod_j (Y_j)^{\nu_j} \right\rangle \Big|_{\beta_{i,i \neq \ell}} \frac{\partial \beta_\ell}{\partial Y_k} \Big|_{h, Y_{j,j \neq k}}, \quad (4.3.35)$$

where

$$\frac{\partial \beta_\ell}{\partial Y_k} = 2 \frac{\langle Y_{N_s} \rangle - \langle Y_k \rangle}{\sigma_Y} Y_\ell + \delta_{\ell k} \left(\frac{\sum_j \langle Y_j \rangle (1 - \langle Y_j \rangle)}{\sigma_Y} - 1 \right) \quad (4.3.36)$$

and $\delta_{\ell k}$ is the Kronecker delta. Concerning the derivative with respect to β_ℓ , Eq. (4.3.26) is used and for the numerator the following expression

$$\frac{\partial}{\partial \beta_\ell} \left[\prod_{j=1}^{N_s} \prod_{i=1}^{\nu_j} (\beta_j + \nu_j - i) \right] \Big|_{\beta_{i,i \neq \ell}} = \prod_{j=1}^{N_s} \prod_{i=1}^{\nu_j} (\beta_j + \nu_j - i) \sum_{i=i}^{\nu_\ell} \frac{1}{(\beta_\ell + \nu_\ell - i)} \quad (4.3.37)$$

is obtained. Derivatives of the denominator are straightforward, since only the sum of β_i appears

$$\frac{\partial}{\partial Y_k} \left[\prod_{i=1}^N (B + N - i) \right] \Big|_{Y_{j,j \neq k}} = \frac{\partial}{\partial B} \left[\prod_{i=1}^N (B + N - i) \right] \frac{\partial B}{\partial Y_k} \Big|_{Y_{j,j \neq k}}, \quad (4.3.38)$$

where

$$\frac{\partial}{\partial B} \left[\prod_{i=1}^N (B + N - i) \right] = \prod_{i=1}^N (B + N - i) \sum_{i=1}^N \frac{1}{(B + N - i)} \quad (4.3.39)$$

and

$$\left. \frac{\partial B}{\partial Y_k} \right|_{Y_{j,j \neq k}} = 2 \frac{\langle Y_{N_s} \rangle - \langle Y_k \rangle}{\sigma_Y}. \quad (4.3.40)$$

In case that third-body reactions are included, the derivatives of the additional term in Eq. (4.3.29) are calculated with the help of Eq. (4.3.36)

$$\begin{aligned} \left. \frac{\partial}{\partial Y_k} \left[\sum_{j=1}^{N_s} t_{b_j} (\beta_j + \nu_j) \right] \right|_{Y_{j,j \neq k}} &= 2 \frac{\langle Y_{N_s} \rangle - \langle Y_k \rangle}{\sigma_Y} \sum_{j=1}^{N_s} t_{b_j} \langle Y_j \rangle + \\ & (t_{b_k} - t_{b_{N_s}}) \left(\frac{\sum_j \langle Y_j \rangle (1 - \langle Y_j \rangle)}{\sigma_Y} - 1 \right). \end{aligned} \quad (4.3.41)$$

4.3.3.2 Turbulent scalar energy transport equation

Under the same hypothesis as for Eq. (4.3.17), the differential form of the transport equation for σ_Y is written as follows

$$\begin{aligned} & \frac{\partial (\langle \rho \rangle \sigma_Y)}{\partial t} + \nabla \cdot (\langle \rho \rangle \sigma_Y \langle \mathbf{V} \rangle) = \\ & = \nabla \cdot \left(\frac{\mu_t}{Pr_{\sigma_Y}} \nabla \sigma_Y \right) + 2 \langle \rho \rangle \frac{\mu_t}{Pr_{\sigma_Y}} \sum_{j=1}^{N_s} \nabla \langle Y_j \rangle \cdot \nabla \langle Y_j \rangle - C_{\sigma_Y} \langle \rho \rangle \frac{\sigma_Y}{\tau_t} \end{aligned} \quad (4.3.42)$$

where cross-correlation terms like $\langle Y'_i \omega_i \rangle$ are neglected as explained above. C_{σ_Y} gives the relation between the rates at which the velocity and species fluctuations are dissipated. A comparison with experimental data in turbulent jet flames obtained the best results for $C_{\sigma_Y} = 2.0$, although local values can range in the interval 0.5-2.0 [154].

4.4 Model validation

In order to validate the assumed PDF approach, simulations for turbulent hydrogen/air flames are performed. For this fuel only a small number of reactions is needed in order to get an almost complete description of the combustion process. Although this does not preserve the results from the influence of the adopted kinetics (see for example subsection 2.2.3), the small size of the chemical mechanism allows to discuss the influence of the single reactions to some extent. Moreover, the chosen testcases exhibit some features to point out the influence of the turbulent fluctuations and the range of applicability of the assumed PDF approach.

4.4.1 Attached, turbulent H₂/air flame (H3 flame)

The axisymmetric, unconfined, turbulent, diffusion hydrogen/air flame presented in the Turbulent Non-premixed Flame Workshop [85] is investigated. A turbulent N₂/H₂ mixture is injected from a 8-mm pipe into a slow coflow under conditions that an attached, statistically-stationary diffusion flame is obtained. Detailed axial and radial profiles of the main species and temperature have been measured along with their fluctuations. Thus, the comparison of both σ_T and σ_Y (Eqs. (4.3.17) and (4.3.42)) with experimental data becomes possible and their influence on

Table 4.1: Boundary conditions for the H3 flame (Section 4.4.1).

	radius(mm)	composition ²	temperature(K)	velocity($\frac{m}{s}$)
fuel inlet	4	H ₂ : .0671 N ₂ : .9329	300	34 ¹
air inlet	70	O ₂ : .23 N ₂ : .77	300	0.2
wall	-	zero gradient	300	0
outflow	-	zero gradient	zero gradient	zero gradient
axis	-	zero gradient	zero gradient	zero gradient

¹ The bulk fuel velocity is given here. Profiles are given in [1].

² The composition is given in mass fractions.

the mean quantities can be evaluated. Moreover, data from other research groups investigating the same testcase are also available [146].

The simulation is carried out on a 5-degree slice using hexahedral elements for the computational grid everywhere but along the axis, where prisms are better suited to fit the geometry. The fuel inflow profiles are taken from numerical simulations [1] and are prescribed at the pipe's exit. The coflow is assumed to be laminar and a small portion of it is included in the simulation in order to take the suction effects near the mixing region into account. Since the fuel and coflow inlets show large differences in their axial momentum, an upstream extension of the fuel inlet (as done in subsection 2.5.5) is considered useless. A summary of the boundary conditions is given in Table 4.1.

The H₂-chemistry is described by the 9-species, 21-reactions mechanism of Ô Connaire et al. [149] already employed to study the hydrogen ignition in subsection 2.2.3. The turbulent transport terms are closed by the standard $k - \epsilon$ turbulence model [200] using $C_1 = 1.6$ (instead of the standard value $C_1 = 1.44$ [200]). This value is chosen to achieve a higher accuracy in the predictions of the spreading rate in bluff-body configurations [38, 41] and axisymmetric jets [208], also in case of a hot coflow [35]. Beside the assumed PDF approach, both the influence of the chemical kinetics and the C_1 turbulence model constant will be investigated.

4.4.1.1 Reference calculation

In order to analyze the influence of different parameters, a reference calculation is performed without taking the influence of turbulent temperature and species fluctuations on the reaction rates (laminar chemistry) into account. Fig. 4.4.1 shows the axial velocity and mixture fraction

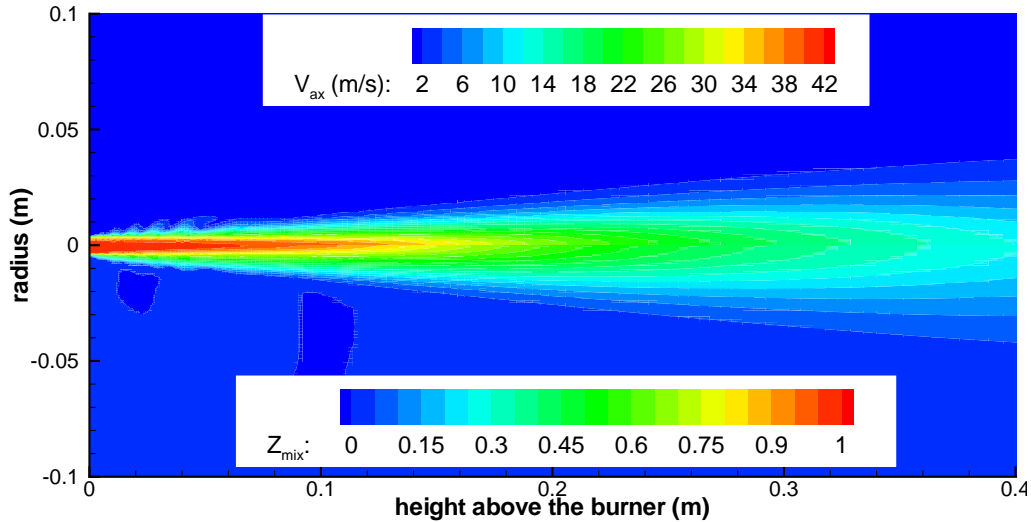


Figure 4.4.1: Axial velocity and mixture fraction distributions for the H3 jet flame.

distributions. The latter is a conserved scalar

$$Z = \frac{2\frac{Z_C}{W_C} + \frac{1}{2}\frac{Z_H}{W_H} + \frac{Z_O|_{in}^{air} - Z_O}{W_O}}{2\frac{Z_C|_{in}^{fuel}}{W_C} + \frac{1}{2}\frac{Z_H|_{in}^{fuel}}{W_H} + \frac{Z_O|_{in}^{air}}{W_O}} \quad (4.4.1)$$

able to describe the mixing of two different streams in non-premixed, hydrocarbon flames [19]. Z_e is the fraction of element e in the mixture and the superscripts *air* and *fuel* refer to the values calculated at air and fuel inlets, respectively. According to its definition, the mixture fraction is bound between zero (air inlet) and one (fuel inlet). Since it is not directly affected by chemical reactions, it is often used to provide a parameter to compare experimental and numerical results independently from the adopted combustion model. In Fig. 4.4.1 the mixture fraction distribution shows a conical core flow in the jet center and a mixing between the streams.

In Fig. 4.4.2 temperature and OH mass fraction distributions are given. Even if the flame structure looks similar to the laminar flames investigated in the previous chapters, a significantly higher ratio between flame length and fuel inlet nozzle (about 90) is observed. The flame is stabilized by the turbulent structures caused by high inlet velocity gradients. The OH distribution (in the same plot) is consistent with the temperature predictions and outlines the mean position of the flame front. Highest concentrations are achieved near the burner exit, where high species gradients occur.

4.4.1.2 Influence of the simulation parameters

The sensitivity with respect to the kinetic mechanism is investigated first. Figure 4.4.3 shows that only small differences in terms of temperature and flame length are obtained if the 9-species, 19-reaction Jachimowski's mechanism [94] is used instead of the \dot{O} Connaire one. Thus, it can

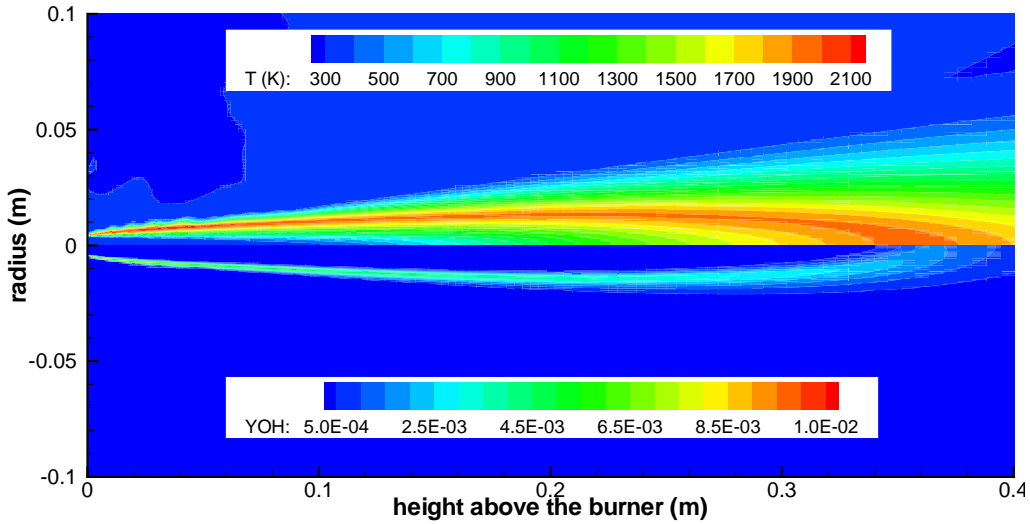
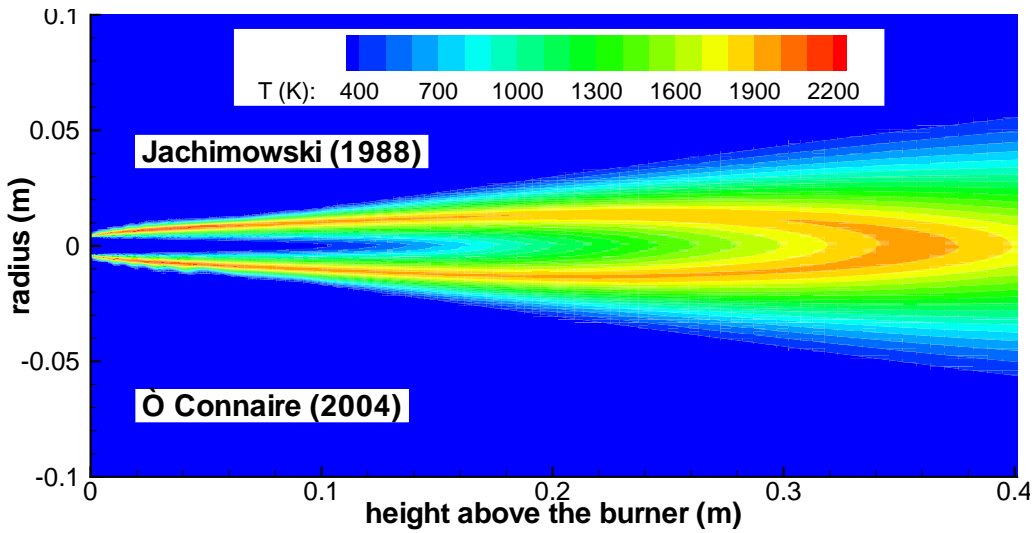
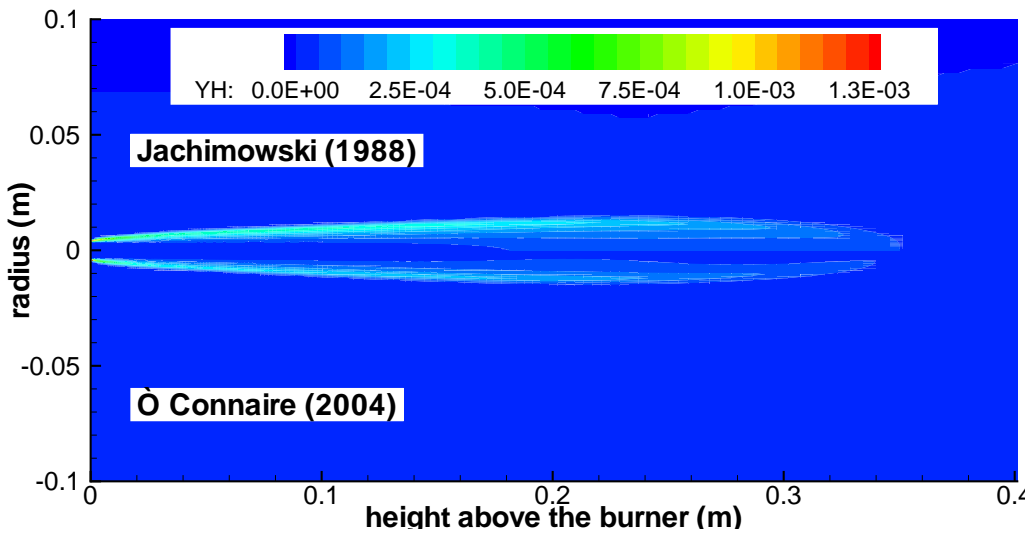


Figure 4.4.2: Temperature and OH distributions for the H3 jet flame.



(a) temperature



(b) H mass fraction

Figure 4.4.3: Influence of the chemical kinetics on the temperature and H distributions of the H3 jet flame.

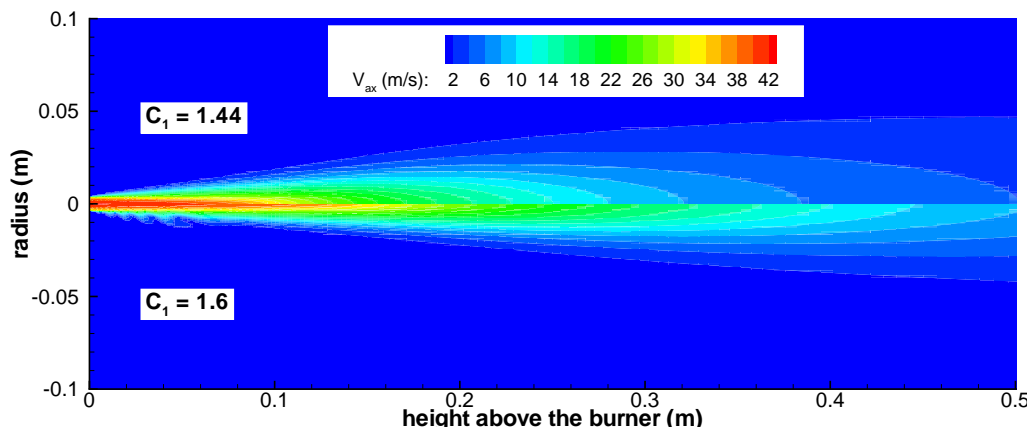
be concluded that flame stabilization is dominated by “diffusion”⁹ of fuel and oxidator into the thin, reactive layer [110]. Once that fuel, air and hot combustion products are mixed at molecular level (below the Kolmogorov scale), reactions can take place and heat is released. Here the diffusion process acts as a bottleneck for the combustion process. However, it should be kept in mind that pollutant formation (i.e. NO_x production, soot) may depend strongly on the adopted kinetics since radical concentrations show a significant sensitivity to the kinetics. As an example, Fig. 4.4.3(b) compares the H radical distributions of both mechanisms and large differences in the peak values and distributions are observed.

The $k - \epsilon$ model is used to close the averaged momentum equations and the closure model parameters are expected to have an influence on the velocity field and consequently the flame behavior. As suggested in Ref. [208], the jet anomaly¹⁰ can be partially solved by a simple change of the constant C_1 in the ϵ equation. In Fig. 4.4.4(a) large differences between simulations using the standard value ($C_1 = 1.44$) and the jet-corrected value ($C_1 = 1.6$) are noticed. Spreading and mixing rates are heavily affected by this constant and the flame is more than 37% shorter if $C_1 = 1.44$ is used. Additionally, radial velocity profiles are flatter and a thicker flame is obtained. The comparison with the experimental data in subsection 4.4.1.4 will show that the jet-corrected value ($C_1 = 1.6$) achieves a better agreement with measurements even if it is not able to improve the results at all stages of the mixing process.

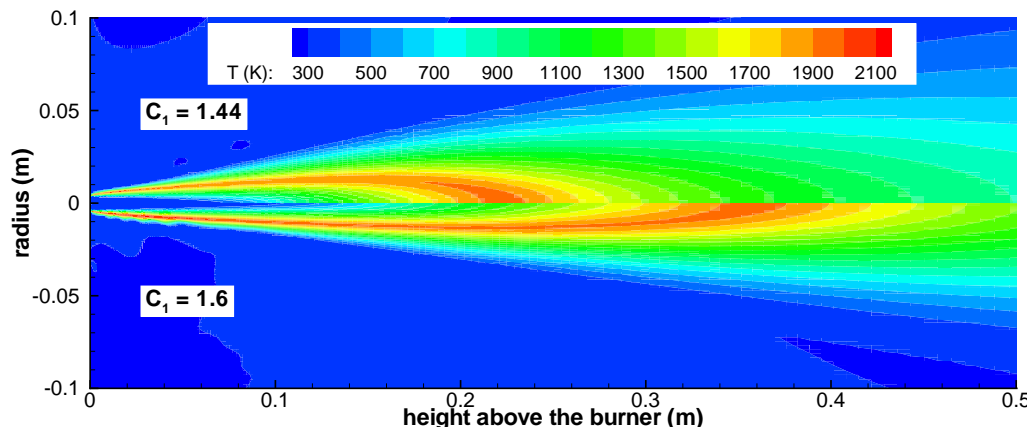
Next, the influence of the molecular transport phenomena is investigated, since laboratory-scale flames are in a Reynolds number interval where they show some sensitivity to differential diffusion [12]. Indeed, even if the testcase is nominally in the turbulent regime the high dissipation rates which occur near the burner exit may be able to damp the turbulent fluctuations. In this case high molecular diffusivities which characterize small radical species (i.e. hydrogen) may play a role. The so-called relaminarization is particular important in the near-field of the burner, where the flame’s stabilization is related to the upstream transport of heat and combustion products. Figure 4.4.5 compares temperature and OH distributions for simulations where differential diffusion or equal diffusivity for all species ($Le = 1$) are used. Beyond different peak temperatures, the most important difference is the position of the stabilization point. If a unity Lewis number is used, a detached flame (not observed in the experiments) is obtained since the relaminarization which takes place at the burner exit damps the turbulent fluctuation and therefore mixing. It becomes clear that in such hydrogen fueled flames the assumption of $Le = 1$ is particularly poor, since H_2 (as well as radicals responsible for the ignition of fresh mixture pockets) has a high molecular diffusivity and can penetrate in the reactive layer more efficiently than the $Le = 1$ hypothesis can predict.

⁹Here the term “diffusion” has a more general meaning, since it includes the convective transport operated by unresolved small turbulent structures.

¹⁰The term “jet anomaly” refers to the fact that the $k - \epsilon$ model underpredicts the spreading rate in plain jets and overpredicts it in axisymmetric configurations.



(a) axial velocity



(b) temperature

Figure 4.4.4: Influence of the C_1 model constant of the $k - \epsilon$ turbulence model on the axial velocity and temperature distributions of the H3 jet flame.

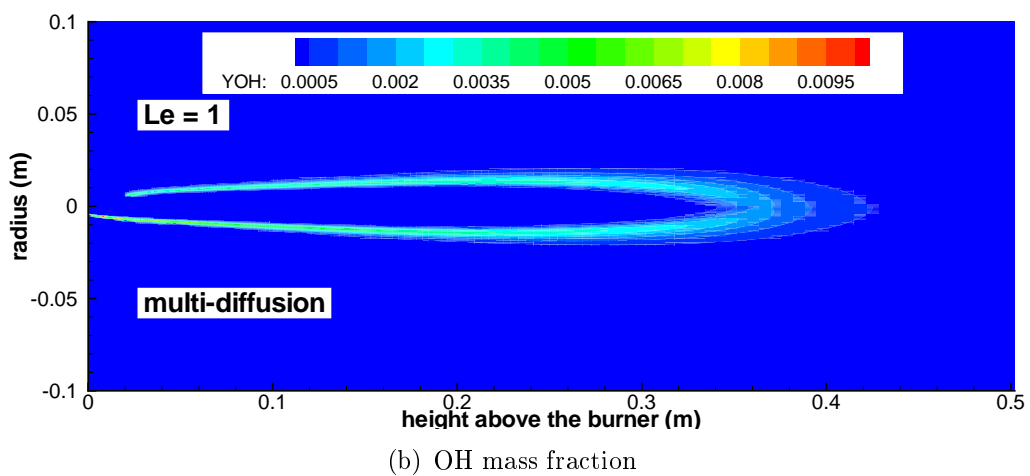
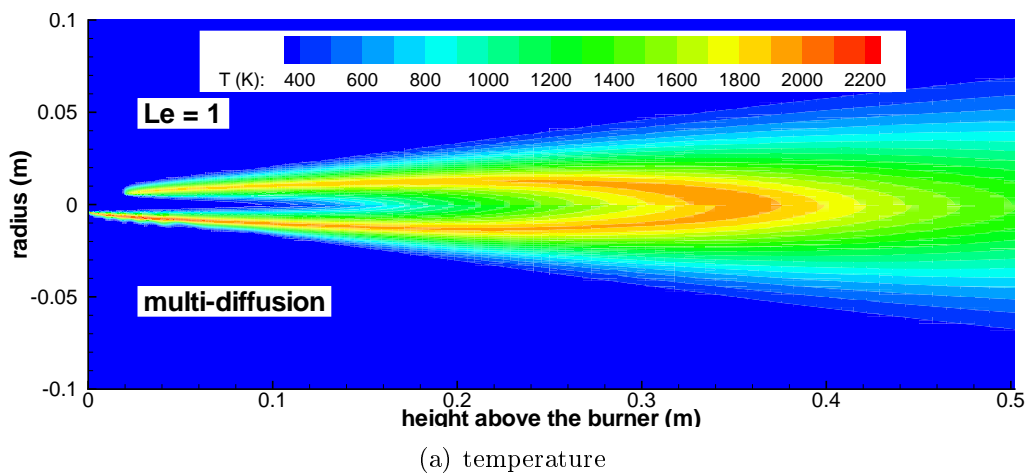


Figure 4.4.5: Influence of the Lewis number on the temperature and OH distributions of the H3 jet flame.

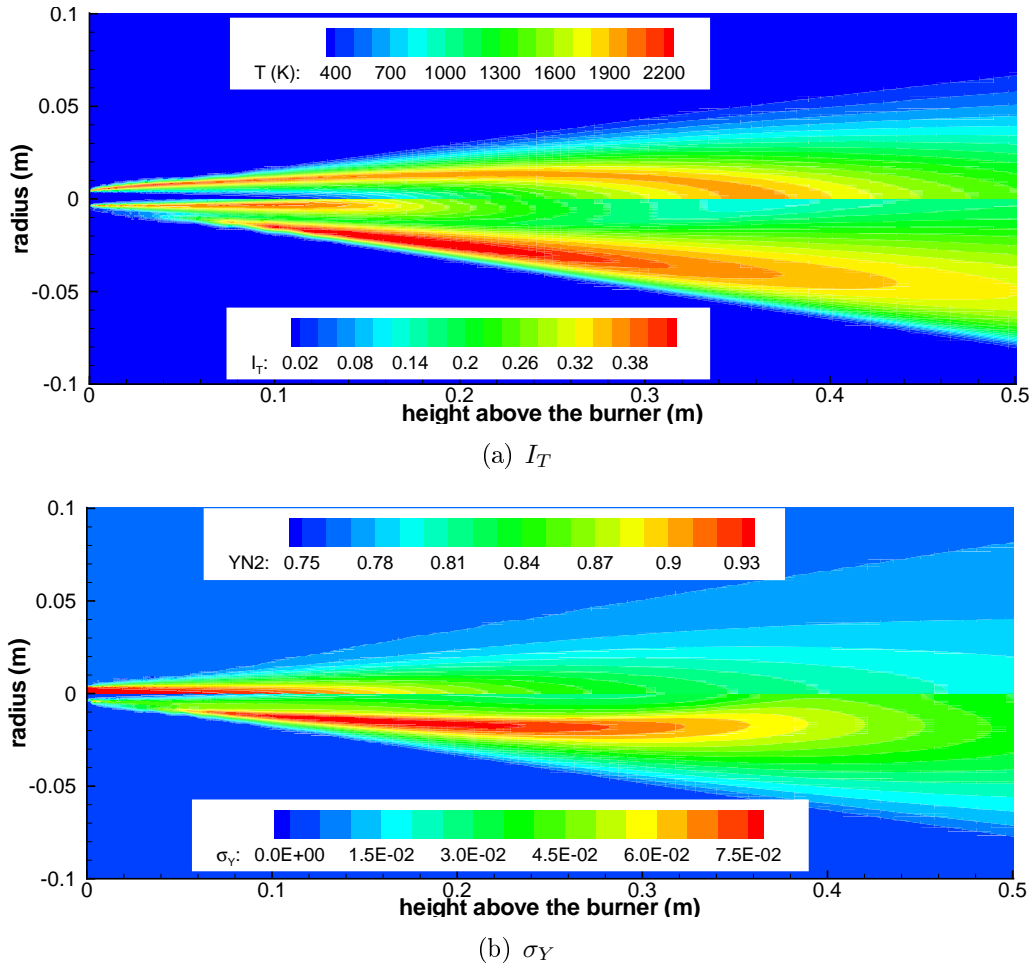


Figure 4.4.6: Temperature, temperature fluctuation intensity and turbulent scalar energy distributions of the H3 jet flame.

4.4.1.3 Influence of the turbulent fluctuations

In this section both the species and temperature turbulent fluctuations are considered in the calculation of the source term. Several simulations have been carried out where σ_T , σ_Y or both are transported and included in the averaged source term calculation. In Fig. 4.4.6 both temperature and species variance distributions are shown next to the temperature and N_2 distributions, respectively. Each simulation has been performed with either σ_T or σ_Y equation activated. It is observed that the flame shape is neither affected by the inclusion of σ_T nor σ_Y . The reasons for this insensitivity can be found in Figs. 4.3.2 and 4.3.3. Since the flame is attached and a cold coflow is used, temperature and species fluctuations are established by the flame itself. That is, the mixture will be ignited at high temperature and low temperature fluctuations in a region of the plane (T, T_f) (see Figs. 4.3.2 and 4.3.3) where the amplification factor is negligible.

This hypothesis is confirmed by the direct comparison of the temperature field with and without temperature-PDF, as done in Fig. 4.4.7(a). No significant differences are observed in the temperature distribution and only a thinner flame is obtained. Nevertheless, similarly to the chemical kinetics, the temperature fluctuations have a large influence on the radical

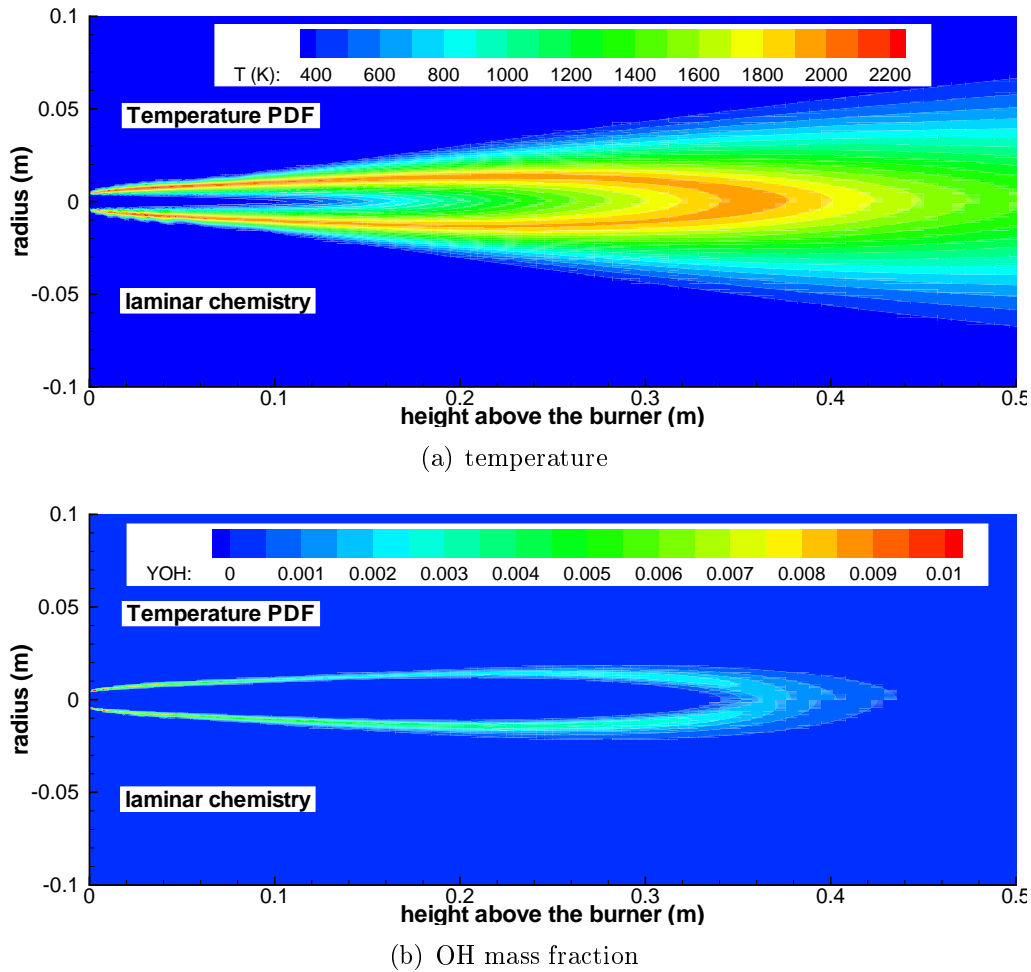


Figure 4.4.7: Effect of the temperature PDF on the temperature and OH distributions of the H3 jet flame.

production, as shown in Fig. 4.4.7(b) for the OH concentration. In case that the temperature-PDF is employed, the reaction zone is thinner and lower OH concentrations are obtained; other species show the same trend. Analogous conclusions may be drawn in case that species fluctuations are taken into account; the results are not shown here for the sake of brevity.

4.4.1.4 Comparison with experimental results

The experimental dataset consists of temperature and main species measurements along the axis and radial profiles at seven heights above the burner. The root mean square (rms) values of the same variables are also provided. In this work both axial and radial profiles (at 2.5, 10 and 50 diameters above the burner) are shown. These heights are chosen to give a good overview of the whole field (i.e. from the near-field mixing to the self-similar regime).

In order to assess the effects of the modified turbulence model constant C_1 on the mixing field, mixture fraction profiles are plotted in Fig. 4.4.8. In the axial plot (Fig. 4.4.8(a)) it is observed that the $C_1 = 1.6$ assumption provides a better agreement in the near-field region, where the flame stabilization takes place. On the other hand, the spreading rate in the far-field region is not well reproduced and the mixture fraction is overpredicted. Since most phenomena

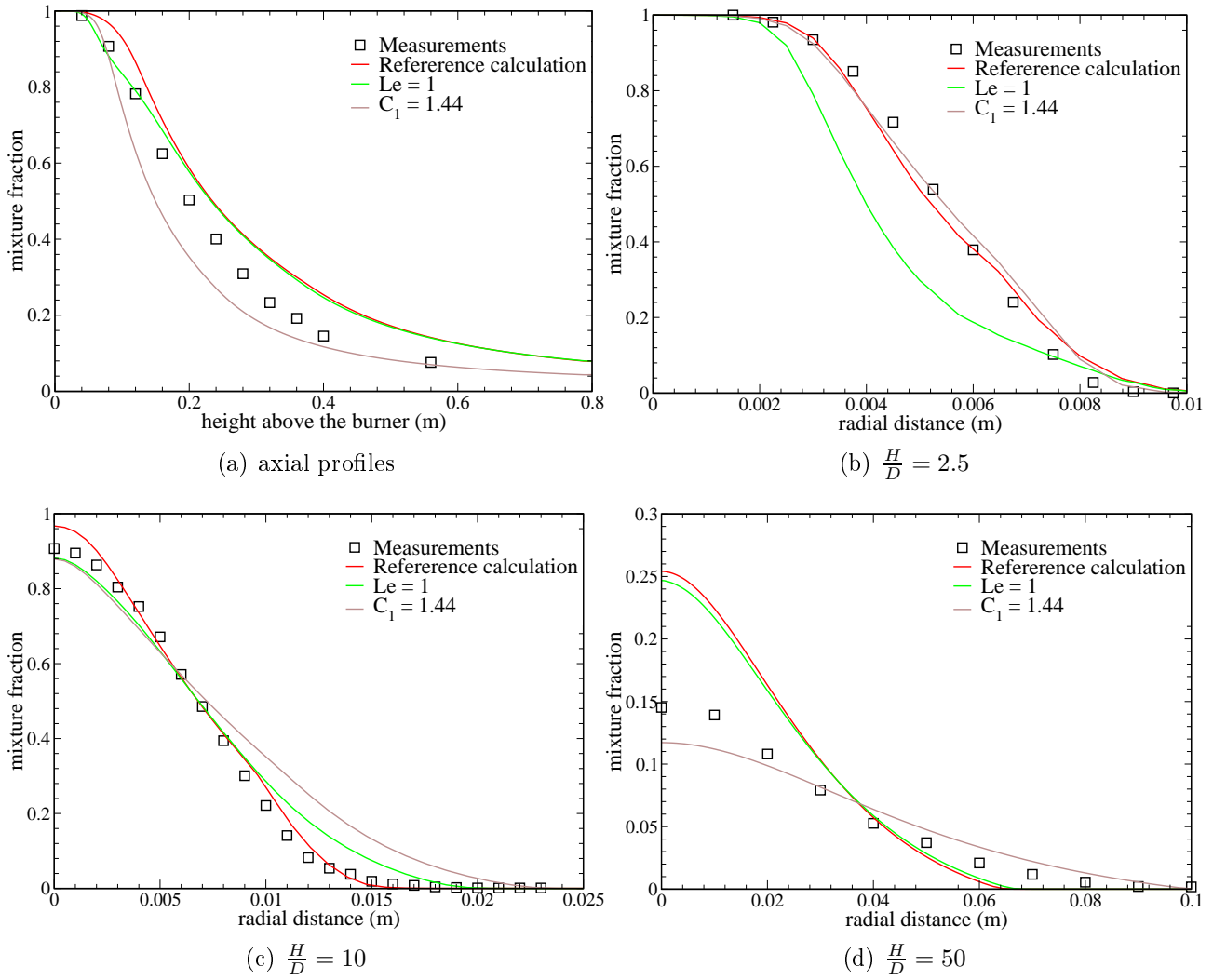


Figure 4.4.8: Mixture fraction profiles for the H3 jet flame.

affecting the flame structure take place near the burner exit (where highest temperature and species gradients occur), the modified constant represents the better choice.

The temperature profiles are shown in Fig. 4.4.9. In case the modified turbulence closure constant C_1 is adopted, a better overall agreement along the axis (Fig. 4.4.9(a)) is achieved. The choice $C_1 = 1.44$ overpredicts the temperature rise, since a higher turbulent kinetic energy and a high turbulent transport are attained. Changes in this modeling constant does not seem to affect the peak temperature, which is overpredicted by both calculations. The position of the temperature peak, which represents the flame length, does not match the experimental data in any of the presented simulation. The radial profiles show that it is well predicted in the near-field whereas larger errors appear further downstream. In comparison, the experimental profiles are wider and the peak is shifted towards the axis. Since the turbulent transport determines the flame's shape, the turbulence model should be responsible for these discrepancies. In particular, a lack of energy and species transport in the radial direction (see also Fig. 4.4.11) is observed. In previous numerical works [146] similar discrepancies in peak temperatures were found, although the use of a more complex correction for axisymmetric jets leads to a better overall agreement [155].

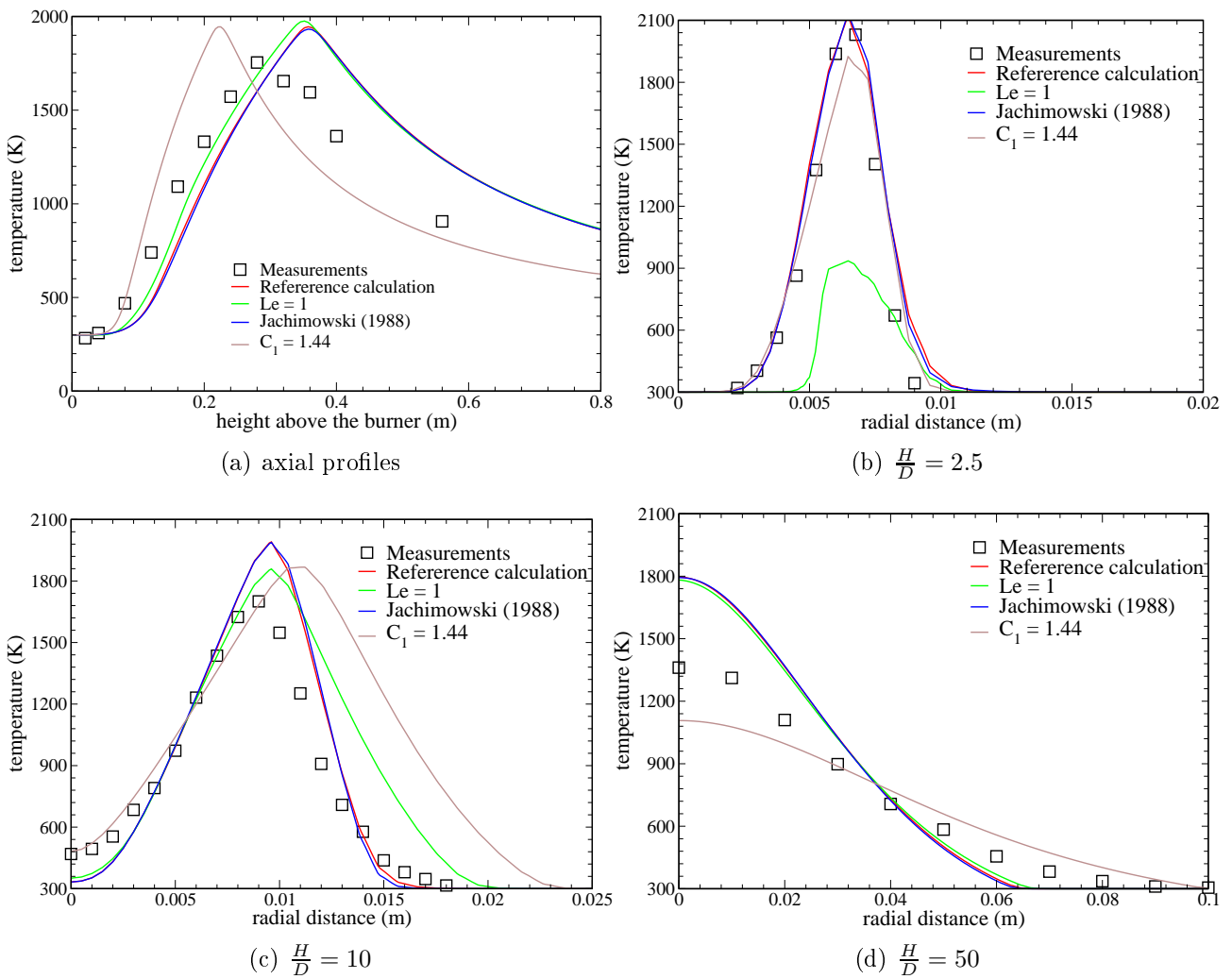


Figure 4.4.9: Temperature profiles for the H3 jet flame: influence of turbulence and thermochemistry modeling.

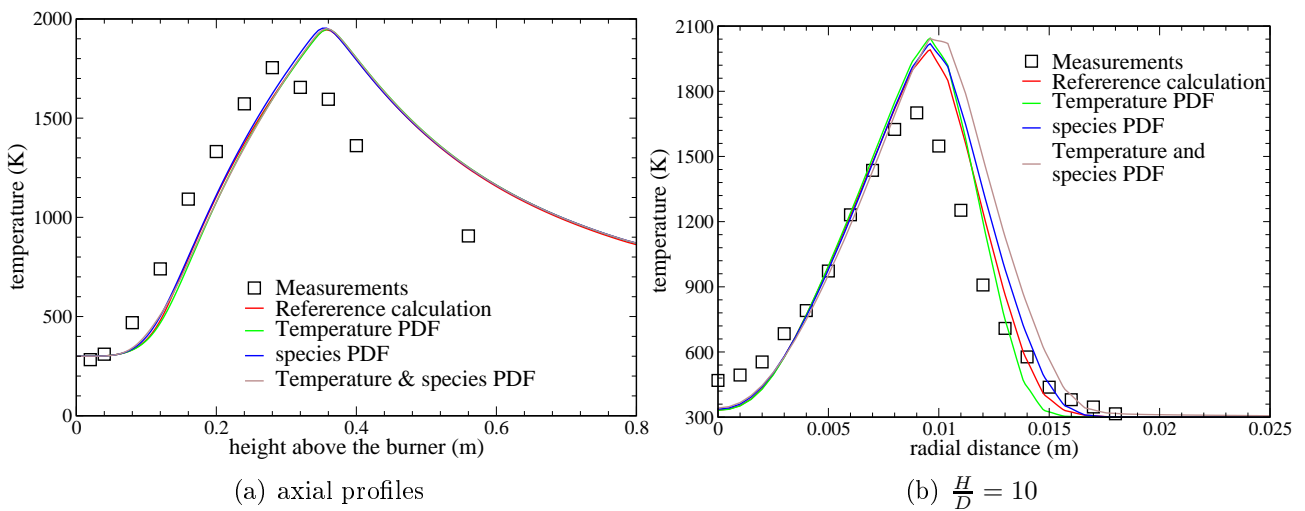


Figure 4.4.10: Temperature profiles for the H3 jet flame: influence of temperature and species turbulent fluctuations.

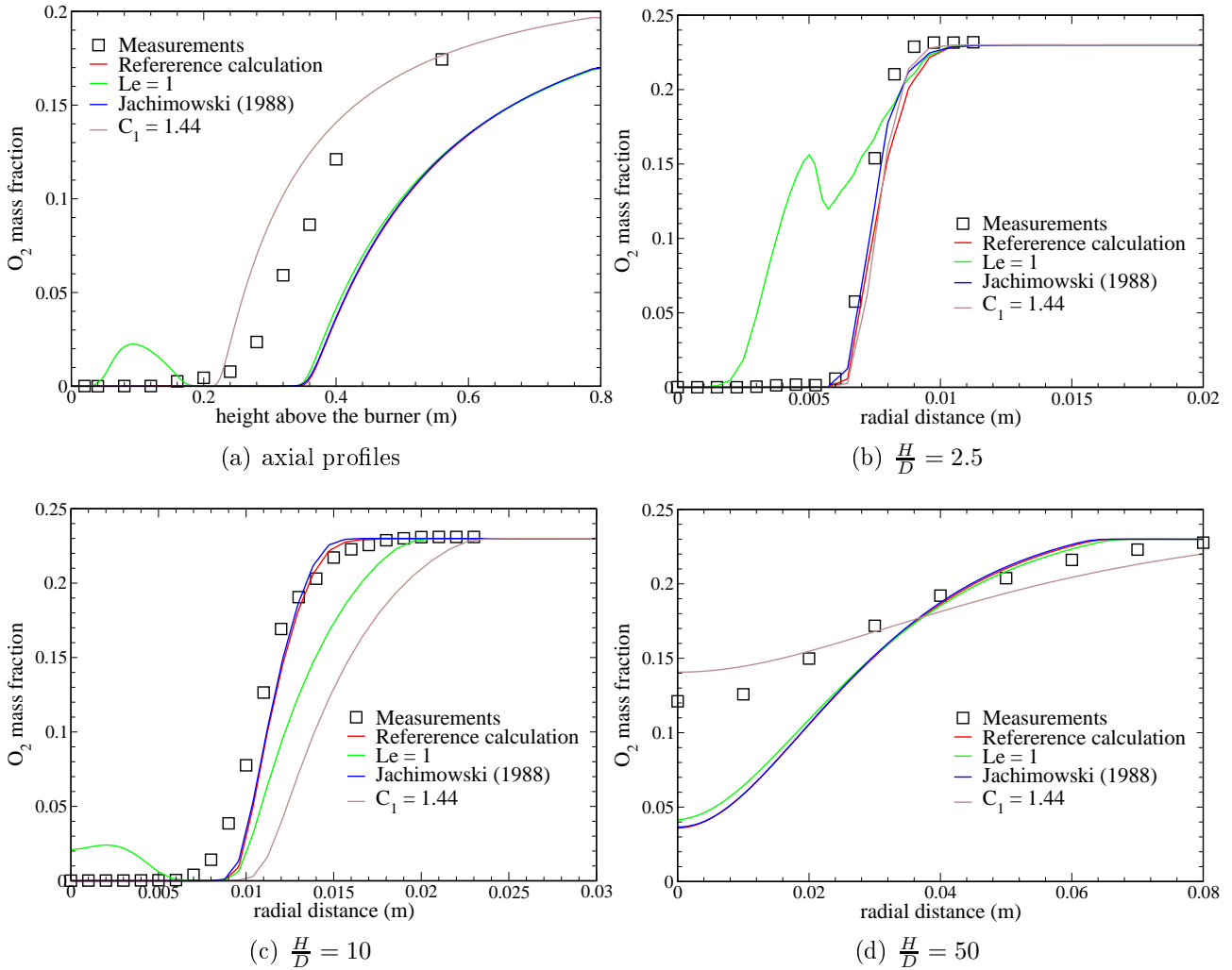


Figure 4.4.11: O_2 mass fraction profiles for the H3 jet flame: influence of turbulence and thermochemistry modeling.

Effects of the temperature and species fluctuations on mean temperature profiles (see Fig. 4.4.10) are marginal. Nevertheless, even if the global reaction rate is similar, the relative importance of single reactions changes if the PDFs are included. An example is given in Fig. 4.4.12 where differences between laminar chemistry and calculations employing temperature- and species-PDFs are given. In particular, the O_2 penetration into the flame core is more pronounced if PDFs are included. Even if these differences seem to be quite small, the high sensitivity with respect to the gas composition of many reactions makes the inclusion of turbulence-chemistry interaction mandatory.

Profiles of I_T (see Eq. (4.3.17)) are plotted in Fig. 4.4.13. Experimental peak values and trends are well reproduced. In the axial plot (Fig. 4.4.13(a)) the second peak is missed what may be partially caused by the discrepancies in the flame length predictions. In spite of discrepancies observed in the temperature predictions, the radial I_T profiles are in good agreement with the measurements, even if the bimodal distributions found at $\frac{H}{D} = 2.5$ and $\frac{H}{D} = 10$ are only partially reproduced. These differences, along with the discrepancies found at $\frac{H}{D} = 50$, may be related to neglected terms in the I_T transport equation (Eq. (4.3.17)).

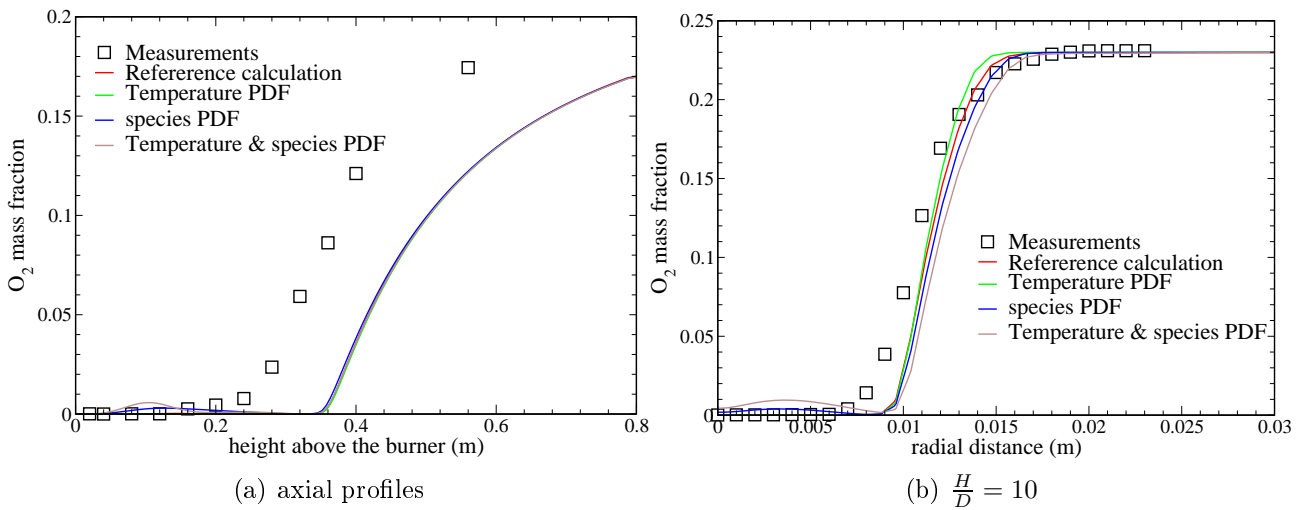


Figure 4.4.12: O₂ mass fraction profiles for the H3 jet flame: influence of temperature and species turbulent fluctuations.

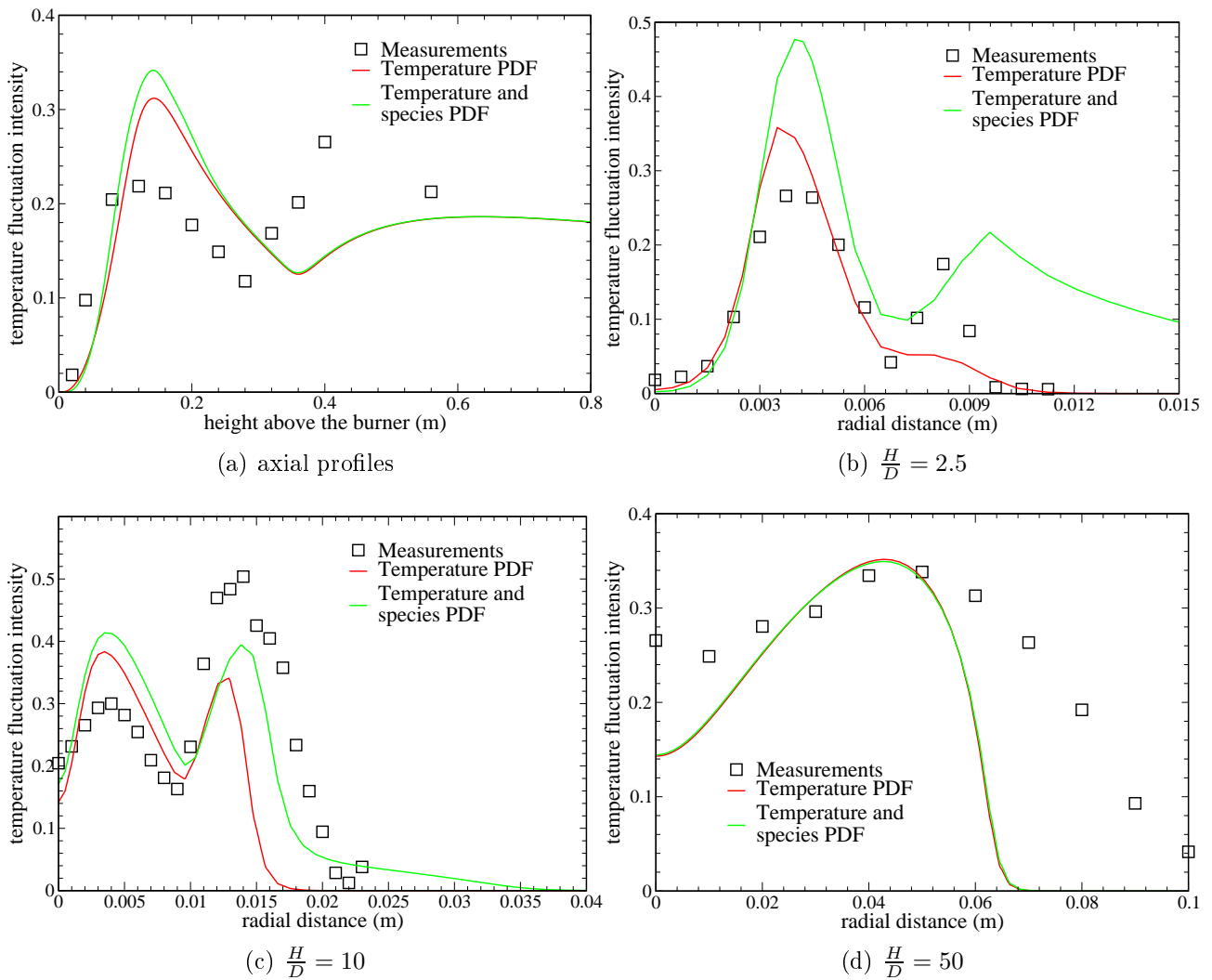


Figure 4.4.13: Temperature fluctuation intensity profiles for the H3 jet flame.

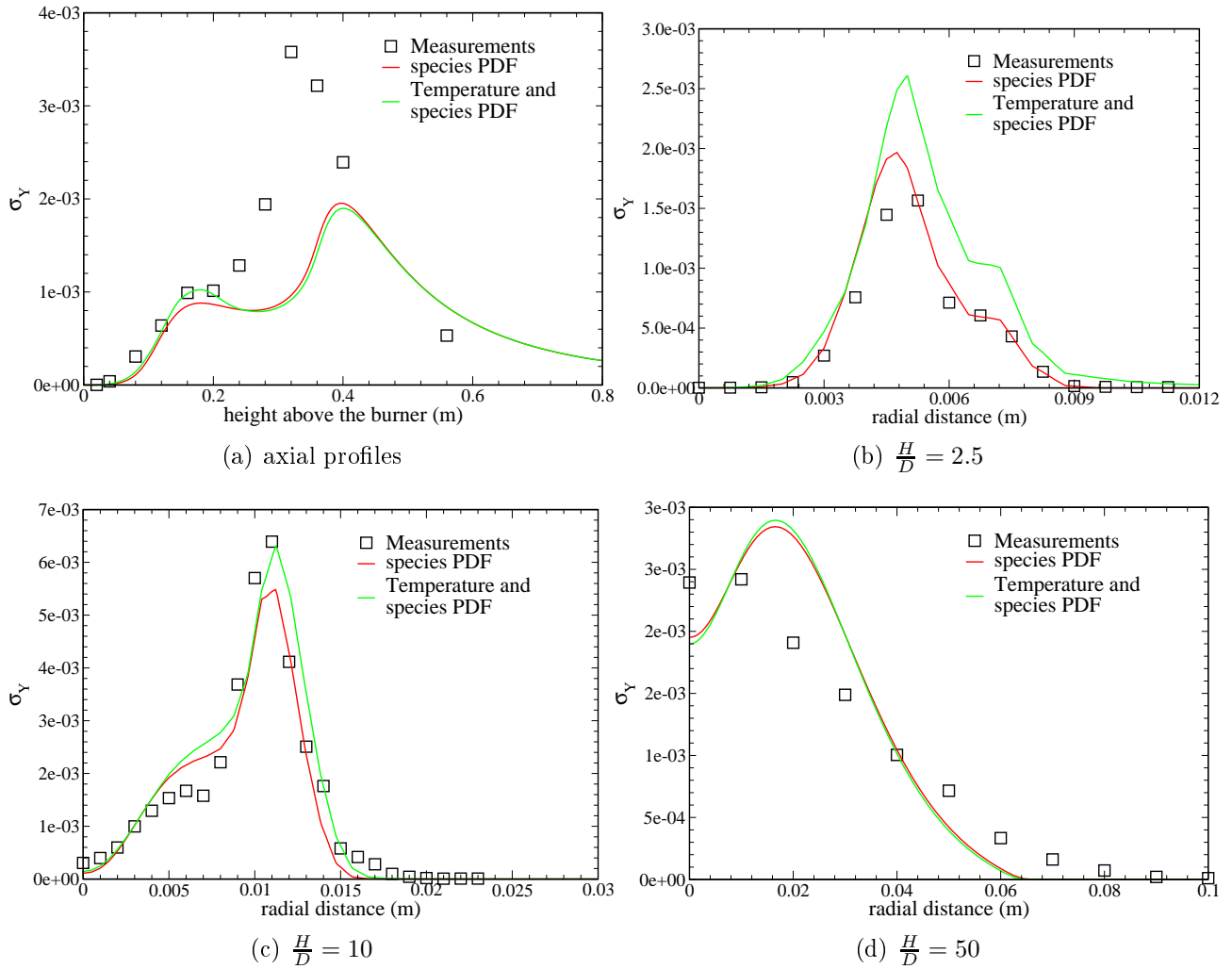


Figure 4.4.14: Turbulent scalar energy for the H3 jet flame.

A comparison of the experimental and simulated σ_Y profiles is given in Fig. 4.4.14. In this case the agreement is excellent, since even bimodal distributions are quite well reproduced. Discrepancies in the far-field may be related to the bad performance of the turbulence model.

4.4.2 Lifted, H₂/air jet flame in vitiated coflow

The second testcase investigated also represents a H₂/N₂ turbulent diffusion jet flame. If compared with the previous one, fuel inflow velocities are significantly higher. Thus, in order to stabilize the combustion a lean, premixed, laminar flat H₂/air flame is used as coflow. In the experiments [28] a lifted flame is observed, with a lift-off distance which shows an extremely high sensitivity to the coflow temperature [201]. In this configuration a strong influence of temperature and species fluctuations is expected, since they are generated before ignition takes place [14]. This is similar to the flame stabilization mechanism in swirled combustion chambers, where hot products form a recirculation zone and ignite the fresh mixture [135]. Similarly, new combustion concepts as MILD and FLOX [123] strongly rely on the interaction of jets with different temperatures [42].

The boundary conditions are given in Table 4.2. Since no velocity measurements have been carried out, a fully-developed fuel inflow is assumed. In order to provide boundary conditions

Table 4.2: Boundary conditions for the lifted H₂/air flame (Section 4.4.2).

	radius(mm)	composition	temperature(K)	velocity($\frac{m}{s}$)
fuel inlet	2.285	H ₂ : .02342 N ₂ : .97658	300	107 ¹
air inlet	200	O ₂ : .17085 N ₂ : .76431 H ₂ O: .06453 OH: 3.1e-4	1045	3.5 ²
outflow	-	zero gradient	zero gradient	zero gradient
axis	-	zero gradient	zero gradient	zero gradient

¹ The bulk value is given here.

² A constant inflow velocity is used for the coflow.

which are consistent with the employed turbulence model, an additional simulation of the fuel pipe delivers the required radial profiles of \mathbf{V} , k and ϵ at the inflow. The vitiated coflow is assumed to be in thermodynamic equilibrium and the composition is calculated accordingly. Concerning the flow regime, it is laminar and a constant velocity inlet is prescribed. Since there are large differences in momentum between fuel and air (see Table 4.2) this approximation is not expected to affect the results. If not stated otherwise, the chemical kinetics presented in Ref. [149] is adopted. 140 elements are used in both axial and radial direction with more cells in regions where strong gradients are expected.

In order to outline the physics of this flame, several simulations have been performed. Variations in chemical kinetics, turbulence model parameters and coflow temperature are investigated since they determine the flame behavior.

4.4.2.1 Reference simulation

In Fig. 4.4.15 temperature and OH distributions are given the reference simulation. Because of the high flow velocity and low hydrogen concentrations of the fuel mixture, a lifted flame in a partially-premixed regime is obtained. As for the ignition problem (subsection 2.2.3), a unique definition of the lift-off distance does not exist. According to Cabra and coworkers [28] it can be defined as the height at which Y_{OH} reaches 600 ppm. In Fig. 4.4.15 the $Y_{OH} = 600$ ppm isoline is superimposed on the OH contours and a lift-off distance of about 13 D is obtained. This value is slightly higher than the experimental value, where a mean value of 10 D has been observed.

Since the boundary conditions (in particular the coflow temperature) are different from what has been discussed in subsection 4.4.1, the phenomena responsible for flame stabilization are different too. Here chemical kinetics, which do not play an essential role in the H3 flame, explain the flame behavior much better than turbulent diffusion does. Mixing between the

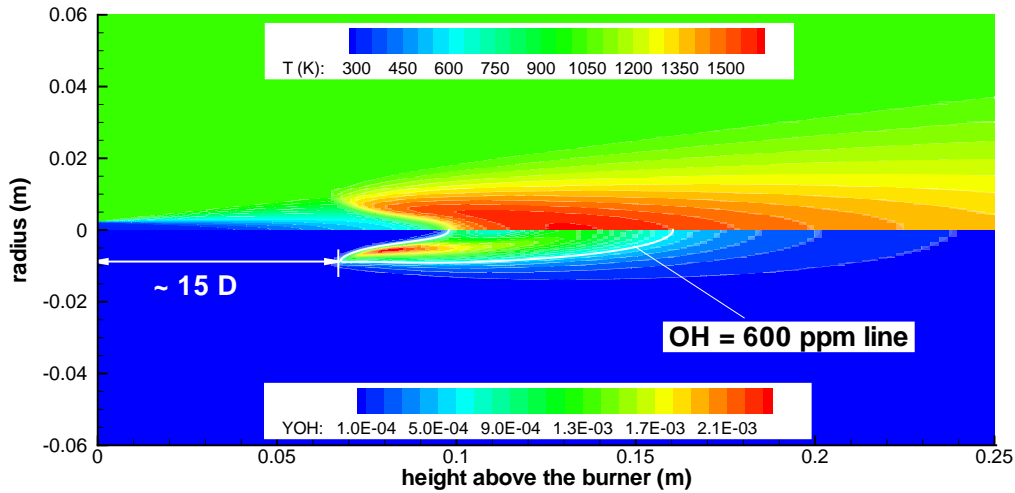


Figure 4.4.15: Temperature and OH distributions of the lifted H_2/air flame [28].

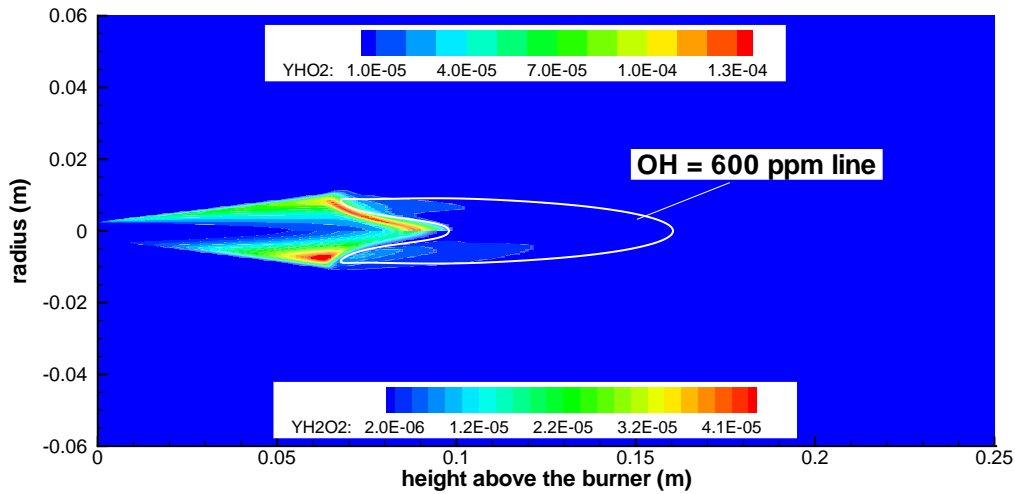


Figure 4.4.16: HO_2 and H_2O_2 distributions of the lifted H_2/air flame [28].

vitiated hot coflow and the cold jet enhances reactions responsible for the production of HO_2 and H_2O_2 which are more active at temperatures below 1000 K



As a side effect, H atoms are produced which again can attack O_2 or H_2 to form more radicals. If H_2O_2 reaches high concentrations the chain-branching reaction



prevails and the mixture is ignited. HO_2 and H_2O_2 plots given in Fig. 4.4.16 support this hypothesis since high concentrations of both species are found well before ignition takes place.

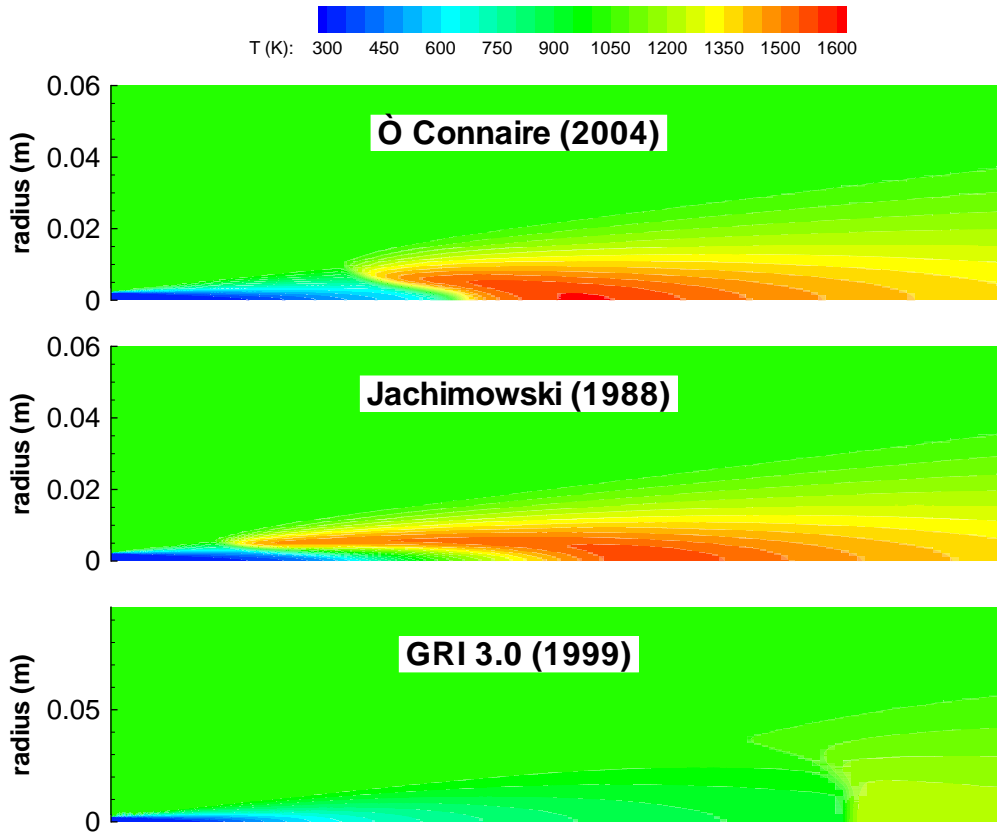


Figure 4.4.17: Influence of the kinetic mechanism on the temperature distribution of the lifted H_2/air flame [28].

4.4.2.2 Influence of the simulation parameters

Some of the kinetic mechanisms described in the subsection 2.2.3 have been tested using this testcase. In Figs. 4.4.17 and 4.4.18 the corresponding temperature and OH distributions are shown. As expected, strong differences in the lift-off distances are observed. They are consistent with the zero-dimensional simulations and the mechanism predicting a shorter ignition delay in the constant-pressure reactor also gives a lower lift-off height. Since all mechanisms are based on the same thermodynamic and transport databases, these discrepancies are essentially due to chemical kinetics effects [127].

It should be noted that the degree of premixing of the jet with the coflow proceeds with increasing height above the burner. That means that the regime at which the flame is stabilized depends on the lift-off distance. In other words, mechanisms which predict large lift-off heights would stabilize the flame under almost premixed conditions. Moreover, with an increased premixing the flame front becomes shorter and more perpendicular to the streamlines, since the flame speed increases. This high and non-linear sensitivity with respect to the kinetic mechanisms has also been found with more complex turbulence-chemistry interaction models, like the transported-PDF approach [30].

The importance of the $\text{HO}_2/\text{H}_2\text{O}_2$ submechanism is endorsed in Fig. 4.4.19, where temperature and OH distributions are obtained by using the complete (9 species, 19 reactions [94]) and the abridged (7 species, 7 reactions [2]) mechanisms of Jachimowski. In the abridged version,

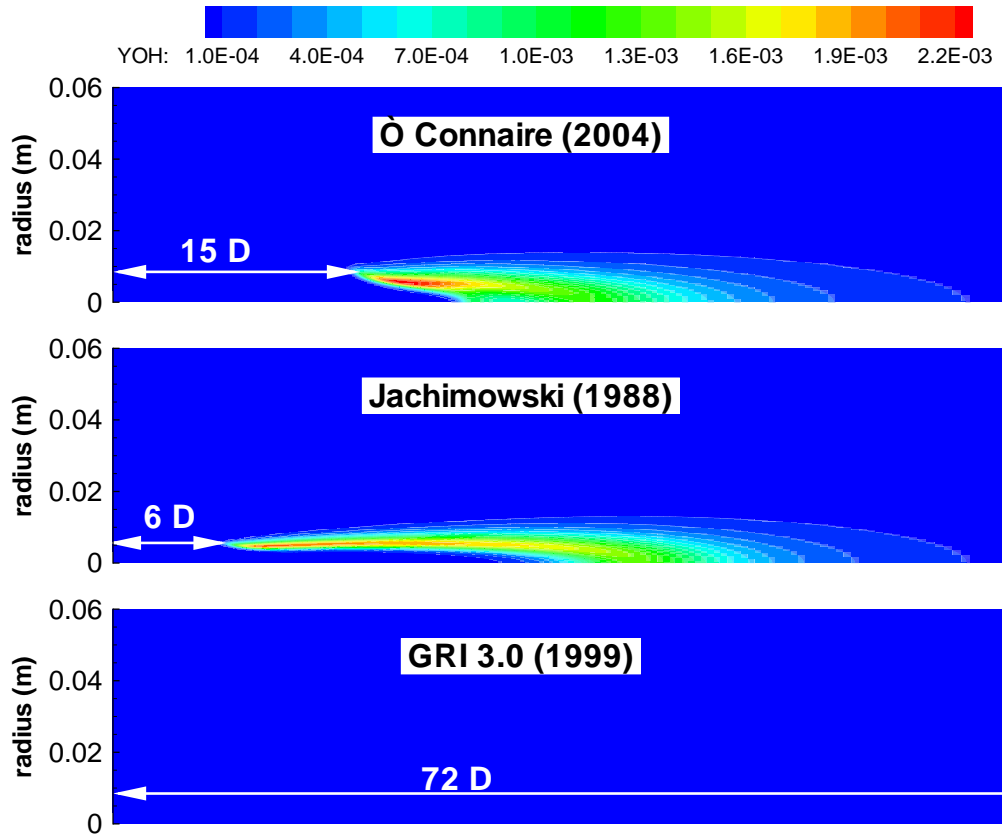
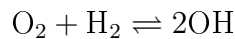


Figure 4.4.18: Influence of the kinetic mechanism on the OH distribution and lift-off distance of the lifted H_2 /air flame [28].

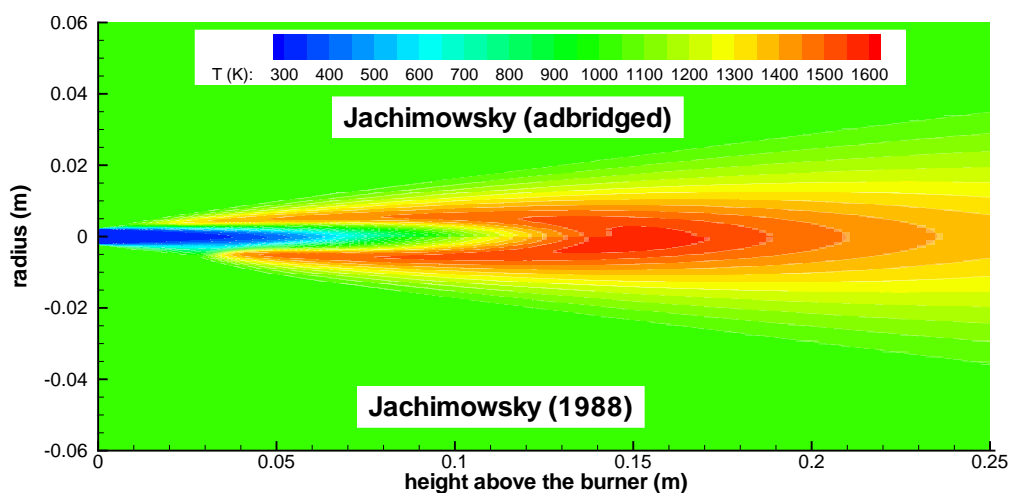
where chemical reactions involving OH_2 and H_2O_2 are neglected, the single reversible reaction



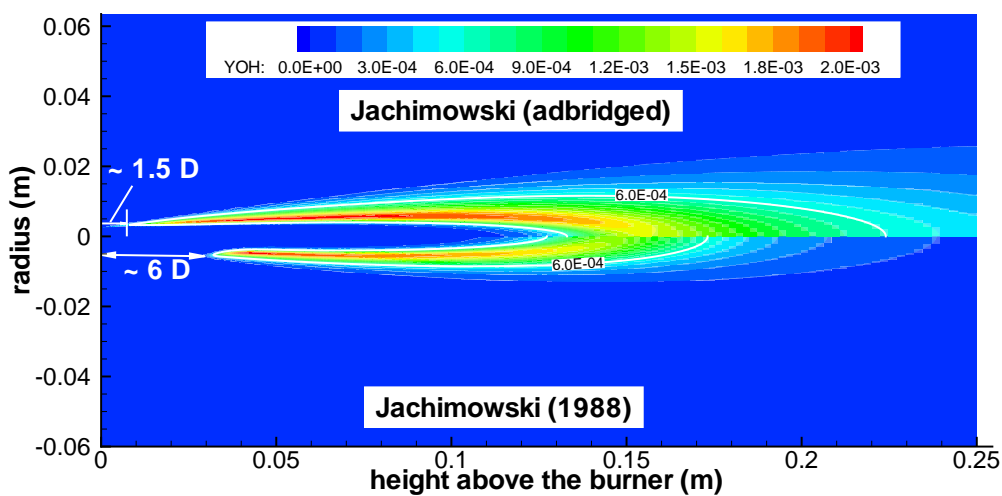
is responsible for ignition. Thus, a pretty smaller lift-off height is predicted, as ignition takes place as soon as fuel and air are mixed. These results are in agreement with DNS studies performed using the same initial compositions in homogeneous turbulence. They highlight the importance of the intermediate species on the ignition delay and, in particular, their interaction with the turbulent eddies may play a fundamental role in starting the combustion process [183].

The high sensitivity of the experiment concerning the boundary conditions is demonstrated in Fig. 4.4.20, where simulations using different coflow temperatures are compared. The observed large differences are in agreement with the results of previous works [31, 201] and can be explained by the fact that ignition takes place in a critical temperature range where the ignition delay shows a high sensitivity to the initial temperature¹¹. Additionally, the lift-off distance is a non-linear function of the coflow temperature. There is a kinetic-based stabilization mechanism which is able to explain this behavior, since the equilibrium between the production

¹¹This has been confirmed by zero dimensional simulations (subsection 2.2.3).



(a) Temperature



(b) OH

Figure 4.4.19: Influence of the HO₂/H₂O₂ submechanism on the temperature and OH distributions of the lifted H₂/air flame [28].

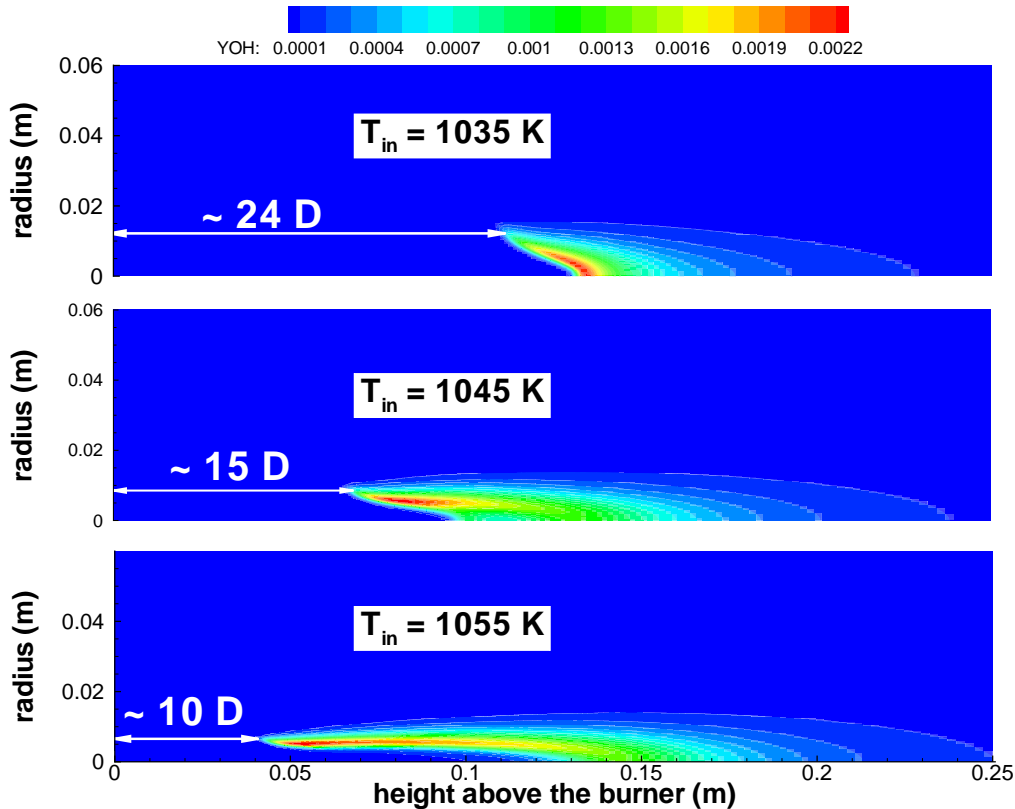


Figure 4.4.20: Influence of the coflow inlet temperature on the OH distribution of the lifted H_2/air flame [28].

of HO_2 and H_2O_2 (Eqs. (4.4.2)-(4.4.5)) and their conversion into O, H and OH is a highly non-linear function of the temperature. Such a high sensitivity has also been observed in another experiment where a lifted CH_4/air flame has been investigated using the same geometry¹² [28].

The influence of the $k-\epsilon$ turbulence model closure constant C_1 on the temperature predictions is shown in Fig. 4.4.22. The lift-off distance (Fig. 4.4.21) is dramatically affected by this constant and a change of 10% causes differences in the lift-off height of 34%. Since a lower value of C_1 increases the turbulent intensity, these results are consistent with three-dimensional DNS simulations [183]. In particular they show that ignition delay in a non-premixed medium decreases with increasing turbulence intensity (i.e. better mixing). An interesting result is that the flame stabilization is shifted towards a diffusion-based mechanism if the original constant is used. This is demonstrated by additional simulations performed with $C_1 = 1.44$ (not shown in this work) where a lower sensitivity with respect to the inlet temperature has been observed.

4.4.2.3 Influence of the assumed-PDF model

Since the temperature and species fluctuations are expected to have a strong influence on the simulations, their effects are first considered separately. Temperature and temperature fluctuation intensity (I_T) fields are shown in Fig. 4.4.23 for a simulation which only takes the temperature fluctuations into account. In this particular case, the ignition takes place where high temperature fluctuations occur, as experimental data also show [29]. The comparison

¹²Further uncertainties may result from the coflow velocity which also may affect the lift-off height [188].

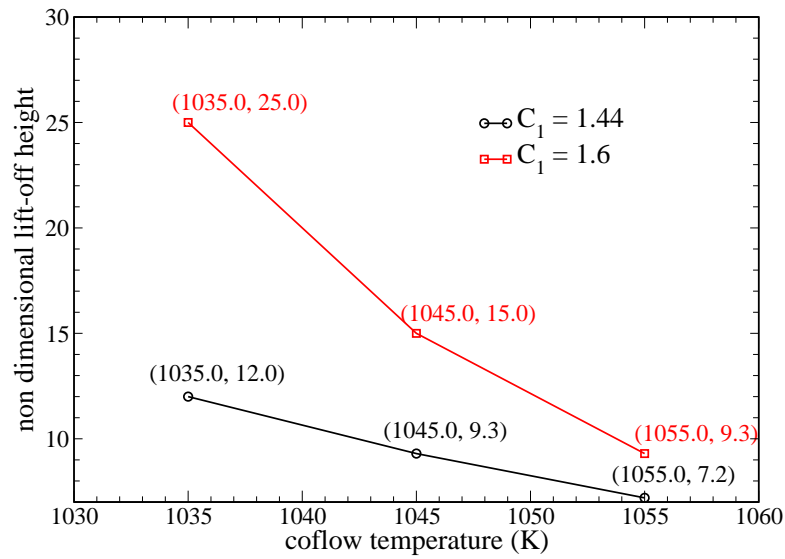


Figure 4.4.21: Non-dimensional lift-off heights as functions of the inlet coflow temperatures with standard and modified C_1 constant of the $k - \epsilon$ turbulence model.

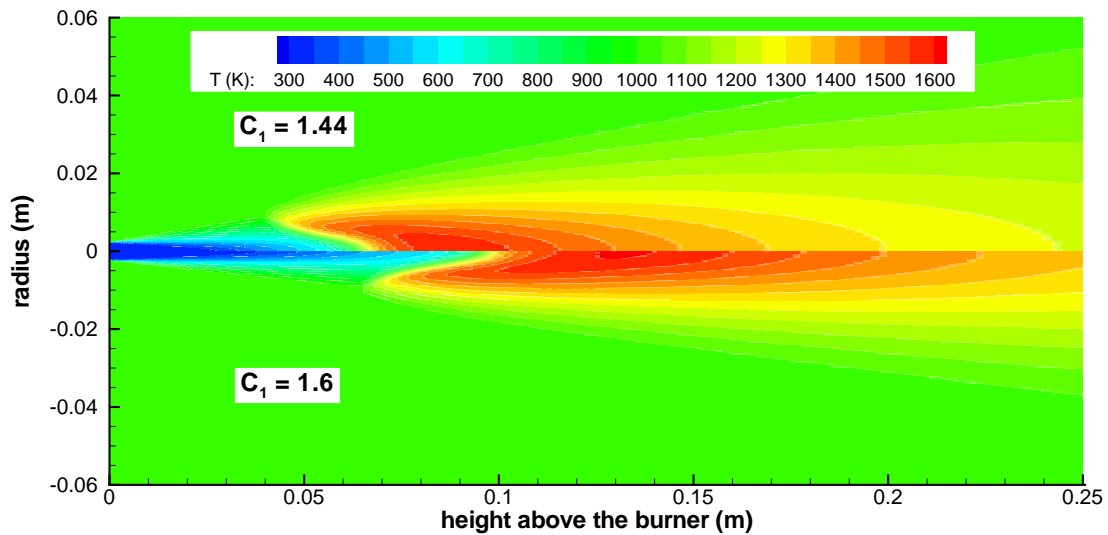


Figure 4.4.22: Influence of the constant C_1 of the $k - \epsilon$ turbulence model on the temperature field of the lifted H_2 /air flame [28].

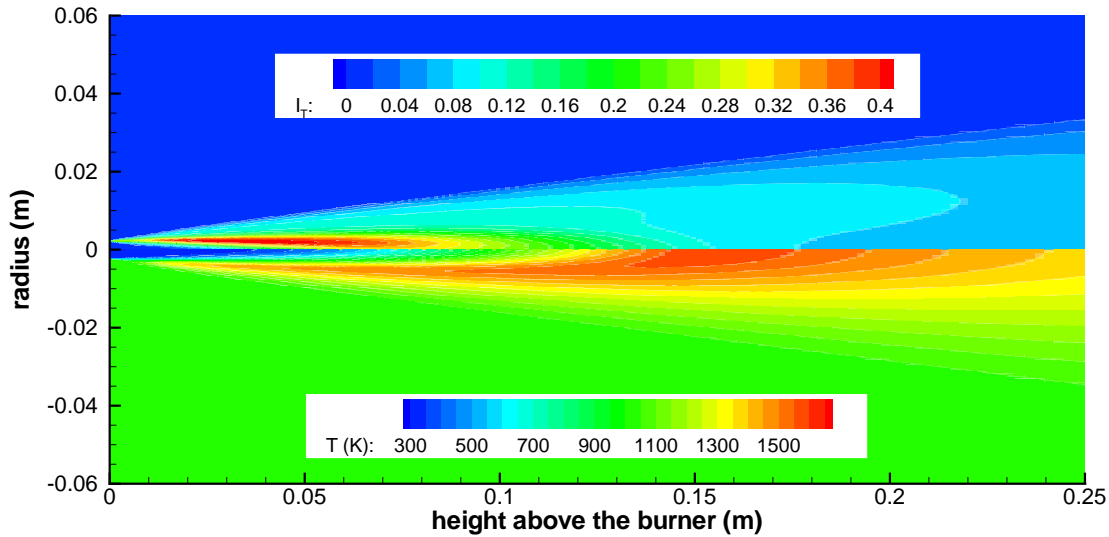


Figure 4.4.23: I_T and temperature fields of the lifted H_2 /air flame [28].

between Fig. 4.4.23 with Fig. 4.4.15 demonstrates the large effect that the temperature PDF may have.

Of course, the impact of the assumed PDF approach depends on the chemical mechanism as may be seen from Fig. 4.4.24. The flame obtained by using the \dot{O} Connaire mechanism is most affected by the temperature fluctuations and the lift-off distance drops to very small values. In case of the Jachimowski scheme the lift-off distance remains nearly unchanged but lower concentrations of OH are obtained. The GRI 3.0 calculations do not seem to be affected by temperature fluctuations at all.

Temperature and σ_Y distributions are plotted in Fig. 4.4.25 for the case that only the joint β -PDF is used. Large variations are observed, both in the ignition delay and in the peak values. In contrast to the temperature PDF, the species PDF seems to suppress mixture reactivity and a slower overall reaction rate is observed. Referring to Figs. 4.3.5 and 4.3.6, this implies that heterogeneous reactions play the most important role.

An overview of the influence of the temperature and species PDFs is given in Fig. 4.4.26. As already observed for the H3 flame, the temperature PDF causes a thinner flame and the species PDF decrease the mixture reactivity [2]. In case of a joint use of both PDFs, a clear prevalence of the temperature fluctuation effects is observed.

4.4.2.4 Comparison with the experimental data

The experimental dataset from Ref. [28] includes mixture fraction, main species concentrations and temperature as well as their corresponding rms values. These profiles are given at different heights above the burner ($\frac{H}{D} = 1, 8, 9, 10, 11, 14, 26$) and along the symmetry axis. In the experiments the ignition takes place at $\frac{H}{D} = 10$ and a comparison of profiles around this height would be strongly affected by the predicted position of ignition. Thus, only radial profiles above $\frac{H}{D} = 10$ together with the axial trends are compared.

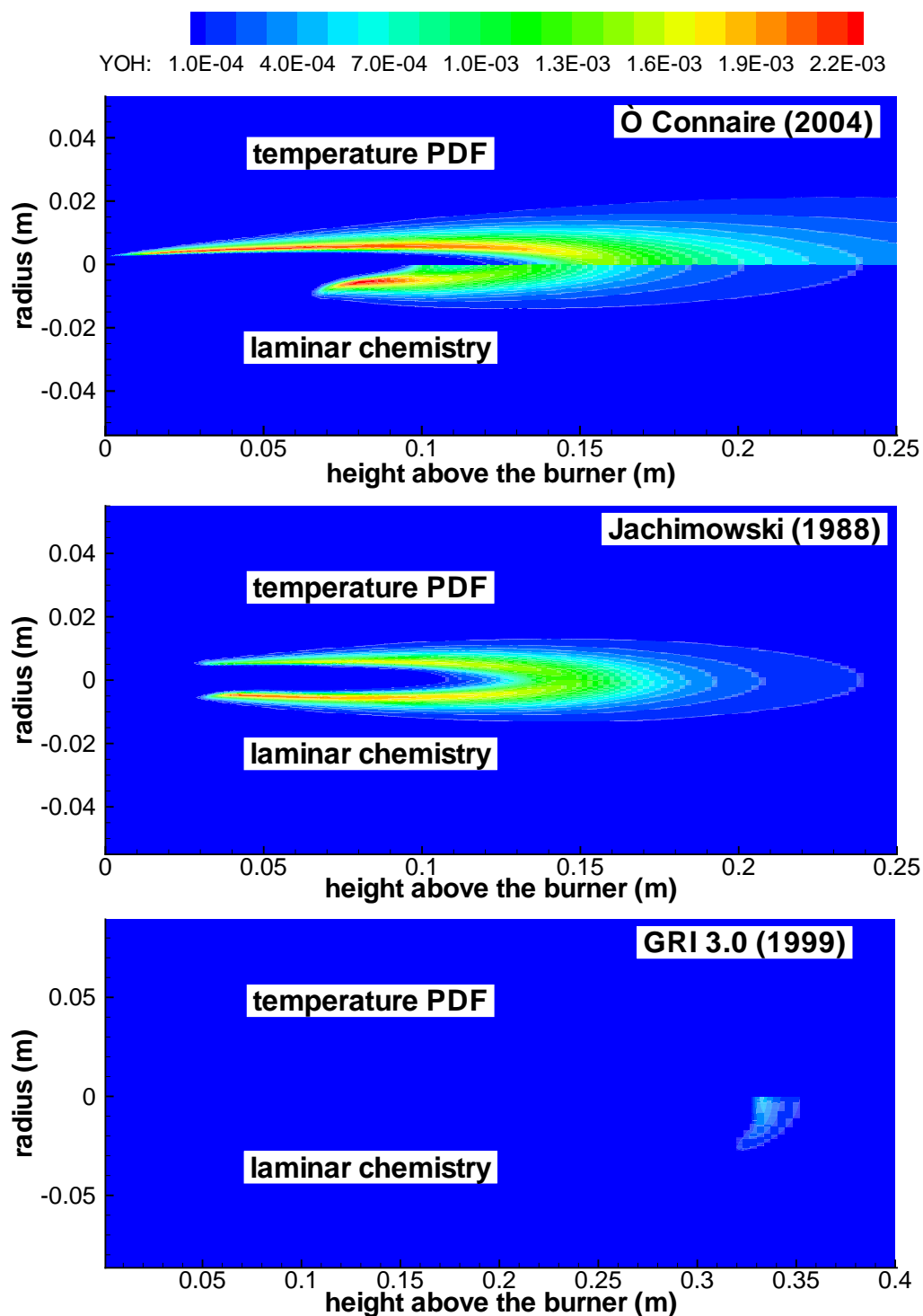


Figure 4.4.24: OH predictions for the lifted H₂/air flame [28] with and without temperature PDF.

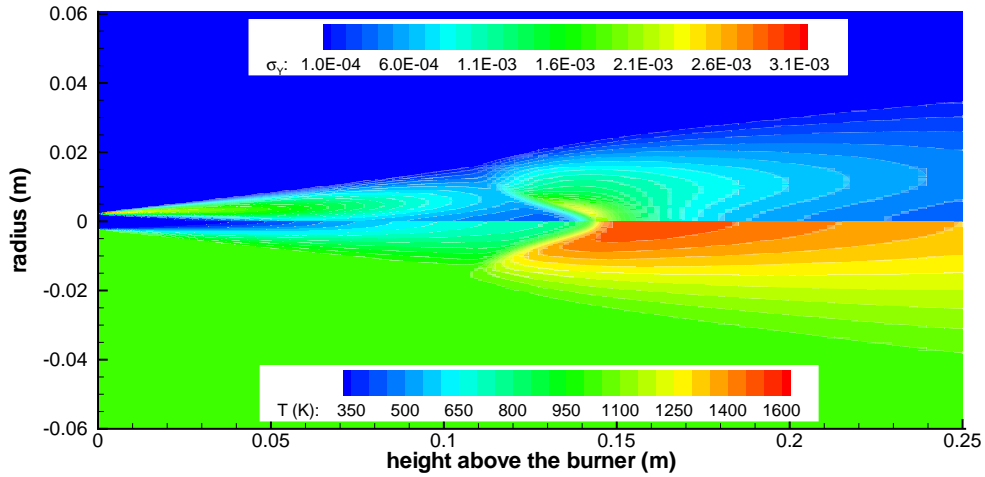


Figure 4.4.25: σ_Y and temperature predictions with the joint β -PDF for the lifted H_2 /air flame [28].

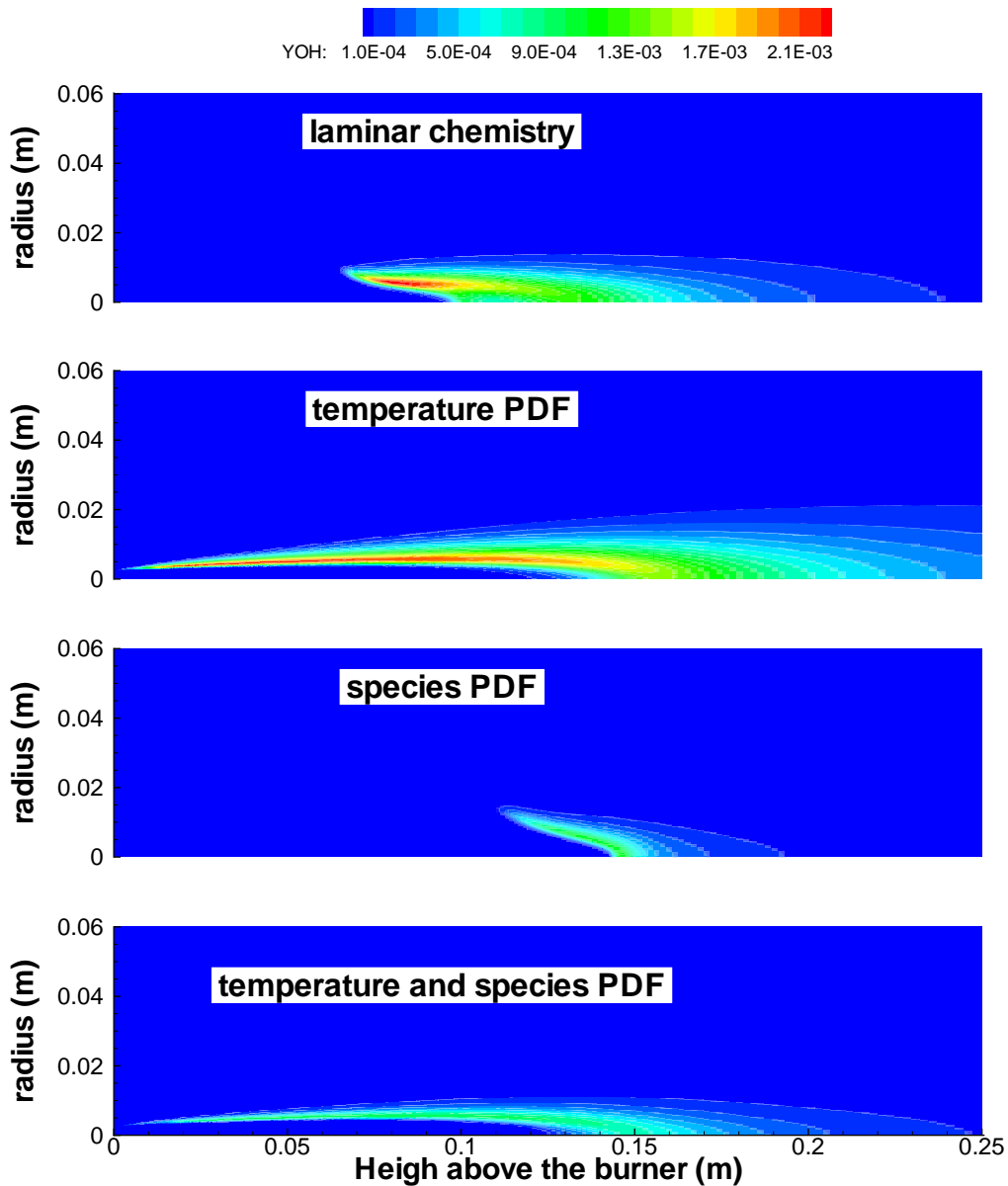


Figure 4.4.26: OH predictions for the lifted H_2 /air flame [28] with and without temperature and species PDFs.

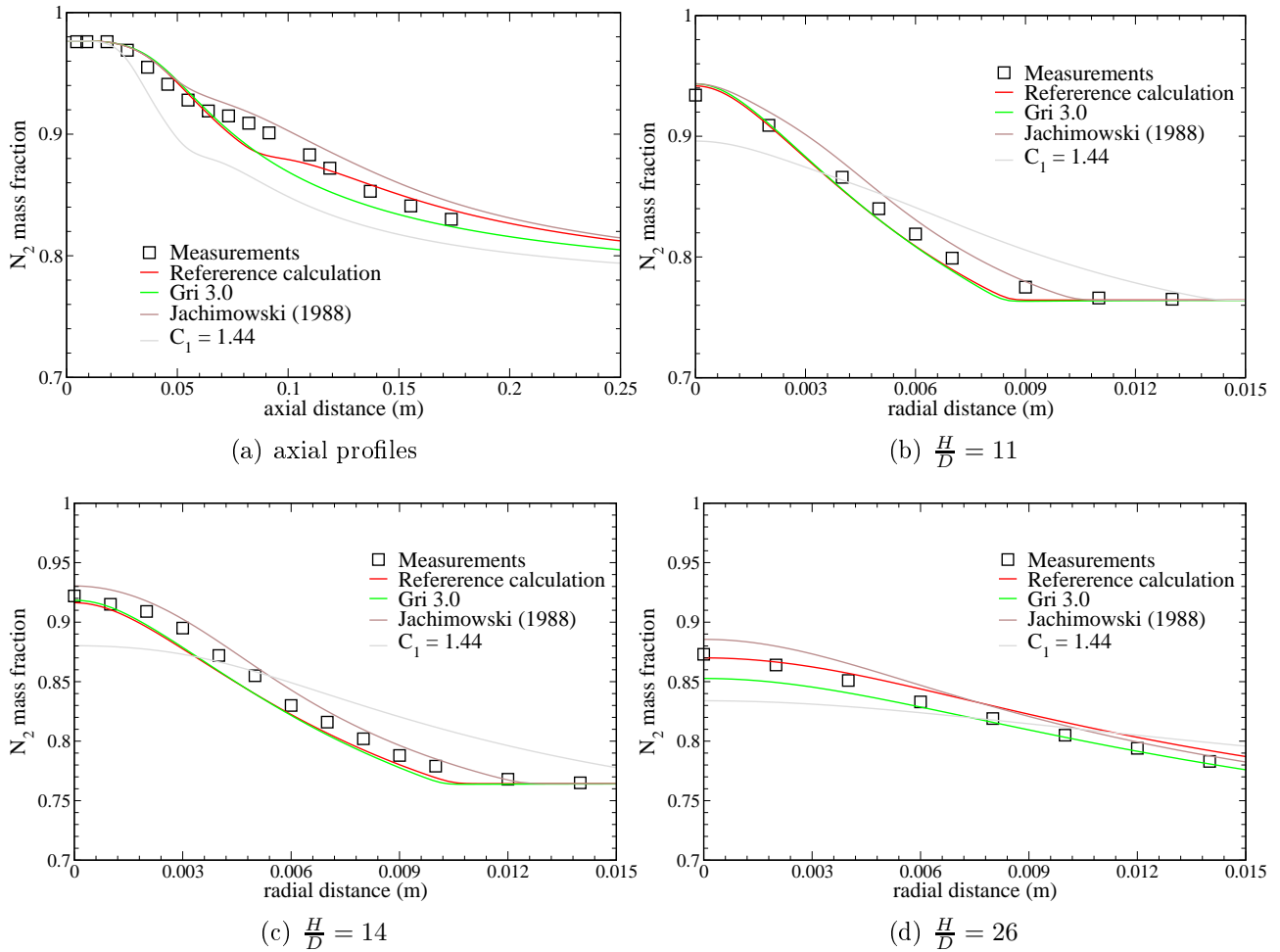


Figure 4.4.27: N_2 mass fraction profiles for the H_2 /air lifted jet flame [28]: influence of turbulence and thermo-chemistry modeling.

The nitrogen profiles shown in Figs. 4.4.27 and 4.4.28 can be used to monitor the influence of the flame on the mixing since experiments outline that only small amounts of NO_x are produced [28]. The plots show that there is a strong interaction between the lift-off distance and mixing since the volumetric expansion due to the combustion damps part of the turbulent fluctuations.

Temperature plots are given in Figs. 4.4.29 and 4.4.30. The profiles at $\frac{H}{D} = 11$ are still strongly affected by the ignition, and larger discrepancies are found. Further downstream the agreement is quite satisfactory even if there are some effects which have to be outlined. Referring to Fig. 4.4.30, the temperature PDF improves the predictions, whereas the exclusive adoption of the β -PDF largely deteriorates the results. The good performance of the Jachimowski mechanism, which does not change if the PDFs are adopted, should also be mentioned. The peak temperatures are slightly overpredicted, probably due to the lack of H_2O radiation losses in the enthalpy equation. Both the axial and radial temperature plots show that the $C_1 = 1.44$ calculation overpredicts the spreading rate and therefore the temperature. These results are in contrast to the work of other researchers [127], which claim that jet flames issued in hot coflows do not suffer from the jet anomaly.

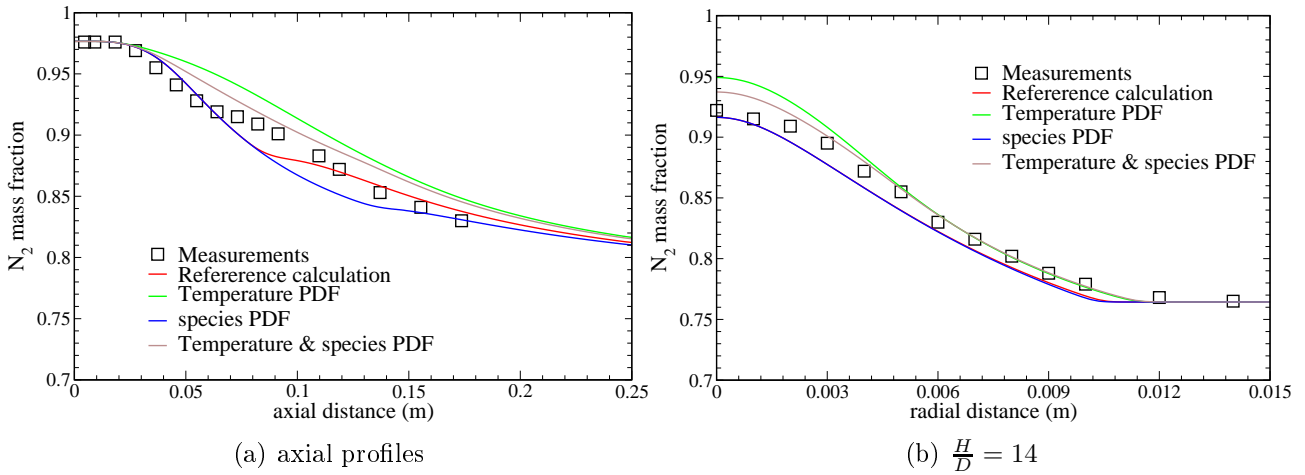


Figure 4.4.28: N_2 mass fractions profiles for the H_2 /air lifted jet flame [28]: influence of temperature and species PDFs.

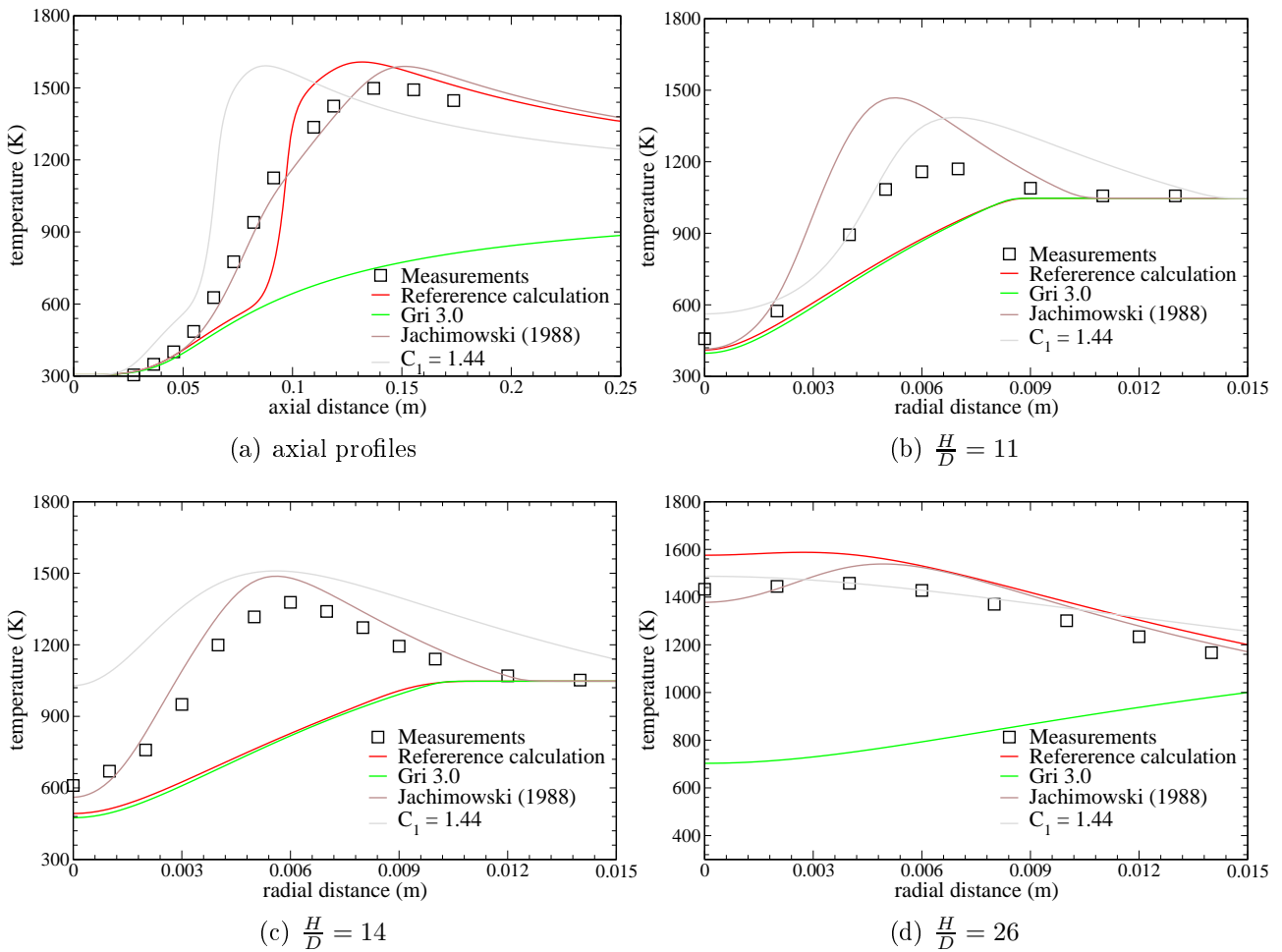


Figure 4.4.29: Temperature profiles for the H_2 /air lifted jet flame [28]: influence of turbulence and thermo-chemistry modeling.

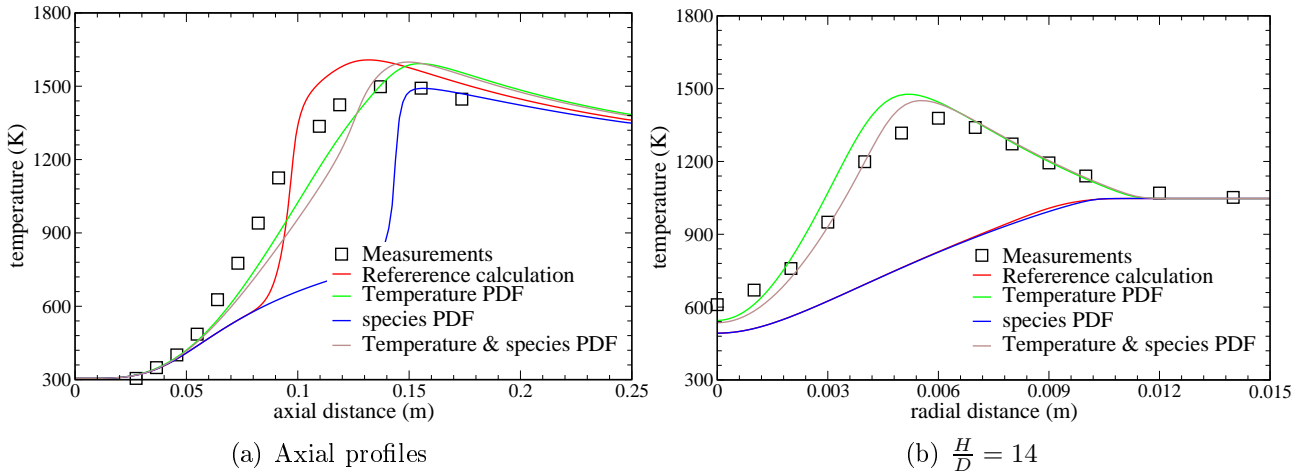


Figure 4.4.30: Temperature profiles for the H_2/air lifted jet flame [28]: influence of temperature and species PDFs.

The hydrogen profiles given in Figs. 4.4.31-4.4.32 are consistent with the above considerations, since the best performance is obtained using Jachimowski's mechanism. Here, the drop of H_2 mass fraction predicted by using the standard $k - \epsilon$ model is evident. At $H/D = 26$ the simulations using both the temperature and species PDFs overpredict the amount of hydrogen, because of the early ignition and the lack of oxygen penetration (see also Fig. 4.4.18).

The temperature fluctuations shown in Fig. 4.4.33 agree very well with the experimental data. Discrepancies are found at $H/D = 26$ which probably are due to the coupling between temperature and species fluctuations, discarded in this work. This missing coupling may also explain the absence of large variations in the I_T profiles if the β -PDF is added to the system.

Profiles of the scalar turbulent energy σ_Y are compared in Fig. 4.4.34. In this case the temperature PDF has a large influence since large variations in the lift-off point and the flame structure are obtained. In particular, the joint use of both PDFs improves the agreement with the experimental profiles.

The presented results demonstrate that the inclusion of the temperature and species fluctuations in the calculation of averaged source terms is necessary in order to predict the ignition delay accurately. Moreover, a strong influence of the temperature and species fluctuations on the results are observed. The temperature fluctuations strongly affect the flame structure, the ignition point and the heat release rate. On the other hand, the species fluctuations do not change the flame behavior significantly, but they have a large influence on the predictions of the minor species.

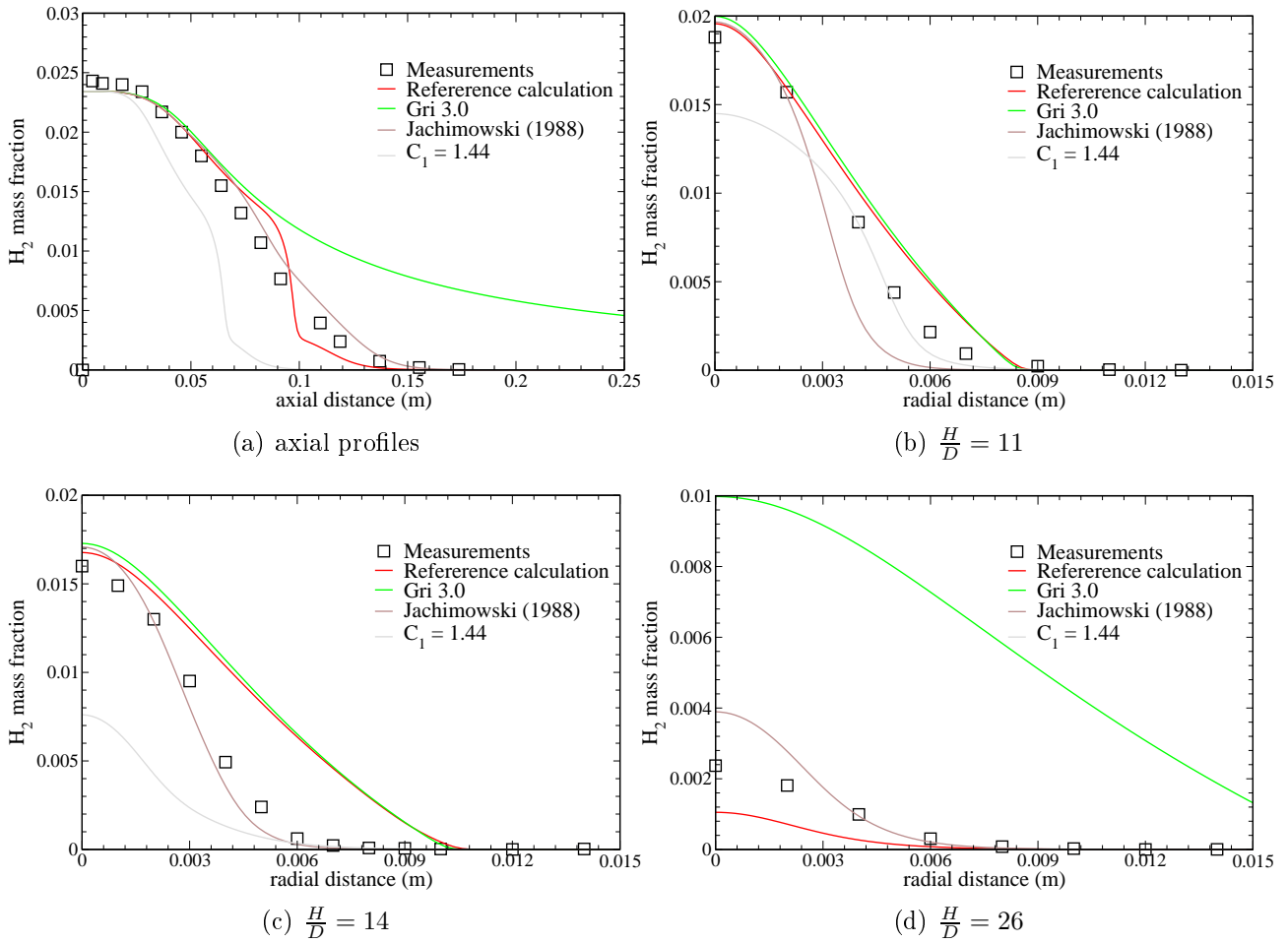


Figure 4.4.31: H_2 mass fractions profiles for the H_2 /air lifted jet flame [28]: influence of turbulence and thermo-chemistry modeling.

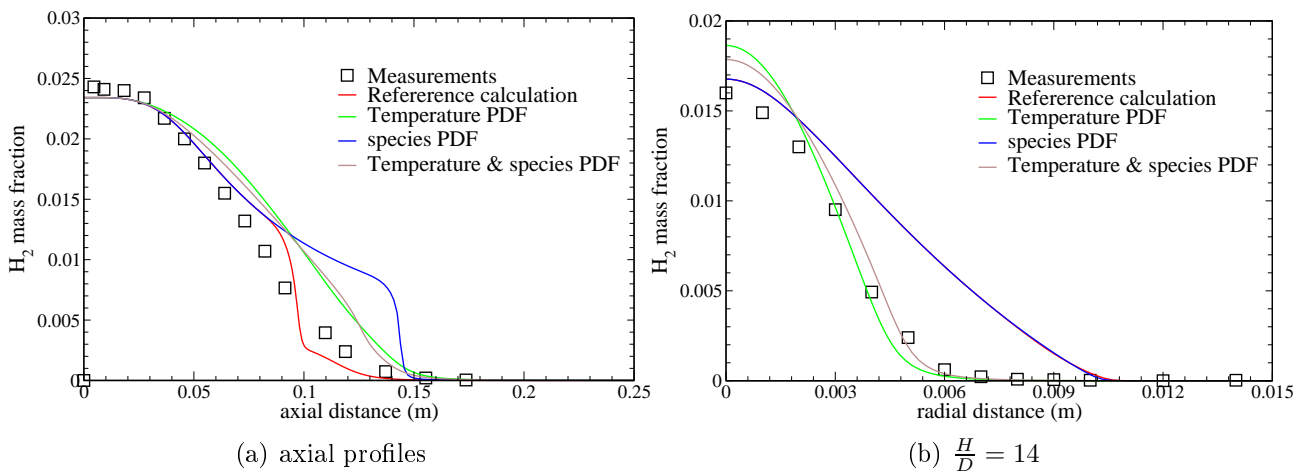
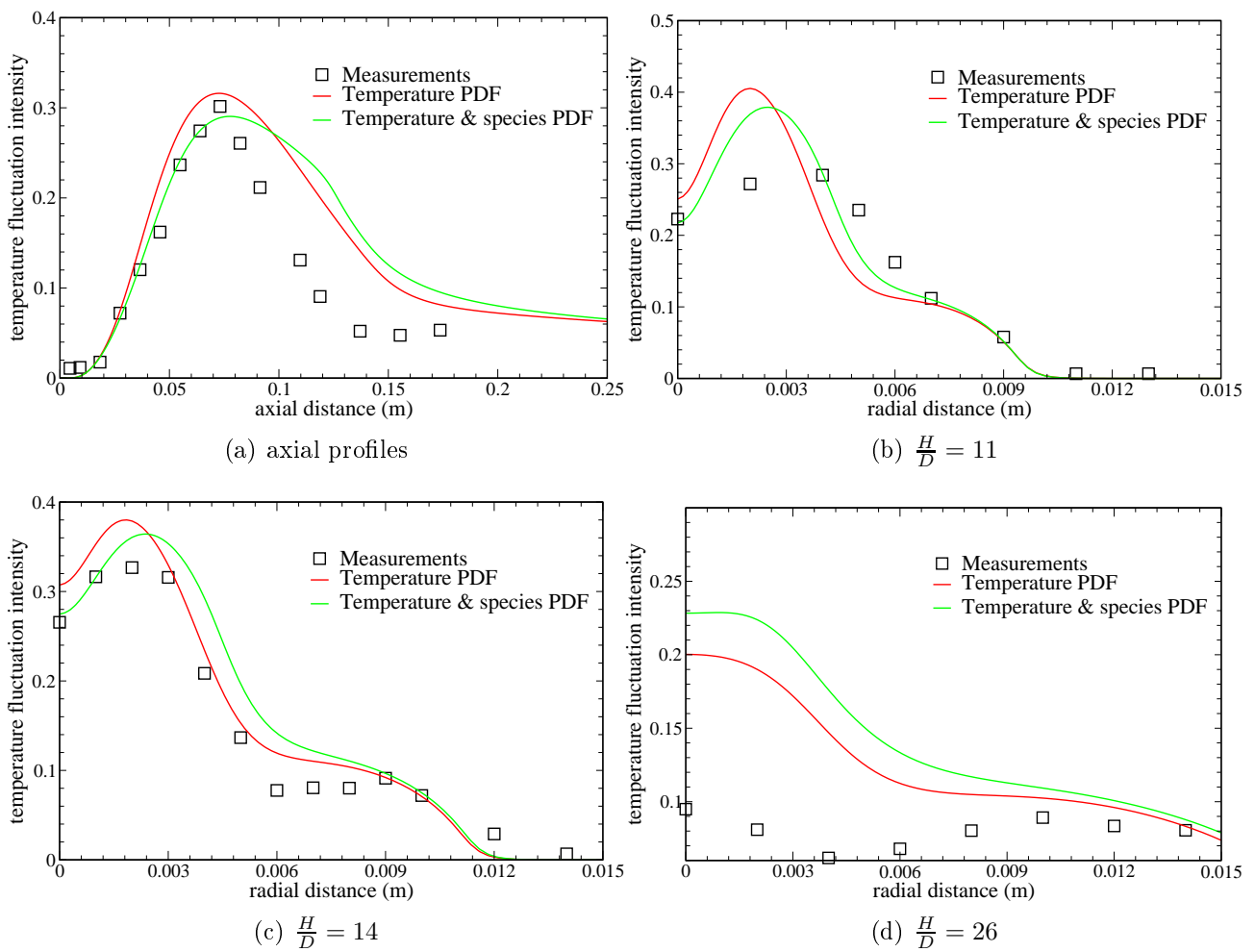


Figure 4.4.32: H_2 mass fractions profiles for the H_2 /air lifted jet flame [28]: influence of temperature and species PDFs.

Figure 4.4.33: I_T profiles for the H_2 /air lifted jet flame [28].

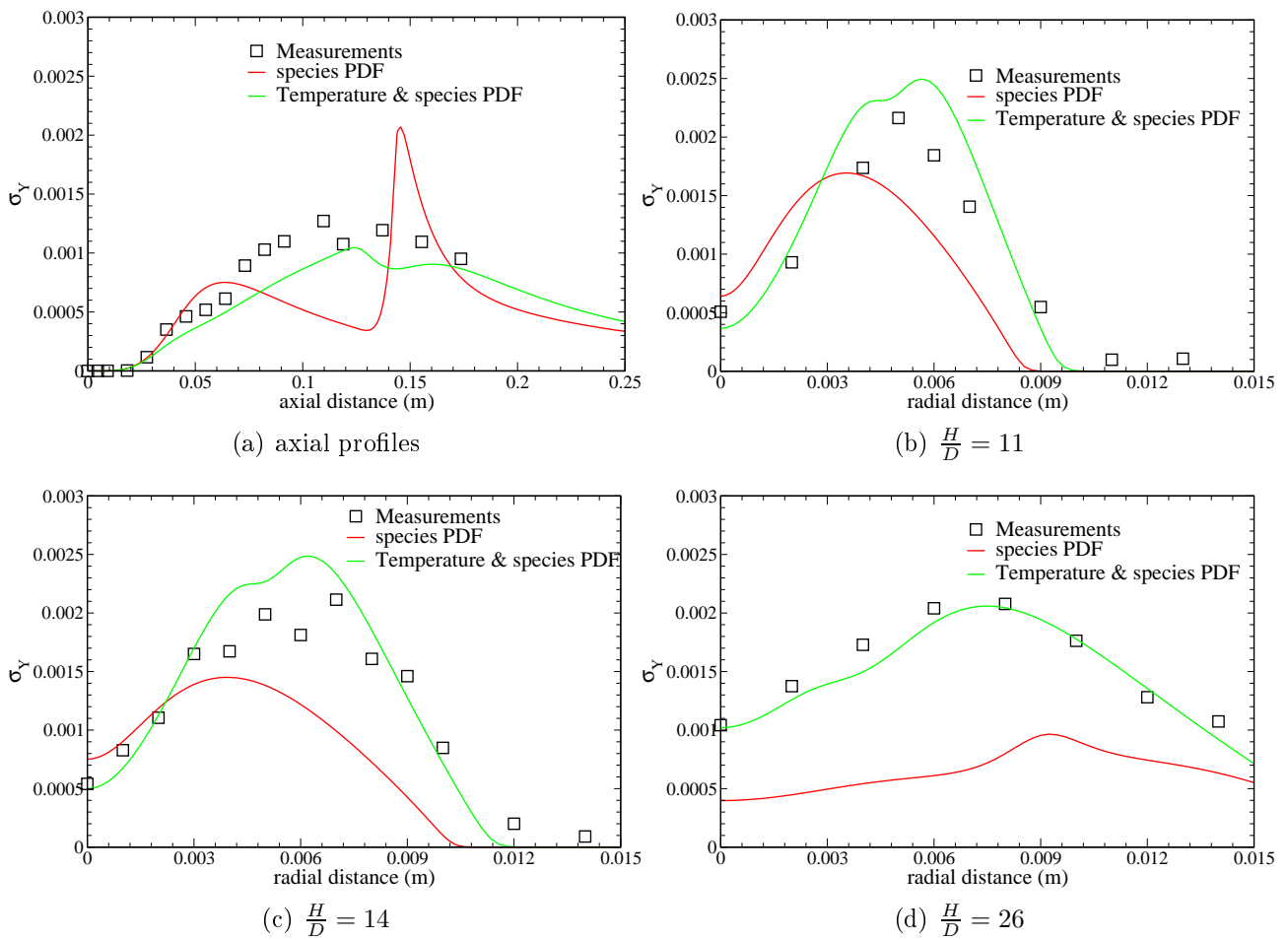


Figure 4.4.34: σ_Y profiles for the H_2 /air lifted jet flame [28].

5 Soot formation in semi-technical scale burners

5.1 Introduction

In this chapter all models developed and validated in the previous parts are employed for the numerical investigation of a semi-technical scale burner. *Semi-technical scale* means that:

- the geometry does not reach the complexity found in industrial real size applications, but is close to them;
- and working conditions (in particular the pressure) are comparable to those of real combustors, even if in the present case pressures are lower because of experimental limitations.

Nevertheless, this investigation already has a high degree of complexity and the flow patterns correspond to those of real devices. On the other hand, semi-technical scale also means that the system runs under controlled boundary and operating conditions, what is impossible in real combustors.

Combustion chambers for propulsion and energy production devices are based on the same design principles (see Fig. 5.1.1):

- A splitting of the incoming air into a primary and a secondary flow. The first usually enters the combustion chamber through a swirler and feeds the main combustion zone. The secondary air is used as coolant medium and to reduce pollutants.
- A reaction zone where air and fuel are mixed and a near stoichiometric combustion is obtained. Since the flow velocities are usually higher than the turbulent flame speed, a mechanical (bluff-body) or fluid dynamic (swirl) flame stabilization mechanism has to be provided. In order to minimize the pressure losses in the combustor, swirled flows are commonly used. Radial pressure gradients caused by the tangential velocity component create large recirculation zones in the combustion chambers. In such regions the premixing of hot combustion products and fresh air promotes ignition.
- Because of mechanical and emission-related reasons, hot gases have to be cooled down before they enter the turbine. Secondary air inflows can be either distributed (i.e. film-cooling systems) or local (i.e. quenching jets). Film cooling is mainly used to protect the

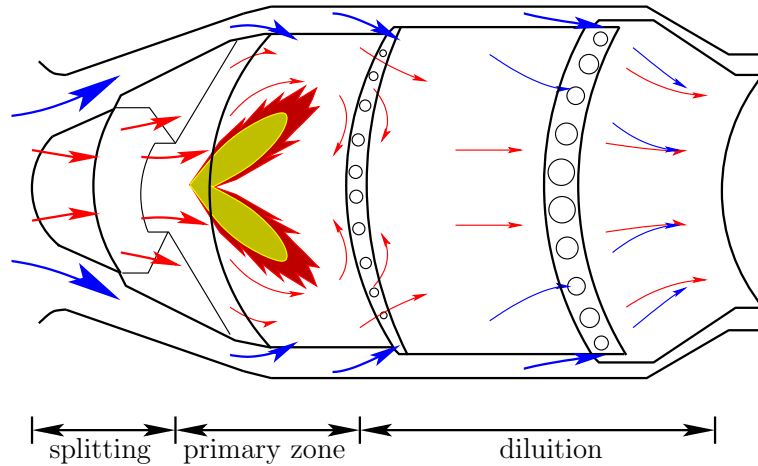


Figure 5.1.1: Schematic representation of a combustion chamber for propulsion applications [114].

chamber walls from high temperatures while quenching jets have a large impact on the pollutant formation and oxidation.

The presented layout is only one out of several possible designs which are currently used. Since the detailed experimental or numerical investigation of industrial devices is infeasible, subscale burners are designed in a way that they retain their most important features. The analysis of such systems at different operating and boundary conditions allow conclusions which may help to improve future combustion chambers.

5.2 The SiA semi-technical scale burner

The SiA semi-technical scale burner is designed to study the soot formation under gas-turbine like conditions [111]. It can work both with gaseous or pre-vaporized fuels at pressures ranging from 1 to 10 bars. In this work ethylene is considered as fuel [111].

A sketch of the simulated geometry is given in Fig. 5.2.1. Since the combustion chamber has a square section, a 90-degree slice is simulated. Swirling air is provided by a double co-swirler nozzle plotted in Fig. 5.2.1(b). The swirler channels are included in the simulations since they provide a strongly non-uniform velocity profile. Both the inner and outer swirlers are fed by a common plenum chamber (not shown). A problematic aspect of the experiments is that the air splitting ratio α_r between the outer and inner swirlers has not been measured. Since an inclusion of the plenum in the simulation is beyond the available computer facilities, information coming from previous works have been used in order to define correctly the inflow conditions. In a work by Lehmann [115] the same geometry (scaled up by a factor of two) has been extensively investigated experimentally and a ratio

$$\alpha_r = \frac{\dot{m}_{outer}}{\dot{m}_{inner}} = 1.5 \quad (5.2.1)$$

between mass inflows of 60% (outer swirler) to 40% (inner swirler) has been measured. In this study this value is used without any modification.

Table 5.1: Experimental conditions for the SiA semi-technical scale burner.

testcase identification	pressure (bar)	ϕ	primary air ($\frac{\text{kg}}{\text{m}^3}$)		oxidation air ($\frac{\text{kg}}{\text{m}^3}$)	Re			swirl number
			inner swirler	outer swirler		inner swirler	outer swirler	secondary	
C2H4-3-1.4-1	3	1.4	1.2e-3	1.7e-3	2.9e-3	4400	6600	6800	.43
C2H4-3-1.4-0	3	1.4	1.2e-3	1.7e-3	0	4400	6600	0	.76
C2H4-5-1.2-1	5	1.2	2.9e-3	4.4e-3	7.3e-3	11000	16500	17300	.41
C2H4-9-1.2-9	9	1.2	5.3e-3	7.9e-3	1.2e-2	20000	29700	27900	.41

In order to investigate quenching effects of the secondary air on the flame and soot formation, air may be injected from pipes located at the corners of the combustor directly in the post-flame zone. Several ratios between primary and secondary air mass flows (ranging from zero to one) have been investigated experimentally.

The corresponding combustor conditions are summarized in Table 5.1. The testcase identification code is based on the fuel name (C_2H_4 in all cases), pressure (in bar), ϕ (in the primary zone only) and the secondary-to-primary mass flux ratio. Non-dimensional numbers are calculated using the conditions at the nozzle exit ($x = -3.0$ cm). The Reynolds numbers are based on the mass fluxes and geometric areas

$$Re_i = \frac{\dot{m}_i}{\mu\sqrt{A_i}}, \quad (5.2.2)$$

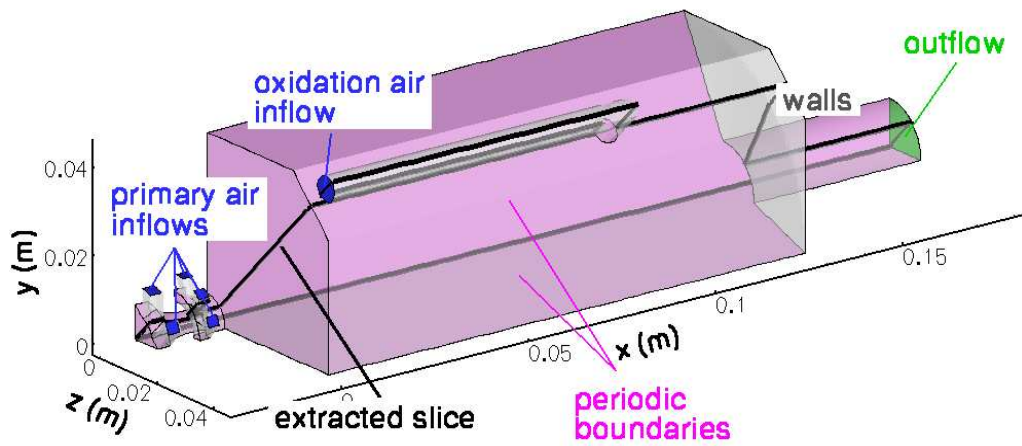
where i either represents the outer, inner or oxidation inlets. The swirl number is defined as the ratio between flux of tangential momentum and axial thrust

$$S_n = \frac{\int_A \rho U_\tau U_{ax} dA}{[\int_A \rho U_{ax}^2 dA + \int_A (p - p_\infty) dA]} \quad (5.2.3)$$

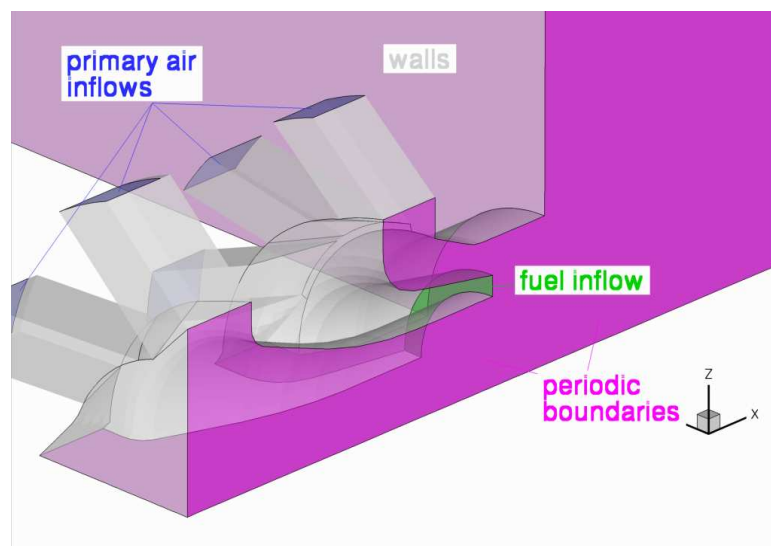
where A is the nozzle exit area. All values given in Table 5.1 are based on the calculated velocity and pressure fields at the nozzle exit. With exception of C2H4-3-1.4-0, a nearly constant swirl number of about 0.41 is obtained. According to [114], those are *weak* swirling flows which should induce small recirculation zones only.

The testcases of Table 5.1 have been chosen in order to investigate the influence of several parameters on the soot formation rate. The investigated thermodynamic conditions (in particular pressure) are still far from industrial requirements, but they allow to draw some conclusions. The first two simulations are performed for the same pressure with and without oxidation air, respectively.

The inlet velocities for the simulations are calculated from the given mass flow rate and are set to be constant at each boundary. Since both swirlers and the oxidation pipe are included



(a) whole domain



(b) swirler

Figure 5.2.1: Computational domain used to simulate the SiA semi-technical scale burner (a) and detail of the air swirling nozzle (b).

in the simulation, the assumption of constant inflow values only has a minor impact on the results. The $k - \epsilon$ turbulence model is used to close the averaged equations and constant turbulent Prandtl and Schmidt numbers of 0.7 are assumed for the modeling of energy and species transport. About 10^5 hexahedral elements have been used for the discretization of swirler, nozzle and combustion chamber with smaller elements in regions where high gradients are expected.

The kinetic scheme proposed by Appel et al. [4] for C₂-fuels is employed to describe the gas phase chemistry and the same modifications presented in Chapter 3 are adopted. The resulting mechanism consists of 71 species and 394 reversible reactions. Soot model parameters are taken from Table 3.1 together with the PAH Arrhenius constants used in the second simulation of Table 3.4.

If not stated otherwise, the temperature and species PDFs presented in Chapter 4 are employed. The influence of temperature fluctuations on the PAH and soot Arrhenius functions has been included in a similar way as for elementary reactions. Due to the properties of the Γ -function, an analytical solution of the soot source term integration is impossible. Thus, the influence of the species fluctuations on the PAH and the soot formation rate is neglected. Averaged Arrhenius functions have been calculated for the [300, 2700] temperature range and turbulent fluctuation intensities up to 0.8. The integrated reaction rates are interpolated by polynomials of 14th order.

5.2.1 General flow features

In this subsection an analysis of the testcase C2H4-3-1.4-1 is given. In Fig. 5.2.2 a three-dimensional representation of the streamlines in the combustor (colored by temperature) is shown. Several aspects can be pointed out:

- both swirlers cause strong tangential velocity components resulting in a sudden expansion in the combustion chamber;
- this, in turn, provides a primary recirculation zone, which stabilizes the flame front near the axis;
- external recirculation zones (not shown for sake of clarity) are located at the chamber corners;
- because of the high momentum of the oxidation jet, a deep penetration of the secondary air is obtained. This causes an enhancement of momentum, energy, and species transport in comparison with simple shear-dominated flows. It should be pointed out that the strong interaction between these cold jets and the flame zone may be not correctly predicted by the $k - \epsilon$ turbulence model, and that the constant Prandtl number hypothesis used in this work may not perform properly [112].

Figure 5.2.3 shows slices of temperature, velocity and O₂ mass fraction at different axial locations. The temperature plot clearly shows that a detached flame is obtained. This feature

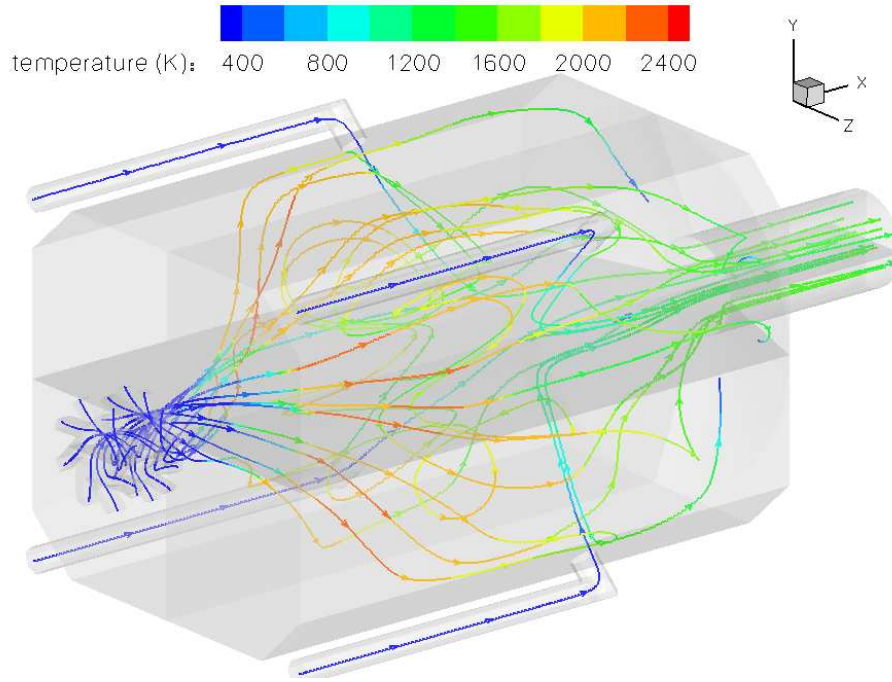


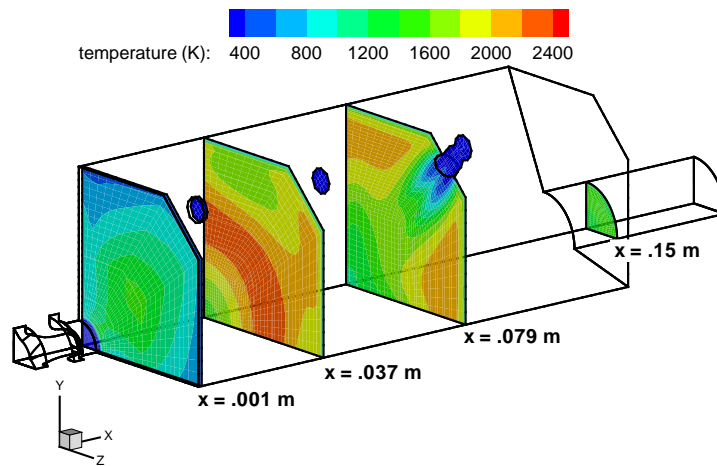
Figure 5.2.2: Three-dimensional representation of streamline in the SiA semi-technical scale combustor (C₂H₄-3-1.4-1 testcase).

is particularly important for the soot formation, since the degree of premixing has a large effect on the sooting characteristics of the flame (see also Chapter 3). The high penetration of the oxidation jet can be seen in Fig. 5.2.3(a). The inclusion of the pipe in the simulation results in a non-uniform velocity profile at the exit of the combustor with two high velocity wings and a slower central core. Because of the small cross section of the pipe, a large part of the hot gases flows sideways directly towards the combustor exit.

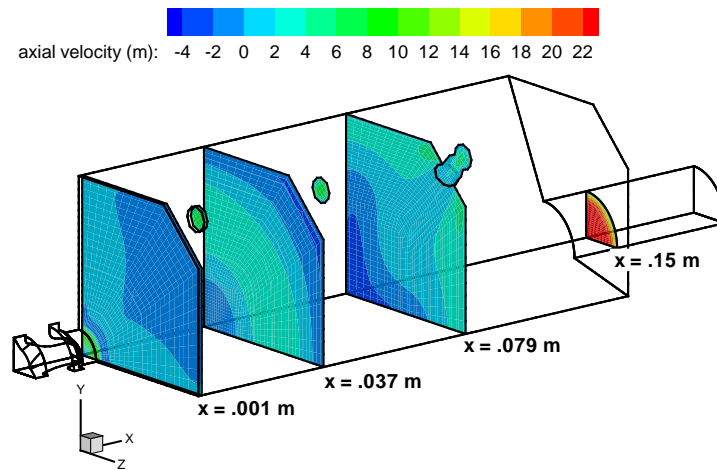
The axial velocity and O₂ plots given in Figs. 5.2.3(b) and 5.2.3(c) show the strong dependence of the primary recirculation zone on the oxidation jet. The momentum of the jet is high enough to reach the chamber axis where it is splitted into forward and backward flowing components. From the amount of oxygen found in the recirculation zone (Fig. 5.2.3(c)) it becomes clear that the backward-oriented one has an important impact on flame stabilization. The temperature and oxygen contours additionally outline how the primary and secondary air flows are separated by the flame front.

In Fig. 5.2.4(c) distributions for temperature (I_T) and species (σ_Y) fluctuation (Eqs. (4.3.11) and (4.3.18)) are given. Beside temperature fluctuations induced by cold walls (isothermal boundary conditions have been assumed), highest I_T values are found near the flame front. Another maximum is reached near the oxidation jet due to its significantly lower temperature. Strong species fluctuations occur mainly near the flame front and to a lower extent near the oxidation air injection.

Soot volume fraction and particle density number distributions are plotted in Fig. 5.2.5. From a comparison of these plots with the temperature distribution given in Fig. 5.2.4(b) it may be concluded that soot is formed in regions where hot gases are mixed with fresh mixture. In comparison to the testcase in Chapter 3, relatively low amounts of soot are observed despite



(a) temperature



(b) axial velocity

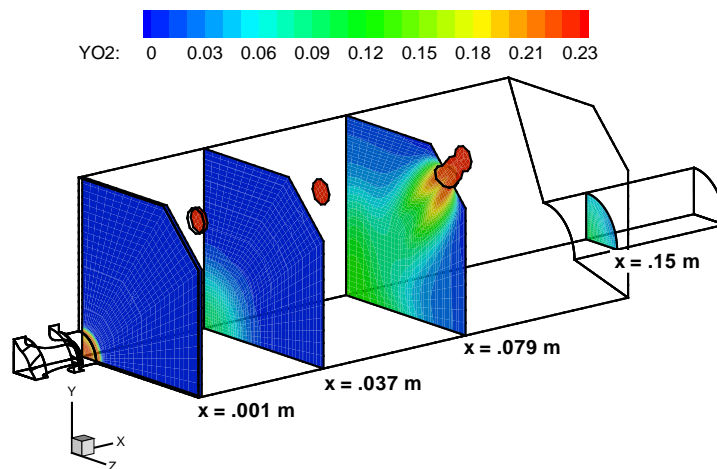
(c) O₂ mass fraction

Figure 5.2.3: Axial slices of temperature, axial velocity and O₂ in the SiA semi-technical scale burner (C₂H₄-3-1.4-1 testcase).

the high pressure conditions. This is mainly due to premixing effects which have a strong influence on the soot formation rate, as shown in Section 3.5.

5.2.2 Influence of turbulence-chemistry interaction

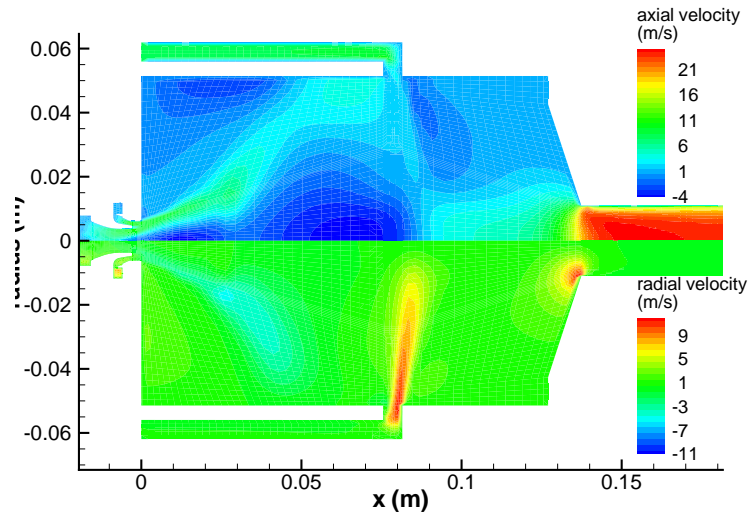
The high temperature and species fluctuations shown in Fig. 5.2.4(c) are expected to have an influence on the flame, ignition delay and soot formation. In order to assess their importance, calculations are performed with and without the assumed PDF approach and results are compared.

Figure 5.2.6 highlights differences between the two sets of simulations concerning both thermodynamic and fluid-dynamic variables. The temperature plot in Fig. 5.2.6(a) points out that a different flame structure is obtained if the influence of turbulent fluctuations on the chemistry is neglected. In this case a nearly attached two-wings flame is obtained in contrast to a single lifted flame predicted by the PDF simulation, which is also observed in the experiments.

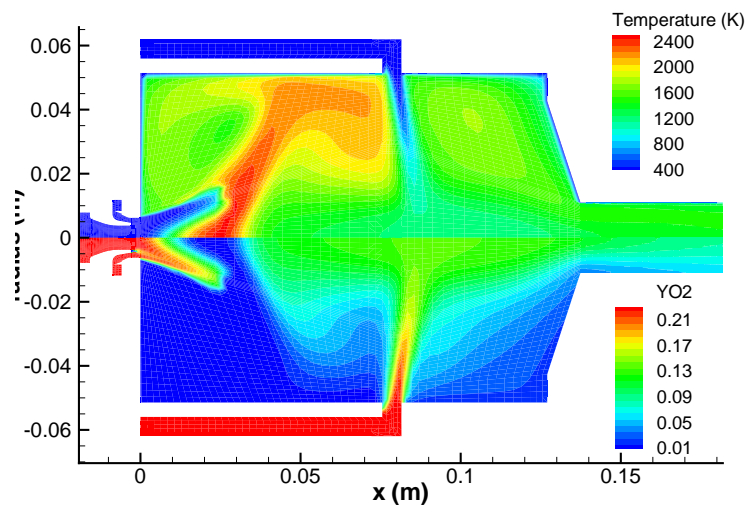
The different positions of the flame fronts are also highlighted by the CH and velocity distributions (Figs. 5.2.6(b) and 5.2.6(c)). It can be noticed that in the laminar flame calculation the flame front is not surrounded by a recirculating region with high temperature. That is, the mixture is not ignited by a stable recirculation zone of hot products, as described in the introduction (see Section 5.1). On the other hand, partial premixing which takes place at the nozzle exit provides conditions (i.e. mixture composition) at which the turbulent flame speed is comparable to the local flow velocities and the flame stabilizes by the turbulent transport of the combustion products. The additional flame front observed in the external region is induced by the secondary vortex located at the chamber basis. It is worth noticing that the experimentally observed flame is detached. Therefore the laminar calculation is erroneous.

The assumed-PDF calculation provides a slightly higher maximum temperature in the primary reaction zone. This is in contrast to the exit temperature, which is higher in the laminar-chemistry calculation (by about 150K). This is mainly due to a stronger acceleration of the gas caused by the mixture ignition near the axis, which lowers the penetration of the oxidation jet and related cooling effects. Additionally, the expansion due to the flame front also reduces the extension of the primary recirculation zone and separates it from the second one. As will be shown later, the assumed PDF approach achieves a better agreement with experimental temperature measurements.

As expected, flame position and stabilization mechanisms have an enormous influence on the sooting characteristics. Figures 5.2.7(a) and 5.2.7(b) show soot volume fraction and particle density number, respectively. Even if large differences in terms of number of soot particles are observed, the most important discrepancy is related to the soot volume fraction. In Fig. 5.2.7(a) a logarithmic scale has to be used in order to make the soot contours in the assumed-PDF calculation better visible. The ratio in soot volume fraction between laminar-chemistry and assumed-PDF model is about 50 and may be attributed to the lower number of soot particles formed. This is related to the lower amount of benzene and higher-mass PAHs (not



(a) axial and radial velocities



(b) temperature and O2 mass fraction

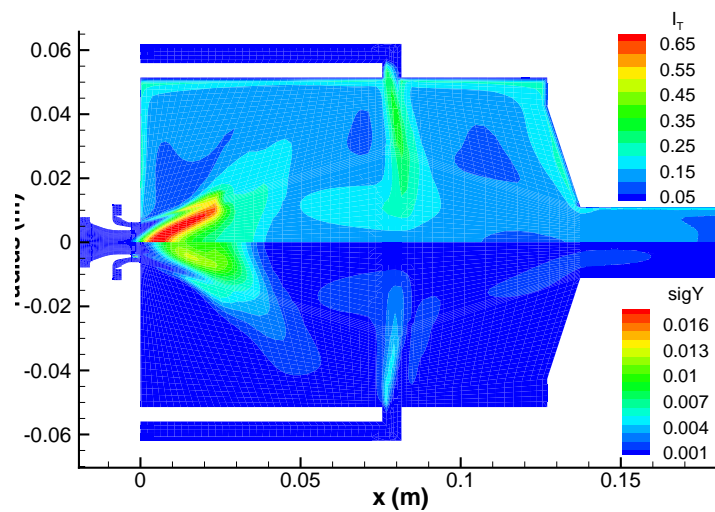
(c) I_T and σ_Y

Figure 5.2.4: Distributions for a 45-degree cross section of the SiA semi-technical scale combustor (C2H4-3-1.4-1 testcase).

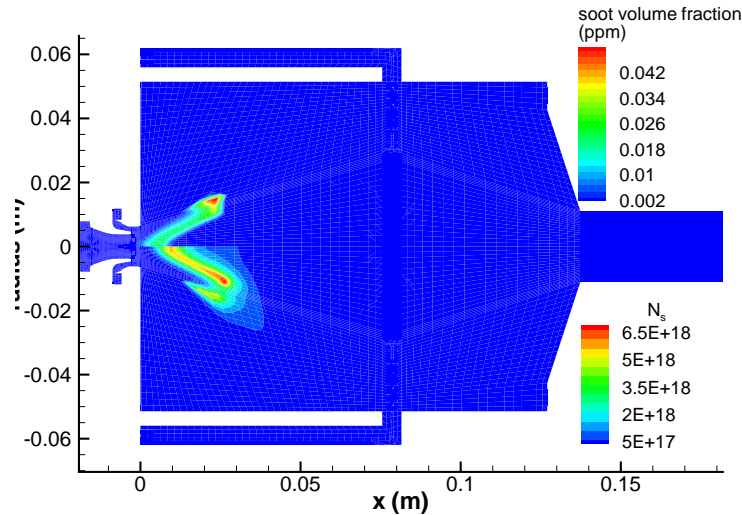


Figure 5.2.5: Soot volume fraction and soot particle density number on a 45-degree cross section of the SiA semi-technical scale combustor (C2H4-3-1.4-1 testcase).

shown here) produced in the fuel-rich region. In Fig. 5.2.7(b) it can also be noticed that in the PDF calculation the soot inception region (marked by high N_s values) is more distributed.

5.2.3 Influence of pressure and oxidation air

A comparison between testcases performed at different pressures is important to verify the sensitivity of the model concerning different operating conditions. Results of the 3 and 9 bar testcases of Table 5.1 will be shown.

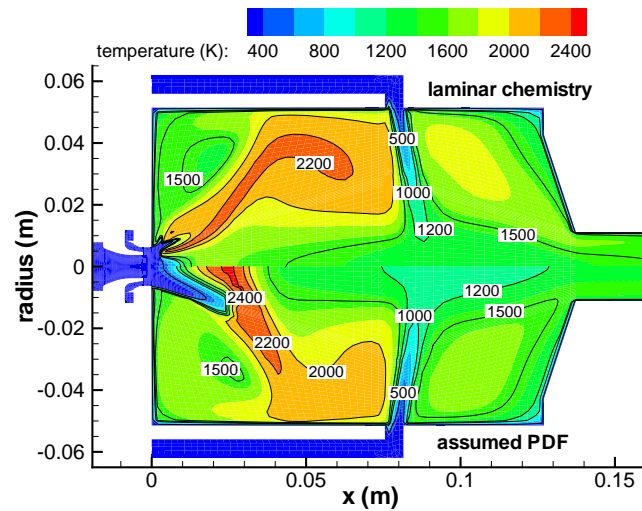
In Fig. 5.2.8 several thermo- and fluid-dynamic variables are compared. The axial velocity field (Fig. 5.2.8(a)) shows that qualitatively similar solutions are obtained and large differences appear only at the chamber exit. The primary recirculation zone (induced by the swirl) increases with increasing pressure and joins the bigger stagnation region (induced by the oxidation air jet).

At higher pressures a higher nominal Reynolds number is obtained¹, as given in Table 5.1. Thus a higher turbulent transport is expected at higher pressure. Turbulent viscosity plots given in Fig. 5.2.8(b) are in agreement with this hypothesis since values calculated at 9 bar are significantly higher than at 3 bar. Temperature plots for both pressures are shown in Fig. 5.2.8(c). With increasing pressure the ignition point moves upstream because of the faster chemistry (see subsection 2.2.3). Moreover, the temperature in the outer recirculation zone is higher and causes an ignition of the mixture in the external region. Exit temperatures are also higher and yield a higher chamber exit velocity.

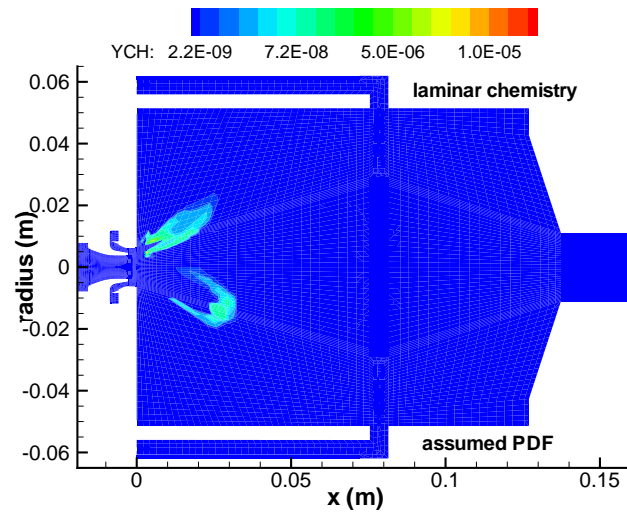
Only relatively small deviations in the maximum values of I_T and σ_Y are observed. As the flame front is shifted upstream, temperature fluctuations move accordingly.

The soot volume fraction distributions are compared in Fig. 5.2.10. As expected, more soot is obtained at higher pressure. This is due to the enhanced formation of soot-related species

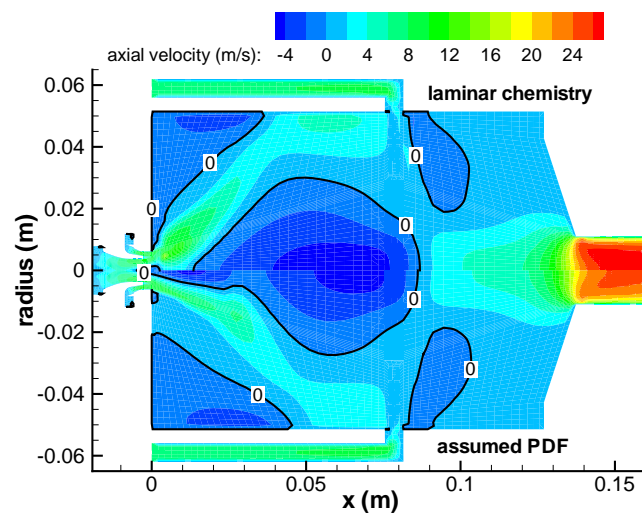
¹According to its definition (Eq. (4.1.1)), at constant velocity the Reynolds number scales linearly with density or, equivalently, pressure.



(a) temperature

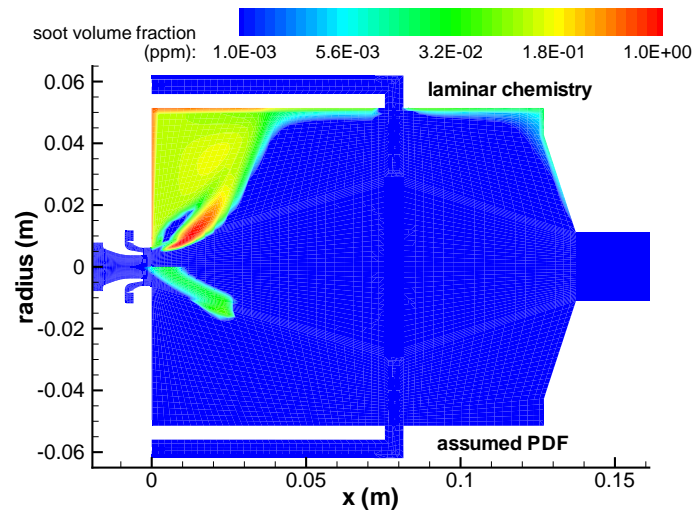


(b) CH mass fraction

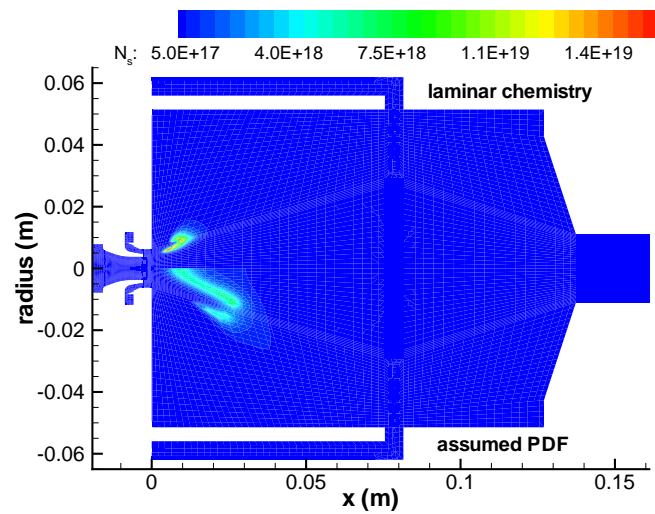


(c) axial velocity

Figure 5.2.6: Comparison between laminar chemistry and the assumed-PDF calculations for the SiA semi-technical scale burner (C₂H₄-3-1.4-1 testcase): thermo- and fluid-dynamic variables.

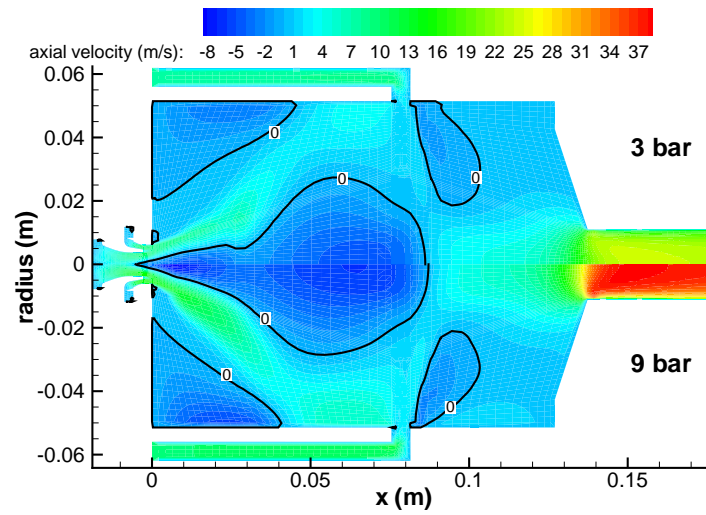


(a) soot volume fraction

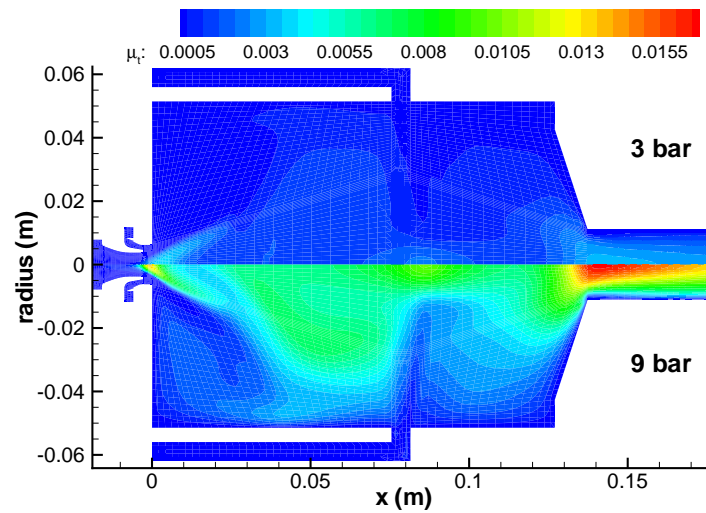


(b) soot particle density number

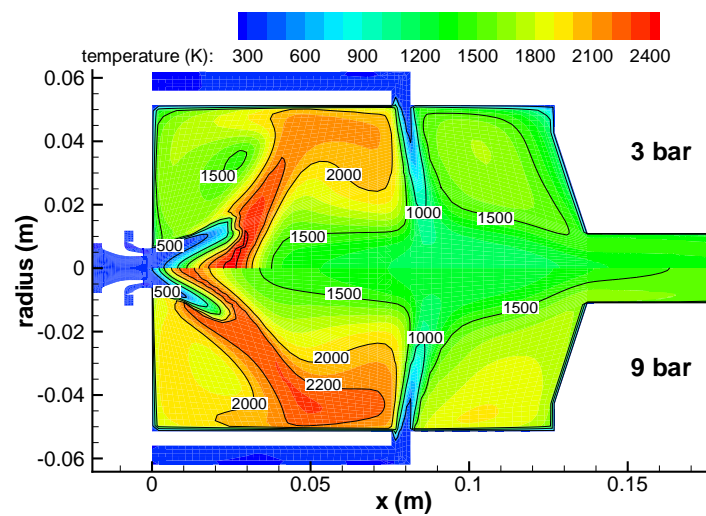
Figure 5.2.7: Comparison between the laminar chemistry and the assumed-PDF calculations for the SiA semi-technical scale burner (C₂H₄-3-1.4-1 testcase): soot volume fraction and soot particle number distributions.



(a) axial velocity



(b) turbulent viscosity



(c) temperature

Figure 5.2.8: Comparison between simulations performed at 3 and 9 bar (C2H4-3-1.4-1 and C2H4-9-1.2-0.9 testcase): thermo- and fluid-dynamic quantities.

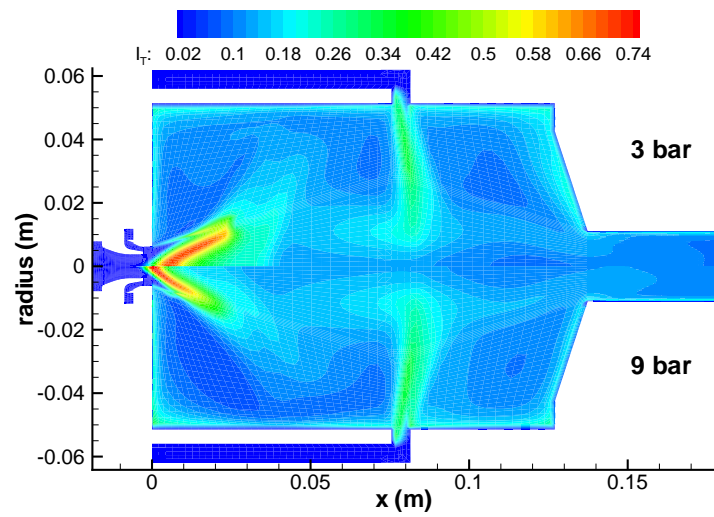
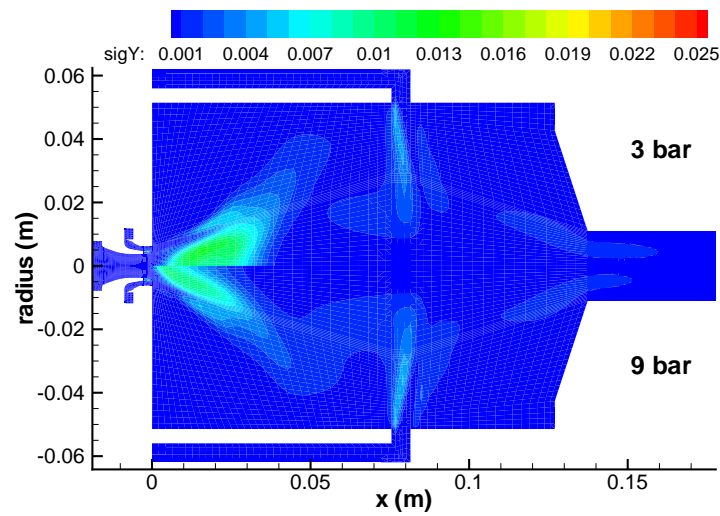
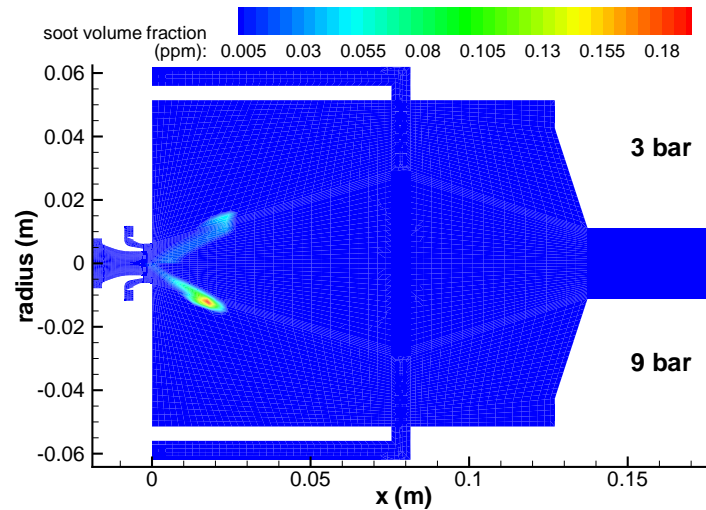
(a) I_T (b) σ_Y

Figure 5.2.9: Comparison between simulations performed at 3 and 9 bars (C2H4-3-1.4-1 and C2H4-9-1.2-0.9 testcase): temperature and species fluctuations.



(a) soot volume fraction

Figure 5.2.10: Comparison between simulations performed at 3 and 9 bars (C2H4-3-1.4-1 and C2H4-9-1.2-0.9 testcase): soot volume fraction.

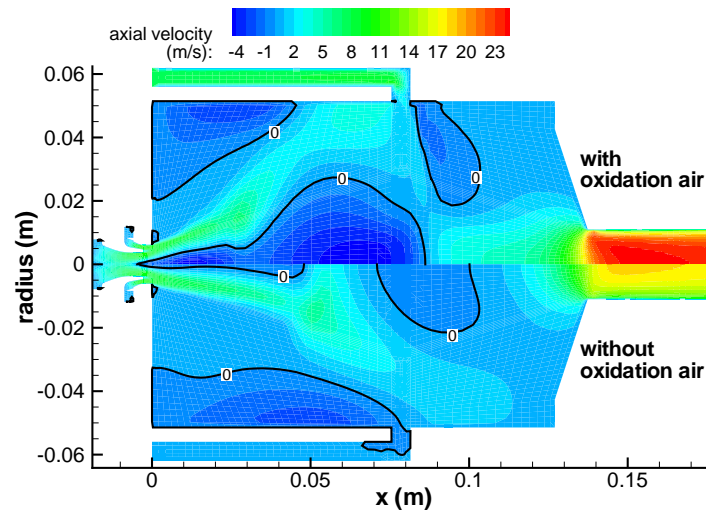
(i.e. acetylene and benzene) and an acceleration of soot-formation reactions, which are at least second-order with pressure (see Eqs. 3.2.4-3.3.18).

A comparison between simulations with and without additional oxidation air is given in Fig. 5.2.11. As discussed above, the injection of additional air has a strong influence on the formation of the primary recirculation zone and on the flame stabilization. As may be seen in Fig. 5.2.11(a), the primary recirculation zone is reduced to a small region near the axis whereas the external one extends up to the oxidation pipe. In the simulation without oxidation air an additional vortex is observed around $x = .1$ m.

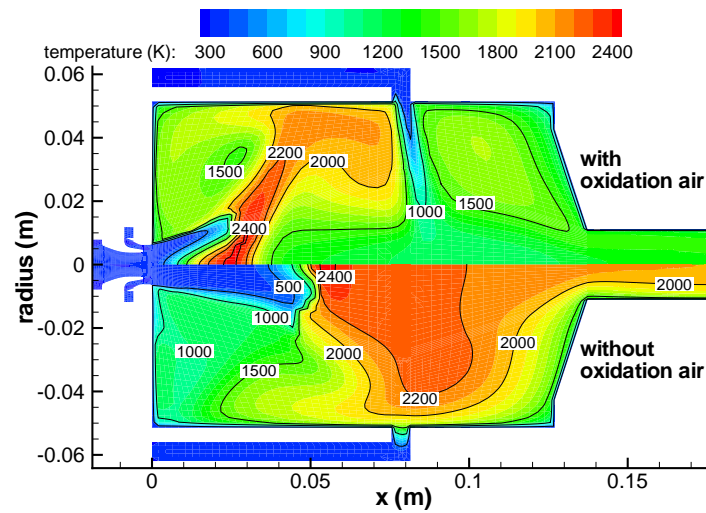
Temperature distributions (Fig. 5.2.11(b)) outline the influence of the oxidation jet on the flame stabilization region and outlet temperature profile. The axial positions of ignition are almost doubled and a large portion of the combustion chamber has temperatures above 2200 K. Even temperature profiles at the chamber's exit are significantly higher with peaks above 2000 K. This highlights the importance of secondary jets to obtain a uniform temperature profile.

In Fig. 5.2.11(c) soot volume fraction distributions are plotted. Even if shifted, similar trends are observed and it is not possible to conclude that secondary air plays an important role in soot oxidation. In the testcase without additional secondary air a layer showing an almost constant soot concentration is obtained.

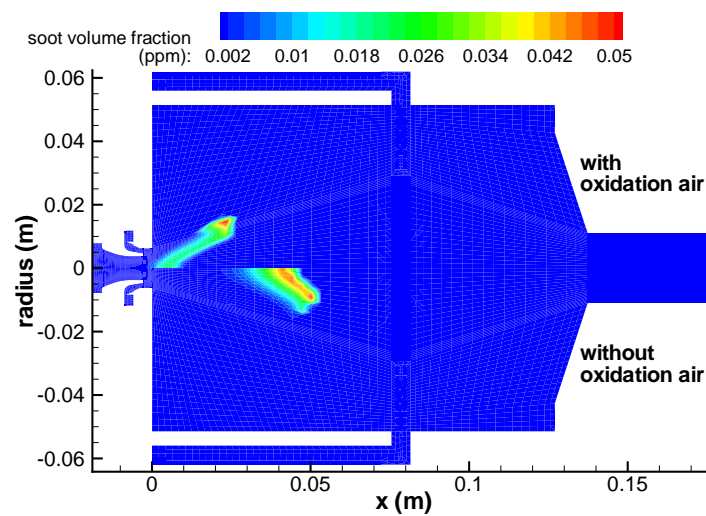
I_T distributions are compared in Fig. 5.2.12. Because of the higher lift-off height of the flame, the 3-bar testcase shows lower temperature fluctuations at the flame location. This, in turn, may have an important role on soot chemistry and may explain why similar distributions are obtained even if completely different flow fields are predicted.



(a) axial velocity



(b) temperature



(c) soot volume fraction

Figure 5.2.11: Comparison between simulations performed with and without oxidation air (C2H4-3-1.4-1 and C2H4-3-1.4-0 testcases).

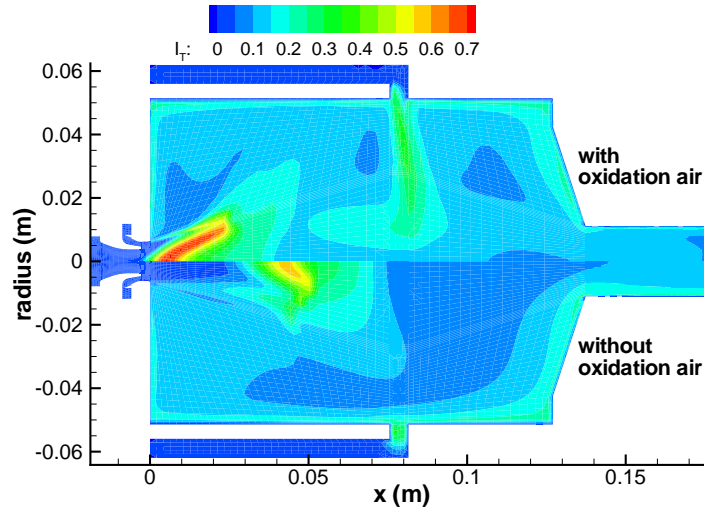


Figure 5.2.12: Temperature fluctuation distributions with and without oxidation air (C2H4-3-1.4-1 and C2H4-3-1.4-0 testcases).

5.2.4 Comparison with experimental data

At the Institute of Combustion Technology the described semi-technical scale combustor has been investigated experimentally. Up to now SV-CARS [186] and Laser Induced Incandescence [116] have been used to measure temperature and soot volume fraction, respectively. PIV velocity measurements [137] are planned for the next future. Even if the available data do not allow a complete analysis of the model, some indications about the quality of the simulations and directions of possible improvements can be extracted.

Axial temperatures are compared in Fig. 5.2.13. As already stated in the previous section, differences between laminar-chemistry and the assumed-PDF combustion model are significant. The lack of a recirculation zone at the nozzle exit has a strong influence on the temperature increase near $x = 0.01$ m. For the same reasons, peak temperatures predicted by the laminar-chemistry model are significantly lower. The large temperature drop observed at $x = .05$ m is well predicted by the assumed-PDF approach, whereas laminar-chemistry calculations do not show any appreciable influence, since the flame front is not located near the axis (see Fig. 5.2.6(a)). In conclusion, a good overall agreement is achieved if the presumed-PDF combustion model is used, even if turbulent transport is still not modeled accurately enough. Discrepancies in maximum temperature and flame front extension may be due to the used constant Prandtl and Schmidt numbers.

Experimentally and numerically observed soot distributions are shown in Figs. 5.2.14 and 5.2.15 for the $z = 0$ plane. Significant discrepancies appear both in the peaks and overall distributions. Several reasons may be the origin of these differences. Since in the investigated combustor a detached flame is observed, a significant premixing degree is obtained before ignition takes place. On the other hand, validation tests for the soot formation model performed in Chapter 3 have shown that the employed kinetic mechanism is not able to provide good

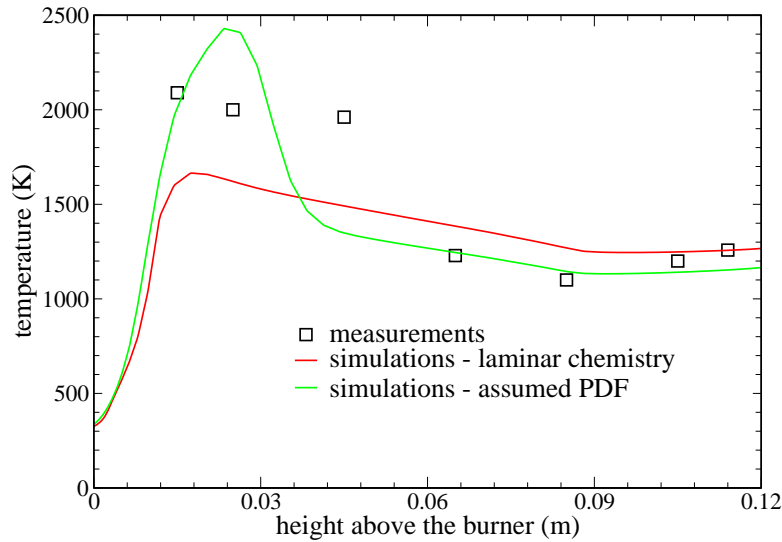
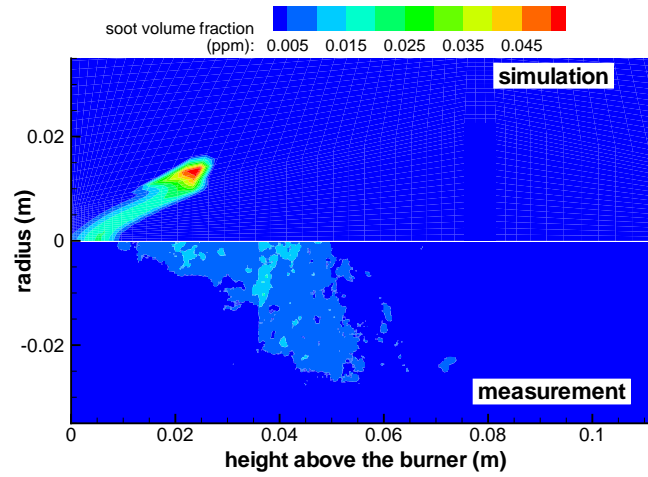


Figure 5.2.13: Comparison of axial temperature profiles for the C2H4-3-1.4-1 testcase.

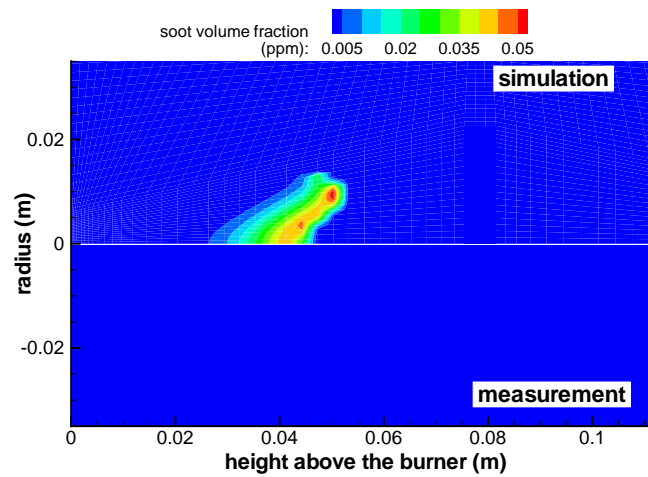
predictions in partially-premixed flames. An example of this deficiency is given in the C2H4-3-1.4-0 simulation, where the flame front is well above the nozzle exit and an almost premixed regime is achieved. For such conditions an almost sooting-free flame is expected, and the large amount of soot observed (comparable with the testcase C2H4-3-1.4-1) may be attributed to the bad performance of the kinetic mechanism.

Simple two-equation turbulence models are not able to correctly predict flows with strong curvature and jets in cross-flow. However, it has to be kept in mind that finite-rate chemistry, soot formation and assumed PDF models require a large amount of CPU time. Therefore, a two-equation turbulence model has been a compromise between the high effort necessary for good chemistry and soot predictions and affordable computational time for complex three-dimensional simulations.

Fig. 5.2.16 shows the comparison between predicted and measured soot volume fraction peak values. Despite the problems discussed above, a good overall agreement is obtained. The model is able to predict pressure effects on the soot formation rate, even if a slope lower than in the experiments is observed.

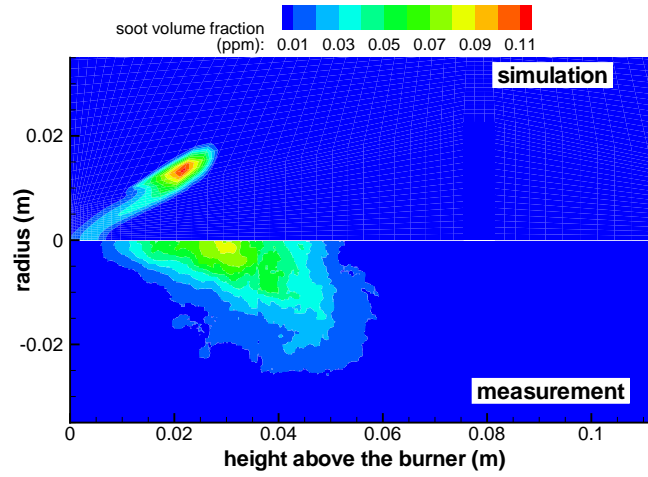


(a) 3-bar testcase, with oxidation air

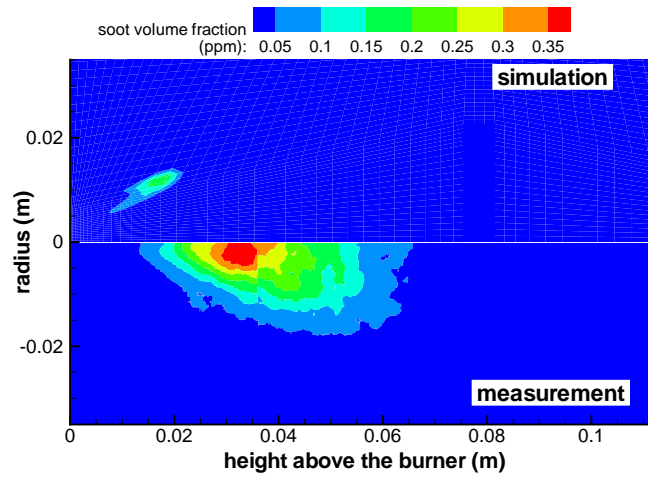


(b) 3-bar testcase, without oxidation air

Figure 5.2.14: Comparison between numerical and experimental soot distributions in the SiA semi-technical scale combustor: 3 bar testcases.



(a) 5-bar testcase



(b) 9-bar testcase

Figure 5.2.15: Comparison between numerical and experimental soot distributions in SiA semi-technical scale combustor: 5 and 9 bar testcases.

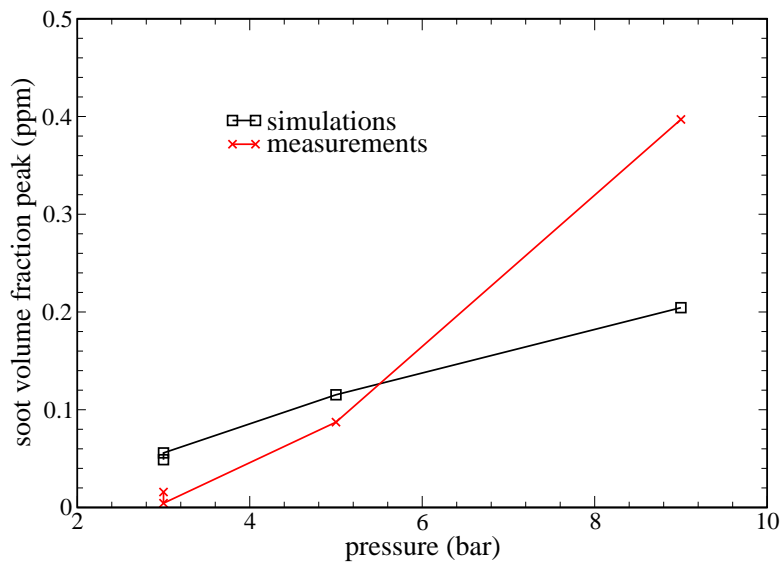


Figure 5.2.16: Comparison between predicted and measured peak soot volume fractions at different pressures.

6 Conclusions

In the present work a new numerical approach for modeling the soot formation in combustion chambers has been presented. The model developed has been validated against simple and complex testcases. In this Chapter a summary of results is given and possible improvements are discussed. Since several topics are touched the discussion is split accordingly.

Finite-rate chemistry model

Both zero-dimensional premixed and multi-dimensional diffusion flames have been used to investigate the newly implemented finite-rate chemistry model. The results show the expected sensitivity with respect to simulation parameters as initial temperature or pressure. A strong influence of the kinetic scheme on ignition (i.e. ignition delay) in constant-pressure reaction calculations as well as in laminar flames has been found. Significant differences in main species concentrations have also been observed. It should be pointed out that due to computational limits it is often not possible to use the best mechanism available. This has to be taken into account in the discussion and assessment of the simulation accuracy, since it may represent a main source of error.

Much attention has been given to boundary conditions and their influence on results. Both kinetic and fluid dynamic effects may play a significant role in the determination of the flame shape. Simulations showed that the inclusion of the burner in the calculation affects flame length and temperature profiles. It was also found that a more complete description of the experimental boundary conditions is important to improve the simulations and understand the combustion phenomena. The finite-rate combustion model has been validated successfully against experimental data. Nevertheless, some of the identified discrepancies could not be explained unambiguously.

Soot formation modeling

Since a straightforward extension of chemical kinetics to soot formation would be unfeasible, a sectional method has been proposed for the soot precursors (Chapter 3). Simple zero-dimensional simulations showed main model features (i.e. a sequential behavior for the formation of the precursors). In diffusion flame configurations different locations are observed where soot formation and oxidation predominate. The effectiveness of several assumptions (i.e. the introduction of a reaction marker) could be justified in the light of a typical flame structure.

The model has been validated against methane/air diffusion flames where a number of modeling parameters have been set up and a critical discussion of their influence is given. The PAH

model has been found to be more sensitive to changes in the Arrhenius parameters (i.e. activation energy) than to the choice of the reaction marker. The lack of comprehensive testcases at higher pressures presently does not allow a more exhaustive validation for gas turbine like conditions.

An additional investigation of premixing effects on the soot formation rate showed some major drawbacks in the performance of the kinetic scheme. In particular, key species in soot formation as C_2H_2 and C_6H_6 often show large discrepancies in fuel-rich regions and this, in turn, has a large influence on the soot profiles. This is especially important for gas turbine combustion chambers where lifted flames and partially premixed regimes are quite common.

Assumed PDF approach

The influences of temperature and species fluctuations due to turbulence on the chemical reaction rates has been discussed in Chapter 4. Fundamental differences between temperature and species amplification factors have been outlined and the strong influence of the non-linear behavior of the Arrhenius function has been pointed out. Analytical trends of the assumed species PDFs were assessed (in case of two-body reactions) whereas only a qualitative influence of the Arrhenius coefficients on the amplification factor could be found.

Both attached and lifted turbulent flames have been simulated in order to establish reciprocal dependencies between flame configuration and PDF contribution. As expected, the observed influence of temperature and species PDFs on the reaction rates and flame shapes is highly testcase-dependent.

Attached flames only show minor changes in structure and temperature field if the assumed PDF approach is included in the calculation. However, some important differences in radical distributions (i.e. OH) have been noticed and they certainly have an impact on the formation of pollutants (i.e. soot formation rate). In lifted flames the influence of PDFs is more pronounced because the ignition point and flame shape are strongly affected by both temperature and species fluctuations. The turbulence model has also been identified as an additional source of error since large variations of the ignition point are observed in the case of changing turbulence modeling constants.

Simulation of the SiA semi-technical scale burner

The models developed are tested under complex conditions by simulating a fully turbulent, sooting semi-technical scale combustor (Chapter 5) with a double swirler nozzle. Both general flow features and sensitivity to boundary and operating conditions have been investigated. The reference simulation highlighted a complex flow pattern with a swirling inflow and additional oxidation air. Under such conditions the $k - \epsilon$ turbulence model is known to be erroneous. Therefore, final conclusions about the simulation quality should be drawn with care.

The flame front location and flow streamlines are heavily affected by the oxidation air because of its high momentum. Since the combustion chamber operates at a low nominal swirl number,

it was found that the oxidation jet causes a large recirculation zone located near the axis. This has been confirmed by a comparison of calculations with and without oxidation air.

Concerning the influence of the operating conditions, simulations at three different pressures have been compared. While flow patterns and temperature distributions do not change significantly and show only a marginal departure from the reference simulation, the soot formation rate increases monotonically with increasing pressure.

The assumed PDF model has a strong influence on the flame configuration for this testcase and a different ignition point is predicted in the laminar chemistry calculation. This, in turn has a large impact on the flow pattern and therefore pollutant formation. Thus, this testcase represents an example where the assumed PDF approach is an essential component in the solution algorithm.

However, there still are significant differences between experimentally and numerically obtained soot volume fraction distributions. In particular, regions with a high soot formation rate have different shapes. While measured soot distributions highlight that soot formation takes place in the whole recirculation region, this is not the case in the numerical simulations, where the sooting region is limited to the flame front. Despite these differences, a good agreement in soot volume fraction peaks is obtained and the pressure dependence is correctly predicted by the model. Thus, the turbulence modeling seems to represent the issue in this configuration and improvements in that direction may help to increase simulation accuracy.

A Determination of the mixture transport properties

The transport of momentum, mass and energy in a fluid is due to collisions among molecules. Rates of exchange of these quantities depend on the species involved and their concentrations. Hence, the determination of the transport coefficients for a mixture of gaseous species is split into two steps:

- first, properties of pure species are calculated in dependence of temperature from molecular parameters and are fitted into polynomials. This procedure is carried out in preprocessing, as local mixture composition does not come into play.
- during the run mixture viscosity, heat conductivity and species diffusivities are calculated according to the local gas composition.

A.1 The calculation of pure species properties

Viscosity, heat conductivity and diffusivity of gaseous species depend on molecular parameters:

- molecular geometry (atomic, linear or polyatomic structure);
- Lennard-Jones potential ϵ^k , normalized with the Boltzmann constant k_b ;
- collision diameter σ^c ;
- dipole momentum d^m ;
- dipole polarity d^p ;
- rotational collision number at the reference rotational temperature z_0 .

The reduced temperature is defined as

$$T^r = \frac{T}{\epsilon^k}, \quad (\text{A.1.1})$$

whereas the effective collision diameter is

$$d^k = \frac{1}{2} \frac{(d^m)^2}{\epsilon^k k_b (\sigma^c)^3}. \quad (\text{A.1.2})$$

These two quantities are necessary to calculate the collision integral

$$\Omega_{lm}^* = \Omega(i, T^r, d^k) \quad (\text{A.1.3})$$

where $l, m = 1, 2$ depend on the transport property (viscosity, heat conductivity or diffusivity). Since the calculation of Ω_{lm}^* is expensive, it is normally obtained from look-up tables.

Viscosity

The viscosity of the i -th species is calculated in dependence of temperature from

$$\mu_i(T) = \frac{5}{16} \sqrt{\frac{\Re M_i T}{\pi}} \frac{1}{N_{av} \sigma_i^c \Omega_{22}^*(T^r, d^k)}. \quad (\text{A.1.4})$$

Diffusivity

The diffusion coefficient for a (i, j) species pair is calculated from mean molecular parameters [162]:

- collision diameter

$$\bar{\sigma}^c = \frac{1}{2} (\sigma_i^c + \sigma_j^c), \quad (\text{A.1.5})$$

- Lennard-Jones potential

$$\bar{\epsilon} = \frac{\sqrt{\epsilon_i^k \epsilon_j^k}}{k_b}, \quad (\text{A.1.6})$$

- harmonic mean of the molecular masses

$$\bar{M} = \frac{2M_i M_j}{M_i + M_j}. \quad (\text{A.1.7})$$

The above parameters and the effective collision diameter d^k have to be corrected according to the polarity of the molecules. In the following expression the subscript p refers to molecular parameters of polar species and np refers to neutral ones. In order to calculate the enhancement factor x_i , two different cases have to be distinguished:

- one species is polar and the other one is not

$$x_i = 1 + \frac{1}{2} \frac{d_{np}^p (d_{np}^M)^2 \sqrt{\frac{\epsilon_p^k}{\epsilon_{np}^k}}}{(\sigma_{np}^c \sigma_p^c)^3 \epsilon_p k_b} \quad (\text{A.1.8})$$

with the effective collision diameter

$$\bar{d}^k = 0; \quad (\text{A.1.9})$$

- both species are polar or neutral; in this case no enhancement factor is used ($x_i = 1$) whereas the effective collision diameter is

$$\overline{d^k} = \frac{d_i^m d_j^m}{2k_b \bar{\epsilon} (\bar{\sigma}^c)^3}. \quad (\text{A.1.10})$$

The corrected molecular parameters are calculated according to the following expressions

$$\overline{\sigma^{c'}} = \overline{\sigma}^c x_i^{\frac{1}{6}}, \quad (\text{A.1.11})$$

$$\bar{\epsilon}' = \bar{\epsilon} \sqrt{x_i}, \quad (\text{A.1.12})$$

$$T_r' = \frac{T}{\bar{\epsilon}'}. \quad (\text{A.1.13})$$

The diffusion coefficient has the following expression

$$D_{ij} = \frac{1}{p} \frac{3}{8} \frac{(\mathcal{R}T)^{\frac{3}{2}}}{N_{av} \sqrt{\pi M} \overline{\sigma}^{c2} \Omega_{11}^* (T_r', \overline{d^k})} F_c^D, \quad (\text{A.1.14})$$

where F_c^D is a correction factor defined by Marrone and Mason [125].

Heat conductivity

In order to calculate heat conductivity, the rotational collision parameter at temperature T is needed

$$z = z_0 f(T_r)$$

where $f(T_r)$ is a function defined by Parker [152]. According to the Lewis number for the i -th species

$$Sc_{ii} = \frac{\mu_i}{\rho D_{ii}} \quad (\text{A.1.15})$$

the following parameter is defined

$$a = \frac{5}{2} - \frac{1}{Sc_{ii}}. \quad (\text{A.1.16})$$

The number of degree of freedom depends on the molecular structure. This, in turns, has an influence on the species heat conductivity. In order to take it into account, two additional parameters (b and c) are introduced:

- for mono- and bi-atomic species they are obtained as follows

$$b = z + \frac{2}{\pi} \left(\frac{5}{2} + \frac{1}{Sc_{ii}} \right), \quad (\text{A.1.17})$$

$$c = 1; \quad (\text{A.1.18})$$

- whereas for polyatomic species they are

$$b = z + \frac{2}{\pi} \left(\frac{5}{3} + \frac{1}{Sc_{ii}} \right), \quad (\text{A.1.19})$$

$$c = \frac{2}{3}. \quad (\text{A.1.20})$$

Each degree of freedom has a separate contribution to the heat conductivity:

- translational

$$F_t = \frac{5}{2} \left(1 - \frac{2}{\pi} \frac{a}{b} \right); \quad (\text{A.1.21})$$

- rotational

$$F_r = \frac{1}{Sc_{ii}} \left(1 + \frac{2}{\pi} \frac{a}{b} \right); \quad (\text{A.1.22})$$

- vibrational

$$F_v = \frac{1}{Sc_{ii}}. \quad (\text{A.1.23})$$

The calculation of the heat conductivity of pure species depends on the molecular structure and a distinction has to be made between different molecule classes:

- for the mono-atomic species the kinetic theory prescribes

$$F = \frac{5}{2} \frac{3}{2} \mathfrak{R}; \quad (\text{A.1.24})$$

- whereas for bi-atomic species

$$F = \left(\frac{3}{2} F_t + F_r \right) \mathfrak{R} + F_v \left(C_v - \frac{5}{2} \mathfrak{R} \right); \quad (\text{A.1.25})$$

- in case of poly-atomic species the non-linear structure yields a different combination of the above terms

$$F = \frac{3}{2} (F_t + F_r) \mathfrak{R} + F_v (C_v - 3\mathfrak{R}). \quad (\text{A.1.26})$$

Once that the total contribution F has been determined, the heat conductivity is calculated as follows

$$\lambda_i = \frac{\mu_i}{M_i F}. \quad (\text{A.1.27})$$

A.1.1 Fitting of the pure species transport coefficients

A calculation of the transport coefficients according to Eqs. (A.1.4), (A.1.14) and (A.1.27) is expensive and should be avoided in the flow solver. Additionally, it can be observed that pure-species properties do not depend on the local mixture composition. Thus, above calculations

are performed in a preprocessing step and results are fitted into polynomials of fourth order. If a generic polynomial function of order n is indicated as

$$P^n(x) = \sum_{i=0}^n a_i x^i \quad (\text{A.1.28})$$

the logarithm of transport coefficients

$$\ln(\mu_i) = P_{\mu_i}^4(\ln T) \quad (\text{A.1.29})$$

$$\ln(\lambda_i) = P_{\lambda_i}^4(\ln T) \quad (\text{A.1.30})$$

$$\ln(D_{ij}) = P_{D_{ij}}^4(\ln T) \quad (\text{A.1.31})$$

are fitted into polynomials of the temperature logarithm. The coefficients a_i are calculated by a least square method [3] using m temperature points which span the interval [300, 3000] K.

A.2 Calculation of the mixture transport coefficients

At the beginning of the every time or under-relaxation step, transport properties of pure species are calculated from polynomials, as described above (Eqs. (A.1.29)-(A.1.31)). Next, transport coefficients for a mixture of gases are obtained as a weighted mean of the pure species properties [129] by

$$\mu_{mix} = \frac{1}{2} \left(\sum_{i=1}^{N_s} X_i \mu_i + \frac{1}{\sum_{i=1}^{N_s} \frac{X_i}{\mu_i}} \right), \quad (\text{A.2.1})$$

$$\lambda_{mix} = \frac{1}{2} \left(\sum_{i=1}^{N_s} X_i \lambda_i + \frac{1}{\sum_{i=1}^{N_s} \frac{X_i}{\lambda_i}} \right), \quad (\text{A.2.2})$$

$$D_{i_{mix}} = \frac{1 - Y_i}{\sum_{j=0, j \neq i}^{N_s} \frac{X_j}{D_{ij}}} \frac{1}{p^n}. \quad (\text{A.2.3})$$

B Elements of numerical methods for Navier-Stokes equations

B.1 Gradient computation

Gradient calculation plays a central role in the determination of the accuracy of a CFD code, since both convective and diffusive terms require it. Variables and their gradients can be calculated either at the cell center (co-located approach) or at the cell interface (staggered approach). In this work a co-located approach is preferred because of its lower memory requirements. As counterpart, this method needs to extrapolate field variables at cell interfaces. Cell gradients are obtained by the Gauss theorem as sum of the face fluxes. This method can be also used if vector gradients are needed: in this case each vector component is processed separately.

The Gauss theorem relates the gradients of a given, continuous field ψ and its fluxes through the cell interface by

$$\int_v \nabla \psi dv = \oint_s \psi \mathbf{n}_s ds. \quad (\text{B.1.1})$$

The discretized form of the above relation averages the gradients within the cell and assumes a constant ψ over each boundary face

$$\nabla \psi = \frac{1}{\Delta v} \sum_s \psi_s \mathbf{n}_s \Delta s. \quad (\text{B.1.2})$$

ψ_s at the cell interface is obtained as the mean between the left and the right values

$$\psi_s = \frac{\psi_L + \psi_R}{2} \quad (\text{B.1.3})$$

B.2 Discretization of the convective terms

The kind of discretization of convective fluxes has a strong influence on code stability and accuracy. A purely explicit discretization would yield a severe limitation of the allowed timestep and unfeasibly long computational times to reach a steady-state solution.

A compromise between stability and accuracy is found if an explicit high-order method is used in conjunction with an implicit upwind part. This algorithm, known as *deferred correction method*, works very well especially when coupled with matrix-free linear solvers (see section (B.5)).

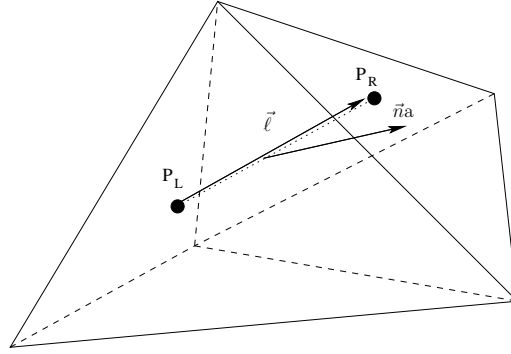


Figure B.2.1: Generic cell-face configuration.

Referring to Fig. B.2.1, the convective term at faces c is discretized as follows

$$F_{\psi}^c(\psi^t, \psi^{t+\Delta t}) = \frac{1}{2} \dot{m} \left([\alpha \Delta \psi \pm \beta \nabla \psi \cdot \ell]^t + \psi_{up} |^{t+\Delta t} \right) \quad (\text{B.2.1})$$

where α and β determine the scheme being used. A first order, fully implicit upwind scheme is obtained with the following settings

$$\alpha = \beta = 0 \quad (\text{B.2.2})$$

However, the use of first order upwind schemes has to be avoided because of their high numerical diffusivity. In order to use a higher order scheme, explicit terms in Eq. (B.2.1) can be added by a corresponding choice of α and β :

- $\alpha = 1$ and $\beta = 0$ result in a second order, Central Discretization Scheme (CDS);
- with $\alpha = 0$ and $\beta = 1$ a second order, Linear Upwind Discretization Scheme (LUDS) is used;
- in case of $\alpha = \beta = \frac{1}{2}$ a third order, Quadratic Upwind Discretization Scheme (QUDS) is obtained.

B.3 Discretization of the diffusive terms

The diffusive flux in the momentum equation has the following form

$$F_{\mathbf{V}}^d = \overline{\mu_{eff}} \left[\left(\overline{\nabla \mathbf{V}} + \overline{\nabla \mathbf{V}^T} \right) \cdot \mathbf{n} + F_{corr}^d \right]^t + \left[\frac{\Delta \mathbf{V}}{\|\ell\|} \mathbf{n} + \frac{1}{3} \overline{\nabla \cdot \mathbf{V}} \mathbf{n} \right]^{t+\Delta t}, \quad (\text{B.3.1})$$

where the overlined terms $\overline{(\)}$ are means between the left and right values whereas $\Delta(\)$ is the difference operator. For the other scalar equations the diffusive flux is

$$F_{\psi}^d = \overline{D_{eff}} \left[\overline{\nabla \psi} \cdot \mathbf{n} + F_{corr}^d \right]^t + \left[\frac{\Delta \psi}{\|\ell\|} \|\mathbf{n}\| \right]^{t+\Delta t}. \quad (\text{B.3.2})$$

In case that highly non-orthogonal unstructured grids are used, it is necessary to include a correction term to avoid negative effects on the results. In both equations (B.3.1) and (B.3.2)

the explicit correction term is used as follows

$$F_{corr}^d = - [\nabla\psi]^t \cdot \left(\frac{\mathbf{n} \cdot \mathbf{n}}{\ell \cdot \mathbf{n}} \right) \quad (\text{B.3.3})$$

B.4 Pressure-velocity coupling

If the Mach number reaches the incompressibility limit (around 0.3), convergence of density-based¹ solvers slows down significantly. The numerical stiffness, due to the large difference between acoustic and flow timescales, increases with decreasing Mach number. In order to overcome this problem, pressure-based solvers have been developed to handle the coupling between pressure and velocity fields [153]. Such an approach is also known as pressure-correction method, since the coupling is realized by means of a correction to the pressure and velocity fields which ensures continuity. Even if originally developed for low Mach number flows, such methods have been extended to compressible regime [92, 93] and reacting flows.

The main idea behind pressure correction methods is to decompose velocity and pressure into two contributions

$$\mathbf{V}^m = \mathbf{V}^{m*} + \alpha_v \mathbf{v}' \quad (\text{B.4.1})$$

$$p^m = p^{m-1} + \alpha_p p' \quad (\text{B.4.2})$$

where α_v and α_p are under-relaxation factors. The algorithm consists of the following steps:

1. a discretized version of the Navier-Stokes equations (Eq. 2.1.4) is solved

$$A\mathbf{V}^{m*} = -\nabla p^{m-1} \quad (\text{B.4.3})$$

and a new velocity field \mathbf{V}^{m*} is obtained. Pressure gradients in Eq. (2.1.4) are estimated from the previous iteration step;

2. since the pressure-velocity coupling has been neglected, the velocity field \mathbf{V}^{m*} does not satisfy the continuity equation. From Eqs. (2.1.3) and (2.1.4) an equation for the pressure corrections p' can be derived

$$\nabla \cdot [D^{-1}\rho(\nabla p')] = \nabla \cdot (\rho\mathbf{V}^{m*}) + \nabla \cdot (\rho\mathbf{v}') \quad (\text{B.4.4})$$

where D represent the diagonal terms of the matrix A in Eq. (B.4.3). The last term in Eq. (B.4.4) is neglected, and equation for the pressure-correction p' is solved. Thus, the

¹Density-based solvers implement directly an equation for the mass conservation, written in term of density

$$\frac{\partial \rho}{\partial t} + \nabla \cdot (\rho\mathbf{V}) = 0$$

pressure p^{m-1} and the velocity \mathbf{V}^{m*} fields are corrected according to Eq. (B.4.2) and

$$\mathbf{v}' = -D^{-1}\nabla p'; \quad (\text{B.4.5})$$

3. additional transport equations (turbulence, species, energy) are solved;
4. steps 1-3 are repeated until a steady state solution is reached.

B.5 Matrix-free linear solvers

An efficient solution of the discretized system of equations represents an important part of the solution algorithm and several acceleration methods have been developed. Since a large number of transport equations have to be solved, in this work matrix-free linear solvers [168] are preferred because they do not need to store matrix coefficients.

A system of N transport equations linearized and discretized on a mesh of n (inner) points² results in a linear system of $N \times n$ unknowns in the form

$$\mathbf{A}\mathbf{x} = \mathbf{b}. \quad (\text{B.5.1})$$

Given a start solution $\mathbf{x}^{(0)}$, the initial error is defined as

$$\mathbf{r}_{(0)} = \mathbf{b} - \mathbf{A}\mathbf{x}_{(0)} \quad (\text{B.5.2})$$

The Bi-Conjugate Gradient Stabilized method [168] belongs to the class of matrix-free, iterative linear solvers which search the solution in the direction of maximum slope. The solution of system (B.5.1) is found by performing the following steps:

1. compute the initial error (B.5.2) and set $\mathbf{r}_{(0)}^* = \mathbf{r}_{(0)}$ and $\mathbf{p}_{(0)} = \mathbf{p}^3$;
2. find the first smoothing coefficient⁴

$$\alpha_{(j)} = \frac{\mathbf{r}_{(j)} \cdot \mathbf{r}_{(0)}}{\mathbf{A}\mathbf{p}_{(j)} \cdot \mathbf{r}_{(0)}}; \quad (\text{B.5.3})$$

3. smooth the residuum

$$\mathbf{s}_{(j)} = \mathbf{r}_{(j)} - \alpha_{(j)}\mathbf{A}\mathbf{p}_{(j)}; \quad (\text{B.5.4})$$

4. calculate the second smoothing coefficient

$$\omega_{(j)} = \frac{\mathbf{A}\mathbf{s}_{(j)} \cdot \mathbf{s}_{(j)}}{\mathbf{A}\mathbf{s}_{(j)} \cdot \mathbf{A}\mathbf{s}_{(j)}}; \quad (\text{B.5.5})$$

²Points lying on boundaries taking Neumann-like boundary conditions have to be considered in the same manner as inner points.

³In this particular case \mathbf{p} is auxiliary vector used in the linear solver.

⁴ α and ω are called “smoothing” or “stabilizing” coefficients since they are introduced to increase the robustness of the original Conjugate Gradient method. See [168] for an overview of the different gradient-based linear solvers.

5. a second smoothing step is performed, the error for the next iteration step is obtained by

$$\mathbf{r}_{(j+1)} = \mathbf{s}_{(j)} - \omega_{(j)} A \mathbf{s}_{(j)} \quad (\text{B.5.6})$$

and a new solution vector is derived

$$\mathbf{x}_{(j+1)} = \mathbf{x}_{(j)} + \alpha_{(j)} \mathbf{p}_{(j)} + \omega_{(j)} \mathbf{s}_{(j)}. \quad (\text{B.5.7})$$

6. In case the convergence criterion is not fulfilled, find a new vector \mathbf{p} for the next iteration

$$\beta_j = \frac{\mathbf{r}_{(j+1)} \cdot \mathbf{r}^*(0)}{\mathbf{r}_{(j)} \cdot \mathbf{r}^*(0)} \frac{\alpha_{(j)}}{\omega_{(j)}} \quad (\text{B.5.8})$$

$$\mathbf{p}_{(j+1)} = \mathbf{r}_{(j+1)} + \beta_{(j)} (\mathbf{p}_{(j)} - \omega_{(j)} A \mathbf{p}_{(j)}); \quad (\text{B.5.9})$$

7. steps 2-6 are repeated until convergence is reached

$$\mathbf{r}_{(j+1)} \leq \epsilon \mathbf{r}_{(0)} \quad (\text{B.5.10})$$

where $\epsilon = .01$ is sufficient to obtain a good approximation of the solution.

In order to accelerate the convergence rate, a preconditioner is used. In this work a simple diagonal preconditioner is added to the system

$$D^{-1} A \mathbf{x} = D^{-1} \mathbf{b} \quad (\text{B.5.11})$$

where the computation of D^{-1} is trivial.

If chemistry is included, a simple diagonal preconditioner may not guarantee an adequate convergence rate. Therefore the Jacobian matrix of the chemical source term (Eq. (2.2.14)) is added to the preconditioner

$$M = D + J_\omega \quad (\text{B.5.12})$$

in order to get a stronger coupling between the species transport equations. The matrix M in Eq. (B.5.12) has a block-diagonal structure ($N_s \times N_s$) and can be inverted by means of a LU direct solver.

C A generalized fitting procedure for Arrhenius functions

C.1 Linearized algorithm

Goal of the fitting procedure is to cast backward reaction rates in the canonical Arrhenius form. For If an Arrhenius function with parameters (A_f, α_f, T_{a_f})

$$k_f(T; A_f, \alpha_f, T_{a_f}) = A_f T^{\alpha_f} \exp\left(-\frac{T_{a_f}}{T}\right) \quad (\text{C.1.1})$$

is evaluated at n points in temperature space $[300, 3000]$, a vector \mathbf{K}_b containing the corresponding backward reaction rates is derived by using the equilibrium constant K_C

$$k_b(T; A_b, \alpha_b, T_{a_b}) = \frac{k_f(T; A_f, \alpha_f, T_{a_f})}{K_C(T, p)}. \quad (\text{C.1.2})$$

For a given set of backward Arrhenius parameters $(A_b^{(\ell)}, \alpha_b^{(\ell)}, T_{a_b}^{(\ell)})$, an approximation of the vector \mathbf{K}_b is represented by

$$k_b^{(\ell)}(T; A_b^{(\ell)}, \alpha_b^{(\ell)}, T_{a_b}^{(\ell)}) = A_b^{(\ell)} T^{\alpha_b^{(\ell)}} \exp\left(-\frac{T_{a_b}^{(\ell)}}{T}\right) \quad (\text{C.1.3})$$

calculated for each point T_i and stored in a vector $\mathbf{K}_b^{(\ell)}$. The interpolation error (in the least square sense) is defined as

$$r^{(l)}(A_b^{(l)}, \alpha_b^{(l)}, T_{a_b}^{(l)}) = |\mathbf{r}^{(l)}| = \mathbf{W}^T (\mathbf{K}_b - \mathbf{K}_b^{(l)})^2 \quad (\text{C.1.4})$$

where \mathbf{W} is the vector containing error weights. Function C.1.4 can be minimized with respect the Arrhenius parameters. This minimum is given by the solution of the 3×3 set of equations

$$\frac{\partial r}{\partial A_b} = 0 \quad (\text{C.1.5})$$

$$\frac{\partial r}{\partial \alpha_b} = 0 \quad (\text{C.1.6})$$

$$\frac{\partial r}{\partial T_{a_b}} = 0 \quad (\text{C.1.7})$$

In order to get a linear system from Eqs. (C.1.5)-(C.1.7), a logarithm of the Arrhenius function is considered

$$\log k_b = \log A_b + \alpha_b \log T - \frac{T_{a_b}}{T}. \quad (\text{C.1.8})$$

If $(\log A_b)$ is regarded as a new variable, Eqs. (C.1.5)-(C.1.7) are linear and a direct solver can be used to find the set (A_b, α_b, T_{a_b}) which minimizes the error defined by Eq. (C.1.4).

C.2 Levenberg-Marquardt iterative method

If the linearization of Eq. (C.1.8) is not applied, an iterative method has to be employed and a new approximation of the solution vector is found at each step as

$$\mathbf{X}^{(l+1)} = \mathbf{X}^{(l)} - H(\mathbf{X}^{(l)}) \mathbf{r}^{(l)} \quad (\text{C.2.1})$$

where $\mathbf{X}^{(l)} = [A_b^{(l)}, \alpha_b^{(l)}, T_{a_b}^{(l)}]^T$ and H is a $n \times n$ matrix which should approximate the inverse of the Jacobian matrix. It can be noticed that Eq. (C.2.1) returns to the Newton's method if $H = J^{-1}$. It is well known that this method converges only if the initial guess is close enough to the solution. Unfortunately, a good initial guess of the Arrhenius parameters is not easy to find since the only constraint is $A_b > 0$. On the other hand, steepest descent methods show a linear convergence and may oscillate in case of high gradients of \mathbf{r} . Therefore, in this work the Levenberg-Marquardt method [3] is used since it can toggle between both methods in order to get an almost monotone convergence of the solution.

In this method the matrix H in Eq. C.2.1 is approximated as follows

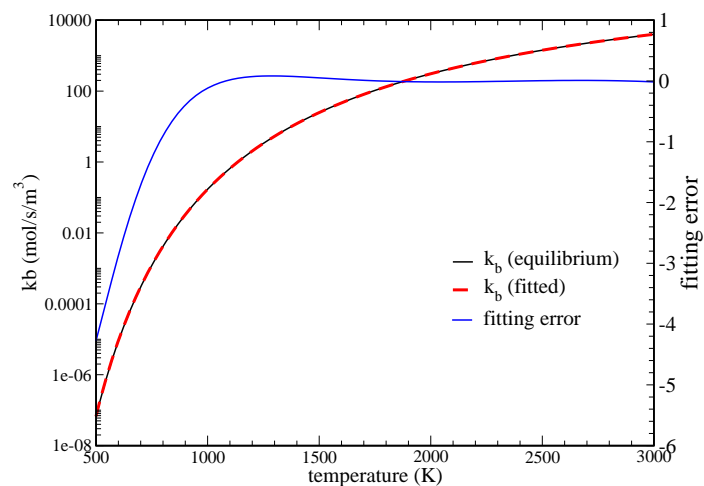
$$H = (J^T J + \lambda I)^{-1} J^T$$

where $\lambda \geq 0$ is the parameter which controls the method's behavior. Since the algorithm starts with large values of λ , a steepest descent method is returned with a convergence rate which is quite insensitive to the initial guess. As $|\mathbf{r}|$ decreases, λ can decrease as well and a second order Newton-like method is recovered.

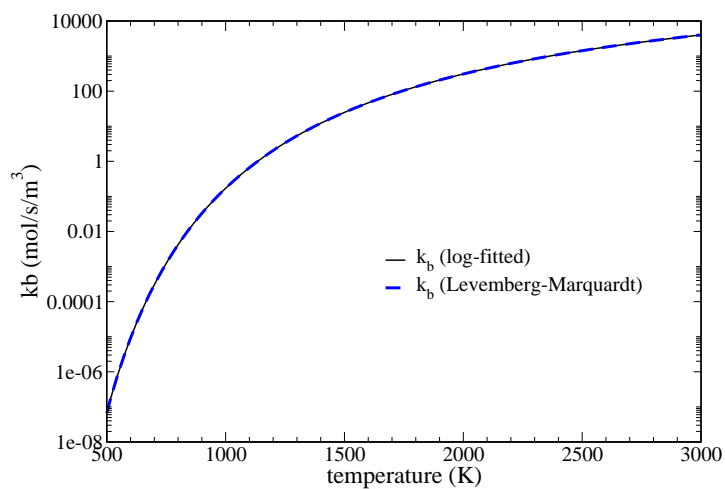
Figure C.2.1(a) shows a comparison between backward Arrhenius rates based on the equilibrium constant (Eq. C.1.2) and its fitted counterpart. The blue line represents the local fitting error

$$err = \frac{k_b - k_{b_i}}{k_b} \cdot 100. \quad (\text{C.2.2})$$

The error is very small at flame-relevant temperatures ($T > 1000$ K), since a weighting vector \mathbf{W} proportional to \mathbf{K}_b was chosen. A comparison between the presented interpolation methods is given in Fig. C.2.1(b). No differences are observed, thus the cheaper log-fitting method can be used if a single vector \mathbf{K}_b has to be fitted. On the other hand, the use of an iterative method is preferred if a smooth sequence of Arrhenius vectors \mathbf{K}_b (i.e. averaged Arrhenius functions in Eq. (4.3.16)) has to be fitted. In this case a previous solution can be used to start the iterative process (C.2.1) for a new calculation and a smooth variation of (A_b, α_b, T_{a_b}) is obtained.



(a) Equilibrium vs log-fitted functions



(b) Log-fitted vs Levenberg-Marquardt methods

Figure C.2.1: Comparison between fitting methods for backward Arrhenius function of reaction $O_2 + H_2 \rightleftharpoons 2OH$ in [101].

Bibliography

- [1] *H3 Jet Flame*, <http://www.tu-darmstadt.de/fb/mb/ekt/flamebase/H3flame/>.
- [2] G.A. Alexopoulos, R.A. Baurle, and H.A. Hassan, *A $k - \omega$ Multivariate Beta PDF for Supersonic Turbulent Combustion*, AIAA paper 93-2197 (1993).
- [3] H.M. Antia, *Numerical Methods for Scientist and Engineers*, second ed., Birkhäuser Verlag, 2002.
- [4] J. Appel, H. Bockhorn, and M. Frenklach, *Kinetic Modeling of Soot Formation with Detailed Chemistry and Physics: Laminar Premixed Flames of C₂ Hydrocarbons*, *Combustion and Flame* **121** (2000), 122–136.
- [5] J. Appel, H. Bockhorn, and M. Wulkow, *A Detailed Numerical Study of the Evolution of Soot Particle Size Distribution in Laminar Premixed Flames*, *Chemosphere* **42** (2001), 635–645.
- [6] A. Aref, B. Baird, and S.R. Gollahalli, *Effects of Flow velocity and Dilution on the Structure of Hydrogen-Air Slot Burner Flames*, AIAA paper 2002-1009 (2002).
- [7] R. Aris, *Vectors, Tensors and the Basic Equations of Fluid Mechanics*, Dover Publications, 1962.
- [8] R. Azzoni, S. Ratti, S.K. Aggarwal, and I.K. Puri, *The Structure of Triple Flames Stabilized on a Slot Burner*, *Combustion and Flame* **119** (1999), 23–40.
- [9] X.S. Bai, M. Balthasar, F. Mauss, and L. Fuchs, *Detailed Soot Modeling in Turbulent Jet, Diffusion Flames*, Twenty-Seventh Symposium (International) on Combustion (The Combustion Institute, ed.), 1998, pp. 1623–1630.
- [10] M. Balthasar and M. Frenklach, *Modeling Soot Aggregate Formation in Premixed Laminar Flames*, Proceedings of the European Combustion Meeting, 2003.
- [11] T.R. Barfknecht, *Toxicology of Soot*, *Progress in Energy and Combustion Science* **9** (1983), 1999–2037.
- [12] R.S. Barlow, J.H. Frank, A.N. Karpetis, and J.-Y. Chen, *Piloted Methane/Air Jet Flames: Transport Effects and Aspects of Scalar Structure*, *Combustion and Flame* **143** (2005), 433–449.

- [13] R. A. Baurle, *Modelling of Turbulent Reacting Flows with Probability Density Functions for Scramjet Applications*, Ph.D. thesis, North Carolina State University, 1995.
- [14] R.A. Baurle, J.P. Drummond, and H.A. Hassan, *An Assumed PDF Approach for the Calculation of Supersonic Mixing Layers*, AIAA paper 92-0182 (1992).
- [15] R.A. Baurle and S.S. Girimaji, *An Assumed PDF Turbulence-Chemistry Closure with Temperature-Composition Correlations*, AIAA paper 99-0928 (1999).
- [16] R.A. Baurle and H.A. Hassan, *Modeling of Turbulent Supersonic H₂-Air Combustion with a Multivariate Beta PDF*, AIAA paper 1993-2198 (1993).
- [17] B.A.V. Bennet, C.S. McEnally, L.D. Pfefferle, and M.D. Smooke, *Computational and Experimental Study of Axisymmetric Coflow Partially Premixed Methane/Air Flames*, *Combustion and Flame* **123** (2000), 522–546.
- [18] D.S. Bento, K.A. Thomson, and Ö.L. Gülder, *Soot Formation and Temperature Field Structure in Laminar Propane-Air Diffusion Flames at Elevated Pressures*, *Combustion and Flame*, in press.
- [19] R.W. Bilger, S.H. Starner, and R.J. Kee, *On Reduced Mechanisms for Methane-Air Combustion in Nonpremixed Flames*, *Combustion and Flame* **80** (1990), 135–149.
- [20] D. A. Bittker, *Detailed Mechanism for Oxidation of Benzene*, *Combustion Science and Technology* **79** (1991), 49–72.
- [21] H. Bockhorn, *Finite Chemical Reaction Rate and Local Equilibrium Effects in Turbulent Hydrogen-Air Diffusion Flames*, Twenty-Second Symposium on Combustion, The Combustion Institute, 1988, pp. 655–664.
- [22] ———, *Modeling of Turbulent Diffusion Flames with Detailed Chemistry*, *Mathematical Modeling in Combustion and Related Topics* (C. Brauner, C.-M. Schmidt-Laine, ed.), Martinus Nijhoff Publishers, 1988, pp. 411–420.
- [23] ———, *Soot formation in combustion*, Springer, 1994 (engl.).
- [24] R. Borghi, *Turbulent Combustion Modeling*, *Prog. Energy Combust. Sci.* **14** (1988), 245–292.
- [25] S. J. Brookes and J. B. Moss, *Measurements of Soot Production and Thermal Radiation From Confined Turbulent Jet Diffusion Flames of Methane*, *Combustion and Flame* **116** (1999), 49–61.
- [26] S.J. Brookes and J.B. Moss, *Predictions of Soot and Thermal Radiation Properties in Confined Turbulent Jet Diffusion Flames*, *Combustion and Flame* **116** (1999), 486–503.

- [27] G.D. Byrne and A.C. Hindmarsh, *Stiff ODE Solvers: A Review of Current and Coming Attractions*, Journal of Computational Physics **70** (1987), 1–62.
- [28] R. Cabra, T. Myhrvold, J.-Y. Chen, R.W. Dibble, A.N. Karpetis, and Barlow R.S., *Simultaneous Laser Raman-Rayleigh-LIF Measurements and Numerical Modeling Results of a Lifted Turbulent H_2/N_2 Jet Flame in a Vitiated Coflow*, Proceeding of the Combustion Institute (The Combustion Institute, ed.), vol. 29, 2002, pp. 1881–1888.
- [29] A. Caldeira-Pires and M.V. Heitor, *Experimental Characterization of Non-Premixed Turbulent Jet Propane Flames*, Experimental Thermal and Fluid Science **23** (2000), 115–132.
- [30] R. Cao and S.B. Pope, *The Influence of Chemical Mechanisms on PDF Calculations of Nonpremixed Piloted Jet Flames*, 4th Joint Meeting of U.S. Sections of Combustion Institute, 2005.
- [31] R.R. Cao, S.B. Pope, and A.R. Masri, *Turbulent Lifted Flames in a Vitiated Coflow Investigated Using Joint PDF Calculations*, Combustion and Flame **142** (2005), 438–453.
- [32] M.J. Castaldi, A.M. Vincitore, and S.M. Senkan, *Micro-structures of Premixed Hydrocarbon Flames: Methane*, Combustion Science and Technology **107** (1995), 1–19.
- [33] M. Champion, *Premixed Turbulent Combustion Controlled by Complex Chemical Kinetics*, Combustion Science and Technology **24** (1980), 23–34.
- [34] R-H. Chen, J.E. Navedo, and L. Chew, *Effects of Fuel Lewis Number on and Damkohler Number Scaling of Nitric Oxide Emission Level of Burke-Schumann Type Flames*, Combustion Science and Technology **127** (1997), 293–318.
- [35] F.C. Christo and B.B. Dally, *Modeling Turbulent Reacting Jets Issuing into a Hot and Diluted Coflow*, Combustion and Flame **142** (2005), 117–129.
- [36] K. Claramunt, R. Cònsul, C.D. Pérez-Segarra, and A. Oliva, *Multidimensional Mathematical Modeling and Numerical Investigation of Co-flow Partially Premixed Methane/Air Laminar Flames*, Combustion and Flame **137** (2004), 444–457.
- [37] R. Cònsul, C.D. Pérez-Segarra, K. Claramunt, J. Cadafalch, and A. Oliva, *Detailed Numerical Simulation of Laminar Flames by a Parallel Multiblock Algorithm Using Loosely Coupled Computers*, Combustion Theory and Modeling **7** (2003), 525–544.
- [38] S.M. Coorea and A. Gulati, *Measurements and Modeling of a Bluff Body Stabilized Flame*, Combustion and Flame **89** (1992), 195–213.
- [39] A. Coppalle and D. Joyeux, *Temperature and Soot Volume Fraction in Turbulent Diffusion Flames: Measurements of Mean and Fluctuating Values*, Combustion and Flame **96** (1994), 275–285.

- [40] A. D'Alessio, A. Di Lorenzo, A. Borghese, F. Beretta, and S. Masi, *Study of the Soot Nucleation Zone of Rich Methane-Oxygen Flames*, Sixteenth Symposium (International) on Combustion (The Combustion Institute, ed.), 1977, pp. 695–708.
- [41] B.B. Dally, D.F. Fletcher, and A.R. Masri, *Flow and Mixing Fields of Turbulent Bluff-body Jets and Flames*, *Combustion Theory and Modelling* **2** (1998), 193–219.
- [42] B.B. Dally, A.N. Karpetsis, and R.S. Barlow, *Structure of Turbulent Non-Premixed Jet Flames in a Diluted Hot Coflow*, *Proceeding of the Combustion Institute* (The Combustion Institute, ed.), vol. 29, 2002, pp. 1147–1154.
- [43] B.B. Dally, A.R. Masri, R.S. Barlow, and G.J. Fiechtner, *Instantaneous and Mean Compositional Structure of Bluff-Body Stabilized Nonpremixed Flames*, *Combustion and Flame* **114** (1998), 119–148.
- [44] W.H. Dalzell and A.F. Sarofim, *Optical Constants of Soot and Their Application to Heat-Flux Calculations*, *Journal of Heat Transfer* (1969), 100–104.
- [45] A. D'Anna and J. H. Kent, *Aromatic Formation Pathways in Non-Premixed Methane Flames*, *Combustion and Flame* **132** (2003), 715–722.
- [46] A. D'Anna and J.H. Kent, *Modeling of Particulate Carbon and Species Formation in Coflowing Diffusion Flames of Ethylene*, *Combustion and Flame* **144** (2006), 249–260.
- [47] M. Di Domenico, P. Gerlinger, and M. Aigner, *Modeling Soot Formation in Methane Diffusion Flames*, AIAA paper 2006-1163 (2006).
- [48] A. Di Lorenzo, A. D'Alessio, V. Cincotti, S. Masi, P. Menna, and C. Venitozzi, *UV Absorption, Laser Excited Fluorescence and Direct Sampling in the Study of the Formation of Polycyclic Aromatic Hydrocarbons in Rich CH₄/O₂ Flames*, Eighteenth Symposium (International) on Combustion (The Combustion Institute, ed.), 1981, pp. 485–491.
- [49] V. Dias, C. Renard, P.J. Van Tiggelen, and J. Vandooren, *Modeling of Soot Precursors in Rich Premixed Ethylene/Oxygen/Argon Flames*, *Proceedings of the European Combustion Meeting*, 2003.
- [50] V. Dias, P.J. Van Tiggelen, and J. Vandooren, *Modeling of Soot Precursors in Several Rich Hydrocarbon/Oxygen/Argon Flames*, *Proceedings of the European Combustion Meeting*, 2005.
- [51] R.A. Dobbins, R.A. Fletcher, and H.-C. Chang, *The Evolution of Soot Precursor Particles in a Diffusion Flame*, *Combustion and Flame* **115** (1998), 285–298.
- [52] L. Dupont, A. El Bakali, Pauwels. J., I. Da Costa, P. Meunier, and H. Richter, *Investigation of Stoichiometric Methane/Air/Benzene (1.5%) and Methane/Air Low Pressure Flames*, *Combustion and Flame* **135** (2003), 171–183.

- [53] A. C. Eckbreth, *Laser diagnostics for combustion temperature and species*, second ed., vol. 3, Taylor and Francis, 1996.
- [54] A.M. El-Leathy, F. Xu, and G.M. Faeth, *Soot Surface Growth and Oxidation in Laminar Unsaturated-Hydrocarbon/Air Diffusion Flames*, AIAA-paper 2002-1116 (2002).
- [55] A. Ern, C.C. Douglas, and M.D. Smooke, *Detailed Chemistry Modeling of Laminar Diffusion Flames on Parallel Computers*, The International Journal of Supercomputer Application and High Performance Computing **XX** (1995).
- [56] V. Eswaran and S.B. Pope, *Direct numerical simulations of the turbulent mixing of a passive scalar*, Physics of Fluids **31** (1988), no. 3, 506–520.
- [57] M. Fairweather, W.P. Jones, and R.P. Lindstedt, *Predictions of Radiative Transfer from a Turbulent Reacting Jet in a Cross-Wind*, Combustion and Flame **89** (1992), 45–63.
- [58] J.H. Ferziger and M. Peric, *Computational Methods for Fluid Dynamics*, Springer, 1997.
- [59] R.O. Fox, *Computational Model for Turbulent Reacting Flows*, Cambridge University Press, 2003.
- [60] S. Frankel, P. Drummond, and H. Hassan, *A Hybrid Reynolds Averaged/PDF Closure Model for Supersonic Turbulent Combustion*, AIAA paper 90-1573.
- [61] S. Fukutani, N. Kuniishi, and H. Jinne, *Flame Structure of an Axisymmetric Hydrogen-Air Diffusion Flame*, Twenty-Third Symposium (International) on Combustion, The Combustion Institute, 1990, pp. 567–573.
- [62] R.L. Gaffney, J.A. White, S.S. Girimaji, and J.P. Drummond, *Modeling Temperature and Species Fluctuations in Turbulent, Reacting Flow*, Computing Systems in Engineering **5** (1994), no. 2, 117–133.
- [63] R.L. Jr. Gaffney, J.A. White, S.S. Girimaji, and J.P. Drummond, *Modeling Turbulent/Chemistry Interactions Using Assumed PDF Methods*, AIAA paper 92-3638 (1992).
- [64] P. Gerlinger, *Investigation of an Assumed PDF Approach for Finite-Rate Chemistry*, AIAA paper 2002-0166 (2002).
- [65] P. Gerlinger, H. Möbus, and D. Brüggemann, *An Implicit Multigrid Method for Turbulent Combustion*, Journal of Computational Physics **167** (2001), 247–276.
- [66] P. Gerlinger, B. Noll, and M. Aigner, *Assumed PDF Modeling and PDF Structure Investigation Using Finite-Rate Chemistry*, Progress in Computational Fluid Dynamics **5** (2005), no. 6, 334–344.

- [67] S. S. Girimaji, *Simulations of Diffusion-Reaction Equations with Implications to Turbulent Combustion Modeling*, ICASE Report 93-69, NASA - Langley Research Center, 1993.
- [68] S.S. Girimaji, *Assumed β -pdf Model for Turbulent Mixing: Validation and Extension to Multiple Scalar Mixing*, *Combustion Science and Technology* **78** (1991), 177–196.
- [69] ———, *A Study of Turbulent Combustion and its Modeling Using a Diffusion Reaction Equation Model*, *International Journal of Engineering Science* **34** (1996), no. 1, 47–58.
- [70] P. Givi, *Model-free Simulations of Turbulent Reactive Flows*, *Progress in Energy and Combustion Science* **15** (1989), 1–107.
- [71] G.M. Goldin and S. Menon, *A Scalar PDF Construction Model for Turbulent Non-Premixed Combustion*, *Combustion Science and Technology* **125** (1997), 47–72.
- [72] ———, *A Comparison of Scalar PDF Turbulent Combustion Models*, *Combustion and Flame* **113** (1998), 442–453.
- [73] F.C. Gouldin and P.C. Miles, *Chemical Closure and Burning Rates in Premixed Turbulent Flames*, *Combustion and Flame* **100** (1995), 202–210.
- [74] S. Granata, F. Cambianica, S. Zinesi, T. Faravelli, and E. Ranzi, *Detailed Kinetics of PAH and Soot Formation in Combustion Processes: Analogies and Similarities in Reaction Classes*, *Proceedings of the European Combustion Meeting*, 2005.
- [75] P.C. Gregory, *Bayesian Logical Data Analysis for the Physical Sciences*, Cambridge University Press, 2005.
- [76] W.L. Grosshandler, *RADCAL: A Narrow-Band Model for Radiation Calculations in a Combustion Environment*, NIST Technical Note 1402, NIST, 1993.
- [77] Ö.L. Gülder, K.A. Thomson, and D.R. Snelling, *Effect of Fuel Nozzle Material Properties on Soot Formation and Temperature Field in Coflow Laminar Diffusion Flames*, *Combustion and Flame* **144** (2006), 426–633.
- [78] H. Guo, F. Liu, and G.J. Smallwood, *Soot and NO Formation in Counterflow Ethylene/Oxygen/Nitrogen Diffusion Flames*, *Combustion Theory and Modeling* **8** (2004), 475–489.
- [79] H. Guo, F. Liu, G.J. Smallwood, and L. Gülder, Ö, *The flame preheating effect on numerical modelling of soot formation in a two-dimensional laminar ethylene-air diffusion flame*, *Combustion Theory and Modelling* **6** (2002), 173–187.
- [80] H. Guo, F. Liu, G.J. Smallwood, and Ö.L. Gülder, *Numerical Study on the Influence of Hydrogen Addition on Soot Formation in a Laminar Ethylene-Air Diffusion Flame*, *Combustion and Flame* **145** (2006), 324–338.

- [81] E. Gutheil and H. Bockhorn, *The Effect of Multi Dimensional PDFs on the Turbulent Reaction Rate in Turbulent Reacting Flows at Moderate Damköler Numbers*, *Physico-Chemical Hydrodynamics* **9** (1987), no. 3/4, 525–535.
- [82] E. Hairer and G. Wanner, *Solving ordinary differential equations II*, Springer Verlag, Berlin, 1991.
- [83] E. Hairer and G. Wanner, *Solving Ordinary Differential Equations*, second ed., Springer Series in Computational Mathematics, vol. II: Stiff and Differential-Algebraic Problems, Springer-Verlag, 1996.
- [84] V.J. Hall-Roberts, A.N. Hayhurst, D.E. Knight, and S.G. Taylor, *The Origin of Soot in Flames, Is the Nucleus an Ion?*, *Combustion and Flame* **120** (2000), 578–584.
- [85] H.P. Hassel (ed.), *TNF2 Workshop*, 1997.
- [86] M. Haudiquert, A. Cessou, D. Stepowski, and A. Coppalle, *OH and Soot Concentration Measurements in a High-Temperature Laminar Diffusion Flame*, *Combustion and Flame* **111** (1997), 338–349.
- [87] E.R. Hawkes and J.H. Chen, *Comparison of Direct Numerical Simulation of Lean Premixed Methane-Air Flames with Strained Laminar Flame Calculations*, *Combustion and Flame* **14** (2006), 112–125.
- [88] M. Herrmann, *Numerical Simulation of Turbulent Bunsen Flames with a Level Set Flamelet Model*, *Combustion and Flame* **145** (2006), 357–375.
- [89] S. Hong, M.S. Wooldridge, H.G. Im, D.N. Assanis, and H. Pitsch, *Development and Application of a Comprehensive Soot Model for 3D CFD Reacting Flow Studies in a Diesel Engine*, *Combustion and Flame* **143** (2005), 11–26.
- [90] B. Hu, B. Yang, and U.O. Koçlu, *Soot Measurements at the Axis of an Ethylene/Air Non-Premixed Turbulent Jet Flame*, *Combustion and Flame* **134** (2003), 93–106.
- [91] F. Inal, G. Tayfur, T.R. Melton, and S.M. Senkan, *Experimental and Artificial Neural Network Modeling Study on Soot Formation in Premixed Hydrocarbon Flames*, *Fuel* **82** (2003), 1477–1490.
- [92] R.I. Issa, *Solution of the Implicit Discretised Fluid Flow Equations by Operator-Splitting*, *Journal of Computational Physics* **62** (1985), 40–65.
- [93] R.I. Issa, A.D. Gosman, and A.P. Watkins, *The Computation of Compressible and Incompressible Recirculating Flows by a Non-iterative Implicit Scheme*, *Journal of Computational Physics* **62** (1986), 66–82.

- [94] C.J. Jachimowski, *An Analytical Study of the Hydrogen-Air Reaction Mechanism with Application to Scramjet Combustion*, Technical Paper 2791, NASA, 1988.
- [95] J. C. Jachimowski, *An Analysis of Combustion Studies in Shock Expansion Tunnels and Reflected Shock Tunnels*, Technical Paper 3224, NASA, 1992.
- [96] W.P. Jones, *Turbulent Reactive Flows*, ch. six, pp. 309–374, Academic Press Ltd, 1994.
- [97] C.R. Kaplan and K. Kailasanath, *Flow-field Effects on Soot Formation in Normal and Inverse Methane-Air Diffusion Flames*, *Combustion and Flame* **124** (2001), 275–294.
- [98] V.R. Katta, T.R. Meyer, C. Montgomery, and W.M. Roquemore, *Studies on Soot Formation in a Model Gas-Turbine Combustor*, AIAA 2005-3777.
- [99] A. Kazakov and M. Frenklach, *Dynamic Modeling of Soot Particle Coagulation and Aggregation: Implementation with the Method of Moments and Application to High-Pressure Laminar Premixed Flames*, *Combustion and Flame* **114** (1998), 484–501.
- [100] A. Kazakov, H. Wang, and M. Frenklach, *Detailed Modeling of Soot Formation in Laminar Premixed Ethylene Flames at a Pressure of 10 bar*, *Combustion and Flame* **100** (1995), 111–120.
- [101] R.J. Kee, J.F. Grcar, M.D. Smooke, and J.A. Miller, *A Fortran Program for Modeling Steady Laminar One-Dimensional Premixed Flames*, Tech. Report SAND85-8240, Sandia Laboratories, Albuquerque, NM, 1985.
- [102] I.M. Kennedy, W. Kollmann, and J.-Y. Chen, *A Model for Soot Formation in a Laminar Diffusion Flame*, *Combustion and Flame* **81** (1990), 73–85.
- [103] I.M. Kennedy, C. Yam, D.C. Rapp, and R.J. Santoro, *Modeling and Measurements of Soot and Species in a Laminar Diffusion Flame*, *Combustion and Flame* **107** (1996), 368–382.
- [104] J. H. Kent, H. Jander, and H. GG. Wagner, *Soot formation in a Laminar Diffusion Flame*, Eighteenth Symposium (International) on Combustion (The Combustion Institute, ed.), 1981, pp. 1117–1126.
- [105] M. Kraft, M. Balthasar, and F. Mauss, *Soot and NO_x Formation in a Stationary Turbulent Combustor*, *Scientific Computing in Chemical Engineering* **2** (1999), 118–125.
- [106] A. Kronenburg, *Double Conditioning of Reactive Scalar Transport Equations in Turbulent Nonpremixed Flames*, *Physics of Fluids* **16** (2004), no. 7, 2640–2648.
- [107] A. Kronenburg, R. W. Bilger, and J.H. Kent, *Modeling Soot Formation in Turbulent Methane-Air Jet Diffusion Flames*, *Combustion and Flame* **121** (2000), 24–40.

- [108] D.F. Kronholm and J.B. Howard, *Analysis of Soot Surface Growth Pathways Using Published Plug-Flow Reactor Data with New Particle Size Distribution Measurements and Published Premixed Flame Data*, Proceedings of the Combustion Institute, vol. 28, 2000, pp. 2555–2561.
- [109] T.S. Kuan and R.P. Lindstedt, *Transported Probability Density Function Modeling of a Bluff Body Stabilized Turbulent Flame*, Proceedings of the Combustion Institute, vol. 30, The Combustion Institute, 2005, pp. 767–774.
- [110] K.K. Kuo, *Principles of Combustion*, first ed., A Wiley-Interscience Publication, 1986.
- [111] O. Lammel, K.P. Geigle, R. Lückcrath, W. Meier, and M. Aigner, *Investigation of Soot Formation and Oxidation in a High-Pressure Gas Turbine Model Combustor by Laser Techniques*, ASME paper GT2007-27902 (2007), In preparation.
- [112] B.E. Launder, *Turbulence*, Topics in Applied Physics (P. Brashaw, ed.), vol. 12, Springer Verlag, 1976.
- [113] C.W. Lautenberger, J.L. de Ris, N.A. Dembsey, J.R. Barnett, and H.R. Baum, *A Simplified Model for Soot Formation and Oxidation in CFD Simulation of Non-Premixed Hydrocarbon Flames*, Fire Safety Journal **40** (2005), 141–176.
- [114] A.H. Lefebvre, *Gas Turbine Combustion*, second ed., Taylor and Francis, 1999.
- [115] B. Lehmann, *Gasfilmdüse II - Ergebnisse von Geschwindigkeits- und Temperaturemessungen in der Modellbrennkammer ohne und mit Verbrennung*, Interner Bericht DLR-IB-92517-2000/B4, DLR, Berlin, 2000.
- [116] A. Leipertz, F. Ossler, and M. Aldén, *Applied Combustion Diagnostics*, ch. Thirteenth, pp. 359–383, Taylor and Francis, 2002.
- [117] A.D. Leonard and J.C. Hill, *A Simple Chemical Reaction in Numerically Simulated Homogeneous Turbulence*, AIAA paper 87-0134 (1987).
- [118] K.M. Leung, R.P. Lindstedt, and W.P. Jones, *A Simplified Reaction Mechanism for Soot Formation in Nonpremixed Flames*, Combustion and Flame **87** (1991), 289–305.
- [119] P. R. Lindstedt, *Simplified Soot Nucleation and Surface Growth Steps for Non-Premixed Flames*, Soot Formation in Combustion (H. Bockhorn, ed.), Springer Series in Chemical Physics, Springer-Verlag, 1994.
- [120] R.P. Lindstedt and E.M. Vaos, *Transported PDF Modeling of High-Reynolds-Number Premixed Turbulent Flames*, Combustion and Flame **145** (2006), 495–511, in press.
- [121] F. Liu, H. Guo, G.J. Smallwood, and Ö. L. Gülder, *Numerical Modelling of Soot Formation and Oxidation in Laminar Coflow Non-smoking and Smoking Ethylene Diffusion Flames*, Combustion Theory and Modelling **7** (2003), 301–315.

- [122] F.C. Lockwood and A.S. Naguib, *The Prediction of the Fluctuations in the Properties of Free, Round-Jet, Turbulent, Diffusion Flames*, *Combustion and Flame* **24** (1975), 109–124.
- [123] D. Lupant, B. Pesenti, P. Evrard, and P. Lybaert, *Numerical and Experimental Characterization of a Self-Regenerative Flameless Oxidation Burner Operation in a Pilot-Scale Furnace*, *Proceedings of the European Combustion Meeting 2005*, 2005.
- [124] M.M. Maricq, *A Comparison of Soot Size and Charge Distributions from Ethane, Ethylene, Acetylene, and Benzene/Ethylene Premixed Flames*, *Combustion and Flame* **144** (2006), 730–743.
- [125] T.R. Marrero and E.A. Mason, *Gaseous Diffusion Coefficients*, *Journal of Physical and Chemistry Reference Data* **1** (1972), no. 1, 1–118.
- [126] A.R. Masri, R.W. Bilger, and R.W. Dibble, *Turbulent Nonpremixed Flames of Methane Near Extinction: Probability Density Function*, *Combustion and Flame* **73** (1988), 261–285.
- [127] A.R. Masri, R. Cao, S.B. Pope, and G.M. Goldin, *PDF Calculations of Turbulent Lifted Flames of H_2/N_2 Fuel Issuing into a Vitiated Co-flow*, *Combustion Theory and Modeling* **8** (2004), 1–22.
- [128] A.R. Masri, P.A.M. Kalt, and R.S. Barlow, *The Compositional Structure of a Swirl-stabilised Turbulent Nonpremixed Flames*, *Combustion and Flame* **137** (2004), 1–37.
- [129] S. Mathur, P.K. Tondon, and S.C. Saxena, *Thermal Conductivity of Binary, Ternary and Quaternary mixtures of rare Gases*, *Molecular Physics* **12** (1967), no. 6, 569–579.
- [130] F. Mauss, T. Schäfer, and H. Bockhorn, *Inception and Growth of Soot Particles in Dependence on the Surrounding Gas Phase*, *Combustion and Flame* **99** (1994), 697–705.
- [131] C.S. McEnally and A.M. Pfefferle, *Experimental Study of Nonfuel Hydrocarbons and Soot in Coflowing Partially Premixed Ethylene/Air Flames*, *Combustion and Flame* **121** (2000), 575–592.
- [132] C.S. McEnally, L.D. Pfefferle, B. Atakan, and K. Kohse-Höinghaus, *Studies of Aromatic Hydrocarbon Formation Mechanisms in Flames: Progress towards Closing the Fuel Gap*, *Progress in Energy and Combustion Science* **in press** (2006).
- [133] C.S. McEnally, A.M. Schaffer, M.B. Long, L.D. Pfefferle, M.D. Smooke, M.B. Colket, and R.J. Hall, *Computational and Experimental Study of Soot Formation in a Coflow, Laminar, Ethylene Diffusion Flame*, *Twenty-Seventh Symposium (International) on Combustion*, 1998, pp. 1497–1595.

- [134] M. McKeand, A. Menon, S. Iyer, S.-Y. Lee, M. Linevsky, T. Litzinger, and R. Santoro, *Effects of NO₂ on Soot Formation in a Laminar Premixed Ethylene-Air Flame*, AIAA 2006-1162 (2006).
- [135] W. Meier, X.R. Duan, and P. Weigand, *Investigations of Swirl Flames in a Gas Turbine Model Combustor II. Turbulence-Chemistry Interactions*, *Combustion and Flame* **144** (2006), 225–236.
- [136] T.R. Melton, F. Inal, and M.S. Senkan, *The Effects of Equivalence Ratio on the Formation of Polycyclic Aromatic Hydrocarbons and Soot in Premixed Ethane Flames*, *Combustion and Flame* **121** (2000), 671–678.
- [137] R.B. Miles, *Applied Combustion Diagnostics*, ch. Seven, pp. 194–223, Taylor and Francis, 2002.
- [138] J.H. Miller, *The Kinetics of Polynuclear Aromatic Hydrocarbon Agglomeration in Flames*, Twenty-Third Symposium (International) on Combustion (The Combustion Institute, ed.), 1990, pp. 91–98.
- [139] R.E. Mitchell, A.F. Sarofin, and L.A. Clomburg, *Experimental and Numerical Investigation of Confined Laminar Diffusion Flames*, *Combustion and Flame* **37** (1980), 227–244.
- [140] R.E. Mitchell, A.F. Sarofin, and R. Yu, *Nitric Oxide and Hydrogen Cyanide Formation in Laminar Methane/Air Diffusion Flames*, *Combustion Science and Technology* **21** (1980), no. 157-167.
- [141] H. Möbus, P. Gerlinger, and D. Brüggemann, *Comparison between Eulerian and Lagrangian Monte Carlo PDF Methods for Turbulent Diffusion Flames*, *Combustion and Flame* **124** (2001), 519–534.
- [142] C. Moreau, J. F. Pauwels, P. Desgroux, and E. Therssen, *Particle Size and Soot Volume Fraction Measurements in Atmospheric Diffusion Flame by Laser Induced Incandescence Combined with Cavity Ring-Down Spectroscopy*, Proceedings of the European Combustion Meeting, 2003.
- [143] J.B. Moss, C.D. Stewart, and K.J. Young, *Modeling Soot Formation and Burnout in a High Temperature Laminar Diffusion Flame Burning under Oxygen-Enriched Conditions*, *Combustion and Flame* **101** (1995), 491–500.
- [144] M.A. Mueller, T.J. Kim, R.A. Yetter, and F.L. Dryer, *Flow Reactor Studies and Kinetic Modeling of the H₂O₂ Reaction*, *Int. J. Chemical Kinetics* **31** (1999), 113–125.
- [145] J.R. Narayan and S.S. Girimaji, *Turbulent Reacting Flow Computations Including Turbulence-Chemistry Interactions*, AIAA paper 92-0342 (1992).

- [146] A. Neuber, G. Krieger, M. Tacke, E. Hassel, and J. Janicka, *Finite Rate Chemistry and NO Molefraction in Non-Premixed Turbulent Flames*, *Combustion and Flame* **113** (1998), 198–211.
- [147] A.M. Nienow, J.T. Roberts, and R.Z. Michael, *Surface Chemistry of Nanometer-Sized Aerosol Particles: Reactions of Molecular Oxygen with 30 nm Soot Particles as a Function of Oxygen Partial Pressure*, *Journal of Physical Chemistry* **109** (2005), no. 12, 5561–5568.
- [148] T. S. Norton, K.C. Smyth, J.H. Miller, and M.D. Smooke, *Comparison of Experimental and Computed Species Concentration and Temperature Profiles in Laminar, Two-Dimensional Methane/Air Diffusion Flames*, *Combustion Science and Technology* **90** (1993), 1–34.
- [149] M. Ó Conaire, H.J. Curran, J.M. Simmie, W.J. Pitz, and C.K. Westbrook, *A Comprehensive Modeling Study of Hydrogen Oxidation*, *Int. J. Chemical Kinetics* **36** (2004), no. 11, 603–622.
- [150] K.C. Oh and H.D. Shin, *The Effect of Oxygen and Carbon Dioxide Concentration on Soot Formation in Non-premixed Flames*, *Fuel* (2005), 1–10.
- [151] B. Öktem, M.P. Tolocka, B. Zhao, H. Wang, and M.V. Johnston, *Chemical Species Associated with the Early Stage of Soot growth in a Laminar Premixed Ethylene-Oxygen-Argon Flame*, *Combustion and Flame* **142** (2005), 364–373.
- [152] J.G. Parker, *Rotational and Vibrational Relaxation in Diatomic Gases*, *Physics of Fluids* **2** (1959), no. 4449-462.
- [153] S.V. Patankar, *Numerical Heat Transfer and Fluid Flow*, Series in Computational Methods in Mechanics and Thermal Science, Hemisphere Publishing Corporation, 1980.
- [154] N. Peters, *Turbulent Combustion*, Cambridge University Press, 2000.
- [155] S.B. Pope, *An Explanation of the Turbulent Round-Jet/Plane-Jet Anomaly*, *AIAA Journal* **16** (1978), 279–281.
- [156] ———, *Probability Distributions of Scalars in Turbulent Shear Flow*, *Turbulent Shear Flows* (F. Launder Bradbury, L.J.S. Durst, ed.), vol. 2, Springer-Verlag, 1979.
- [157] ———, *A Rational Method of Determining Probability Distributions in Turbulent Reacting Flows*, *Journal of Non-Equilibrium Thermodynamics* **4** (1979), no. 5.
- [158] ———, *The Statistical Theory of Turbulent Flames*, *Philosophical Transactions of the Royal Society of London* **291A** (1979), 529–568.
- [159] ———, *Computations of Turbulent Combustion: Progress and Challenges*, Twenty-Third Symposium on Combustion, The Combustion Institute, 1990, pp. 591–612.

- [160] ———, *Turbulent Flows*, Cambridge university press, 2000.
- [161] I.K. Puri, S.K. Aggarwal, S. Ratti, and R. Azzoni, *On the Similitude Between Lifted and Burner-Stabilized Triple Flames: A Numerical and Experimental Investigation*, *Combustion and Flame* **124** (2001), 311–325.
- [162] Reaction Design, *CHEMKIN Theory Manual*.
- [163] H. Richter, M. Braun-Unkhoff, S. Granata, J. Yu, E. Goos, N.A. Slavinskaya, P. Frank, W.H. Green, and J.B. Howard, *Computational Investigation of PAH and Soot Formation in Premixed Ethylene Flames*, Proceedings of the European Combustion Meeting, 2005.
- [164] H. Richter, S. Granata, W.H. Green, D.F. Kronholm, and J.B. Howard, *Detailed Modeling of PAH and Soot Formation in Flames*, Proceedings of the European Combustion Meeting, 2003.
- [165] H. Richter and J. B. Howard, *Formation of Polycyclic Aromatic Hydrocarbons and their Growth to Soot - A Review of Chemical Reaction Pathways*, *Progress in Energy and Combustion Science* **26** (2000), 565–608.
- [166] H. Richter and J.B. Howard, *Formation and Consumption of Single-Ring Aromatic Hydrocarbons and Their Precursors in Premixed Acetylene, Ethylene and Benzene Flames*, *Physical Chemistry Chemical Physics* **4** (2002), 2038–2055.
- [167] J.F. Roesler, S. Martinot, C.S. McEnally, L.D. Pfefferlee, J.-L. Delfau, and C. Vovelle, *Investigating the role of methane on the growth of aromatic hydrocarbons and soot in fundamental combustion processes*, *Combustion and Flame* **134** (2003), 249–260.
- [168] Yousef Saad, *Iterative methods for sparse linear systems*, second ed., Society for Industrial and Applied Mathematics, Philadelphia, PA, 2003.
- [169] R.J. Santoro, H.G. Semerjian, and R.A. Dobbins, *Soot Particle Measurements in Diffusion Flames*, *Combustion and Flame* **51** (1983), 203–218.
- [170] T.J. Santoro, T.T. Yeh, J.J. Horvath, and H.G. Semerjian, *The Transport and Growth of Soot Particles in Laminar Diffusion Flames*, *Combustion Science and Technology* **53** (1987), 89–115.
- [171] S. Senkan and M. Castaldi, *Formation of Polycyclic Aromatic Hydrocarbons (PAH) in Methane Combustion: Comparative New Results from Premixed Flames*, *Combustion and Flame* **107** (1996), 141–150.
- [172] K. Seshadri and N. Peters, *Asymptotic Structure and Extinction of Methane-Air Diffusion Flames*, *Combustion and Flame* **73** (1988), 23–44.

- [173] K. Seshady and N. Peters, *The Inner Structure of Methane-Air Flames*, *Combustion and Flame* **81** (1990), 96–118.
- [174] K. Siegmann, K. Sattler, and H.C. Siegmann, *Clustering at High Temperatures: Carbon Formation in Combustion*, *Journal of Electron Spectroscopy and Related Phenomena* **126** (2002), 191–202.
- [175] J. Singh, R.I.A. Patterson, M. Kraft, and H. Wang, *Numerical Simulation and Sensitivity Analysis of Detailed Soot Particle Size Distribution in Laminar Premixed Ethylene Flames*, *Combustion and Flame* **145** (2006), 117–127.
- [176] W.A. Sirignano, *Fluid Dynamics and Transport of Droplets and Sprays*, Cambridge University Press, 1999.
- [177] M.S. Skjøth-Rasmussen, P. Glarborg, M. Østberg, J.T. Johanness, Livbjerg. H., A.D. Jensen, and T.S. Christensen, *Formation of Polycyclic Aromatic Hydrocarbons and Soot in Fuel-rich Oxidation of Methane in a Laminar Flow Reactor*, *Combustion and Flame* **136** (2004), 91–128.
- [178] G.P. Smith, D.M. Golden, M. Frenklach, N.W. Moriarty, B. Eiteneer, M. Goldenberg, C.T. Bowman, R.K. Hanson, S. Song, Jr Gardiner, W.C., V.V. Lissianski, and Z. Qin, *Gri mech 3.0*, 1999, http://www.me.berkeley.edu/gri_mech/.
- [179] M. D. Smooke, C. S. McEnally, L.D. Pfefferle, R.J. Hall, and M.B. Colket, *Computational and Experimental Study of Soot Formation in a Coflow, Laminar Diffusion Flame*, *Combustion and Flame* **117** (1999), 117–139.
- [180] M.D. Smooke, P. Lin, J.K. Lam, and M.B. Long, *Computational and Experimental Study of a Laminar Axisymmetric Methane-Air Diffusion Flame*, Twenty-Third Symposium (International) on Combustion, 1990, pp. 575–582.
- [181] M.D. Smooke, M.B. Long, B.C. Connelly, M.B. Colket, and R.J. Hall, *Soot Formation in Laminar Diffusion Flames*, *Combustion and Flame* **143** (2005), 613–628.
- [182] M.D. Smooke, R.E. Mitchell, and D.E. Keyes, *Numerical Solution of Two-Dimensional Axisymmetric Laminar Diffusion Flames*, *Combustion Science and Technology* **67** (1989), 85–122.
- [183] S. Sreedhara and K.N. Lakshmisha, *Autoignition in a Non-premixed Medium: DNS Studies on the Effects of Three-dimensional Turbulence*, *Proceedings of the Combustion Institute*, vol. 29, The Combustion Institute, 2002, pp. 2051–2059.
- [184] S.E. Stein and A. Fahr, *High-Temperature Stabilities of Hydrocarbons*, *Journal of Physical Chemistry* **89** (1985), 3714–3725.

- [185] C.D. Stewart, K.J. Syed, and J.B. Moss, *Modeling Soot Formation in Non-Premixed Kerosine-Air Flames*, *Combustion Science and Technology* **75** (1991), 211–226.
- [186] W.P. Stricker, *Applied Combustion Diagnostics*, ch. Six, pp. 155–193, Taylor and Francis, 2002.
- [187] J.C. Tannenhill, D.A. Anderson, and R.H. Pletcher, *Computational Fluid Mechanics And Heat Transfer*, Series in Computational Methods and Physical Processes in Mechanics and Thermal Sciences, Taylor and Francis, 1997.
- [188] S.D. Terry and K.M. Lyons, *Low Reynolds Number Turbulent Lifted Flames in High Coflow*, *Combustion Science and Technology* **177** (2005), 2091–2112.
- [189] P.A. Tesner, E.I. Tsygankova, L.P. Guilazetdinov, V.P. Zuyev, and G.V. Loshakova, *The Formation of Soot from Aromatic Hydrocarbons in Diffusion Flames of Hydrocarbon-Hydrogen Mixtures*, *Combustion and Flame* **17** (1971), 279–285.
- [190] T. D. Knorre Tesner, P. A. Snegiriova, *Kinetics of Dispersed Carbon Formation*, *Combustion and Flame* **17** (1971), 253–260.
- [191] K.A. Thomson, L. Gülder Ömer, J. W. Elizabeth, R.A. Fraser, G.J. Smallwood, and D.R. Snelling, *Soot Concentration and Temperature Measurements in Co-anular, Nonpremixed CH₄/air Laminar Flames at Pressure up to 4 MPa*, *Combustion and Flame* **140** (2005), 222–232.
- [192] W. Tsang, *Important Factors in the Development of Combustion Mechanisms for Realistic Fuels*, AIAA paper 2002-1098 (2002).
- [193] M.S. Tsurikov, K.P. Geigle, V. Krüger, Y. Schneider-Kühnle, W. Stricke, R. Lückerrath, R. Hadeff, and M. Aigner, *Laser-based Investigation of Soot Formation in Laminar Premixed Flames at Atmospheric and Elevated Pressure*, *Combustion Science and Technology* **177** (2005), 1835–1862.
- [194] L. Vervisch, D. Veynante, J.P.A.J. van Beeck, P. Flohr, D.C. Haworth, F. Lacas, K.M. Lyons, and D. Honoré, *Turbulent Combustion*, Von Karman Lecture Series, 2005.
- [195] W.G. Vincenti and C.H. Jr Kruger, *Introduction to Physical Gas Dynamics*, second ed., John Wiley and Sons, 1965.
- [196] H. Wang and M. Frenklach, *Enthalpies of Formation of Benzenoid Aromatic Molecules and Radicals*, *Journal of Physical Chemistry* **97** (1993), 3867–3874.
- [197] ———, *Transport Properties of Polycyclic Aromatic Hydrocarbons for Flame Modeling*, *Combustion and Flame* **96** (1994), 163–170.
- [198] J. Warnatz, U. Mass, and R.W. Dibble, *Combustion*, third ed., Springer-Verlag, 2001.

- [199] Z. Wen, S. Yun, M.J. Thomson, and M.F. Lightstone, *Modelling Soot Formation in Turbulent Kerosene/Air Jet Diffusion Flames*, *Combustion and Flame* **135** (2003), 323–340.
- [200] C.D. Wilcox, *Turbulence Modeling for CFD*, second ed., DCW Industries, 2004.
- [201] Z. Wu, S.H. Starner, and R.W. Bilger, *Lift-off Heights of Turbulent H₂/N₂ Jet Flames in a Vitiated Coflow*, Australian Symposium on Combustion and The 8th Australian Flames Days, 2003.
- [202] A. Wulff and J. Hourmouziadis, *Technology Review of Aeroengine Pollutant Emissions*, *Aerospace Science and Technology* **8** (1997), 557–572.
- [203] F. Xu and G.M. Faeth, *Structure of the Soot Growth Region of Laminar Premixed Methane/Oxygen Flames*, *Combustion and Flame* **121** (2000), 640–650.
- [204] F. Xu, K.-C. Lin, and G.M. Faeth, *Soot Formation in Laminar Premixed Methane/Oxygen Flames at Atmospheric Pressure*, *Combustion and Flame* **115** (1998), 195–209.
- [205] Y. Xu, M.D. Smooke, P. Lin, and M.B. Long, *Primitive Variable Modeling of Multidimensional Laminar Flames*, *Combustion Science and Technology* **90** (1993), 289–313.
- [206] B. Zamuner and F. Dupoirieux, *Numerical Simulation of Soot Formation in a Turbulent Flame with a Monte-Carlo PDF Approach and Detailed Chemistry*, *Combustion Science and Technology* **158** (2000), 407–438.
- [207] B. Zhao, Z. Yang, M.V. Johnston, H. Wang, A.S. Wexler, M. Balthasar, and M. Kraft, *Measurements and Numerical Simulation of Soot Particle Size Distribution Functions in a Laminar Premixed Ethylene-Oxygen-Argon Flame*, *Combustion and Flame* **133** (2003), 173–188.
- [208] X. Zhou, Z. Sun, G. Brenner, and F. Durst, *Combustion Modeling of Turbulent Jet Diffusion H₂/air Flame with Detailed Chemistry*, *International Journal of Heat and Mass Transfer* **43** (2000), 2075–2088.
- [209] A. Zucca, D.L. Marchison, A.A. Barresi, and R.O. Fox, *Implementation of the Population Balance Equation in CFD Codes for Modeling Soot Formation in Turbulent Flames*, *Chemical Engineering Science* **61** (2006), 87–95.

Lebenslauf

Persönliche Daten

Name	Massimiliano Di Domenico
Geburtsdatum	24.10.1977
Geburtsort	Rom (Italien)
Staatsangehörigkeit	Italienisch

Schulbildung

1983-1988	Scuola elementare “Massimiliano Kolbe”, Rom
1988-1991	Scuola media “Domenico Savio”, Rom
1991-1993	Instituto Tecnico Industriale, Rom
1993-1996	Instituto Tecnico Aeronautico “Francesco de Pinedo”, Rom

Studium

1996-2001	Universitá degli Studi di Roma “La Sapienza”, Facoltá di Ingegneria Aerospaziale, Rom
März 2002	Laurea in Ingegneria Aerospaziale

Berufliche Tätigkeit

März 2002-Juli 2002	Entwicklung und Optimierung eines Strömungscodes am “Dipartimento di Meccanica e Aeronautica”, Facoltá di Ingegneria Aerospaziale, Rom
seit 2002	Wissenschaftlicher Mitarbeiter am DLR in Stuttgart, Institut für Verbrennungstechnik